Development and application of *in vitro* approaches to assess the interactions of aerosolised drugs with pulmonary mucus

Safar M. Alqahtani, BSc. Pharm., MSc.

Thesis submitted to the University of Nottingham for the degree of Doctor of Philosophy in Pharmacy

December 2018

Abstract

Studies centered on pulmonary drug delivery have primarily focused on new device technologies to improve the generation of aerosols and their deposition in the respiratory system. Although considerable progress has been made in this field, no significant superior treatment of respiratory diseases has been achieved in recent times. One of the principal reasons is a scarcity in knowledge concerning inhaled/aerosol drug fate post-deposition in the lungs. The first barrier encountered by inhaled drugs in the pulmonary system is the mucus layer. This plays a protective role that is believed to be largely achieved by its ability to act as a physical barrier but also hinders molecular diffusion.

The impeding nature of the mucus on aerosolised drug permeation is poorly understood. Indeed, the effects of direct interactions between mucus and inhaled drugs have been largely overlooked and most of the available evidence on mucus-drug interactions are related to the gastrointestinal tract.

In this doctoral thesis, the main aim was to gain a better understanding of the relationship between the physicochemical properties of aerosolised pulmonary agents and their diffusion across the pulmonary mucus layer. This knowledge would provide valuable information for the development of more effective pulmonary agents.

The first objective was to develop and characterise an *in vitro* mucus model suitable for drug permeation studies. That was comprised of a thin mucus layer derived from pig trachea covering the semi-permeable membrane of Transwell® inserts. Rheometric measurements on pig tracheal mucus secretions after a

Abstract

cleaning procedure to remove blood contaminants demonstrated that the obtained mucus was non-Newtonian. Furthermore, cryogenic-scanning electron microscopy (cryo-SEM) revealed pore sizes with diameters of ~400 ± 200 nm. The barrier properties of the mucus model were verified by measuring the diffusion of various fluorescent dyes across mucus layers coating the Transwell® inserts. This revealed that the physicochemical properties of the compounds influenced their permeation rate with lipophilic dyes preferentially binding to the mucus layer.

A global metabolic profiling approach was applied to characterise the low molecular weight compounds present in pig tracheal mucus before and after the cleaning procedure. A total of 816 metabolites were common to both sets of raw and cleaned mucus samples. Approximately 50% of those were lipids, products of amino acid metabolism and carbohydrate metabolism, which was in line with the previously reported composition of human bronchial mucus.

A deposition system consisting of a Penn-Century MicroSprayer® mounted into a holder glass desiccator was successfully assembled to allow aerosolisation of test molecules at the surface of the mucus layers. After optimisation of the distance between the MicroSprayer® and the Transwell® inserts, the volume of the spray and the geometrical arrangement of the Transwell® inserts underneath the spray, a reproducible dose could be delivered onto four Transwell® inserts.

Ipratropium bromide, glycopyrronium bromide, salbutamol sulphate, formoterol and indacaterol maleate were chosen as model pulmonary agents to investigate the effect of drug physicochemical properties on their interactions with airway mucus using the *in-vitro* mucus model and aerosoliser system previously developed.

Abstract

The extent of drug retention within the mucus layer varied between the compounds tested. Although no significant correlation could be established due to the low number of drugs studied, logP appeared the most important physico-chemical parameter driving drug affinity for pulmonary mucus.

This PhD thesis has led to the development of simple *in vitro* systems to investigate the effect of the mucus layer on drug fate in the lungs and has identified mucus as a possible barrier to drug diffusion, in particular, for lipophilic compounds.

Acknowledgments

In the name of Allah, the Most Gracious and the Most Merciful. All praise to Allah for the strength and his blessing in completing this work.

Foremost, I would like to express my sincere gratitude to my supervisor, Dr. Cynthia Bosquillon, for accepting me as a member of her research laboratory and for her belief in my ability to complete this work. I highly appreciate her continuous support of my research, as well as for her motivation, enthusiasm, patience, and immense knowledge. She shared every single concern about my project and her office door was always open to me, so I never hesitated to knock on her door to ask about any difficulties, and she always helped me to overcome my obstacles and suggested new ideas to foster my creative thinking. She guided me throughout the whole period of my research and the writing up of this thesis. She was like a member of my family and directed me on the right path in a humble manner, always keeping a sense of humour when I lost mine. I could not imagine having a better supervisor and mentor for my research.

Besides my supervisor, I would like to thank my co-supervisors, Prof. Clive Roberts and Dr. Snow Stolnik-Trenkic, for their insightful comments, encouragement, and challenging questions that helped me to be more creative in fulfilling the main aim of this work.

Many thanks go to Al-Kharj city, Saudi Arabia, where my sponsor is located, Prince Sattam bin Abdulaziz University (PSAU). This work would not have been possible without the financial support of PSAU. Despite the fact that I am not required to repay PSAU's generous sponsorship, I feel strongly that this is a

Acknowledgments

Acknowledgments

technique. I am also thankful to Dr. Franco Falcone and his PhD student, Mohammed Alissa, for allowing me use the SDS-PAGE technique and assisting me in their laboratory.

My metabolomics study was facilitated by the presence of several individuals. I convey a special acknowledgement to the staff and students at the Centre for Analytical Bioscience (CAB), BSB, School of Pharmacy, University of Nottingham, who made an impact on this work due to their invaluable experience related to several of the LC-MS instruments. I wish to express my special thanks for their continuous support and help, in particular to the centre's research leader, Prof. David Barrett, and the chief experimental officer, Dr. Catherine Ortori. Also, my gratitude goes to the mass spectrometry research officer, Dr. Salah Abdelrazig, and the former PhD students, Dr. Ngamratanapaiboon Surachai and Dr. Mohammed Al-Natour, for their guidance regarding the untargeted metabolomics characterisations of pig tracheal mucus. The period that I spent it in the metabolomics field gave me many valuable insights which will help my society after I return to Saudi Arabia.

Although I do not know their names, I wish also to thank the construction workers in my neighbour's building who supplied me with free timber so I could engage in my hobby for this research when I became a joiner, to some extent, and made the stand as well as the introduced internal surface of my developed aerosoliser system.

I would also like to thank all of the friends whom I have made during my stay in Nottingham. I cannot mention all of their names, as these would fill several pages, but thanks for all the laughs, coffees and great company. Thanks for always cheering me up during the darkest times of my PhD journey with a

Acknowledgments

barbeque, theme park trip, or a quick trip to discover more about the UK during our educational journey.

I am deeply indebted to my brothers and sisters who supported me in every possible way to ensure the completion of this work, especially my family's mathematician, Dr. Zuhur Alqahtani, the beautiful mind who advised me on some of the more complicated calculations within this thesis.

My gratitude also goes to my little angels, my sons, Yazan and Taym, who arrived during this work. I remember Yazan's birth, who arrived at midnight after a labour of 18 hours. Although my experimental batch for that day was discarded, I received the most beautiful gift from Allah, my firstborn son. Meanwhile, Taym's arrival did not wait for me to finish my experiment in the laboratory. I just received a call to come to home as soon as possible as the new arrival was coming soon. Basically, he did not appreciate the long laboratory preparation I have been engaged in that day and refused to wait for a short while so that I could finish my experiment. Instead, he insisted on entering the world, regardless of how important that experiment was, as he knew that I would be the happiest man ever if I saw him.

My small children, I feel sorry for not being able to be at home with you most of the time. I hope you will forgive your father for those days where I went to the laboratory while you were still asleep in the morning and returned at night after you were in bed, without seeing you. However, I would like to thank you both for crying every night, which I felt sounded almost better than a Beethoven symphony. These melodies that awoke me every night made me constantly aware of my responsibility to give you a better life through completing this work.

Acknowledgments

Words fail to express my appreciation of my wife, Nora. She was always there, cheering me up, and stood by me through both the good times and the bad. I cannot thank her enough for taking responsibility for looking after our family. She woke me up every morning, prepared breakfast and put snacks in my backpack. When I returned home in the evening, a delicious dinner was awaiting me, and she never once complained about the monotony of these days for her. She has been very patient during my PhD journey, and I admit that I am lucky to have a woman like her beside me.

My father, Moraya - how can I acknowledge this man! I tried to write something down, rubbed it out, rewrote it, and rubbed it out again, trying to express my feelings about the most powerful man in my life. From my childhood, I was compelled by my curiosity to asking constant, annoying questions to find out the whys and wherefores of things and he answered all of my questions, no matter how basic they were. I do not remember a day when I asked him to register me for a scientific club or a training course and he turned me down. He has always encouraged me and my brothers and sisters and continues to do so, in an incredible way, reminding us of the importance of being knowledgeable in order to make our mark in this world. "Thanks, my father." I write it from the bottom of my heart.

Acknowledgments

Last but not the least, what can I say to thank the special one? What can I say to a person who was illiterate and refused to go to the school to take care of her children and their education until they had graduated as physicians, a dentist, pharmacists, college professors, an investigation officer, and an information technologist, after which she attended elementary school herself and graduated at the age of fifty? "Thanks", my mother, Thamra! I cannot think of more appropriate words to say besides that one simple, yet powerful word. She is worthy of gratitude every single day for the way in which she raised her family, maintained her grace, balanced schedules, and blessed others. Today, and every day, I am thankful for the gift she is, as a mother, friend, mentor and hero. Many people never get to meet the person they look up to but I was fortunate enough to be raised by mine. I wish to thank her for humbling herself by putting my needs (and more often wants) above her own. Thanks for sacrificing innumerable hours to help with projects, take care of ailments, or simply spend a huge amount of time bonding with me. Thanks for the constant prayers over and for me. Thanks for the old days, when a home-cooked meal was waiting for me after a long day. Thanks for displaying grace amidst storms. Thanks for showing me how to be strong. Thanks for laughing with me so hard that we cried. Thanks for memories I will never forget, and a legacy I will feel proud to continue.

Table of contents

List of figures

List of tables

Abbreviations

ABC transporters	ATP-binding cassette
ACI	Anderson cascade impactor
AIC	Air-liquid interface
APCI	Atmospheric pressure chemical ionisation
APIs	Active pharmaceutical ingredients
BSA	Bovine serum albumin
CC	Cascade centripeter
CE	Capillary electrophoresis
CFC	Chlorofluorocarbon
COPD	Chronic obstructive pulmonary disease
CV	Coefficient of variation
dd-H_2O	Double-distilled water
DI	Direct injection
DMSO	Dimethyl sulfoxide
DPIs	Dry powder inhalers
EICs	Extracted ion chromatographs
ESI	Electrospray ionisation
FDA	Food and drug administration
FIB-SEM	Focused ion beam-scanning electron microscopy
FITC	Fluorescein isothiocyanate isomer I
FT-IR	Fourier-transform infrared
GC	Gas chromatography

GIT	Gastrointestinal tract
HBSS	Hank's balanced salt solution
HEPES	4-(2-hydroxyethyl)-1-piperazineethanesulfonic acid
HFA	Hydrofluoroalkane
HILIC	Hydrophilic interaction chromatography
HMDB	Human metabolome database
LC	Liquid chromatography
LCC	Liquid covered culture
LC-MS	Liquid chromatography mass spectrometry
LDI	Laser desorption ionisation
LLOQ	Lower limit of quantification
MDIs	Metered dose inhalers
MS	Mass spectrometer
MSLI	Multistage liquid impinger
MW	Molecular weight
NGI	Next generation impactor
NMR	Nuclear magnetic resonance
OATs	Organic anion transporters
OCTs	Organic cation transporters
OPLS-DA	Orthogonal partial least squares discriminant analysis
PCA	Principle component analysis
PEG	Poly(ethylene glycol)
PK	Pharmacokinetic
pMDIs	Pressurised metered dose inhalers
PSA	Polar surface area

QTOF	Quadrupole–time-of-flight.
RCTs	Randomised clinical trials
RPC	Reversed phase chromatography
RT	Retention time
SD	Standard deviation
SDS	Sodium dodecyl sulfate
SDS-PAGE	Sodium dodecyl sulfate-polyacrylamide gel electrophoresis
SEM	Standard error of the mean
SLC	Solute carrier
SPE	Solid phase extraction
TEER	Transepithelial/Transendothelial Electrical resistance
TEM	Transmission electron microscopy
TICs	Total ion chromatographs
TOF	Time-of-flight
TSI	Twin stage impinger

Chapter 1 - General introduction

1.1. Pulmonary drug delivery

As an important boundary between the environment and the organism, the respiratory system is exposed to particle pollution, potential pathogenic microorganisms and toxic gases during inspiration (Plopper, 1996). A sophisticated host defence system is present in the respiratory system and can be found from the nostrils to the alveoli, to act as a protection mechanism from offending agents (Twigg III, 1998). The system includes air filtration, mucociliary clearance, sneezing, and coughing (which is more of a mechanical defence mechanism). Chemical defence mechanisms come about through surfactants, antioxidants, and anti-proteases. The immune system has a defensive role, which tightly controls inflammation and neutralises assaults to prevent damage to alveoli (Twigg III, 1998, Nicod, 1999).

From a drug delivery perspective, host defence systems need to be overcome as these barriers can hinder therapeutic drugs in reaching targeted areas throughout the respiratory system.

Lung-targeted therapy for delivery of active principles to ease several pulmonary symptoms started with the most recent common ancestor of all living humans more than 4000 years ago when deadly nightshade (*Atropa belladonna*) leaves were smoked to treat cough symptoms (Gonda, 2000, Patton and Byron, 2007).

Ever since, in particular in the last 60 years, important progresses have been made in the discovery of new drugs suitable for pulmonary delivery. Currently, effective delivery to the respiratory system is achieved by more than 30 active

pharmaceutical ingredients (APIs) (Hou et al., 2015, Forbes et al., 2011). Nowadays, drug delivery using the pulmonary system represents the best option to treat asthma, chronic obstructive pulmonary disease (COPD), cystic fibrosis, and other lung diseases. However, it has also been explored as an administration route that is interesting and convenient for systemic delivery, particularly for drugs such as peptides and proteins that are inappropriate for oral delivery due to their rapid degradation by gastrointestinal tract (GIT) enzymes (Patton et al., 2004, Agu et al., 2001).

Several advantages have been noted for pulmonary delivery compared with other administration routes. It is a non-invasive route where patients' compliance is improved compared with the parenteral route. Also, the respiratory system represents a good candidate for systemic absorption because it provides a large surface area of ~140 m^2 in the alveolar area, whereas the upper airways represent 1–2 m^2 (Weibel and Gomez, 1962), with high solute permeability (Weibel and Gomez, 1962, Patton, 1996). Moreover, the alveolar region is known by its extensive vasculature with high blood flow (5 L/min), in addition to a thin diffusion path to the bloodstream with a length of 150 μm (Ducreux and Vanbever, 2007). Furthermore, the deposited high drug concentrations at the site of action would permit lower doses of administration and, hence, a significant reduction in side effects (Labiris and Dolovich, 2003). However, several physiological barriers need to be overcome by drug molecules to reach their site of action.

1.1. Lung physiological barriers to pulmonary drug delivery

The primary function of the lung is to ensure effective gas exchange (i.e., blood oxygenation and the removal of carbon dioxide from the body through inspired air and pulmonary blood distribution). However, at the same time, it prevents foreign materials (e.g., bacteria, pollen, particulates, tobacco smoke) from penetrating the system.

The respiratory system anatomy provides a number of barriers to the materials that are inhaled. For successful inhalation, these barriers need to be overcome to ensure effective penetration of the drug into the respiratory system and obtain the desired treatment outcome.

1.1.1. Human respiratory system anatomy

The lungs are very complex organs. The airways are commonly described as dichotomous branched systematic tubes where the branch number increases from the trachea moving to the bronchi to terminate at the alveoli.

Two functional regions divide the respiratory system into conducting and respiratory zones. The nasal cavity and sinuses, nasopharynx and oropharynx, larynx, trachea, bronchi, and bronchioles are part of the conducting airway, which condition and filter inspired air. From the trachea to the terminal bronchus, dichotomous branches form two daughter branches – characterised by shorter length and smaller diameters when compared with the parent bronchi (Weibel, 1991).

The number of branches for each new airway generation is doubled, and an exponentially increasing cross-sectional area is associated with each new

generation. Generation 0 (trachea) to 16 (terminal bronchioles) are the conducting zone. Generations 17 to 23 are bronchioles, alveolar ducts, and alveolar sacs, which comprise the respiratory zone (Figure 1.1.1). The number of branches from the bronchial tree to alveoli increases from 6 (minimum) to 28–30 (maximum) (Plopper, 1996).
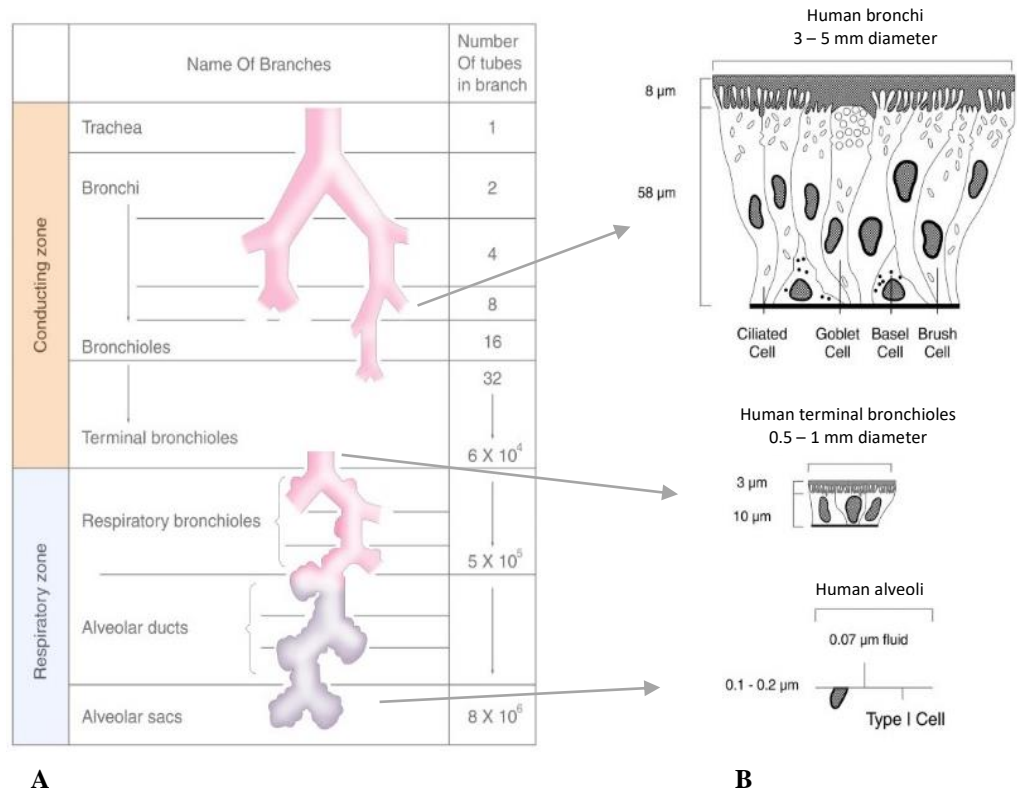
Figure 1.1.1. (A) Airways structure. Reprinted from Human Physiology, 2001. (B) Differences in regional epithelial cell thickness and epithelial lining fluid (reprinted from (Patton, 1996).

The alveolar epithelium and capillary beds provide an air–blood barrier (alveolar-capillary barrier) which allows gas exchange bye passive diffusion to take place. Passive diffusion occurs rapidly due to the extensive surface area and extreme thinness (0.1–0.5 μm) of the air–blood barrier (Plopper, 1996).

The lung parenchyma in which gas exchange occurs (alveolar capillary networks, alveoli, and alveolar sacs) represents approximately 85% of the total

lung volume. The bronchi and bronchioles (the conducting zones) comprise 6–10% of total lung volume, whereas the remaining volume consists of vascular nervous tissue (Plopper, 1996, Gehr, 1984).

Blood is supplied to the lungs through two circulation systems: the bronchial and pulmonary circulatory systems (Staub, 1991). The bronchial circulation, which is under high pressure, is part of the systemic circulatory system. Approximately 1% of cardiac output is received by the bronchial circulatory system, which supplies pulmonary blood vessels, airways (the conducting zone) and lymph nodes with nutrients and oxygenated blood as well as conditioning the inspired air (Staub, 1991).

In contrast, an extensive low-pressure vascular system forms the pulmonary circulation. The alveolar capillaries are perfused by this system to ensure that sufficient gas exchange and nutrients are provided to the alveolar walls.

Medium-sized bronchi and bronchiole walls reveal anastomoses between pulmonary and bronchial arterial circulations (Chediak and Wanner, 1990).

1. General introduction
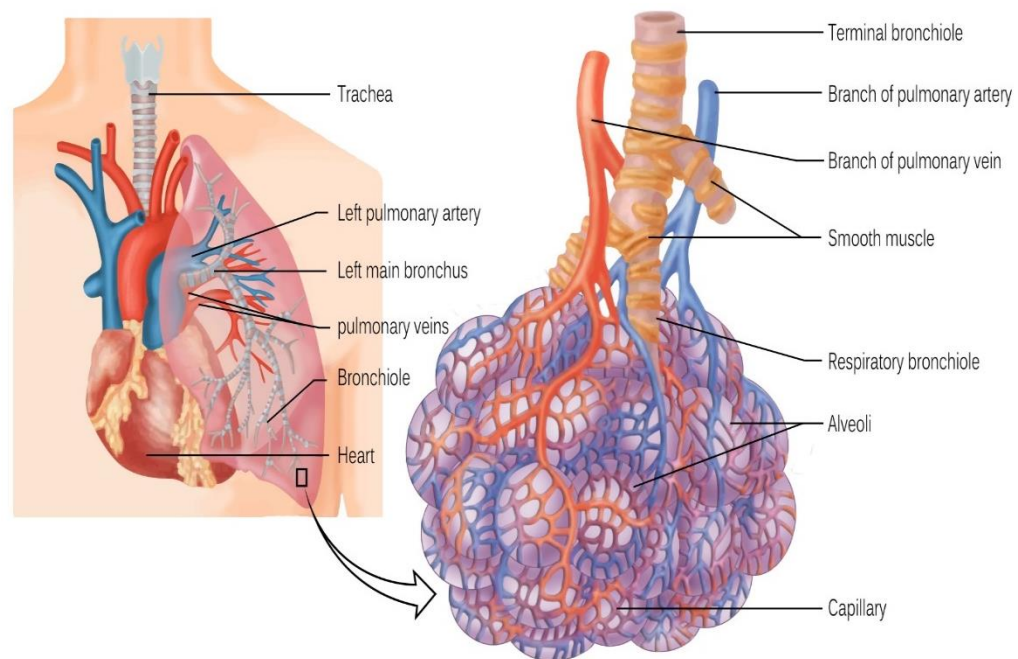
Figure 1.1.2. Human lung anatomy. Reprinted from Human Physiology, 2001.

These intimate interactions between the respiratory and circulatory systems by means of an intensive vasculature guarantee the required gas exchange for the organism to survive when oxygen is inhaled.

Transportation of inhaled oxygen occurs from the lungs to the blood, whereas carbon dioxide, the metabolic product, is eventually eliminated by exhalation after being transported from the blood to the lungs.

This process is called "respiration"; the combined two distinct movements of inspiration and expiration. About 500–600 mL of air is taken in by healthy lungs at a rate of about 5–6 L/min (Hughes, 2009). The regulation of respiration movements is performed by the contraction and relaxation of the diaphragm. Airway smooth muscle, a tissue that is attached to cartilage at the trachea back in the upper airways, also modulates the bronchomotor tone. Airway smooth muscle also surrounds the lower airways in the bronchi region. The main

function of airway smooth muscle is to contract as an effective pump to regulate bronchomotor tone, but also plays a part in the clinical conditions associated with inflammation events such as asthma, chronic bronchitis and cystic fibrosis (Panettieri Jr et al., 2008, Mitchell, 2009).

1.1.2. Airway epithelium

Epithelial cells form a continuous layer and line the entire respiratory system. The epithelium of the lungs undergoes continuous renewal because it is a dynamic tissue, with a 30–50 days turnover rate. It plays an important part in preserving normal function of the lungs. It maintains the air conduit from and to alveoli, and also acts as a barrier to foreign objects (e.g., bacteria, pollen, particulates, tobacco smoke) (Crystal et al., 2008).

The lung epithelium has been found to be composed of about 50 cell types. The major cell types are secretory, ciliated, undifferentiated, basal and columnar cells, whereas there are also other, less numerous cell types, such as neuroendocrine and neural cells (Crystal et al., 2008). From the conducting zone moving towards the respiratory zone, the cell types are varied to adapt the functional role and defence mechanisms for each region (Figure 1.1.3). The upper airway epithelium is known as a "pseudostratified epithelial tissue" which is composed of basal cells, secretory goblet cells and ciliated cells. The latter two types are tall cells and can reach a thickness of ~60 μm. This length helps the cells in their role of mucociliary clearance. Secretory Clara cells and thinner cuboidal cells characterise the bronchiolar epithelium. Finally, extremely thin (<100 nm) alveolar cell types I and II are located in the alveolar zone. Alveolar

macrophages (phagocytes) "patrol" the air-side of alveoli (BéruBé et al., 2010, Crystal et al., 2008, Patton and Byron, 2007).

As mentioned above, one of the functions of the lung epithelium is to provide protection of the respiratory system from foreign particles. It does so due to a number of defensive actions, including the production of anti-inflammatory, antioxidant and antibacterial molecules, and mucociliary clearance.

The second line of the defence mechanism against foreign objects takes place through intercellular junctions, which create an efficient selective and tight barrier against insults from the external environment. The barrier permeability is regulated by tight junctions that modulate molecule flow between apical and basolateral sides, where the "tightness" of the epithelial barrier appears to be reduced from the conducting to respiratory zones (BéruBé et al., 2010, Patton and Byron, 2007).
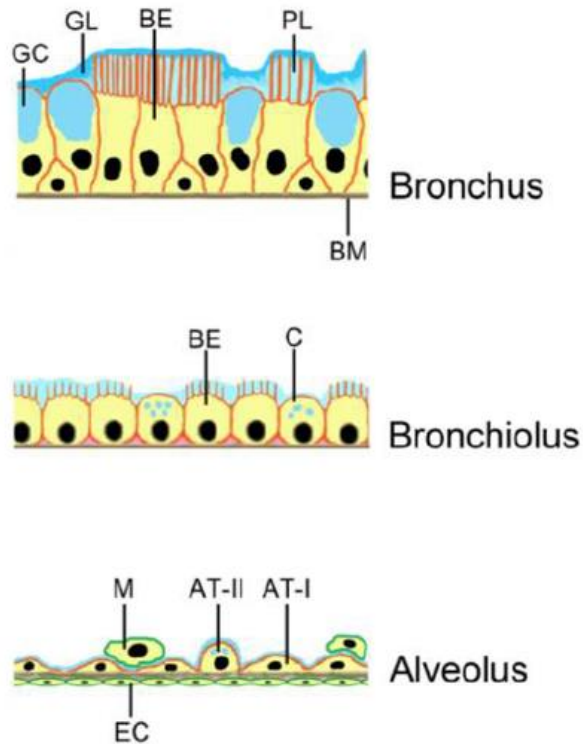
Figure 1.1.3. Respiratory system barriers. Major cell types of the lung epithelium: mucus-producing goblet cells (GC); basement membrane cells (BM); columnar bronchial epithelial cells with cilia (BE); Clara cells (C); AT-I cells (AT-I); AT-II cells (AT-II); endothelial cells (EC). Non-epithelial barriers: periciliary layer (PL) and gel layer (GL) of mucus, and alveolar macrophages (M). Reproduced from (Fröhlich and Meindl, 2015).

1.1.3. Non epithelial barriers

Two types of fluid line the epithelium of the respiratory system. The two fluids, mucus layer and surfactants, characterise the two areas of the airway system. Mucus is a complex hydrogel, secreted by goblet cells, that covers many epithelial surfaces within the human body. It consists of water, glycoproteins (mucins), proteins, salts, lipids, enzymes, DNA and cellular debris. The mucus layer that coats epithelial cells is the first barrier to an efficient drug delivery system. However, the presence of mucus is important for the protection and lubrication of the underlying tissue. Hence, the epithelial mucus layer protects

epithelial cells from contact with toxins and pathogens and lubricates the underlying tissue, which limits mechanical damage (Atuma et al., 2001).

In fact, the composition, thickness and microstructure of the mucus layer acts as a strong barrier to the deposited material, and prevents it from penetrating and reaching the underlying epithelium. Moreover, due to its viscoelastic properties, mucus is continuously cleared easily by the coordinated beating of ciliated cells, which is called the "mucociliary escalator" (Cone, 2009, Haghi et al., 2014, Lansley, 1993).

The rheological properties of mucus is due to its mucin content, which displays affinities for forming aggregated gels (mucus) with non-Newtonian properties (viscoelastic heterogeneous gel) (Quraishi et al., 1998). Therefore, the viscosity and elasticity of mucus will change in combination with shear rate and shear stress variations (non-linear). The deformation resistance decreases at high shear rates.

Mucin protein architecture is characterised by a preponderance of O-glycosylated serine/threonine-rich tandem repeat domains (Evans and Koo, 2009). The weak non-covalent links of glycoproteins is mainly responsible of the mucus gel flexibility, which suggests that they are easily disrupted by small shear forces (Bernkop-Schnürch et al., 2001)

The respiratory mucus layer thickness, 10–60 μm, is extensively reduced until replacement of mucus by a thin layer of alveolar surfactant of thickness ~0.07 μm that takes place in the alveolar region (Lai et al., 2009b, Patton and Byron, 2007).

The presence of alveolar surfactant characterises the alveoli. Alveolar surfactant is secreted by alveolar type II and Clara cells, which comprise a mixture of phospholipids and proteins.

Also, macrophages are found in the alveoli. These are also specialised cells which represent the first host defence mechanism in the alveolar epithelium. These cells engulf and then digest insoluble deposited foreign materials. These specialised cells also generate a number of pro- and anti-inflammatory extracellular proteins called "cytokines" (Haghi et al., 2014).

1.2.   Pulmonary drug delivery devices

Worldwide, the industry provides ~500 million inhalers for asthma treatment (Dalby and Suman, 2003). The main strategy of asthma and COPD treatment is inhalation of medications to reach the diseased region in the respiratory system. This can be attained by three major devices: nebuliser, "pressurized metered-dose inhalers" (pMDIs or MDIs) or "dry powder inhalers" (DPIs).

To choose which device is to be given to the patient is based mainly on the ease of patient usage and the device that provides the required drug dose with negligible side effects. A systematic review on the clinical effectiveness and cost-effective studies for these different inhalation devices has not been carried out.

1.2.1. MDIs

MDIs are the most commonly used type of inhaler because they are quick and convenient to use. They are also relatively inexpensive. A MDI is a small device that consists of a pressurized canister, the primary tool that holds the drug to be

aerosolised. Many asthma bronchodilators are administered by an MDI (Georgopoulos et al., 2000). They are also used by patients who suffer from other lung diseases, such as COPD and bronchitis.

A MDI comprises five parts: drug, propellant, metering valve, canister and mouthpiece. A compressed/liquefied gas is used as the propellant in the MDI. Most pulmonary agents are poorly soluble in propellant and, consequently, they are formulated as micronized suspensions. The propellant gas in MDIs is mainly hydrofluoroalkane (HFA). Chlorofluorocarbon (CFC) gas was considered to be the propellant of choice due to its high chemical stability, non-flammability, low pulmonary toxicity, purity, and compatibility with a container-closure system before it was banned due to environmental concerns. Nevertheless, MDIs containing a HFA have some advantages. For example, salbutamol MDIs with a HFA propellant are softer, aerosols are warmer, and they necessitate lower spray force than a CFC based inhaler (Boccuzzi et al., 2000). Also, they are known to be more ozone-friendly than CFC propellants (Ali, 2010).

Figure 1.2.1 shows the primary functional parts of an MDI.
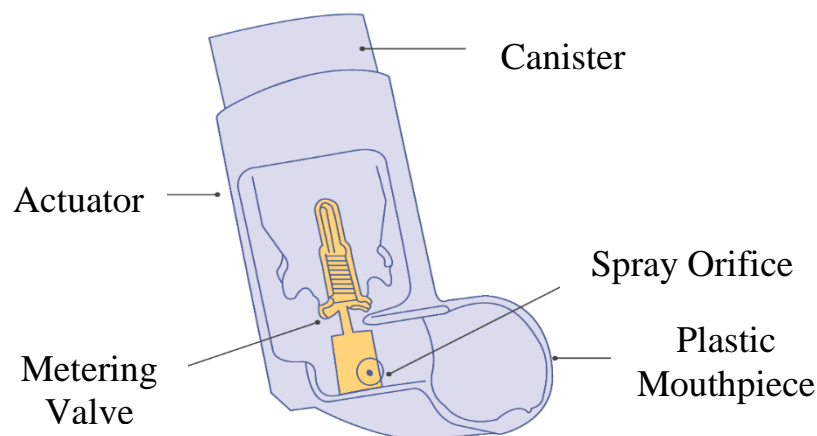
Figure 1.2.1. Primary functional parts of an MDI in which the drug formulation is loaded in the canister. Taken from (Ali, 2010).

1.2.2. DPIs

A DPI is a breath-activated inhaler that aerosolises a dose of micronised drug in the solid state. The drug is generated, weighed, and packed in the container in a powder form, so decomposition or microbiological contamination are minimal compared with solution or suspension formulations (Frijlink and De Boer, 2004).

The dispersion of the powdered drug into particles occurs by the patient's inspiration force instead of by chemical propellants. Compared with a MDI, the inhalation strength required in a DPI is greater.

Four basic steps occur when a DPI is operated: dose metering, aerosolization, disaggregation, and direction of the aerosol towards the patient's mouth. These features are achieved thanks to the inhaler primary and secondary functional parts. All types of DPI marketed currently share similar primary parts which determine inhaler performance with regard to: generating a fine-particle fraction; dose delivered; de-agglomeration of the powder (Frijlink and De Boer, 2004). All the primary parts are assembled to house a pre-measured single/multiple dose unit. The secondary features are usually for enabling ease of handling and to protect the drug formulation from moisture.

Powder Formation

Dose measuring
System

Mouthpiece

Dry powder
De-agglomeration
Principle
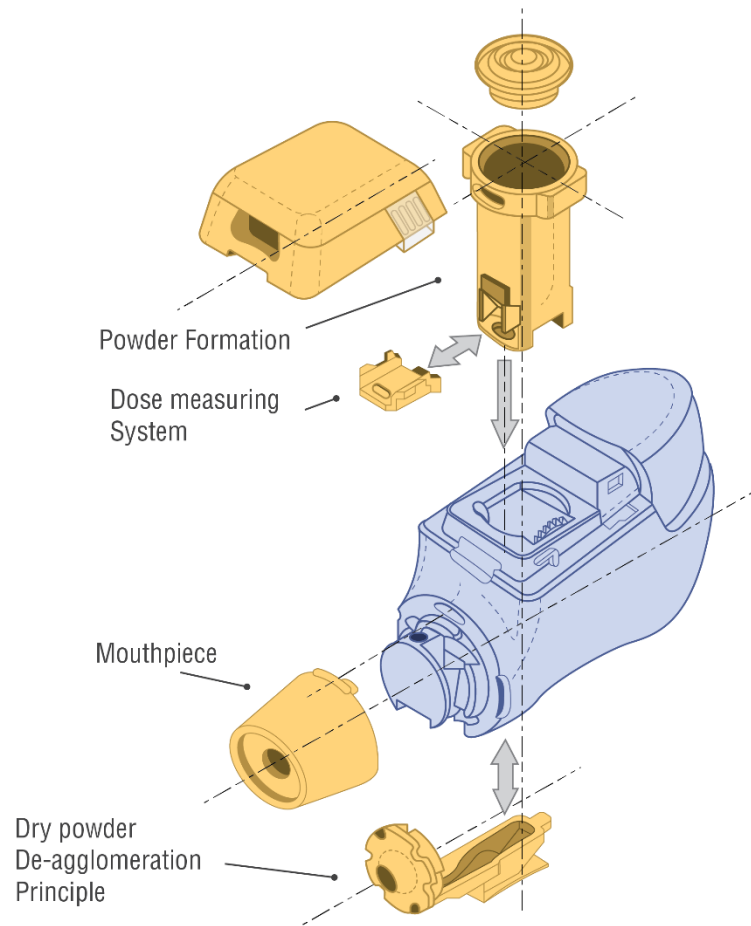
Figure 1.2.2. Primary functional parts of a classic DPI (schematic). Reproduced from (De Boer et al., 2006).

There is no standardised mode of operation for DPIs, in contrast to MDIs due to a wide variety of designs. The major drawback of DPIs is that the patient must generate a flow rate of $\geq$30 L/min to disaggregate the dry powder. Hence, the effectiveness of DPIs is highly dependent on the age, sex, breathing cycle, and disease status of the patients.

1.2.3. Nebulisers

Nebulisers have been available since the mid-19th century, when atomisers were invented, and are now considered to be a common method for producing medical aerosols.

In the nebulisers, compressed air, oxygen, or ultrasonic power is used to break drug solutions/suspensions into droplets for inhalation (i.e., a device converts the drug into a fine mist).

Nebulisers are categorised into these two forces: (1) jet (or pneumatic) small-volume nebulisers; (2) ultrasonic nebulisers. Typically, the administration of aerosols is through a mask or mouthpiece. Aerosol droplets are generated after applying a gas jet or ultrasonic waves.

Jet nebulisers depend on the venturi effect, whereas ultrasonic nebulisers convert alternating current to generate high-frequency acoustic energy using the converse piezoelectric effect (Rau, 2002).

Differences in the brands of nebulisers have important roles and perhaps a greater effect than formulation differences (O'Riordan, 2002). Several advantages of jet nebulisation have been noted, including that usage effectiveness involves simple, tidal breathing, and that dose modification and adding ingredients is possible. Drawbacks include the intake duration as well as equipment size. Figure 1.2.3 shows the primary functional parts of a jet nebuliser.

The second type of nebuliser employs ultrasonic methods and usually produces a higher output compared with jet nebulisers but, nevertheless, the average aerosol particle is larger (Rau, 2002). Although ultrasonic nebulisers share similar advantages to jet nebulisers, the former are more expensive and

considered to be fragile compared with the latter. However, drug degradation is highly likely in ultrasonic nebulisers, and they may not nebulise suspensions very well.

Overall and regardless of the applied force, the advantages of nebuliser are their ease of use as well as the high doses that can be delivered. Moreover, they are free of propellant and effective in paediatric and elderly patients. However, the major disadvantages of nebulisers are their large size as well as the required cleaning steps. Furthermore, a power source is required for the machine to be running in addition to the noise produced when in operation.
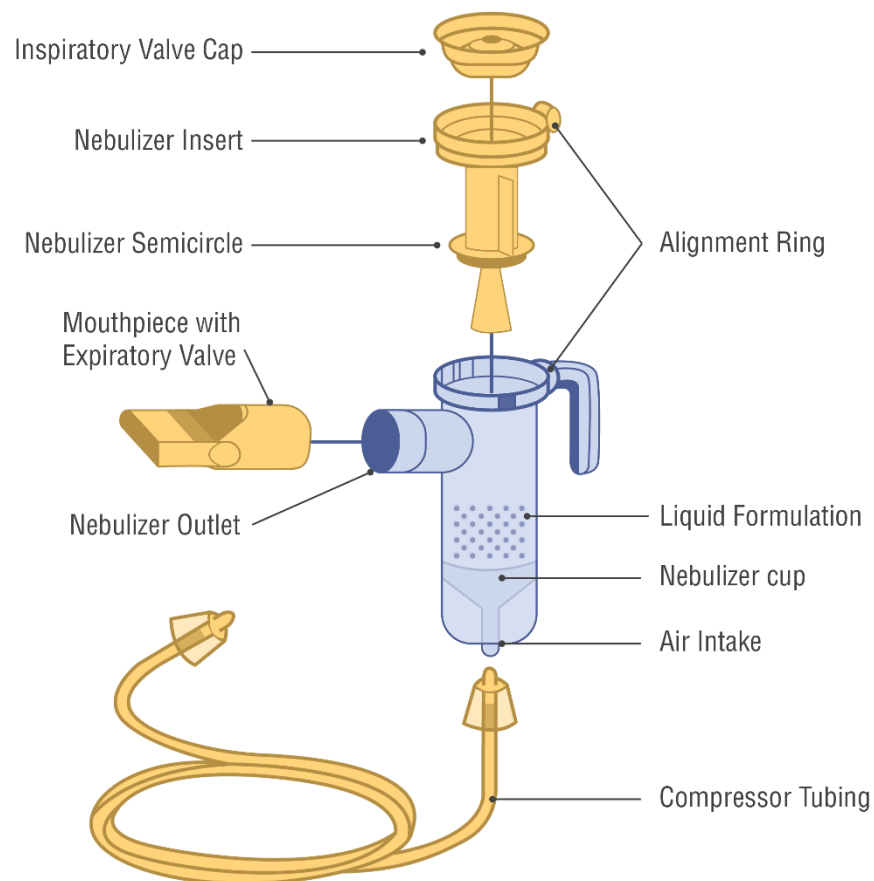
Figure 1.2.3. Primary functional parts of a jet nebuliser. Reproduced from PARI Respiratory Equipment Incorporated (Midlothian, VA, USA).

1.3.   Intrapulmonary aerosol deposition

The fundamental role of inhalation therapy is to deposit inhaled aerosols on the lung wet surface. The amount of aerosols deposited and their deposition sites depends on several factors, including both the physical properties of the inhaled aerosol (such as size and density) and the specific features of the subject who inhales these aerosols (such as respiratory flow rate, mode of breathing (oral or nasal), and tidal volume) (Schulz, 1998).

The three mechanisms described below represent the major aerosol deposition mechanisms in the lung (Schulz, 1998):

1. **Impaction:** the probability of an aerosol being deposited in the lung by impaction depends on their mass (which is defined by size and density) and on their travelling velocity in the airways.

2. **Sedimentation:** the probability of an aerosol being deposited in the lung by gravitational sedimentation depends on its residence time in each lung compartment and its settling velocity.

3. **Diffusion:** The diffusional deposition mechanism occurs by Brownian motion of surrounding gas molecules for only the smallest aerosols (i.e., it is effective for aerosols of size <0.5 μm).

The aerodynamic diameter of aerosols is the key factor determining the effective deposition of drug aerosols in the lung. For efficient entry from the conducting to respiratory zone, it is deemed essential that the aerodynamic diameter of an aerosol ranges between 1 μm and 5 μm (Patton and Byron, 2007, Patton et al., 2004).

When discussing the deposition of aerosols, the respiratory tract is commonly divided into two sections: (1) the extra-thoracic region, which is divided into

nasopharyngeal and oropharyngeal spaces, and (2) the intra-thoracic region, which is composed of tracheobronchial and alveolar spaces. When the respiratory tract is exposed to aerosols, different sizes of aerosols will be deposited in different regions in the lung (Figure 1.4.1) Typically, larger aerosols will not pass beyond the pharynx, whereas smaller drug aerosols will penetrate the airway, where they deposit in bronchial and alveolar regions (Newman, 1985). In particular, in the nasopharyngeal and oropharyngeal spaces, where inertial impaction is the major deposition mechanism and a higher flow rate is present, ~80% of 10-μm aerosols are captured. In contrast, the dominant deposition mechanisms in the tracheobronchial region are inertial impaction and gravitational sedimentation, where aerosols <5 μm are deposited. The end point is in the alveolar region, where the key deposition mechanism is gravitational sedimentation, whereas aerosols of size <0.5 μm are deposited by diffusional displacement (Schulz, 1998).
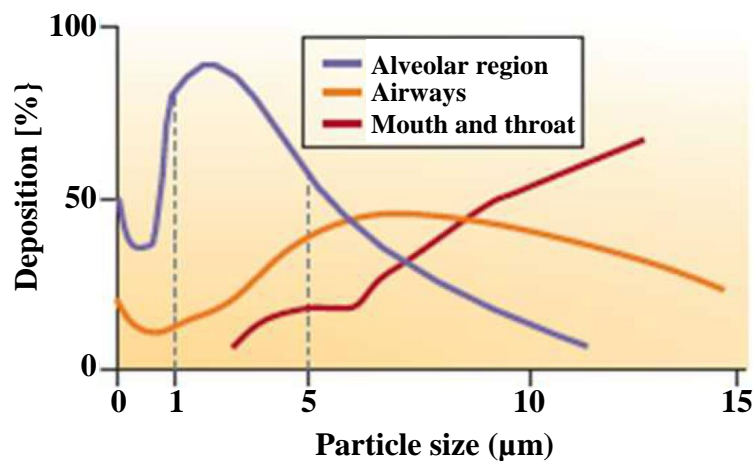
Figure 1.3.1. Regional deposition of inhaled aerosols in the lung as a function of aerodynamic diameter. Reproduced from (Patton and Byron, 2007).

Also, one of the important parameters in the regional deposition of aerosols within the lung is the flow rate. Indeed, if inhalation by the patient is too forceful, most of the aerosols will likely deposit in the extra-thoracic region, while deposition in the deeper part of the lung will, consequently, decrease (Patton and Byron, 2007).

1.4. Fate of inhaled aerosols after deposition on the lung epithelium

The fate of inhaled aerosols after being deposited in the lining of the lung has not yet been entirely revealed. It has been alleged to be patient-dependent, and hence affected by the physiological parameters of breathing of the patient (tidal volume, inhalation air flow, and respiration rate). However, it can also be controlled by manipulating the physicochemical characteristics of the APIs and finished products (Newman, 1985).

Inhaled aerosols can be in a form of "micronised" particles or liquid droplets. In the case of micronised particles, they need to be dissolved in the lining fluid so that the active ingredient can be absorbed across the epithelium tissue (Patton et al. 2004). The thickness of lining fluids varies from the upper airways to the respiratory system end point (alveoli), and micronised particles that deposit the deepest in the lungs are immersed in the smallest volume of lining fluid (Olsson et al., 2011).

If the micronised particle dissolves, the free pulmonary agent molecule will move across the mucus layer and then reach the epithelium depending on its physicochemical properties (hydrophobicity, molecular weight, charge).

1.4.1. Drug absorption

The absorption route depends on the deposition site of aerosols and on the characteristics of the drug. Absorption is highly dependent on the physicochemical properties of the medicinal compound, including solubility and molecular weight (Ibrahim and Garcia-Contreras, 2013). Different routes are described for drugs to permeate across the epithelium tissue, including active and passive transport mechanisms (Figure 1.4.1) (Ibrahim and Garcia-Contreras, 2013, Olsson et al., 2011):

Paracellular transport

Paracellular transport is mostly regulated by the tight junctions that form channel points between epithelial cells, consequently creating an intact physical barrier. Tight junctions consist of the transmembrane proteins occludin, claudin, and junctional adhesion protein. They control the passive diffusion of ions and small charged solutes. Assessment of the tightness of tight junctions is performed by transepithelial electrical resistance (TEER) measurements. It has been shown that from the trachea to the bronchi, the electrical resistance is decreased but in the alveoli, it increases again. However, due to the high blood flow and the thin walls of the alveoli compared to regions prior to the distal airways, it is commonly acknowledged that paracellular transport is the highest in the alveolar region (Dorsainvil White et al., 2016, Pacurari et al., 2017, Eaton et al., 2009). Paracellular transport via tight junctions has been reported to be the preferred absorption route for small hydrophilic drugs, and small peptides such as insulin.

Transcellular transport

The major transport mechanism for a drug to be efficiently absorbed, is the transcellular route. The latter is considered to be mainly by passive diffusion,

nevertheless, diffusion mechanisms regulated by vesicles like caveolae or transport proteins are also possible.

Passive diffusion is the tendency of a molecule to be transferred to a point of lower concentration coming from a point of higher concentration, i.e., according to a concentration gradient. The main route of absorption of lipophilic inhaled molecules seems to be transcellular diffusion (Olsson et al., 2011, Patton et al., 2010).

Transporters have been known to play a key part in the absorption and distribution of drugs alongside passive diffusion (Sugano et al., 2010). Transporters can improve cellular uptake by facilitating the permeation of drugs across the cell membrane, particularly for those that do not easily diffuse through the cell membrane by passive diffusion. Transporters make use of different mechanisms to fulfil their functions, such as counter-ion transport and membrane potential. This is the case for the solute carrier (SLC) transporters family, which includes organic cation transporters (OCTs) and organic anion transporters (OATs). Nevertheless, other transporter types efflux molecules out of the cell membrane through an ATP-dependent mechanism, as seen in the ATP-binding cassette family (ABC transporters).

It is believed that transporters work together with passive diffusion to influence the absorption of a drug molecule into the epithelial cell layer. Transporters also seem to have a role in modulating drug intracellular concentration, thereby affecting their efficacy and toxicity levels (Ibrahim and Garcia-Contreras, 2013). Many transporters have been found to be expressed in the pulmonary system; nevertheless, their role in the pharmacokinetics and pharmacodynamics of

inhaled pulmonary agents is still unclear (Bosquillon, 2010, Gumbleton et al., 2011).

The *vesicle-mediated* absorption process occurs when a drug molecule is transferred into the cell cytoplasm using caveolae (membrane lipid raft vesicles). These vesicles are small invaginations ranging from 10 nm to 100 nm located on the cell membrane which are believed to be involved in the transport of macromolecules such as proteins. Formation of these vesicles is typical of alveolar epithelial cells (Kim and Malik, 2003).
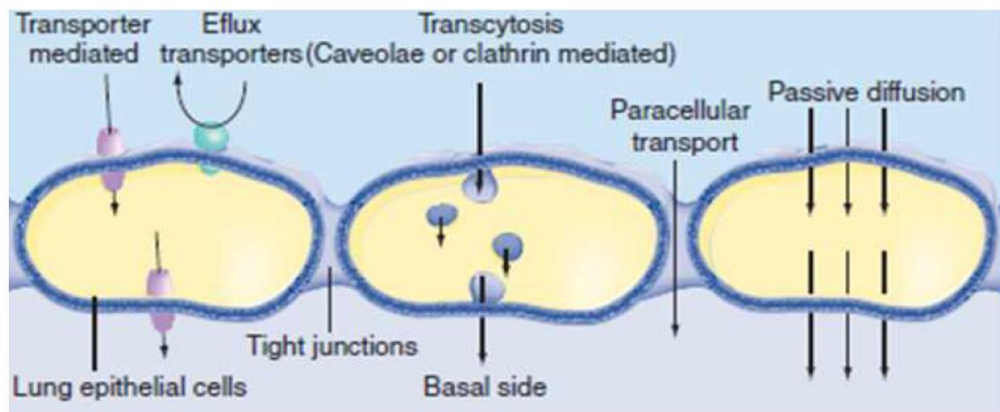
Figure 1.4.1. Possible mechanisms of inhaled drugs absorption across lung epithelial cells. Reproduced from (Ibrahim and Garcia-Contreras, 2013).

1.4.2. Drug elimination

The lungs have distinctive mechanisms for elimination of xenobiotics from their surface. Once landed on the deposition site, drugs face three possible clearance mechanisms: the primary innate defence process by mucociliary clearance, lymphatic circulation after uptake by macrophages, and degradation by enzymes.

1. General introduction

Aerosols which are deposited in the trachea and bronchi (the upper airways) and insufficiently absorbed are eliminated by mucociliary clearance and this, eventually, will cause a significant reduction in the amount of absorbed molecules. Mucociliary clearance, as mentioned above, is the first line in the lung's defence against foreign materials deposited in the tracheobronchial region. The clearance mechanism occurs by continuous removal of the mucus gel layer towards the mouth by the wave-like movement of ciliated cells (Cone, 2009, Haghi et al., 2014, Ibrahim and Garcia-Contreras, 2013, Lansley, 1993).

The pulmonary lymphatic system contributes to the clearance of protein and fluid that have filtered from the vascular compartment into the lung tissue and thus, assists in preventing fluid accumulation in the lungs.The lymphatic vessels are located near the small airways and blood vessels, but are not present in the alveolar walls (Leak and Jamuar, 1983, Puchelle et al., 1995).

Xenobiotic substances can undergo degradation by enzymes such as the metabolic cytochrome P450 enzymes, which are found in the cytoplasm of lung epithelial cells. Nevertheless, it is worth mentioning that this enzymatic activity is less in the lung compared with that in the liver (Ibrahim and Garcia-Contreras, 2013).

However, it is noteworthy that the elimination mechanisms and clearance of foreign materials (in particular insufficiently absorbed aerosol) are deemed necessary in the respiratory system because their long-term presence in the lung epithelium might result in chronic lung inflammation. Secretion of excessive inflammatory mediators may cause a severe lung injury (Oberdörster et al., 1992).

1.5. Mucus as a barrier for drugs

As described previously, mucus is a gel and thus, exhibit properties of a soft, deformable, elastic solid and a viscous fluid (Fahy and Dickey, 2010). Normal mucus is composed of 97% water and 3% of mucins, non-mucin proteins, lipids, salts, and cellular debris.

Mucins can be either secreted or membrane-bound; the former are important for mucus viscoelasticity, whereas the latter are involved in pathogen binding and cellular adhesion (Ha and Rogers, 2016). Mucins are encoded by MUC genes and synthesised in both goblet cells (secreted mucins) and submucosal glands (membrane-bound mucins). There are 17 discovered genes that encode mucins in the human genome (Fahy and Dickey, 2010). Significant differences have been observed in the formation and subsequent glycosylation of different mucins, which implies they fulfil specific roles in specific physiological environments (Rose and Voynow, 2006). Two of these MUC genes, MUC5AC and MUC5B, are strongly expressed in the human airways.

Mostly, mucins have terminal cysteine-rich domains that can form disulfide bonds resulting in a cross-linked network that imparts the properties of a gel. This viscoelastic gel allows cellular surface protection and maintenance of cellular water balance (Cone, 2009). Mucin can act as a barrier to the diffusion of foreign molecules. However, it allows the permeation of specific molecules such as some therapeutic or toxin molecules that are able to reach the cells underneath (Round et al., 2002).

It is important to note that mucins and other mucus constituents primarily form a mesh structure which traps particles larger than its pore size that vary from 100 nm to several micrometres (Kirch et al., 2012). Moreover, mucins contain 50 to

90% carbohydrates whose terminal sugars contain carboxyl or sulfate groups. They are therefore highly anionic proteins which could bind positively charged molecules.

It has been suggested that two major processes might stop aerosols from being transported readily through the mucus layer. Either particles will be hindered by the size of the mesh spacing between the mucin fibers or the drug molecules will adhere to the mucus components, in particular, mucin fibers. This can also be referred to as (i) size filtering or as (ii) interaction filtering were electrostatic and/or hydrophobic forces, hydrogen bonds and/or specific binding interaction trap the molecule within the mucin network (Olmsted et al., 2001, Lieleg and Ribbeck, 2011). Size filtering cannot hinder inhaled drug molecules because the size of the pore is ≥100-times larger than the molecules of the most common therapeutic agents. However, mucus-drug molecule interactions could retard drug absorption regardless of the drug molecular size. Figure 1.5.1 shows the difference between these two processes (Lieleg and Ribbeck, 2011).
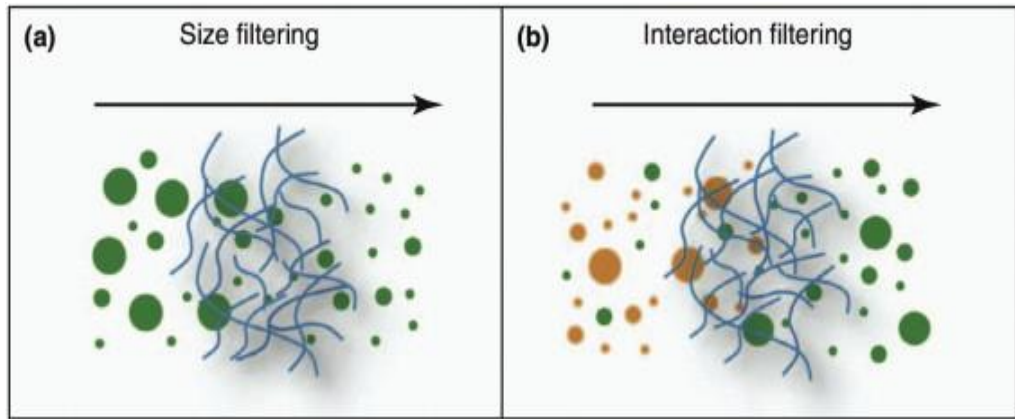
Figure 1.5.1 Two major processes that could hinder aerosols from being transported readily through a mucus layer. (a) Size filtering allows only particles which are smaller than the pores of the mesh spacing to diffuse through the mucus while larger objects are retained. (b) Interaction filtering allows the passage of droplet/particle aerosols based on their surface properties: orange aerosols strongly interacts with the mucus polymer matrix which thus traps them, while green aerosols weakly interact with mucin fibres and hence can pass across the mucus layer. Reproduced from (Lieleg and Ribbeck, 2011).

1.5.1. Mucus–drug size filtering

The pore size of a typical sample of human cervical mucus has been found to be 20–200 nm with a 100-nm average pores diameter according to scanning electron microscopy (SEM) (Olmsted et al., 2001, Saltzman et al., 1994). Pig jejunum mucin was found to have a similar pore size distribution by atomic force microscopy (Round et al., 2012). Other studies have shown that the upper range of pore size for human cervicovaginal mucus is ≥500 nm (Lai et al., 2007, Wang et al., 2011). Images produced from cryo-SEM showed the pore size of horse native bronchial mucus was of a strongly heterogenous nature. The pore diameter ranged from 100 nm to several micrometers with very thick scaffold walls in comparison with hydroxyethyl cellulose gels (Kirch et al., 2012).

1. General introduction

The diffusion of several macromolecules, up to 186,000 Da in molecular weight through pig gastric mucus revealed a molecular weight dependent retarding effect of the mucus (Desai et al., 1992). Although no absolute molecular weight cut-off was observed, macromolecules >30,000 Da were greatly retarded by the mucus.

The penetration of carboxyl polystyrene- and amine-modified polystyrene particles across pig buccal mucosa has been reported where it was shown that a range of 20 nm and 200 nm particles could penetrate the mucus barrier (Roblegg et al. (2012)). Detailed studies were carried out on the diffusion of coated nanoparticles with various polymers and non-coated nanoparticles (100–500 nm) across cystic fibrosis, human cervicovaginal, and chronic rhinosinusitis mucus (Lai et al., 2007, Lai et al., 2011, Lai et al., 2009a, Suk et al., 2009). Those studies showed some nanoparticles interacted with mucus while others did not. The nanoparticles that did not interact with mucins could permeate at a rate close to that in water, suggesting that the mucus hydrogel exhibits a mesh structure with a low viscosity. Surprisingly, nanoparticles of size 200 nm and some nanoparticles of size 500 nm exhibited higher diffusion rates than otherwise similar nanoparticles of size 100 nm. As steric obstruction cannot explain these findings, the diffusion rate of the 100-nm particles must have been reduced by adhesive interactions with mucus components. These could have been greater for the smallest particles due to their higher degree of curvature.

Size filtering is unlikely to hinder inhaled drug molecules because the size of the pores within the mucus are ≥100-times larger than the molecules of the most common therapeutic agents. However, mucus-drug molecule interactions could retard drug absorption regardless of the drug molecular size.

1.5.2. Mucus–drug interaction filtering

Most of the mucus-drug interaction studies have been carried out using mucus from the GIT system, presumably because the GIT remains the main and most popular route for drug delivery. Therefore, much of the available evidence on mucus-drug interactions pertains to the gastrointestinal tract.

A diffusion study of testosterone and several barbiturates (with logP ranging from −1.47 to 3.32) in HT29 cells and Caco-2 cells for comparison because they do not form a mucus layer was undertaken by Behrens et al. (Behrens et al., 2001). Like the Caco-2 cell-line, HT29 cells are human colon adenocarcinoma cells that differentiate into monolayers with tight-junction connections, so they are suitable for permeation investigations. It was shown that all drugs with a positive logP displayed lower permeation in HT29 mucus-producing cells compared with Caco-2 cells even though the TEER of Caco-2 cells was 4-times higher. These outcomes could be explained by the powerful role of hydrophobic interactions between the positive logP molecules and the mucus layer, which tend to show affinity for lipophilic molecules. However, a second investigation using identical cell lines contradicted previous findings as the mucus layer did not appear to be a barrier for the test compounds (Pontier et al., 2001). Although the TEER for Caco-2 cells was similar in the two studies, the discrepancy between the two studies may have been due to the higher TEER of HT29 cells in the study by Pontier et al., which was 10-times higher than that in the study by Behrans et al or the fact that the test compounds had different physico-chemical properties in the two studies

Previously, testosterone had been shown to extensively bind to the mucus layer of pig stomachs and intestines (MacAdam, 1993). Similarly, hydrophilic drugs

displayed lower affinity for pig intestinal mucus and higher diffusion across the mucus layer than lipophilic drugs (Matthes et al., 1992b, Matthes et al., 1992a). In contrast, another study did not show a clear relationship between mucus interaction and lipophilicity (Niibuchi et al., 1986). The permeability of several compounds with logP ranging from −3.1 to 3.3 was measured across: (1) native pig intestinal mucus, (2) individual mucus components such as mucin protein and a lipid mixture composed of 82% linoleic acid, 12% cholesterol, and 6% Soybean phosphatidylcholine and 3) an artificial mucus model reconstituted from the major mucus components mucin, lipids, protein, and DNA (Karlsson et al., 1993, Larhed et al., 1998, Larhed et al., 1997, Wikman et al., 1993). It was suggested that not only mucin hindered the permeation of lipophilic compounds but also lipids present in the mucus. Permeation of the hydrophilic compound mannitol did not change following an increased concentration of mucin or lipid. Investigation of the permeation of four hydrophilic acyclovir derivatives with logP ranging from −1.57 to −1.08 across native pig mucus or the buffer used for comparison (Legen and Kristl, 2001) revealed only acyclovir permeated the mucus to a lower extent than the buffer. These findings could reflect the fact that the chosen drug molecules were not lipophilic enough to have some affinity for the mucus model. The authors nevertheless observed some evidence of electrostatic binding when polar compounds with ionized functional groups were tested.

Interactions of several drug compounds with mucin have been studied and compared with bovine serum albumin (BSA) interactions, which has no carbohydrate residues (Bhat et al., 1995, Bhat et al., 1996). The affinity for mucin of all the drugs studied was of the same magnitude regardless of their

chemical structure and ionization state. Higher affinities to BSA were observed for most of the drugs, which could be predicted due to the absence of carbohydrate residues. It was suggested that the interactions involved in the affinity of drugs to mucin fibers were due to hydrophobic and Van der Waal's forces and not electrostatic charges. Nevertheless, this assumption would be in contrast to other investigational studies that have reported electrostatic charges to be significant in drug–mucus interactions, however, decreased binding forces were associated with increased ionic strength in the solution (Niibuchi et al., 1986, Kearney and Marriott, 1987). Electrostatic binding between drugs or ions possessing positive charges to the components in mucus possessing negative charges is predicted. One study showed that diffusion of hydrogen ions in the native mucus of rat small intestines was dramatically reduced compared with their diffusion in a buffer solution due to ionic interactions (WINNE and VERHEYEN, 1990). Counter ions such as Al^{3+}, Fe^{3+}, Ca^{2+} and Na^+ interact electrostatically with mucin fibers, but the binding is dependent on the pH of the environment, and the pH is increased in solutions of low ionic strength. Hence, high ionic strength reduces the charge effectiveness of ionizable functional groups, possibly by counter-ion binding/shielding (Crowther and Marriott, 1984).

The effect of ionisation on drug permeability across a pig gastric mucus layer was investigated by Shaw et al. (Shaw et al., 2005). A comparison between paracetamol (pKa = 9.5) and ibuprofen (pKa = 5.2) revealed that transport across mucus was pH-dependent for ibuprofen. Increasing the pH of the mucus from 2 to 8 resulted in a higher diffusion rate of ibuprofen while no change in paracetamol diffusion was observed, likely due to the drug remaining in a non-

ionized form. This effect might be explained by the fact that the change from the non-ionized form of ibuprofen to the ionized form made the molecule less lipophilic, resulting in less binding to mucin proteins.

In the only study that has evaluated the role of airway mucus on drug permeation, human bronchial epithelial cells Calu-3 cells were grown under both air-liquid conditions (AIC) and conventional submerged conditions (LCC). In AIC, Calu-3 layers have been showed to be covered by a mucus layer while in LCC, the mucus is diluted in the culture medium (Grainger et al, 2006). The transepithelial transport of several poorly soluble drugs (testosterone, diazepam and cinnarizine) and more hydrophilic drugs (metoprolol, mannitol and propranolol) were compared in both models (Saaby and Müllertz, 2012). The compound with the highest logP, cinnarizine (5.5) did not permeate through AIC Calu-3 cells. Compounds with a lower logP, but still considered to be lipophilic (logP = 3–4), showed a significantly lower permeability across layers maintained in AIC compared with those grown in LCC. However, for the other hydrophilic low-logP compounds, a similar permeability was observed in both culture types. It is worth mentioning that a major limitation of this investigation is that Calu-3 cell layers exhibit different characteristics when grown in AIC or LCC, e.g., differences can be observed in TEER, morphology, expression of transporters, and other epithelial characteristics (Grainger et al., 2006). This suggests the differences in molecular transport observed might have been due to many other factors than just the presence or absence of a mucus layer.

1.6. Aim and objectives of the project

Investigations into pulmonary drug delivery has focused mainly on new device technologies to improve the generation of aerosols and their deposition in the respiratory system. Although considerable progresses have been made and studies are ongoing in this field, there has been no real significant advance in the management of respiratory diseases by the inhaled route in recent years. A major reason is a lack of knowledge on inhaled drug fate post-deposition in the lungs. Improvements of the aerosol performance alone are no longer sufficient for successful inhalation therapy; a paradigm shift is required, with a greater focus on understanding the pulmonary barriers to therapeutic molecular diffusion.

Despite the reported interactions between airway mucus and inhaled toxins in the literature, very minor attention has been given to pulmonary mucus-drug interactions (Gerde et al., 1993, Gerde and Scholander, 1987). On the contrary, for oral delivery, numerous studies have been conducted to evaluate drug-mucus interactions and suggested that those may result in limited drug bioavailability and this is mainly due to the fact that oral route is considered as the primary administrative route of choice for a large number of important drugs.

Hence, considering the scarcity of studies on the impact of the pulmonary mucus layer on the permeability of inhaled drugs across the lung epithelial barrier, the principal aim of this PhD project was to gain a better understanding on how the physicochemical properties of pulmonary agents might affect their interactions with airway mucus.

The first objective of the project was to develop and characterise an *in-vitro* lung mucus model that would allow measurements of the trans-mucus permeation of inhaled molecules. This diffusional model would be based on semipermeable

Transswell® insert membranes coated with pig tracheal mucus. The barrier properties of the mucus model were initially verified by measuring the diffusion fluorescent dyes different physicochemical properties across the mucus layers and a metabolomics type analysis was carried out to monitor potential changes in the composition of the mucus model upon various preparation steps.

The second objective of this work was to develop an inexpensive and operationally simple *in-vitro* system to reproducibly deposit spray aerosols onto the mucus layers.

Finally, the mucus layers and aerosolisation system developed were exploited to investigate the impact of the physicochemical properties of inhaled drugs on their permeation across the mucus barrier.

1.7. References

AGU, R. U., UGWOKE, M. I., ARMAND, M., KINGET, R. & VERBEKE, N. 2001. The lung as a route for systemic delivery of therapeutic proteins and peptides. *Respiratory research,* 2**,** 198.

ALI, M. 2010. Pulmonary drug delivery. *Handbook of Non-Invasive Drug Delivery Systems.* Elsevier.

ATUMA, C., STRUGALA, V., ALLEN, A. & HOLM, L. 2001. The adherent gastrointestinal mucus gel layer: thickness and physical state in vivo. *American Journal of Physiology-Gastrointestinal and Liver Physiology,* 280**,** G922-G929.

BEHRENS, I., STENBERG, P., ARTURSSON, P. & KISSEL, T. 2001. Transport of lipophilic drug molecules in a new mucus-secreting cell culture model based on HT29-MTX cells. *Pharmaceutical research,* 18**,** 1138-1145.

BERNKOP-SCHNÜRCH, A., KAST, C. E. & RICHTER, M. F. 2001. Improvement in the mucoadhesive properties of alginate by the covalent attachment of cysteine. *Journal of Controlled Release,* 71**,** 277-285.

BÉRUBÉ, K., PRYTHERCH, Z., JOB, C. & HUGHES, T. 2010. Human primary bronchial lung cell constructs: the new respiratory models. *Toxicology,* 278**,** 311-318.

BHAT, P. G., FLANAGAN, D. R. & DONOVAN, M. D. 1995. The limiting role of mucus in drug absorption: Drug permeation through mucus solution. *International journal of pharmaceutics,* 126**,** 179-187.

1. *General introduction*

BHAT, P. G., FLANAGAN, D. R. & DONOVAN, M. D. 1996. Drug binding to gastric mucus glycoproteins. *International journal of pharmaceutics,* 134**,** 15-25.

BOCCUZZI, S. J., WOGEN, J. & ROEHM, J. B. 2000. Use of hydrofluoroalkane propellant delivery system for inhaled albuterol in patients receiving asthma medications. *Clinical therapeutics,* 22**,** 237-247.

BOSQUILLON, C. 2010. Drug transporters in the lung—do they play a role in the biopharmaceutics of inhaled drugs? *Journal of pharmaceutical sciences,* 99**,** 2240-2255.

CHEDIAK, A. D. & WANNER, A. 1990. The circulation of the airways: anatomy, physiology and potential role in drug delivery to the respiratory tract. *Advanced Drug Delivery Reviews,* 5**,** 11-18.

CONE, R. A. 2009. Barrier properties of mucus. *Advanced drug delivery reviews,* 61**,** 75-85.

CROWTHER, R. S. & MARRIOTT, C. 1984. Counter-ion binding to mucus glycoproteins. *Journal of pharmacy and pharmacology,* 36**,** 21-26.

CRYSTAL, R. G., RANDELL, S. H., ENGELHARDT, J. F., VOYNOW, J. & SUNDAY, M. E. 2008. Airway epithelial cells: current concepts and challenges. *Proceedings of the American Thoracic Society,* 5**,** 772-777.

DALBY, R. & SUMAN, J. 2003. Inhalation therapy: technological milestones in asthma treatment. *Advanced drug delivery reviews,* 55**,** 779-791.

DE BOER, A., HAGEDOORN, P., GJALTEMA, D., GOEDE, J. & FRIJLINK, H. 2006. Air classifier technology (ACT) in dry powder inhalation: part 3. Design and development of an air classifier family for the Novolizer®

multi-dose dry powder inhaler. *International journal of pharmaceutics,* 310**,** 72-80.

DESAI, M., MUTLU, M. & VADGAMA, P. 1992. A study of macromolecular diffusion through native porcine mucus. *Experientia,* 48**,** 22-26.

DORSAINVIL WHITE, S. H., MOLINA, S. A., CAPALDO, C. T., SCHLINGMANN, B. L. & KOVAL, M. H. 2016. Alcohol Consumption Increases Claudin-18 Turnover in Alveolar Epithelial Cells. *The FASEB Journal,* 30**,** 972.1-972.1.

DUCREUX, J. & VANBEVER, R. 2007. Crucial biopharmaceutical issues facing macromolecular candidates for inhalation: the role of macrophages in pulmonary protein clearance. *Respir Drug Deliv Eur,* 2007**,** 31-41.

EATON, D. C., HELMS, M. N., KOVAL, M., BAO, H. F. & JAIN, L. 2009. The contribution of epithelial sodium channels to alveolar function in health and disease. *Annual review of physiology,* 71**,** 403-423.

EVANS, C. M. & KOO, J. S. 2009. Airway mucus: the good, the bad, the sticky. *Pharmacology & therapeutics,* 121**,** 332-348.

FAHY, J. V. & DICKEY, B. F. 2010. Airway mucus function and dysfunction. *New England Journal of Medicine,* 363**,** 2233-2247.

FORBES, B., ASGHARIAN, B., DAILEY, L. A., FERGUSON, D., GERDE, P., GUMBLETON, M., GUSTAVSSON, L., HARDY, C., HASSALL, D. & JONES, R. 2011. Challenges in inhaled product development and opportunities for open innovation. *Advanced drug delivery reviews,* 63**,** 69-87.

1. General introduction

FRIJLINK, H. & DE BOER, A. 2004. Dry powder inhalers for pulmonary drug delivery. *Expert opinion on drug delivery,* 1**,** 67-86.

FRÖHLICH, E. & MEINDL, C. 2015. In vitro assessment of chronic nanoparticle effects on respiratory cells. *Nanomaterials-Toxicity and Risk Assessment.* InTech.

GEHR, P. 1984. Respiratory tract structure and function. *Journal of Toxicology and Environmental Health, Part A Current Issues,* 13**,** 235-249.

GEORGOPOULOS, D., MOULOUDI, E., KONDILI, E. & KLIMATHIANAKI, M. 2000. Bronchodilator delivery with metered-dose inhaler during mechanical ventilation. *Critical care (London, England),* 4**,** 227-234.

GONDA, I. 2000. The ascent of pulmonary drug delivery. *Journal of pharmaceutical sciences,* 89**,** 940-945.

GRAINGER, C. I., GREENWELL, L. L., LOCKLEY, D. J., MARTIN, G. P. & FORBES, B. 2006. Culture of Calu-3 cells at the air interface provides a representative model of the airway epithelial barrier. *Pharmaceutical research,* 23**,** 1482-1490.

GERDE, P., MUGGENBURG, B. A., SABOURIN, P. J., HARKEMA, J. R., HOTCHKISS, J. A., HOOVER, M. & HENDERSON, R. 1993. Disposition of polycyclic aromatic hydrocarbons in the respiratory tract of the Beagle dog: II. The conducting airways. *Toxicology and applied pharmacology,* 121**,** 319-327.

GERDE, P. & SCHOLANDER, P. 1987. A mathematical model of the penetration of polycyclic aromatic hydrocarbons through the bronchial lining layer. *Environmental research,* 44**,** 321-334.

1. General introduction

GUMBLETON, M., AL-JAYYOUSSI, G., CRANDON-LEWIS, A., FRANCOMBE, D., KREITMEYR, K., MORRIS, C. J. & SMITH, M. W. 2011. Spatial expression and functionality of drug transporters in the intact lung: objectives for further research. *Advanced drug delivery reviews,* 63**,** 110-118.

HA, E. V. & ROGERS, D. F. 2016. Novel therapies to inhibit mucus synthesis and secretion in airway hypersecretory diseases. *Pharmacology,* 97**,** 84-100.

HAGHI, M., ONG, H. X., TRAINI, D. & YOUNG, P. 2014. Across the pulmonary epithelial barrier: Integration of physicochemical properties and human cell models to study pulmonary drug formulations. *Pharmacology & therapeutics,* 144**,** 235-252.

HOU, S., WU, J., LI, X. & SHU, H. 2015. Practical, regulatory and clinical considerations for development of inhalation drug products. *asian journal of pharmaceutical sciences,* 10**,** 490-500.

HUGHES, J. 2009. *Physiology and practice of pulmonary function*, Association for Respiratory Technology and Physiology.

IBRAHIM, M. & GARCIA-CONTRERAS, L. 2013. Mechanisms of absorption and elimination of drugs administered by inhalation. *Therapeutic delivery,* 4**,** 1027-1045.

KARLSSON, J., WIKMAN, A. & ARTURSSON, P. 1993. The mucus layer as a barrier to drug absorption in monolayers of human intestinal epithelial HT29-H goblet cells. *International journal of pharmaceutics,* 99**,** 209-218.

1. General introduction

KEARNEY, P. & MARRIOTT, C. 1987. The effects of mucus glycoproteins on the bioavailability of tetracycline. III. Everted gut studies. *International journal of pharmaceutics,* 38**,** 211-220.

KIM, K.-J. & MALIK, A. B. 2003. Protein transport across the lung epithelial barrier. *American Journal of Physiology-Lung Cellular and Molecular Physiology,* 284**,** L247-L259.

KIRCH, J., SCHNEIDER, A., ABOU, B., HOPF, A., SCHAEFER, U. F., SCHNEIDER, M., SCHALL, C., WAGNER, C. & LEHR, C.-M. 2012. Optical tweezers reveal relationship between microstructure and nanoparticle penetration of pulmonary mucus. *Proceedings of the National Academy of Sciences,* 109**,** 18355-18360.

LABIRIS, N. & DOLOVICH, M. 2003. Pulmonary drug delivery. Part I: physiological factors affecting therapeutic effectiveness of aerosolized medications. *British journal of clinical pharmacology,* 56**,** 588-599.

LAI, S. K., O'HANLON, D. E., HARROLD, S., MAN, S. T., WANG, Y.-Y., CONE, R. & HANES, J. 2007. Rapid transport of large polymeric nanoparticles in fresh undiluted human mucus. *Proceedings of the National Academy of Sciences,* 104**,** 1482-1487.

LAI, S. K., SUK, J. S., PACE, A., WANG, Y.-Y., YANG, M., MERT, O., CHEN, J., KIM, J. & HANES, J. 2011. Drug carrier nanoparticles that penetrate human chronic rhinosinusitis mucus. *Biomaterials,* 32**,** 6285-6290.

LAI, S. K., WANG, Y.-Y., CONE, R., WIRTZ, D. & HANES, J. 2009a. Altering mucus rheology to "solidify" human mucus at the nanoscale. *PloS one,* 4**,** e4294.

LAI, S. K., WANG, Y.-Y. & HANES, J. 2009b. Mucus-penetrating nanoparticles for drug and gene delivery to mucosal tissues. *Advanced drug delivery reviews,* 61**,** 158-171.

LANSLEY, A. B. 1993. Mucociliary clearance and drug delivery via the respiratory tract. *Advanced drug delivery reviews,* 11**,** 299-327.

LARHED, A. W., ARTURSSON, P. & BJÖRK, E. 1998. The influence of intestinal mucus components on the diffusion of drugs. *Pharmaceutical research,* 15**,** 66-71.

LARHED, A. W., ARTURSSON, P., GRÅSJÖ, J. & BJÖRK, E. 1997. Diffusion of drugs in native and purified gastrointestinal mucus. *Journal of pharmaceutical sciences,* 86**,** 660-665.

LEAK, L. V. & JAMUAR, M. P. 1983. Ultrastructure of pulmonary lymphatic vessels. *American Review of Respiratory Disease,* 128**,** S59-S65.

LEGEN, I. & KRISTL, A. 2001. Comparative permeability of some acyclovir derivatives through native mucus and crude mucin dispersions. *Drug development and industrial pharmacy,* 27**,** 669-674.

LIELEG, O. & RIBBECK, K. 2011. Biological hydrogels as selective diffusion barriers. *Trends in cell biology,* 21**,** 543-551.

MACADAM, A. 1993. The effect of gastro-intestinal mucus on drug absorption. *Advanced drug delivery reviews,* 11**,** 201-220.

MATTHES, I., NIMMERFALL, F. & SUCKER, H. 1992a. Mucus models for investigation of intestinal absorption mechanisms. 1. Validation and optimization of the model. *Die Pharmazie,* 47**,** 505-515.

MATTHES, I., NIMMERFALL, F. & SUCKER, H. 1992b. Mucus models for investigation of intestinal absorption mechanisms. 2. Mechanisms of drug interactions with intestinal mucus. *Die Pharmazie,* 47**,** 609-613.

MITCHELL, H. 2009. Airway smooth muscle contraction–Perspectives on past, present and future. *Pulmonary pharmacology & therapeutics,* 22**,** 363-369.

NEWMAN, S. P. 1985. Aerosol deposition considerations in inhalation therapy. *Chest,* 88**,** 152S-160S.

NICOD, L. 1999. Pulmonary defence mechanisms. *Respiration,* 66**,** 2-11.

NIIBUCHI, J.-J., ARAMAKI, Y. & TSUCHIYA, S. 1986. Binding of antibiotics to rat intestinal mucin. *International journal of pharmaceutics,* 30**,** 181-187.

O'RIORDAN, T. G. 2002. Formulations and nebulizer performance. *Respiratory care,* 47**,** 1305-12; discussion 1312-3.

OBERDÖRSTER, G., FERIN, J., GELEIN, R., SODERHOLM, S. C. & FINKELSTEIN, J. 1992. Role of the alveolar macrophage in lung injury: studies with ultrafine particles. *Environmental health perspectives,* 97**,** 193.

OLMSTED, S. S., PADGETT, J. L., YUDIN, A. I., WHALEY, K. J., MOENCH, T. R. & CONE, R. A. 2001. Diffusion of macromolecules and virus-like particles in human cervical mucus. *Biophysical journal,* 81**,** 1930-1937.

OLSSON, B., BONDESSON, E., BORGSTRÖM, L., EDSBÄCKER, S., EIREFELT, S., EKELUND, K., GUSTAVSSON, L. & HEGELUND-

1. General introduction

MYRBÄCK, T. 2011. Pulmonary drug metabolism, clearance, and absorption. *Controlled pulmonary drug delivery.* Springer.

PACURARI, M., MAY, I. & TCHOUNWOU, P. 2017. Effects of lipopolysaccharide, multiwalled carbon nantoubes, and the combination on lung alveolar epithelial cells. *Environmental toxicology,* 32**,** 445-455.

PANETTIERI JR, R. A., KOTLIKOFF, M. I., GERTHOFFER, W. T., HERSHENSON, M. B., WOODRUFF, P. G., HALL, I. P. & BANKS-SCHLEGEL, S. 2008. Airway smooth muscle in bronchial tone, inflammation, and remodeling: basic knowledge to clinical relevance. *American journal of respiratory and critical care medicine,* 177**,** 248-252.

PATTON, J. S. 1996. Mechanisms of macromolecule absorption by the lungs. *Advanced Drug Delivery Reviews,* 19**,** 3-36.

PATTON, J. S., BRAIN, J. D., DAVIES, L. A., FIEGEL, J., GUMBLETON, M., KIM, K.-J., SAKAGAMI, M., VANBEVER, R. & EHRHARDT, C. 2010. The particle has landed—characterizing the fate of inhaled pharmaceuticals. *Journal of aerosol medicine and pulmonary drug delivery,* 23**,** S-71-S-87.

PATTON, J. S. & BYRON, P. R. 2007. Inhaling medicines: delivering drugs to the body through the lungs. *Nature Reviews Drug Discovery,* 6**,** 67.

PATTON, J. S., FISHBURN, C. S. & WEERS, J. G. 2004. The lungs as a portal of entry for systemic drug delivery. *Proceedings of the American Thoracic Society,* 1**,** 338-344.

PLOPPER, C. G. 1996. Structure and function of the lung. *Respiratory system.* Springer.

1. General introduction

PONTIER, C., PACHOT, J., BOTHAM, R., LENFANT, B. & ARNAUD, P. 2001. HT29-MTX and Caco-2/TC7 monolayers as predictive models for human intestinal absorption: Role of the mucus layer. *Journal of pharmaceutical sciences,* 90**,** 1608-1619.

PUCHELLE, E., GIROD DE BENTZMANN, S. & HIGENBOTTAM, T. 1995. Airway secretions and lung liquids. In brewis, rAL, editor. *Respiratory Medicine***,** 97-111.

QURAISHI, M., JONES, N. & MASON, J. 1998. The rheology of nasal mucus: a review. *Clinical Otolaryngology & Allied Sciences,* 23**,** 403-413.

RAU, J. L. 2002. Design principles of liquid nebulization devices currently in use. *Respiratory care,* 47**,** 1257-75; discussion 1275-8.

ROBLEGG, E., FROEHLICH, E., MEINDL, C., TEUBL, B., ZAVERSKY, M. & ZIMMER, A. 2012. Evaluation of a physiological in vitro system to study the transport of nanoparticles through the buccal mucosa. Nanotoxicology, 6, 399-413.

ROSE, M. C. & VOYNOW, J. A. 2006. Respiratory tract mucin genes and mucin glycoproteins in health and disease. *Physiological reviews,* 86**,** 245-278.

ROUND, A., BERRY, M., MCMASTER, T., STOLL, S., GOWERS, D., CORFIELD, A. & MILES, M. 2002. Heterogeneity and persistence length in human ocular mucins. *Biophysical Journal,* 83**,** 1661-1670.

SAABY, L. & MÜLLERTZ, A. 2012. Transepithelial Transport in Calu-3 Cells Grown Under LCC and AIC Conditions: Impact of Mucus on Drug Permeability. *T. Loftsson (Ed.), CRS Nordic Chapter Meeting 2012, University of Iceland, Reykavik, Iceland (2012), p. 81*.

1. General introduction

SALTZMAN, W. M., RADOMSKY, M. L., WHALEY, K. J. & CONE, R. A. 1994. Antibody diffusion in human cervical mucus. *Biophysical journal,* 66**,** 508.

SCHULZ, H. 1998. Mechanisms and factors affecting intrapulmonary particle deposition: implications for efficient inhalation therapies Holger Schulz. *Pharmaceutical Science & Technology Today,* 1**,** 326-344.

SHAW, L. R., IRWIN, W. J., GRATTAN, T. J. & CONWAY, B. R. 2005. The influence of excipients on the diffusion of ibuprofen and paracetamol in gastric mucus. *International journal of pharmaceutics,* 290**,** 145-154.

STAUB, N. C. 1991. *Basic respiratory physiology*, Churchill Livingstone.

SUGANO, K., KANSY, M., ARTURSSON, P., AVDEEF, A., BENDELS, S., DI, L., ECKER, G. F., FALLER, B., FISCHER, H. & GEREBTZOFF, G. 2010. Coexistence of passive and carrier-mediated processes in drug transport. *Nature reviews Drug discovery,* 9**,** 597.

SUK, J. S., LAI, S. K., WANG, Y.-Y., ENSIGN, L. M., ZEITLIN, P. L., BOYLE, M. P. & HANES, J. 2009. The penetration of fresh undiluted sputum expectorated by cystic fibrosis patients by non-adhesive polymer nanoparticles. *Biomaterials,* 30**,** 2591-2597.

TWIGG III, H. L. 1998. Pulmonary host defenses. *Journal of thoracic imaging,* 13**,** 221-233.

WANG, Y.-Y., LAI, S. K., SO, C., SCHNEIDER, C., CONE, R. & HANES, J. 2011. Mucoadhesive nanoparticles may disrupt the protective human mucus barrier by altering its microstructure. *PloS one,* 6**,** e21547.

WEIBEL, E. R. 1991. Design of airways and blood vessels considered as branching trees. *The lung: scientific foundations,* 1**,** 1061-1071.

WEIBEL, E. R. & GOMEZ, D. M. 1962. Architecture of the Human Lung: Use of quantitative methods establishes fundamental relations between size and number of lung structures. *Science,* 137**,** 577-585.

WIKMAN, A., KARLSSON, J., CARLSTEDT, I. & ARTURSSON, P. 1993. A drug absorption model based on the mucus layer producing human intestinal goblet cell line HT29-H. *Pharmaceutical research,* 10**,** 843-852.

WINNE, D. & VERHEYEN, W. 1990. Diffusion coefficient in native mucus gel of rat small intestine. *Journal of Pharmacy and Pharmacology,* 42**,** 517-519.

Chapter 2 - Development of an *in-vitro* mucus model

2.1. Introduction

As previously stated in the general introduction, mucus acts as a barrier against pathogens by preventing them to reach the lung epithelium (Hida et al., 2011). Similarly, mucus is also considered a potentially efficient barrier to the delivery of drugs. Hence, it is highly desirable to develop active pharmaceutical ingredients (APIs) that are capable of crossing a mucus barrier. However, to date, no standardised protocol has been established for mucus permeation studies.

2.1.1. Mucus models

A number of mucus models have been described in the literature, that vary from simple mucin and artificial mucus to natural rat, pig, horse or human mucus, and from simple *ex-vivo* to closed *in-vivo* models (Dawson et al., 2004, Li et al., 2011a). Pathologic mucus has also been used in several studies as well as mucus secreted from specific cells (Lai et al., 2011). *In-vitro* mucus models that have been described in the literature as well as their advantages and disadvantages are presented here.

- *Mucin*

Reconstitution of mucin-only solutions with different solutes is the basis of the simplest models. Mucin reconstituted by mixing with sodium carbonate and a sodium phosphate buffer adjusted to pH 6.5 and then, spread at the surface of Transwell-Snapwell® inserts has been used to investigate the impact of mucus

2. Development of an in-vitro mucus model

on the absorption of microspheres intended for use as oral vaccine delivery vehicles across the intestinal mucosa.(Norris and Sinko, 1997).

- *Artificial mucus*

Reconstituted artificial pig gastric mucus has been prepared by mixing pig gastric mucin 60 mg/mL, bovine serum albumin (BSA), dipalmitoylphosphatidylcholine, and 4-(2-hydroxyethyl)-1-piperazineethanesulfonic acid (HEPES) buffer (pH 7.4). The permeation of poly(d,l-lactic- *co*-glycolic) acid (PLGA) nanoparticle gene carriers was measured in that model (Dawson et al., 2004). Additionally, a reconstituted pig gastric mucus solution was produced by mixing pig gastric mucin (40 mg/mL) and isotonic phosphate buffer (pH 7.4) containing sodium azide followed by two cycles of centrifugation (27 000 x rpm for 15 mins) and dialysis. This was used to test drug binding to mucus (Bhat et al., 1996a).

- *Natural mucus*

Native pig intestinal mucus has been used to investigate the gastrointestinal mucus effect on particle transport using real-time multiple particle tracking. Pig intestines were obtained from a local slaughter-house and stored on ice prior to mucus scraping. The intestine was cut open and any waste material was removed. With a spatula, mucus was gently scraped and stored at $-80\ ^{\circ}\text{C}$ until examination. Particle mobility in the gastrointestinal mucus was strongly dependent on surface charge with cationic particles being transported 20–30 times slower than anionic particles (Crater and Carrier, 2010). Moreover, it was demonstrated that rather than mucin glycoproteins, lipids present in pig intestinal mucus reduced the diffusion of drugs in native intestinal mucus (Larhed et al., 1998).

Furthermore, pig gastric mucus was used as a mucus model to evaluate the permeability of common analgesic drugs. The stomachs of freshly slaughtered fasted pigs were acquired from a local slaughter-house. Each stomach was opened, any food content removed and the stomach was then washed with double-distilled water. A smooth-faced spatula was used to collect the mucus which was then homogenised and stored at 4 °C before use. Measurement of the permeability of analgesic drugs, paracetamol and ibuprofen, across pig gastric mucus revealed the mucus layer significantly retarded the movement of both drugs (Shaw et al., 2005).

Crude rat intestinal mucus has also been collected to study liposome transport across mucus (Li et al., 2011b). Rats were fasted overnight before being sacrificed. The intestines were cut opened and waste was removed by rinsing with saline. With a cover slide, the mucus was then gently scraped and aliquoted in Eppendorf vials. The samples collected were stored at −80 °C until use.

At a pulmonary level, the effect of the bronchial mucus layer against nanoparticles transport was studied (Kirch et al., 2012) using horse bronchial mucus. This was acquired from the bronchial distal region of healthy horses during bronchoscopy before being stored at −80 °C until use.

More clinically relevant, mucus has also been collected from humans. Undiluted cervicovaginal secretions from women were obtained using a self-sampling collection device following a protocol approved by the Institutional Review Board of the Johns Hopkins University. The device was inserted into the vagina for one minute, removed, and placed into a 50 mL centrifuge tube. Samples were then centrifuged at 1000 rpm for 2 min to collect the mucus secretions(Tang et

al., 2009). Those were employed to investigate the diffusion of nanoparticles of different composition across mucus.

Shuster et al. (Schuster et al., 2013) used human non-lung disease airway mucus samples to investigate nanoparticle mobility in respiratory mucus. Samples were collected by endotracheal intubation. At the end of surgery, the endotracheal tube was removed from the patient, the balloon cuff was cut and placed in a 50 mL centrifuge tube. Following that, the samples were centrifuged at 1000 rpm for 30 seconds which then yield an average volume of 0.5 mL of mucus. Mucus samples were then stored at at −20 °C until use.

- *Pathogenic mucus*

Natural but pathologic mucus obtained from cystic fibrosis patients expectorated sputum was used to investigate the penetration of non-adhesive polymeric nanoparticles (Suk et al., 2009).

- *mucus producing cell lines*

At a cellular level, many studies have been reported on mucus models derived from different cell lines such as HT29 and Calu-3 cell lines. Mucus producing cell lines use washed mucus layer as a reference in the examination of mucus-drug interaction. The HT29 cell line was established in 1964 from a patient with colorectal adenocarcinoma. HT29-H cells, a mucus producing sub clone of the HT29 cell line, has been used as a mucus secreting cell line model to investigate molecular diffusion (Karlsson et al., 1993). Another cellular mucus study was conducted using the Calu-3 cell line, human bronchial epithelial cell line, to investigate mucus barrier characteristics (Vllasaliu et al., 2011).

However, in-vitro mucus models possess advantages and disadvantages which needs to be addressed. For instance, native (natural) mucus is considered the ideal study model, however it has drawbacks. Firstly, mucus sources are not easily accessible. Secondly, inter-individual variability means that there are differences in mucus composition, therefore different physical and chemical properties exist between samples (Sanders et al., 2000). Pooling mucus from different individuals can nevertheless decrease the inter-individual variation among different batches. Storage of mucus samples at -20 °C is common as it has been shown not to induce significant structural changes (Sanders et al., 2000). For instance, freeze-thaw cycles have been shown not to exert any adverse effects on mucus viscoelasticity. Moreover, such storage conditions did not influence drug diffusion rates (Larhed et al., 1997). However, storage of cervicovaginal mucus at 25 °C resulted in slight evaporation losses, but this effect was reduced when the samples were stored at -20 °C (Boskey et al., 2003). Pigs are quite large animals that produce sufficient mucus to perform multiple experiments. Furthermore, it has been reported that pig and human mucus are similar in terms of molecular composition and structure (Kararli, 1995). However, it is important to note that different animals of the same species may exhibit different mucus properties (Groo et al., 2013). Consequently, pig mucin has been used as a mucus substitute. Purified mucin (type II) and unpurified mucin (type III) are two forms of pig gastric mucin that are commercially available and are compositionally stable. However, other components contained in mucus, such as proteins, lipids, or salts are not present in this commercial product. Reconstituted mucus has therefore been used by many researchers as detailed previously. Interestingly, no suppression in sample variability was

2. *Development of an in-vitro mucus model*

noted when reconstituted mucus was compared with crude mucus, which revealed some heterogeneity and non-uniformity of reconstituted mucus when used in *in-vitro* prepared mucus models (McGill and Smyth, 2010).

The extraction of mucin from pig gastric mucus samples has been shown to disrupt disulphide bridges, which impedes gel formation and results in a weaker sol-gel transition pH (lower than 4) (Griffiths et al., 2009). Sol fractions of cystic fibrosis mucus were generated by a separation process and compared with the gel fraction (Bhat et al., 1996b). Alterations in the mucin structure in the sol phase were observed under transmission electron microscopy (TEM), revealing a highly branched structure.

Although mucin is prepared in natural mucus concentrations and mixed with the other compositions of mucus, differences in diffusion outcomes compared to native mucus have been demonstrated. For example, anionic particle mobility in purified pig gastric mucin has been reported to be markedly higher than in crude intestinal mucus (Crater and Carrier, 2010). This difference in mobility is mainly due to the difference in the mesh spacing of purified mucin compared to native mucus as well as compositional differences between the two models. Moreover, during the purification process, mucin degradation occurs, which also may lead to outcome differences. Cationic particle mobility was similar in both models, which included highly concentrated mucin. This result can be attributed to the binding of cationic particles to the negatively charged mucin. Hence, Crater and Carrier concluded that less heterogeneous particle transport rates for anionic particles were observed in purified mucin due to lower spacing mesh porosity heterogeneity. The higher heterogeneity of native mucus compared to purified mucin was observed microscopically (Crater and Carrier, 2010).

An inverse correlation between the logP of drugs and their permeability in pig intestinal mucus (Larhed et al., 1997) has been reported, but no such relationship was observed for pig gastric mucin, while the permeability for lipophilic molecules of comparable size were significantly reduced in pig intestinal mucus. Therefore, natural mucus seems ideal for *in-vitro* assays. However, the sourcing of a high number of animals from which mucus can be collected is very challenging. Nevertheless, working with abattoirs allows for large quantities of animal mucus to be obtained.

2.1.2. Diffusion systems

Several protocols have been developed to assess drug interactions with mucus; which include mucoadhesion assays (Petit et al., 2012), pharmacokinetic (PK) and radioactivity studies, through to *in-vivo* experiments (Poquet et al., 2008, Takatsuka et al., 2006), assessment of binding properties and diffusion experiments (Ezpeleta et al., 1999).

To study drug permeation profiles, several systems have been introduced such as multiple particle tracking (Tang et al., 2009), the filtering and centrifugation of two samples tubes (Grubel and Cave, 1998) side-by-side systems (Bhat et al., 1995, Bhat et al., 1996b), and side-on-three compartment systems (Shaw et al., 2005).

One of the most commonly used diffusion model methods is the side-on-three compartment diffusion model. The diffusion cell consists of donor and acceptor compartments with a central compartment containing the mucus model. To evaluate drug permeation, the drug is placed in the donor compartment and its

arrival in the acceptor compartment over a period of time is measured. The mucus barrier is located centrally between the two compartments.

Since the mucus is located between semipermeable membranes between the compartments allowing permeation of drugs or particles; their ability to retain the molecule must be known to differentiate the membrane effects from the mucus permeation. Different side-on-three compartments have been developed, including diffusion chambers (i.e. side-by-side diffusion cells) featuring a customised membrane holder (Figure 2.1.1) (Bhat et al., 1995, Bhat et al., 1996b).
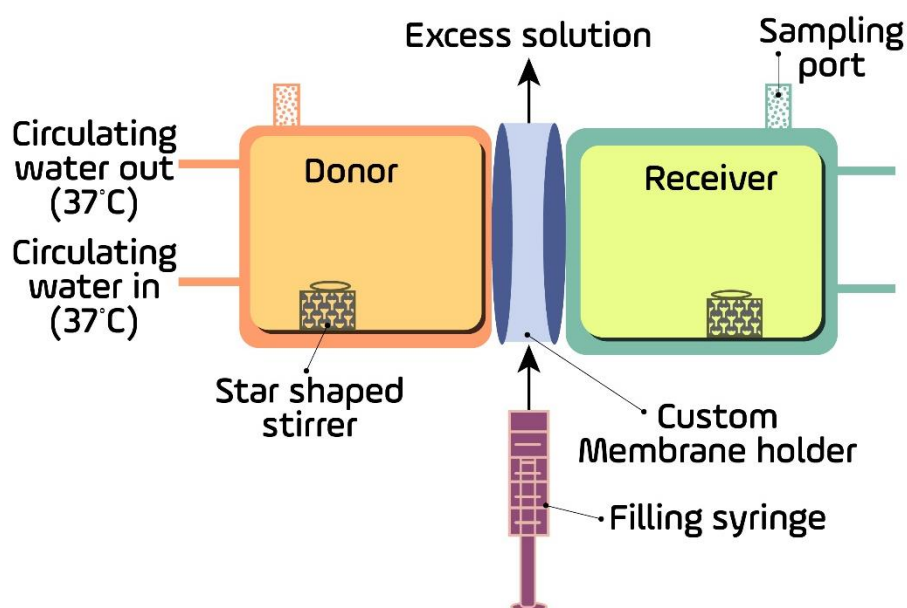
Figure 2.1.1. Schematic representation of side-by-side diffusion cell with a customised membrane, reproduced from (Bhat et al., 1995)

However, these diffusion protocols are inhibited by some limitations such as detection and quantification capabilities. Radio-labelled drugs have been used to detect radioactive delivery routes using a liquid scintillation counter.

2. Development of an in-vitro mucus model

However, specific and expensive equipment is required, which necessitates strict adherence to safety rules to detect radioactivity, rendering such methods inaccessible. Complex equipment is required for multiple particle tracking including appropriate filters, specific software, glass chambers, fluorescent particles and a silicon intensified target camera equipped with an objective lens (100x oil immersion).

Furthermore, one of the widely used diffusion systems is the modified Franz diffusion cells for mucus diffusional investigations. For example, intestinal mucus of rats mounting in a modified Franz diffusion cell was used to study the diffusion characteristics of different liposome types (Li et al., 2011b). Furthermore, the transport of photosensitisers across artificial cystic fibrosis mucus using a modified Franz cell diffusion system was successfully monitored (Donnelly et al., 2007). However, the thickness of the mucus layer in most of the investigations using Franz cell diffusion system reached 3 mm, and hence, do not reflect the endogenous mucus thickness.

A diffusion system based on a mucus layer formed in the donor compartment of Transwell® inserts has been described (Friedl et al., 2013). However, no detailed protocol on the preparation of the mucus layers is available and those were reported to have a thickness of 929 ± 115 μm, which is two orders of magnitude higher than the thickness of the airway mucus.

2.1.3. Aim

The aim of the work detailed in this chapter was to characterise and validate an *in-vitro* lung mucus model for studying the permeation of different molecules with various physicochemical properties.

Semipermeable Transwell® insert membranes coated with pig tracheal mucus was chosen as a respiratory mucus model. Transwell® inserts were chosen as a diffusion model since they would allow the deposition of aerosolised drugs at the surface of the mucus layers.

First, the viscoelastic behaviour of pig tracheal mucus and its internal structure were analysed to provide microstructural surface information and verify that the preparation steps did not affect the mucus properties. Protein composition was also analysed to ensure that essential proteins were not lost during the cleaning steps. Following the development of this model, the reproducibility of different mucus batches was evaluated by determining the permeability profile of a fluorescent marker using optimised volumetric conditions. Finally, the influence of fluorescent dye physicochemical properties, including salt composition, on their mucus diffusion was evaluated to assess the mucus model barrier properties.

2.2. Materials and methods

2.2.1. Materials

Pig tracheas were sourced from RB Elloitt and Son Ltd, Stud Farm abattoir, Calow, Chesterfield, Derbyshire, UK. Transwell® inserts (0.4 μm pore size, polyester membrane, 1.2 mm diameter, sterile), 12-well plates, 48-well plates and black 96-well plates were purchased from Corning Inc. – Life Science (NY, USA). Water was supplied by ELGA LabWater, Veolia Water Solutions and Technologies, UK (Distilled and deionised water (18.2 MΩ) was prepared using a Purelab Ultra water purification system).

Hank's balanced salt solution (HBSS), sodium chloride, caffeine, Lucifer yellow CH dipotassium and Lucifer yellow CH dilithium, fluorescein isothiocyanate isomer I (FITC), Rhodamine B base, Rhodamine 123, Rose Bengal, Tris-Cl, sodium dodecyl sulfate, glycerol, and bromophenol blue were purchased from Sigma-Aldrich, St. Louis, USA. Tris-Glycine 4-20% TGX mini gel was purchased from BIO-RAD, London, UK.

2.2.2. Mucus preparation

Formation of the final mucus layer involved several steps (Figure 2.2.1). Batches of pig tracheas were obtained from healthy adult pigs, both females and males, from a local abattoir (RB Elloitt and Son Ltd). Each trachea (approximate length: 15–20 cm) was incised longitudinally and the edges were pinned to a support to keep them open. The mucus was gently scraped off with a spatula and pooled together in plastic tubes. Raw mucus samples were stored at -20 °C and thawed at room temperature prior to cleaning. Mucus aliquots were diluted to 1:10 with 0.1M NaCl and stirred at 4 °C for 30 min. The resulting suspension was

2. *Development of an in-vitro mucus model*

centrifuged at 14,000 rpm at 4 °C for 15 min (Eppendorf® Refrigerated Microcentrifuge, Model 5417R). The supernatant containing blood residues and debris was discarded. If the mucus did not appear clean, the process was repeated until visibly clean mucus (blood-free and clear) was obtained. The cleaned mucus was stored at -20 °C until needed.

To coat Transwell® inserts with a layer of mucus, 12 µL of mucus was resuspended in 0.1M NaCl to obtain a final volume of 300 µL (Cingolani, 2016). The mucus suspension was transferred onto the Transwell® membrane in a 12-well cell culture plate. The plate was centrifuged at 1,500 rpm for 15 mins (Multifuge 3S, Heraeus). The supernatant was then removed and 500 µL of HBSS was placed in the basolateral chamber. The mucus was left overnight to stabilise and to allow for the evaporation of excess water.
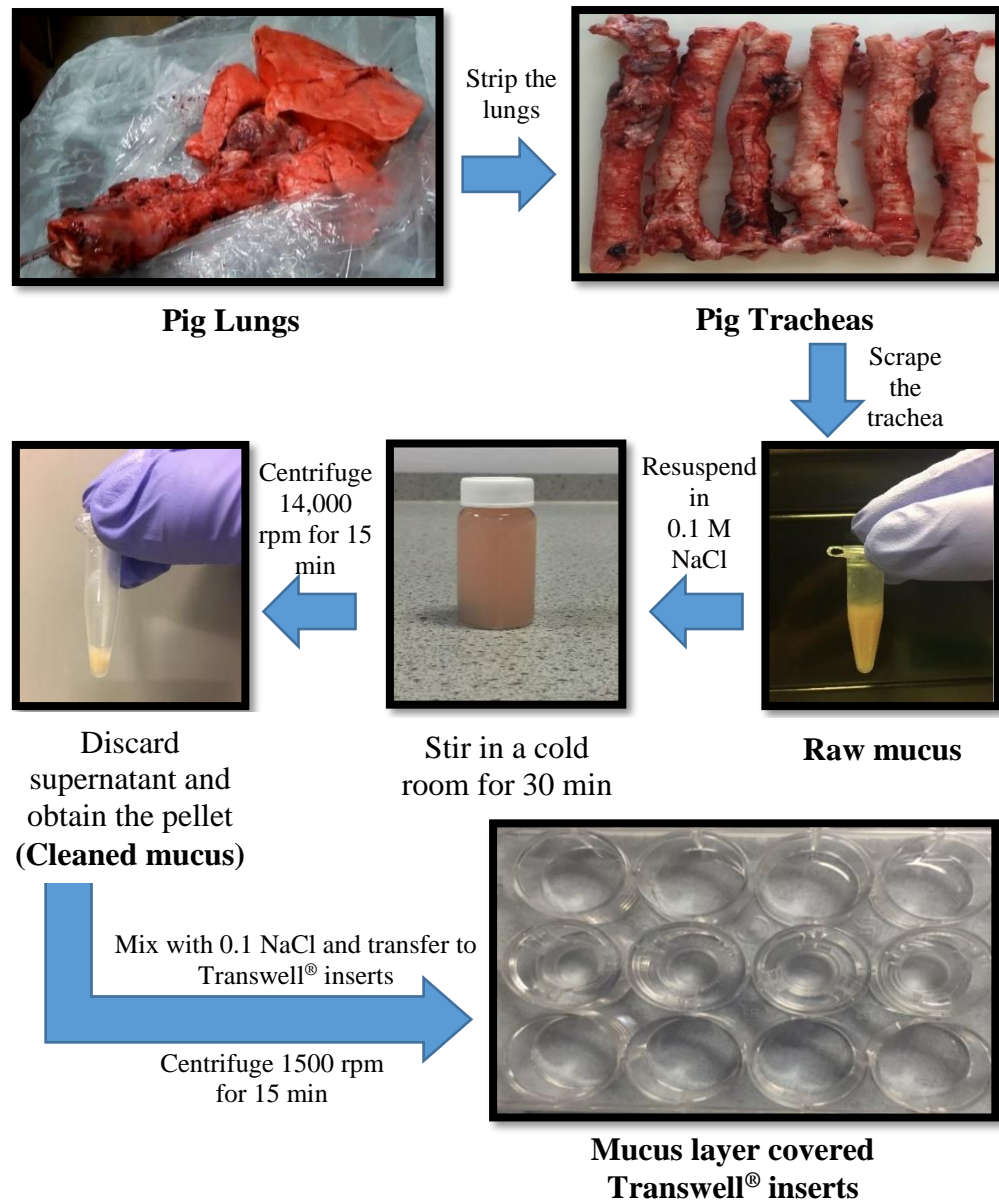
Figure 2.2.1. A schematic flowchart describing the preparation of a mucus layer covering Transwell® insert using raw pig respiratory mucus.

2.2.3. Staining of the pig mucus layer coating Transwell® inserts

The mucus was stained with Alcian Blue to visualise coverage of the Transwell® inserts. Twelve µL of cleaned mucus was resuspended in a solution of 10% Alcian blue (3% acidic acid) in double-distilled water (dd-H_2O) to reach a total

volume of 300 µL. The resulting suspension was transferred onto a Transwell®

insert housed in a 12-well cell culture plate. The plate was centrifuged at 1,500

rpm for 15 mins (Multifuge 3S, Heraeus). The supernatant was removed and

images of the surface of the insert coated with mucus were acquired by a 12-

megapixel camera.

2.2.4. Mucus viscosity

2.2.4.1. Poiseuille flow between parallel plates

A Viscosizer TD (Malvern Instruments Ltd., Malvern, UK) was used for mucus

viscosity measurements. A cleaned mucus sample (5 µL) and a reference sample

of known viscosity (caffeine) were injected into a looped fused silica capillary

tube (Optronis GmbH, Kehl, Germany) of 75 µm and 360 µm inner and outer

diameters, respectively. The capillary was 130 cm in length, and the first and

second windows were located at a distance of 44 cm and 85 cm, respectively,

from the inlet end (Figure 2.2.2). The temperature of the capillary tube and the

autoampler tray was set to 37 °C or 5 °C, respectively.

The samples were transported in the capillary tube by applying a pressure of 150

mBar under a linear flow of ultrapure water with a linear velocity of 2.4 mm/s.
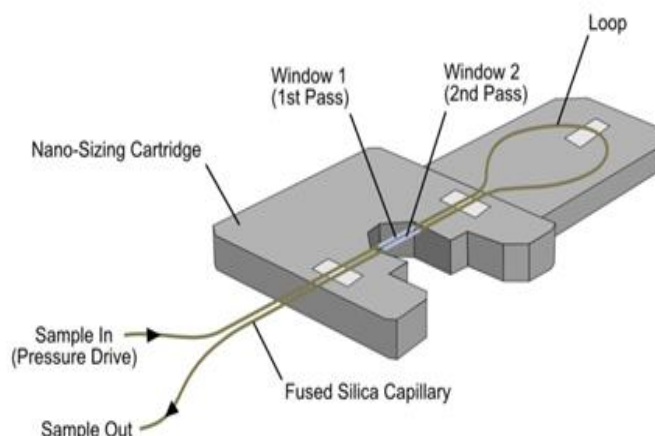
Figure 2.2.2. Schematic representation of the Viscosizer TD, showing the dual capillary window designed to give high precision measurements of transit times between windows 1 and 2, providing accurate viscosity measurements.

2.2.4.2.   Cone-plate rheometer

A cone-plate rheometer was also used to assess mucus viscosity (Modular Compact Cone-Plate Rheometer MCR 302; Anton Paar GmbH, Germany) where the mucus is placed between a plate and a cone. A CP50-2-SN30270 cone of 49.972 mm diameter, angle 2.016º, and truncation of 211 µm was used. A constant speed was maintained to induce laminar shearing movement and analysis was carried out at 37 °C. Eight points per decade were used for three decades with the shear rate increased logarithmically from 1 to 1000 s^{-1}. A total of 25 points were made, with one point per min, the sample volume was 1.2 mL, and Rheoplus software (Anton Paar GmbH, Germany) was used to analyse the results. Both raw and cleaned mucus were analysed in triplicate. A range of shear rates were used to assess if the mucus samples exhibited non-Newtonian behaviour.

2.2.5. Sodium dodecyl sulfate-polyacrylamide gel electrophoresis (SDS-PAGE)

The protein components of raw and cleaned mucus were compared. Both samples were resuspended in non-reducing sample buffer (NRSB) containing 100 mM Tris-Cl (pH 6.8), 4% sodium dodecyl sulfate (SDS), 20% glycerol, and 0.2% bromophenol blue (1:1 ratio). Then, the samples were vortexed for one min before being centrifuged at 10,000 rpm for 15 min. The supernatant was then heat-denatured at 100 °C for five min before loading 15 µL into precast Tris-Glycine 4-20% TGX mini gel and separating mucus proteins through SDS-PAGE analyses for 90 min at 100 V using a Mini-PROTEAN™ Tetra Cell (Faure et al., 2002).

After SDS-PAGE, the Tris-glycine gel was stained with InstantBlue™ stain for one hour and de-stained with ultrapure water until protein band resolution was visualised.

2.2.6. Cryogenic-scanning electron microscopy (Cryo-SEM)

Cryo-SEM was used to study mucus physical properties and to investigate if the intensive mucus preparation steps affected the internal structure of the final *in-vitro* mucus layer. Three mucus preparations from the same mucus batch were chosen for examination: raw mucus, "cleaned" mucus, and a mucus layer (Figure 2.2.3). In the first experiment, raw and cleaned mucus samples (5 µL) were placed onto a brass rivet in the sample stage and a second rivet was placed on top. In the second experiment, the final mucus preparation (a Transwell® insert surface coated with a layer of mucus) was cut and secured to the sample stage by two springs (Figure 2.2.4).

2. Development of an in-vitro mucus model
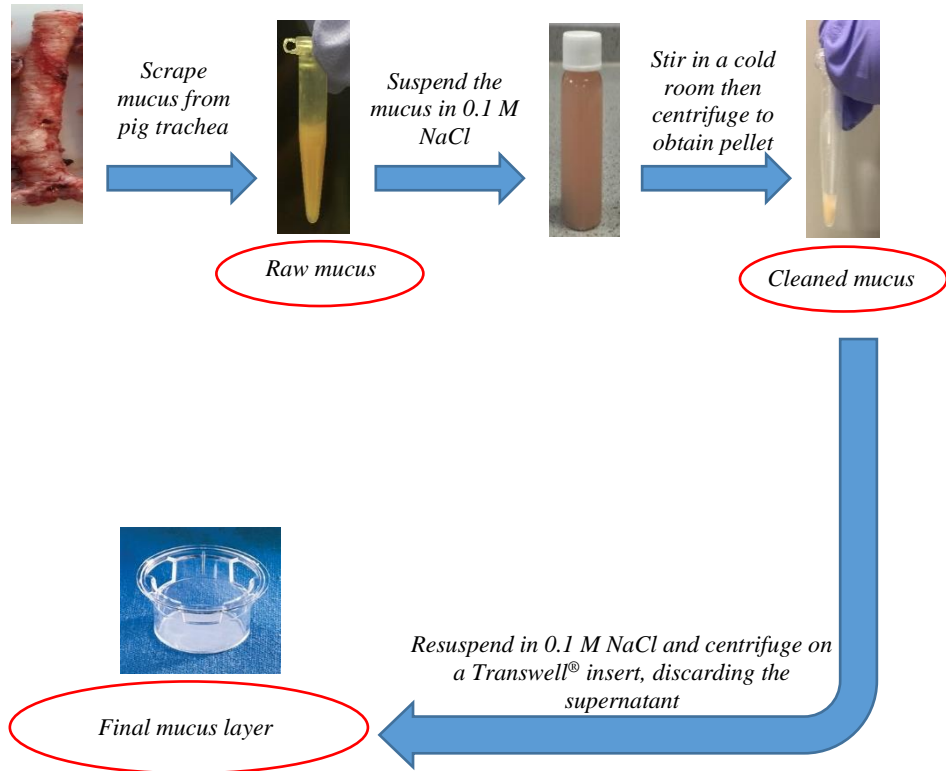
Figure 2.2.3. Mucus was prepared from the same batch in three stages (raw mucus, cleaned mucus, and a mucus layer) for cryo-SEM analysis.
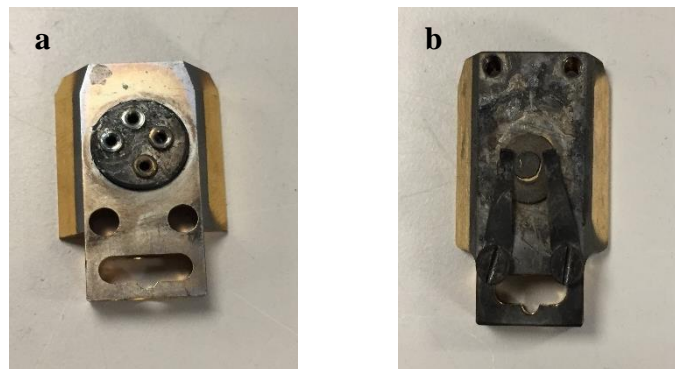
Figure 2.2.4. Cryo-SEM sample sledges. (a) Four brass rivets were placed into the sample sledge (stage). (b) A sample sledge with two springs to hold the Transwell® inserts covered by a mucus layer.

For all cryo-SEM experiments presented in this chapter, the samples were rapidly frozen in nitrogen slush before being transferred to a sample-prep stage (under vacuum) in a Quorum 3010T cryogenic SEM preparation system. Where

rivets were used as mounts, the tops of the rivets were knocked off to fracture the sample. This was followed by sublimation at -90 °C for the required time to remove water from the sample surface. The samples were sputter coated using the in-chamber Pt source at 10 mA for 60 s. Samples were then transferred into the SEM chamber (under vacuum) and imaged using an accelerating voltage of 10 kV on an FEI Quanta 200 3D focused ion beam-scanning electron microscope (FIB-SEM). The working distance was ca.15 mm, which was varied to ensure that the best images were obtained, while the beam current at 10 kV was 0.23 nA.

2.2.7. Optimisation of the apical/basolateral volumes for mucus diffusion studies

The apical to basolateral (A→B) permeability of the fluorescent dye Lucifer yellow CH dipotassium across the mucus layers was monitored over two hours using different volumes of the fluorescent dye solution in the Transwell® apical chamber and HBSS buffer in the basolateral chamber.

Different volumes of Lucifer yellow CH dipotassium solution in HBSS (100 µM) were placed in the apical chamber: 550 µL, 300 µL or 100 µL and a corresponding volume of 1500 µL, 1000 µL, or 500 µL of fresh pre-warmed HBSS was respectively added to the basolateral chamber. A sample (50 µL) was immediately taken from the apical side and diluted 10 times (time zero) to allow for the determination of the initial fluorescent donor concentration. Samples (200 µL) were withdrawn from the basolateral side after 5, 10, 15, 20, 30, 60, and 120 min, and replaced with 200 µL of fresh pre-warmed HBSS to maintain the initial basolateral volume. Then, 100 µL of each withdrawn sample was

transferred to a black 96-well plate (Nunc F96, Scientific Laboratory Supplies, Nottingham, UK). The sample concentration of Lucifer yellow CH dipotassium was measured using a Tecan (SPARK 10M) plate-reader, and the fluorescence intensity was measured at $\lambda_{em} = 427$ nm and $\lambda_{ex} = 535$ nm. Experiments were performed across mucus layers or empty Transwell® inserts) for each volumetric design (n = 4).

The calibration curve used to quantify the concentration of Lucifer yellow CH dipotassium in the samples from each time-point was obtained using standard solutions of Lucifer yellow CH dipotassium in HBSS at various concentrations (see Appendix I, Figure A-1).

2.2.8. Reproducibility of different mucus batches

Four batches of pooled mucus were used to verify the reproducibility of the mucus layer model. The apical to basolateral (A→B) permeability of fluorescein isothiocyanate (FITC, 10 µM in 0.1% dimethyl sulfoxide; DMSO) across the mucus layers was monitored for two hours. One-hundred microliters of 10 µM FITC (HBSS, 0.1% DMSO), which was placed in the apical chamber and 500 µL of HBSS (0.1% DMSO) was placed in the basolateral chamber. A sample (50 µL) was taken from the apical side and diluted 10 times to allow for the determination of the initial fluorescent donor marker concentration. Samples (200 µL) were withdrawn from the basolateral side after 10, 20, 30, 40, 60, 90, and 120 min, and replaced with 200 µL of fresh pre-warmed HBSS (0.1% DMSO). One-hundred microliters of the withdrawn samples were transferred to a black 96-well plate (Nunc F96, Scientific Laboratory Supplies, Nottingham, UK). The concentration of FITC in the samples was quantified using a Tecan

(SPARK 10M) plate-reader and monitored by measuring the fluorescence intensity at λ_{em} = 490 nm and λ_{ex} = 540 nm. The experiments were performed four times (N = 4), using four mucus layers per replicate (n = 4).

The calibration curve used to quantify the concentration of FITC in the samples was drawn from standard solutions of FITC in HBSS (0.1% DMSO) at various concentrations (see Appendix I, Figure A-2).

2.2.9. Impact of the mucus barrier on the permeation of various fluorescent dyes

Five fluorescent dyes with different physicochemical characteristics were tested in the mucus layer model:. Lucifer yellow CH dipotassium, FITC, Rhodamine B base, Rhodamine 123, and Rose Bengal

Stewart (Stewart, 1978, Stewart, 1981) revolutionised the fluorescence dye field by introducing the dye Lucifer yellow, which is highly and flexibly fluorescent. Lucifer is one of the names for Satan, but the reason for this choice has not been clarified. It has been used in thousands of investigations and has contributed to the study of many cell types (Hanani, 2012). FITC is the major derivative of fluorescein, a synthetic organic compound that is widely used as a fluorescent tracer in many applications. In cell biology, it is used for a wide range of applications including labelling and tracking cells (Parish, 1999). Rhodamine dyes are also used for many biological applications, including specific binding to proteins and biological tissue staining (Bakkialakshmi et al., 2013). One Rhodamine B base is a rhodamine derivative, which is used in a large variety of applications as an important xanthene dye, such as for quantum counting, dye lasers, and photosensitisation (Ponchel and Irache, 1998). Rhodamine 123 is
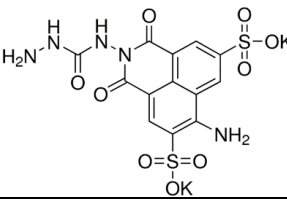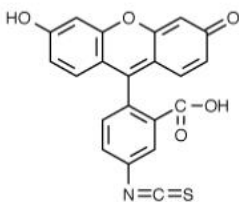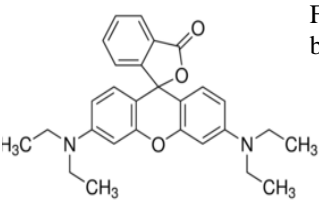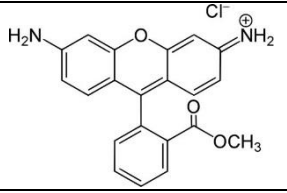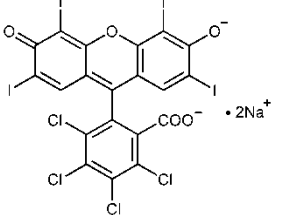
another derivative of rhodamine which has a permanently cationic charge that is used widely in cell biology, especially as a tracer dye (Forster et al., 2012). Ghnem discovered Rose Bengal in 1882 and was originally prepared as an analogue of fluorescein (Alexander, 2010). Its name is derived from a flower and a region (the rose and Bengal, respectively).

Lucifer yellow CH dipotassium, Rhodamine B base, Rhodamine 123, and Rose Bengal were prepared as 100 µM solutions in HBSS. Due to its high fluorescence intensity, FITC was prepared as a 10 µM solution in HBSS (0.1% DMSO).

2. Development of an in-vitro mucus model

Table 2.2.1. Characteristics of the various fluorescent dyes used in the mucus permeation studies.

Name	Structure	Form	Solubility* (logP)	Excitation spectrum (λ_{max}/nm)**	Emission spectrum (λ_{max}/nm)**
Lucifer Yellow		Acid in a salt form	1 mg is dissolved in 1 mL of H_2O (-2.57^)	427	535
FITC		Free acid	20 mg is dissolved in 1 mL ethanol	490	540
Rhodamine B Base		Free base	1 mg is dissolved in 1 mL of ethanol	544	680
Rhodamine 123		Base in a salt form	1 mg is dissolved in 1 mL of ethanol	540	590
Rose Bengal		Acid in a salt form	100 mg is dissolved in 1 mL of H_2O (9.26 ^^)	549	620

*manufacturer specification sheet (solubility)

**optimised λ_{max}/nm.

^(The United States Environmental Protection Agency, 2017) Available at: https://comptox.epa.gov/dashboard/dsstoxdb/results?search=DTXSID6040167

^^(The Food Database, 2017) Available at: http://foodb.ca/compounds/FDB015530

67

The method for Lucifer yellow CH dipotassium and FITC permeation has been detailed previously in sections 2.2.7 and 2.2.8, respectively. The procedure used to measure the diffusion of the Rhodamine dyes (Rhodamine B base and Rhodamine 123) and Rose Bengal was similar to that used for Lucifer yellow measurements, as described in section 2.2.7.

The calibration curve used to quantify the amount of Rhodamine B base, Rhodamine 123, and Rose Bengal in the test samples was drawn from their standard solutions in HBSS at various concentrations (see Appendix I, Figure A-3).

2.2.10. Effect of different salts on the permeation of the same fluorescent dye across a mucus layer

A mucus layer permeation investigation using Lucifer yellow CH dilithium salt and Lucifer yellow CH dipotassium salt was undertaken to assess whether different salts have an impact on the compound permeation across mucus (Figure 2.2.5). To this end, the optimised protocol described in section 2.2.7 was followed.
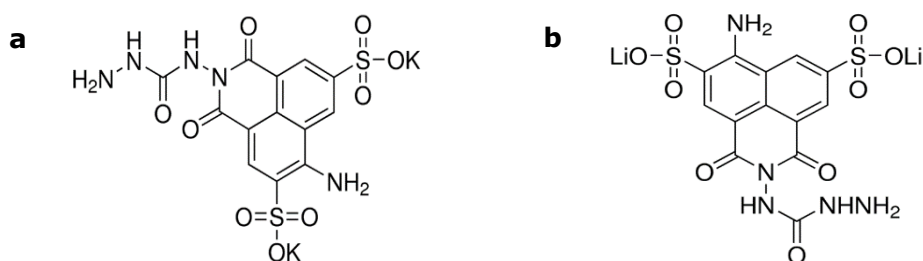
Figure 2.2.5. Lucifer Yellow CH chemical structure, (a) dilithium salt, (b) dipotassium salt.

The calibration curve used to quantify the amount of Lucifer yellow CH dilithium and Lucifer yellow CH dipotassium in the samples was drawn from their standard solutions in HBSS at various concentrations (see Appendix I, Figure A-4).

2.2.11.Statistical analysis

Statistical analysis was performed using GraphPad Prism 6.02. The unpaired t-test (multiple comparisons) was used to compare two groups. Significant differences between experimental groups were defined when the p-value was less than 0.05.

2.3. Results and discussion

2.3.1. Staining of Transwell® inserts coated a pig tracheal mucus layer

In many published experimental setups described to study the interactions of drugs or drug delivery systems with mucus, the mucus layer is typically constrained between two semipermeable membranes (Müller et al., 2014). This was incompatible with the purpose of this study as those membranes would prevent drug solution/aerosols from making full contact with the mucus. Therefore, in order to perform an effective *in-vitro* assessment which mimics conditions *in-vivo*, the need arose to develop Transwell® based *in-vitro* system containing a thinner layer of pig tracheal mucus. Although such systems had been described previously (Friedl et al., 2013), it is notable that there were no clear and defined protocols within the literature that explained how the mucus was spread over the Transwell® inserts. To achieve, twelve microliters of mucus were added to 12-well Transwell® inserts and the cell culture plates housing the inserts were centrifuged, according to the protocol previously optimised by Dr. Emanuela Cingolani (Cingolani, 2016). Polyvalent basic water-soluble Alcian-Blue dye, its blue colour due to the presence of copper in the molecule, was used to enhance the visualisation of the mucus. When applied in 3% acetic solution (pH 2.5), it stains both carboxylated and sulfated acid mucopolysaccharides and sulfated and carboxylated sialomucins (Ramakrishnan and Sulochana, 2012). Alcian blue staining confirmed that addition of 12 μL of mucus onto the Transwells enabled full coverage of the permeable membrane by the mucus (Figure 2.3.1).

2. Development of an in-vitro mucus model
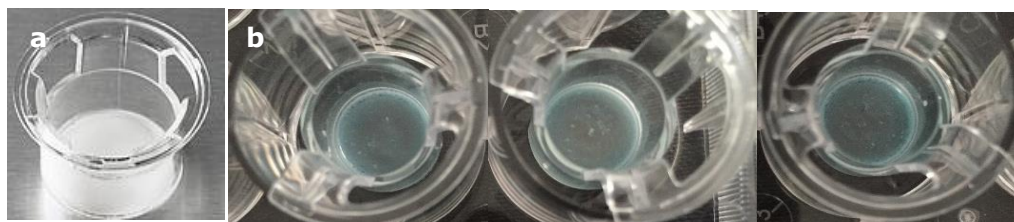
Figure 2.3.1. Transwell® inserts coated with pig mucus. (a) Empty Transwell® inserts; (b) Pig mucus covered Transwell® inserts under optimised preparation conditions (12 µL) stained with Alcian-Blue.

The human upper airway contains a mucus layer that varies in thickness, depending on the location. However, it is reported to be 55 ± 5 µm in the bronchioles (Lai et al., 2009a). Hence, a 50 µm thickness corresponds to $\approx$5.0 µL of mucus if the mucus coating is considered as a cylinder, with the semipermeable membrane of the Transwell® inserts as a base (growth area = 1.12 cm^2). Coating the Transwell® inserts with only 5.0 µL of mucus was insufficient to achieve uniform coverage and a higher mucus volume of 12 µL was necessary, as described (Figure 2.3.1.b) (Cingolani, 2016). This mucus volume, corresponding to a thickness of $\approx$100 µm, is about twice that of the mucus film that lines the upper airway in humans. However, both the thickness and volume of the mucus film are recognised as playing an important role in drug permeation and absorption, and therefore the even and complete coating of mucus across the whole surface of the Transwell® inserts was considered essential. Hence, 12 µL of mucus was selected due to the need for complete surface coverage of the Transwell® inserts.

Interestingly, the thickness of mucus secretion at the surface of the airway epithelial cell line Calu-3 cultured in air-liquid interface (ALI) conditions, has been estimated to be $\approx$100 µm, although there is a probability of volume overestimation due to mucus rehydration during TEER measurements (Grainger

et al., 2009). Cell-free mucus layers and Calu-3 layers could therefore be used in parallel to assess how the presence of the airway epithelium underneath the mucus layer might impact on drug mucus binding.

2.3.2. Mucus characterisation

2.3.2.1. Viscosity

2.3.2.1.1. Poiseuille flow between parallel plates

Cleaned mucus samples were injected into the Viscosizer TD to measure viscosity. The system measures the transit time of a sample through the capillary tube between windows 1 and 2 (Figure 2.2.2). This time was used to calculate the specific viscosity (η_{sp}) of the sample using Poiseuille's law:

$$\eta_{sp} = \left(\frac{\Delta t - \Delta t_0}{\Delta t_0}\right)\left(\frac{2L}{l_1 + l_2}\right),$$

where Δt and Δt_0 are the transit times between windows 1 and 2, for the cleaned mucus sample and for the reference (caffeine) sample, respectively; l_1, l_2 and L are the capillary lengths to window 1 and window 2, and the total length of the capillary, respectively. From the generated data, $\Delta t = 73.8$ seconds while $\Delta t_0 = 13.54$ seconds. Hence, $\eta_{sp} = 5.47$ cp.

From this result we can calculate the absolute viscosity (η) of the cleaned mucus sample using the caffeine sample as a reference of known viscosity (η_{ref}):

$$\eta = \eta_{ref} * \eta_{sp},$$

As the reference caffeine viscosity was 2.49, the absolute viscosity of the cleaned mucus was 13.61 cp (13.61 mPa.s). However, typical mucus secretions exhibit a viscosity ~2000-fold higher than water (Lai et al., 2009b) while the obtained value was only ~14-fold higher (13.61 cp). This suggests that the

capillary might have been obstructed by the gelled component of the mucus, only allowing the least viscous components through. Hence, this instrument was deemed unsuitable for our needs and an alternative measuring technique was used.

2.3.2.1.2. Cone-plate rheometer

The measured viscosity of the raw and cleaned mucus samples is detailed in Figure 2.3.2. Raw mucus was shown to have a lower viscosity, and a statistically significant difference in viscosity was observed between raw and cleaned mucus at shear rates lower than 5 s^{-1}, $p > 0.05$. This can be attributed to a possible concentration of the mucus during the cleaning procedure. For shear rates that exceeded 5 s^{-1}, the difference in the viscosity profiles of both samples was insignificant.
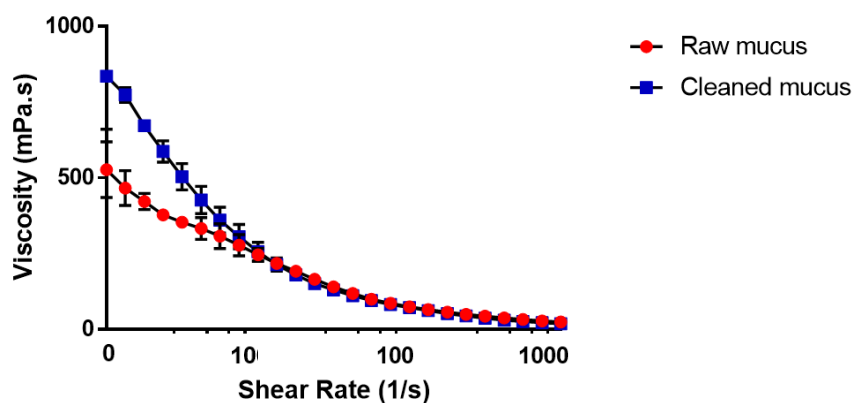
Figure 2.3.2. The viscosity of raw and cleaned mucus (triplicates) at different shear rates. Analyses were carried out at 37 °C. Eight points per decade were used for three decades with the shear rate increasing logarithmically from 1 to 1000 s^{-1}. A total of 25 points were made (one point per min). Data are presented as mean ± SD (n = 3).

At a shear rate of 1 s⁻¹, cleaned mucus exhibited a viscosity of ~850 mPa.s, which is in a close agreement with that of the respiratory mucus reported in the literature (1000 mPa.s) (Roselli and Diller, 2011). Mucus was found to be non-Newtonian across the range of shear rates applied where the mucus samples' viscosity decreased with increasing shear rate. This relatively consistent decrease in the viscosity of mucus obtained from trachea with increasing shear rate was in accordance with the literature, where it is extensively reported that mucus exhibits non-Newtonian fluid behaviour and exhibits shear-thinning behaviour (Cone, 2009b). The trend at the higher shear rates can be attributed to the adhesive interactions between mucin fibres. It is reported that at the physiological maximum shear rate (10^3 - 10^5 s⁻¹), the mucus viscosity approached that of water, as shown in Figure 2.3.2. (Cone, 2009a).

2.3.2.2. Sodium dodecyl sulfate polyacrylamide gel electrophoresis (SDS-PAGE)

The protein content of the raw and cleaned mucus samples was tested using SDS-PAGE to investigate if the intensive treatment subjected to the cleaned mucus would result in distortion of the protein profile compared to raw mucus (Figure 2.3.3).
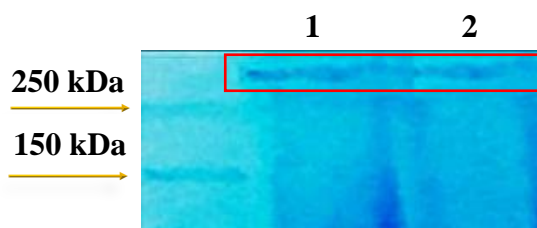
Figure 2.3.3. SDS-PAGE of the two mucus types (1; raw mucus, 2; cleaned mucus). Equal loading volume was used in both gel wells using Tris-Glycine 4-20% TGX mini gel stained with Coomassie blue.

The maximum molecular weight in the ladder of Precision Plus Protein™ pre-stained standards is 250 kDa. Both raw and cleaned samples exhibited similar bands above 250 kDa with no band corresponding to a lower MW observed. In terms of protein identification, mucins are known to be challenging due to their high molecular weight (200 kDa-200 MDa), heavily glycosylated nature (up to 90%), and size (Rg 10–300 nm) (Kesimer and Sheehan, 2012). However, our main aim in this analysis was to verify the presence of similar bands for both mucus types and was not to profile the mucus proteins.

2.3.2.3. Cryogenic-scanning electron microscopy (cryo-SEM)

A freshly extracted raw mucus sample derived from pig trachea and a cleaned mucus preparation from the same starting material (5 µL; see Figure 2.2.1 for the sample cleaning protocol) were placed onto brass rivets held within a sample sledge and sublimated for 5 min, followed by imaging by cryo-SEM (Figure 2.3.4).
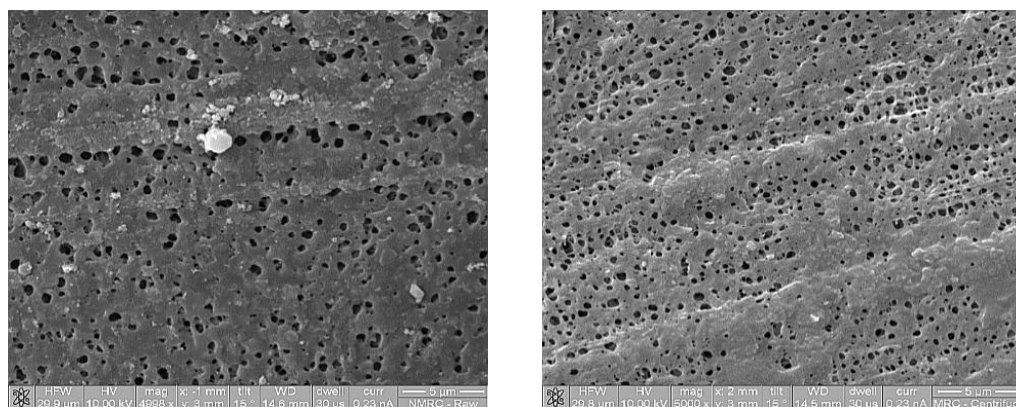
Figure 2.3.4. Cryo-SEM images of raw mucus (raw mucus; left) and the middle preparation stage of mucus, i.e. "cleaned mucus", (right) placed onto brass rivets via sublimation at −90°C for 5 min. Preparations show a porous structure that is believed to be filled with liquid phase. The scale bars represent 5 µm. The magnification is ×5,000.

Figure 2.3.4. reveals a porous structure and a high degree of similarity between the two mucus preparation stages. The raw mucus appeared most likely to have a greater degree of hydration and associated unwanted biological debris (5.9% coverage of pores, calculated by imageJ®) when compared with the cleaned mucus preparation, which accordingly showed a more porous nature with pores covering 12.0% of the mucus surface, according to imageJ calculation. An SEM-image of the cleaned mucus with a viewing magnification ×12,000 revealed pore sizes with diameters ~400 ± 200 nm (Figure 2.3.5), in close agreement with the range of pore sizes observed previously in mucus gel cryo-SEM imaging of horse bronchioles (~100 nm and voids of several micrometres) (Kirch et al., 2012).

Different mucus glycoproteins obtained from various secretory epithelia, including respiratory, gastric and cervical mucosae, can be compared as previous studies have revealed a similar macromolecular architecture of the secreted mucus (Sheehan et al., 1986). Thus, the pore sizes observed here for the pig tracheal mucus were also consistent with those of undiluted, healthy human cervicovaginal mucus (CVM) which were reported to be in the range 50–1800 nm, with an average of ~340 ± 70 nm (Lai et al., 2010).
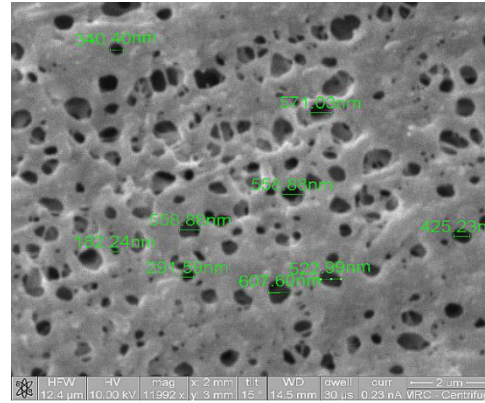
Figure 2.3.5. Cryo-SEM image showing the pore sizes of cleaned mucus on a brass rivet following sublimation at −90°C for 5 min. Approximately, pores ranged from 200 to 600 nm in diameter. The scale bars represent 2 µm. The magnification is ×12,000.

A mucus layer covering a Transwell® insert was prepared from the same batch of raw and cleaned mucus that was imaged in Figure 2.3.4. using brass rivets as the mount. Due to the fact that the mucus could not be scraped from one Transwell® insert then to be placed onto the brass rivet because of the difficulty of getting 5 µL to be filled in the brass rivet from the Transwell® insert, the mucus layer was cut with the membrane of the Transwell® insert and placed onto the sample sledge and sublimated for 5 min, followed by imaging by cryo-SEM (Figure 2.3.6).
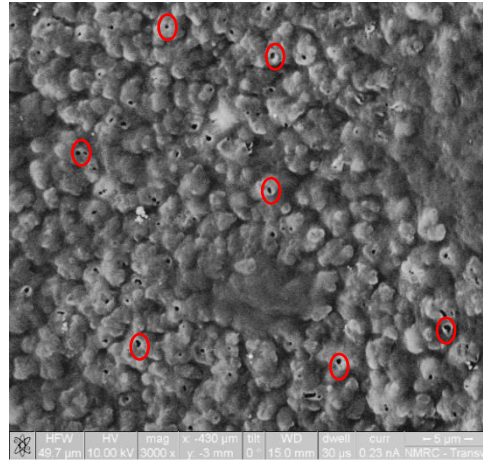
Figure 2.3.6. Cryo-SEM image of the mucus layer that was cut from a Transwell® insert and placed directly over the sample sledge with sublimation at −90°C for 5 min. The red circles highlight very small pores in the hydrogel film. The scale bars represent 5 µm. The magnification is ×3,000.

The image with magnification ×3,000 in Figure 2.3.6. suggests a water-like structure with surface coverage (SC%) of pores 1.1% estimated by the ImageJ®. This is proposed to be due to the presence of excess water and insufficient sublimation time, which affected the outcome from the sputter chamber (Efthymiou, 2017). Hence, increasing the sublimation (etch) time may be necessary due to the difference in the frost and surface water, which is higher in the case of the Transwell® insert sample sledge compared to the native and cleaned mucus. In the case of raw and cleaned mucus samples placed on fractured brass rivets, a clean fracture surface and no apparent surface water could be observed (Figure 2.3.4), meaning that a sublimation time of only 5 min was sufficient to reveal the pores. For a mucus layer covering a Transwell® insert, more water had therefore to be removed to view the pores and allow for a comparison between the three stages of mucus preparation. A 10-min sublimation therefore subsequently applied to remove more water (Figure 2.3.7).
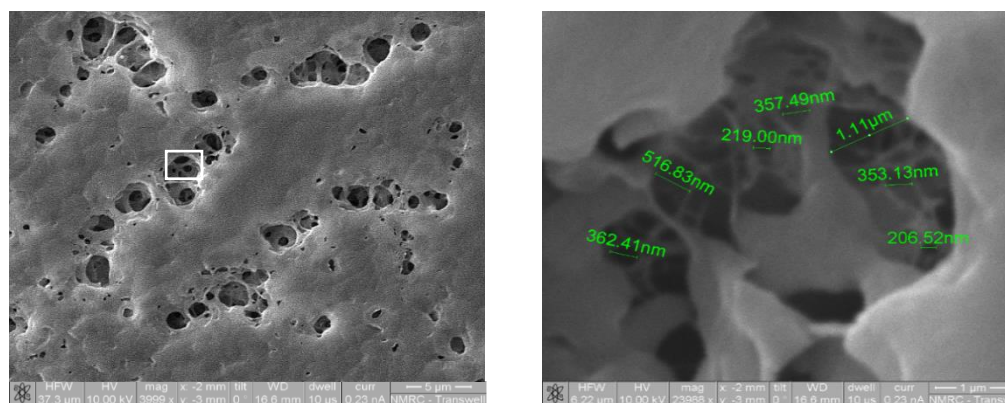
Figure 2.3.7. Cryo-SEM image of the Transwell® insert covered with a mucus layer placed directly over the sample sledge using sublimation at −90°C for 10 min. The cryo-SEM image of the final mucus layer preparation stage shows the strongly heterogeneous nature of the mesh spacing as large and small pores can be seen (left image). Moreover, an enlarged image of the mucus (right), which shows the section of the left-hand image marked with a square, shows a thick polymer scaffold wall. The scale bars represent: 5 and 1 μm, while the magnification: ×4,000 and ×24,000, left and right images, respectively.

A more porous structure is apparent in Figure 2.3.7. (10-min sublimation) compared to the data in Figure 2.3.6. (5-min sublimation); likely due to improved water removal.

The right-hand image in Figure 2.3.7. does show a pore size ranging from 200–600 nm, i.e., in the same range as previously observed (Figure 2.3.5). Thus, the the mucus layer mounted on Transwell® inserts is clearly a porous material. However, it shows a different internal organisation when compared to the raw and cleaned mucus preparations (Figure 2.3.4). The raw and cleaned mucus samples filled a brass rivet and a second rivet was placed on top to allow the physical fracture of the samples. In the case of mucus layers covering Transwell® inserts, the polyester membrane was cut and placed over the sample

sledge before the water was sublimed. This is a collapsing down mechanism, without any fracturing occurring.

Furthermore, when samples are placed inside the cryo-chamber, sublimation begins by heating them from the sides and bottom. Therefore, mucus over a polyester plastic membrane would not be sublimed in the same way as mucus that is exposed on a brass rivet.

For improved comparison of the three stages of mucus preparation, mucus layers formed on Transwells were subsequently scraped off the membrane. All samples were placed onto brass rivets (5 µL each) in a sample sledge and sublimated for 10 min (Figure 2.3.8).

2. Development of an in-vitro mucus model
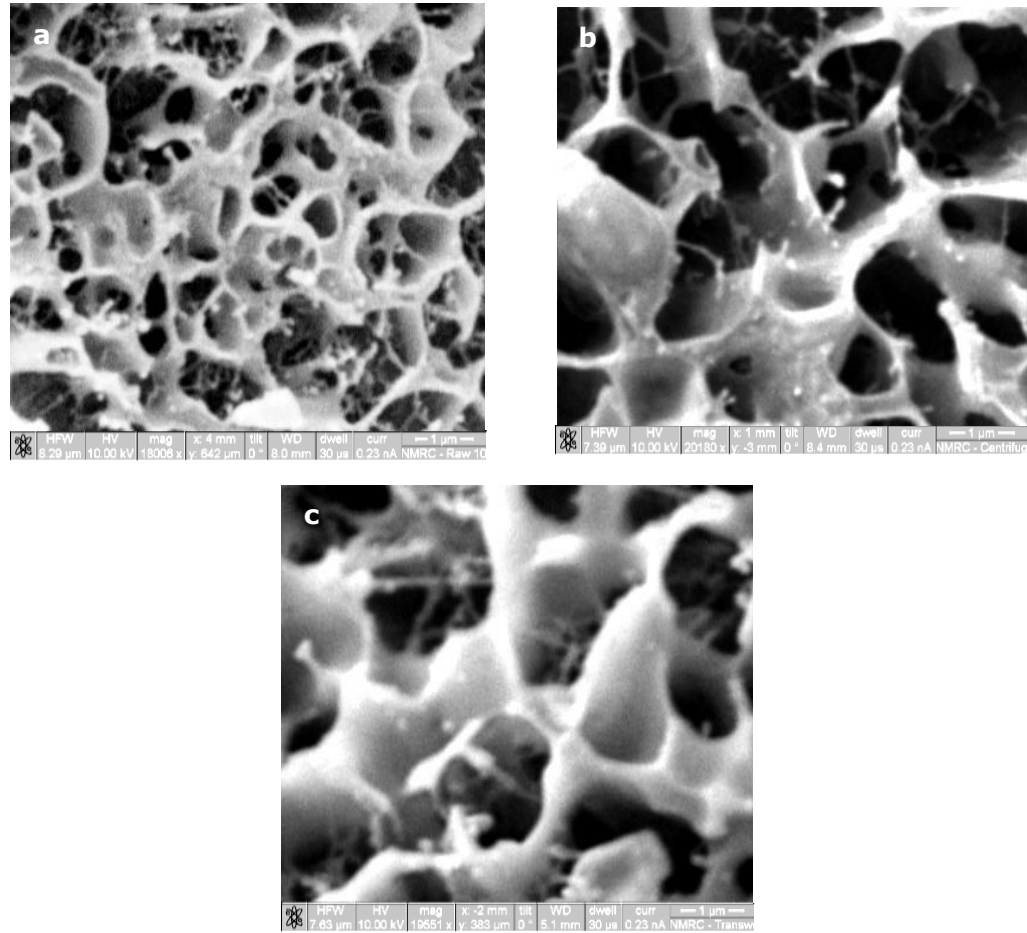
Figure 2.3.8. Cryo-SEM image of different mucus preparation stages. (a) raw mucus, (b) cleaned mucus, and (c) mucus scraped from Transwell® inserts. All samples were placed onto brass rivets and sublimed at −90°C for 10 min. The scale bars represent 1 μm. The magnification is ~×19,000. The image resolution was enhanced by Luminance HDR® software.

Following this method, the images of the three mucus-preparation stages (Figure 2.3.8) showed a high degree of similarity in terms of internal structure. However, the raw mucus showed a thicker scaffold when compared with the two other preparation stages. These data suggest that raw mucus is filled with liquid and biological debris. Increasing the sublimation time to 10 min revealed the mesh spacing within the mucus scaffold, while 5-min sublimation (Figure 2.3.4) resulted in a porous structure with poor integration of the mucus scaffold. The

very thick scaffold in all stages of mucus preparation (Figure 2.3.8) may be composed of thick mucin bundles, as proposed in a previous study (Lai et al., 2010). These bundles of thick mucin provide mechanical strength to the mucus scaffold and act as sieve, playing an important role in mucus rheology and restricting the diffusion of other substances according to their size (Kirch et al., 2012).

The mucus scaffold of pig tracheal mucus was notably similar to that displayed in SEM images of mucus secretions from air interface-cultured Calu-3 cells, pig intestinal mucus and horse bronchial mucus (Boegh et al., 2013, Kirch et al., 2012, Stentebjerg-Andersen et al., 2011).
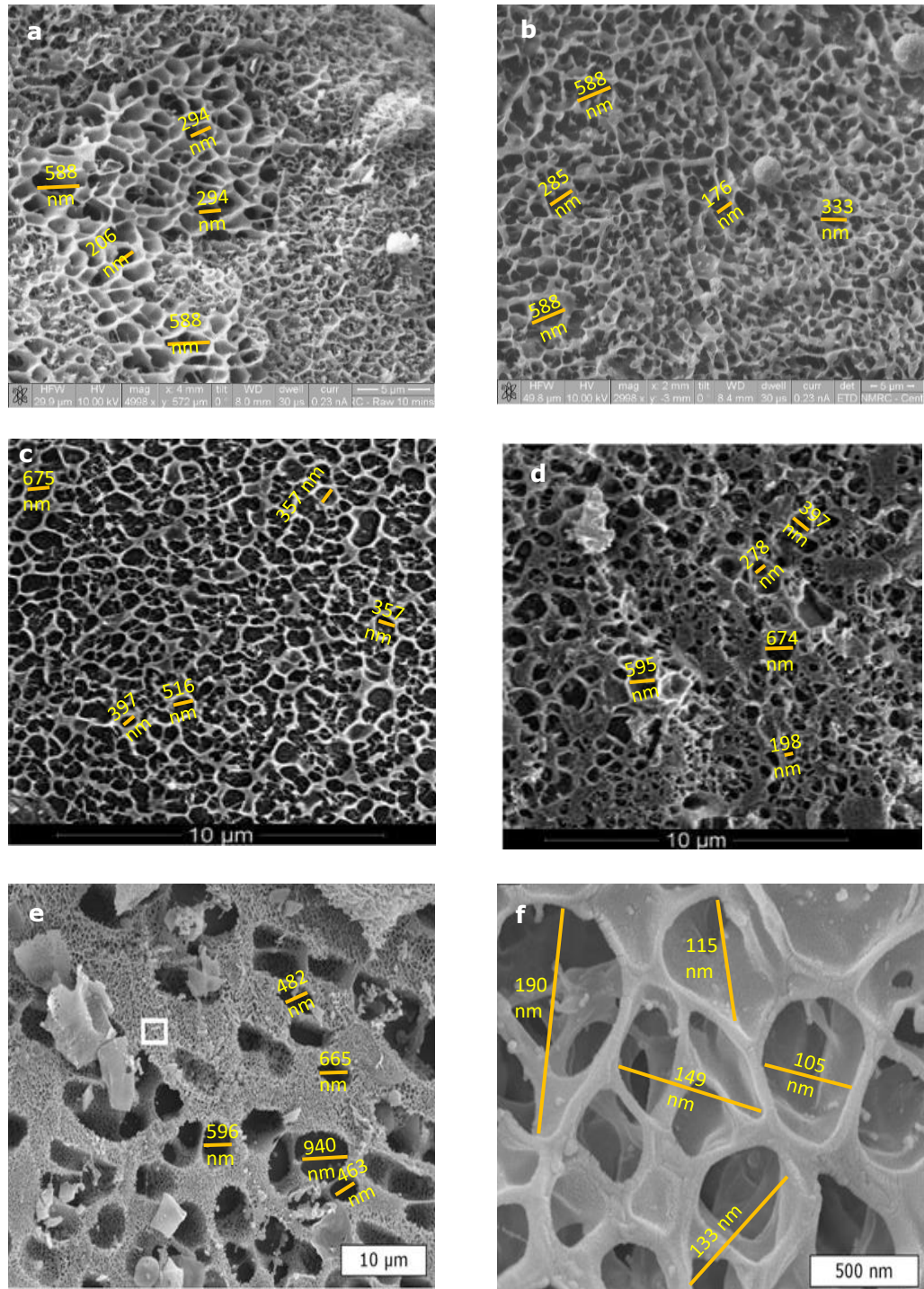
Figure 2.3.9. Cryo-SEM image of mucus from different biological systems. (a) Raw mucus. (b) Cleaned mucus. (a) and (b) show data obtained in this study by placing samples onto brass rivets with sublimation at −90°C for 10 min. (c) Mucus secretions from air interface-cultured Calu-3 cells that were cultured for 16 days (reproduced from (Boegh et al., 2013)). (d) pig intestinal mucus obtained from a piece of jejunum isolated from a fasted pig (reproduced from (Stentebjerg-Andersen et al., 2011)). (e and f) Native respiratory mucus

obtained from the distal region of the bronchia during bronchoscopy of a healthy horse (taken from (Kirch et al., 2012)). (f) Shows an enlargement of the area indicated with a square in (e). Pore sizes were measured using the ImageJ®.

The mucus scaffolds from different species and biological systems appeared to share a porous internal organisation. However, mucus obtained from animals were obviously thicker and more heterogeneous than that isolated from air interface-cultured Calu-3 cell monolayers. This is probably because Calu-3-secreted mucus is not affected by other biological debris.

In summary, intensive preparation of raw mucus from pig trachea to form a layer covering a Transwell® insert, did not result in observable differences in the overall mucus structure. However, the raw mucus appears denser, which is proposed to be mainly due to the presence of extraneous biological debris.

2.3.3. Optimisation of the apical/basolateral volumes for permeation measurement across mucus layers

A volume of 500, 250, and 50 µL of 100 µM Lucifer yellow CH dipotassium solution were added to the apical side and 1500, 1000, and 500 µL of HBSS buffer to the basolateral side of the Transwell® insert, respectively. The permeation profile of the dye across mucus layers and empty Transwell® inserts are shown in Figure 2.3.10.

2. Development of an in-vitro mucus model
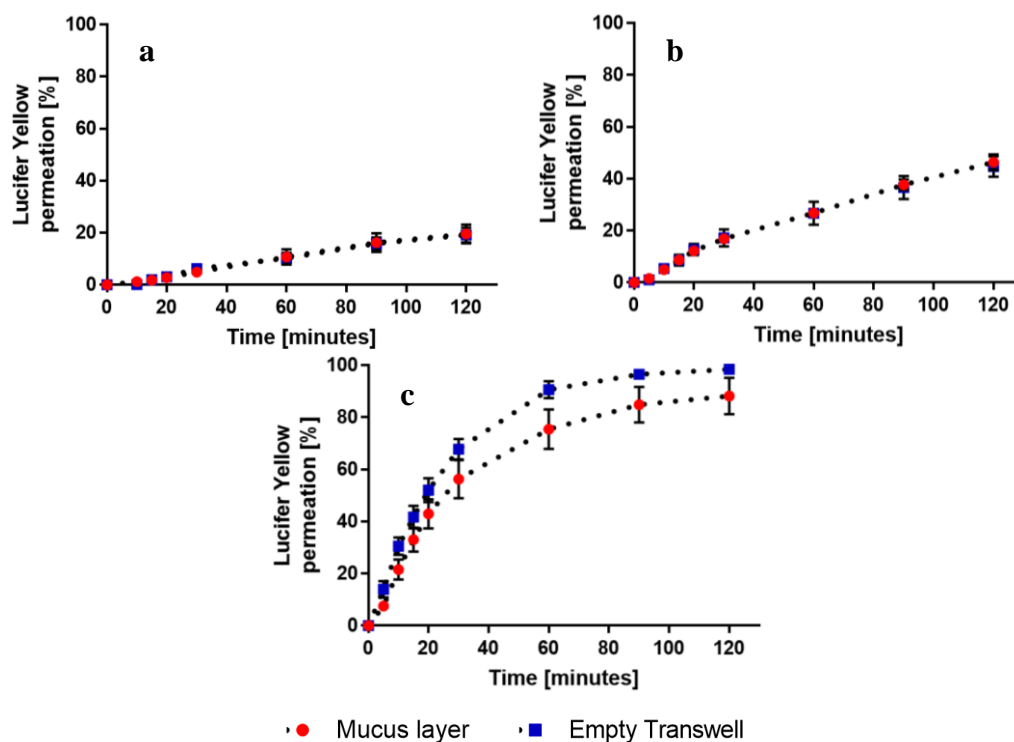
Figure 2.3.10. Apical to basolateral (A→B) permeation profile of Lucifer yellow CH dipotassium (100 µM) after a) 500, b) 250, and c) 50 µL of the dye solution were added to the apical compartment of the Transwell® inserts and 1500, 1000, and 500 µL of HBSS were added to the basal compartment respectively. Data are expressed as the cumulative percentage of the initial dose applied recovered basolaterally and are presented as mean ± SD (n = 4).

When 500 µL and 1500 µL were used, respectively, in the apical and basolateral chambers of the Transwell® inserts (Figure 2.3.10 (a)), the dye concentration at the first time-point (five min) could not be detected as it was below the lower limit of quantification (LLOQ). Furthermore, after two hours, only 20 ± 4% (SD) of the initial Lucifer yellow CH dipotassium dose had permeated into the basolateral chamber. This was expected as at the last time-point (120 min), Lucifer yellow CH dipotassium was visibly still present in the apical compartment. The permeation profile across the mucus layer and empty inserts were not significantly different (p > 0.05), which could have been due to the

dilution of the mucus layer by the large volume of fluid in the apical chamber. Hence, a reduction in the volumes added to the apical and basolateral sides was deemed necessary. The volume of Lucifer yellow CH dipotassium in the apical compartment and HBSS buffer in the basolateral compartment were reduced to 250 µL and 1000 µL, respectively. In those conditions, $46 \pm 8\%$ (SD) of the dye permeated across the mucus layer and empty Transwell® inserts (Figure 2.3.10 (b)). However, this remained low. Therefore, the volumes in the insert chambers were further decreased to 50 µL in the apical side and 500 µL in the basal side. This resulted in $88 \pm 8\%$ (SD) and $98 \pm 1\%$ (SD) of the applied dose diffusing across the mucus layer and an empty semipermeable membrane, respectively, within two hours ($p < 0.05$; Figure 2.3.10 (c)). Hence, close to 100% of the Lucifer yellow dose could cross the empty Transwell® inserts, indicating that the apical fluid volume and the uncoated diffusion system did not act as diffusional barriers. Therefore, those volumes (50/500) were used in the following experiments.

The impact of mucus on the permeation profile of Lucifer yellow is observed in Figure 2.3.10 (c). The 10% significant difference between permeation through the mucus layered Transwell® inserts and the empty Transwell® inserts was observed at all test intervals and this permeation profile between the two types of Transwell® inserts can be explained by the hydrophilicity of the Lucifer yellow CH dipotassium compound, which is soluble in water at 1mg/mL and has a logP of –2.57. Although the mucus network forms a physical barrier to diffusion, the numerous negative charges of mucins probably allow Lucifer yellow CH dipotassium, which possesses two negative charges, to permeate quickly due to the lack of charge attraction.

2.3.4. Reproducibility of different mucus batches

To assess the reproducibility of the mucus layer, a lipophilic fluorescent dye (FITC) was used for permeation studies. This fluorescent dye was predicted to be retained in the mucus layer to a higher extent than Lucifer yellow and thus a higher contrast between its permeation profile in the presence or absence of mucus in the Transwell® insert was expected.
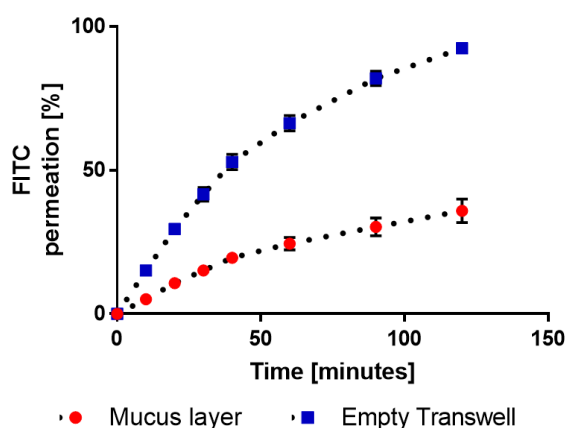
Figure 2.3.11. Apical to basolateral (A→B) permeation profile of FITC (10 µM) after 50 µL of the dye solution was added to the apical compartment of the Transwell® inset and 500 µL of HBSS (0.1% DMSO) was added to the basolateral compartment. Data are expressed as the cumulative percentage of the initial dose applied recovered basolaterally and are presented as mean ± SEM (N = 4, n = 4).

Only 5% of the FITC initial dose crossed the mucus layer during the first 10 mins, while a three-fold increase was observed at the same time-point in the empty Transwell® inserts. A similar observation was made at each time-point with only $36 \pm 4\%$ (SD) of FITC permeating through the mucus layer in 120 min while $92 \pm 2\%$ (SD) crossed the empty Transwell® inserts ($p < 0.05$), indicating that the mucus layer restricted the diffusion of FITC. The experiment was

reproduced with four different mucus batches to estimate the reproducibility of the mucus preparation. Low standard error of the mean values and no statistical difference between the individual permeation profiles ($p > 0.05$) were observed, demonstrating the reproducibility of the mucus model developed.

FITC presents partial negative charges at physiological pH, which may exclude the electrostatic binding theory between charged mucins and FITC as they both possess negative charges. Therefore, hydrophobic interactions may explain the limited amount of FITC crossing the mucus over the 2h of the experiment.

2.3.5. Role of the mucus barrier in the permeation of fluorescent dyes

Mucus acts as a barrier to the penetration of foreign molecules but also allows diffusion of specific molecules from the surface of the mucus layer towards the epithelial cell layer (Round et al., 2002). The extent and rate of permeation across the mucus barrier depends on the physiochemical properties of the drugs to which it is exposed (Khanvilkar et al., 2001). Hence, this experimental work was carried out to assess the diffusion of five fluorescent dyes with different physicochemical characteristics across the mucus layer, i.e. Lucifer yellow CH dipotassium, FITC, Rhodamine Base, Rhodamine 123, and Rose Bengal. Their chemical structures are shown in the methodology section 2.2.9.

To our knowledge, this is the first attempt to study the influence of the physicochemical properties of fluorescent dyes on their diffusion across a mucus layer *in-vitro*.

In addition to the previously tested compounds (Lucifer yellow and FITC), the permeation of three other fluorescent dyes (Rhodamine B, Rhodamine 123, and

2. Development of an in-vitro mucus model

Rose Bengal) across mucus layers was investigated. Rhodamine B is hydrophilic in nature, but this is not the only factor that may influence its permeation through mucus. Rhodamine B base bears tertiary amino groups, which may lead to electrostatic interactions with mucin fibres that bear negative charges (Ponchel and Irache, 1998, Woodley, 2001). Similarly, Rhodamine 123 presents a permanently positive charge that should theoretically electrostatically interact with negatively charged mucins. In contrast, Rose Bengal is a lipophilic and negatively charged fluorescent dye. Figure 2.3.12 shows the permeation of these fluorescent dyes across mucus layers.
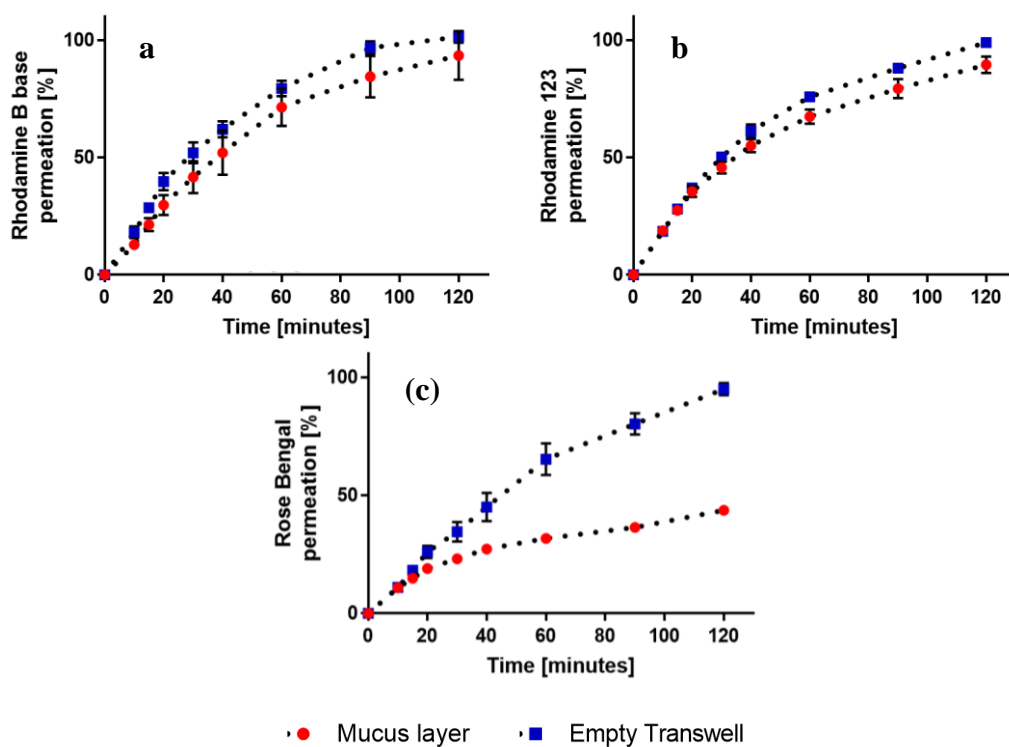
Figure 2.3.12. Apical to basolateral (A→B) permeation profile of a) Rhodamine B base, b) Rhodamine 123, and c) Rose Bengal (100 µM) across the mucus layer and empty Transwell® inserts. The dyes were delivered as a 50 µL solution to the apical compartment while 500 µL of the buffer (HBSS) was added to the basal compartment. Data are expressed as the cumulative percentage of the initial dose applied recovered basolaterally and are presented as mean ± SD (n = 4).

2. *Development of an in-vitro mucus model*

As shown in Figure 2.3.12 (a), there was no significant difference between the permeation profiles of Rhodamine B across the mucus layer or the insert membrane ($p > 0.05$). Therefore, its anticipated binding to the mucin fibres was not confirmed experimentally. However, information on the pKa of the amino groups are lacking in the literature. Therefore, their ionisation status in HBSS (at pH of approximately 7.4) remains unknown. Surprisingly, there was no difference between the permeation profile of the permanently positive charged molecule, Rhodamine 123, across the mucus layer or empty Transwell® inserts samples over the first 40 min ($p > 0.05$), Figure 2.3.12 (b). However, significant differences emerged from 40 mins onwards ($p < 0.05$) but only a 10 % difference in the cumulative amount permeated by the end of the experiment. Rhodamine 123, thus, easily permeated the mucus layer. This may be due to the salts present in the HBSS buffer solution acting as negatively charged counter ions and dragging the dye across the mucus layer.

Furthermore, being hydrophilic compounds, Rhodamine B and Rhodamine 123 have likely more affinity for the aqueous phase in mucus, which may play a role in their molecular diffusion rate (Lillehoj and Kim, 2002).

The permeation profile of Rose Bengal was different across the mucus layer and empty Transwell® inserts (Figure 2.3.12 (c)). The difference was significant from 15 mins onwards ($p < 0.05$). Rose Bengal is soluble in water (1 mg/mL), which according to the manufacturer is due to the presence of the sodium counter ions. Actually, the human metabolome database (HMDB) reports Rose Bengal without sodium salt to have a logP of 6.02 or 9.26 in two different laboratories (Virtual Computational Chemistry Laboratory and ChemAxon, respectively), indicating its highly hydrophobic nature, which may explain its high affinity for

the mucus layer. This permeation study revealed that the sodium ions could not facilitate the dye permeation across the mucus layer. As they act as a solubility enhancers in aqueous media, they indeed fade away in solution.

2.3.6. Effect of different salts of the same fluorescent dye on the permeation across a mucus layer

In general, different salts are used to enhance the solubility and bioavailability of oral solid dosage forms. For instance, the absorption of diclofenac after oral administration depends primarily on the salt form. The potassium salt form has been reported to diffuse faster than the sodium salt, since the latter is less water soluble (Altman et al., 2015). Therefore, the sodium salt is used for the sustained-release formulations, while the potassium salt of diclofenac is intended for immediate release, usually for acute pain treatment, such as for migraine.

In this PhD project, we wanted to examine whether the salt had an effect on diffusion rate of the same compound through mucus. Figure 2.3.13. depicts the permeation of Lucifer yellow dipotassium and Lucifer yellow dilithium salts.
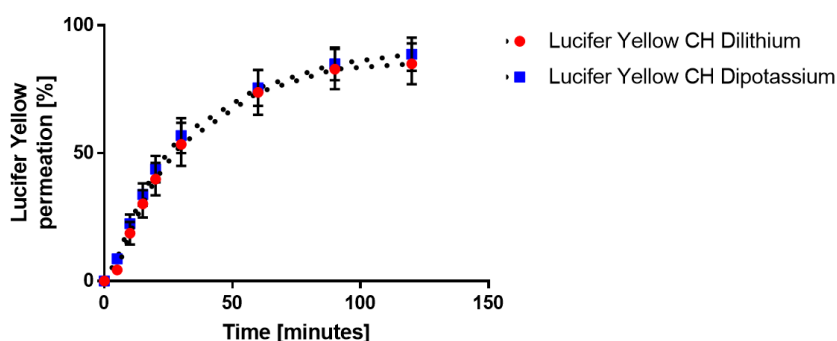
Figure 2.3.13. Apical to basolateral (A→B) permeation profile of Lucifer yellow dipotassium and dilithium salts (100 µM) across the mucus layer. The dyes were delivered as a 50 µL solution in the apical compartment while 500 µL of the buffer (HBSS) was added to the basal compartment. Data are expressed as the

cumulative percentage of the initial dose applied recovered basolaterally and are presented as mean ± SD (n = 4).

Lucifer yellow CH dipotassium and its dilithium analogue showed identical permeation profiles, $p > 0.05$. However, it is important to mention that there is a paucity of data detailing the impact of the salt counter-ion on the performances of inhaled medicines *in-vivo*. One study investigated the co-administration of salbutamol with different counter-ions (Patel et al., 2016). The data revealed that when administered with an excess of the 1-hydroxy-2-naphthoate (1H2NA) counter-ion, a superior bronchodilator effect was obtained compared to the salbutamol base and sulphate analogues ($p < 0.05$). However, it is worth mentioning that the investigated counter-ion (H12NA) is highly lipophilic molecule compared with the marketed counter-ion (sulphate). This makes it a more lipophilic ion-pairing agent compared to the sulfate. Assuming that salbutamol and 1H2NA are forming an ion-pair in solution, the overall complex would be more lipophilic compared to the sulphate counterion complex, and hence one may expect the former to show greater affinity to tissue.

However, our results give a preliminary indication that different salts may not affect mucus drug permeation. This nevertheless warrants further investigation.

2.4.   Conclusion

An in vitro mucus model consisting of coating Transwell® inserts with 12 μL of porcine tracheal mucus was successfully developed and deemed suitable for measuring compound permeability across airway mucus. The preparation stages were succeeded to reach a cleaned mucus as a thin layer without affecting the internal structure of this final mucus layer. Furthermore, an experimental design involving an apical volume of 50 μL and a basolateral volume of 500 μL was deemed suitable for measuring compound permeability across the mucus layers. Finally, the impact of mucus on the diffusion of fluorescent dyes revealed that this was mainly a barrier for lipophilic molecules whereas electrostatic interactions were less notable.

2.5. References

ALEXANDER, W. 2010. American Society of Clinical Oncology, 2010 Annual Meeting and Rose Bengal: From a Wool Dye to a Cancer Therapy. *Pharmacy and Therapeutics,* 35**,** 469-478.

ALTMAN, R., BOSCH, B., BRUNE, K., PATRIGNANI, P. & YOUNG, C. 2015. Advances in NSAID development: evolution of diclofenac products using pharmaceutical technology. *Drugs,* 75**,** 859-877.

BAKKIALAKSHMI, S., SELVARANI, P. & CHENTHAMARAI, S. 2013. Fluorescence quenching of Rhodamine B base by two amines. *Spectrochimica Acta Part A: Molecular and Biomolecular Spectroscopy,* 105**,** 557-562.

BHAT, P. G., FLANAGAN, D. R. & DONOVAN, M. D. 1995. The limiting role of mucus in drug absorption: Drug permeation through mucus solution. *International journal of pharmaceutics,* 126**,** 179-187.

BHAT, P. G., FLANAGAN, D. R. & DONOVAN, M. D. 1996a. Drug binding to gastric mucus glycoproteins. *International journal of pharmaceutics,* 134**,** 15-25.

BHAT, P. G., FLANAGAN, D. R. & DONOVAN, M. D. 1996b. Drug diffusion through cystic fibrotic mucus: Steady-state permeation, rheologic properties, and glycoprotein morphology. *Journal of pharmaceutical sciences,* 85**,** 624-630.

BOEGH, M., FOGED, C., MÜLLERTZ, A. & MØRCK NIELSEN, H. 2013. Mucosal drug delivery: barriers, in vitro models and formulation strategies. *Journal of Drug Delivery Science and Technology,* 23**,** 383-391.

2. *Development of an in-vitro mucus model*

BOSKEY, E. R., MOENCH, T. R., HEES, P. S. & CONE, R. A. 2003. A self-sampling method to obtain large volumes of undiluted cervicovaginal secretions. *Sexually transmitted diseases,* 30**,** 107-109.

CINGOLANI, E. 2016. *In-vitro investigation of factors affecting the fate of dry powders in the lung.* PhD thesis.

CONE, R. A. 2009a. Barrier properties of mucus. *Adv Drug Deliv Rev,* 61**,** 75-85.

CONE, R. A. 2009b. Barrier properties of mucus. *Advanced drug delivery reviews,* 61**,** 75-85.

CRATER, J. S. & CARRIER, R. L. 2010. Barrier properties of gastrointestinal mucus to nanoparticle transport. *Macromolecular bioscience,* 10**,** 1473-1483.

DAWSON, M., KRAULAND, E., WIRTZ, D. & HANES, J. 2004. Transport of polymeric nanoparticle gene carriers in gastric mucus. *Biotechnology progress,* 20**,** 851-857.

DONNELLY, R. F., MCCARRON, P. A., CASSIDY, C. M., ELBORN, J. S. & TUNNEY, M. M. 2007. Delivery of photosensitisers and light through mucus: investigations into the potential use of photodynamic therapy for treatment of Pseudomonas aeruginosa cystic fibrosis pulmonary infection. *Journal of controlled release,* 117**,** 217-226.

EFTHYMIOU, C. 2017. Investigating the Mesoscale of β-lactoglobulin Fibril Hydrogels.

EZPELETA, I., ARANGOA, M. A., IRACHE, J. M., STAINMESSE, S., CHABENAT, C., POPINEAU, Y. & ORECCHIONI, A.-M. 1999. Preparation of Ulex europaeus lectin-gliadin nanoparticle conjugates and

their interaction with gastrointestinal mucus. *International journal of pharmaceutics,* 191**,** 25-32.

FAURE, M., MOENNOZ, D., MONTIGON, F., FAY, L. B., BREUILLE, D., FINOT, P. A., BALLEVRE, O. & BOZA, J. 2002. Development of a rapid and convenient method to purify mucins and determine their in vivo synthesis rate in rats. *Anal Biochem,* 307**,** 244-51.

FORSTER, S., THUMSER, A. E., HOOD, S. R. & PLANT, N. 2012. Characterization of Rhodamine-123 as a Tracer Dye for Use In In vitro Drug Transport Assays. *PLoS ONE,* 7**,** e33253.

FRIEDL, H., DUNNHAUPT, S., HINTZEN, F., WALDNER, C., PARIKH, S., PEARSON, J. P., WILCOX, M. D. & BERNKOP-SCHNURCH, A. 2013. Development and evaluation of a novel mucus diffusion test system approved by self-nanoemulsifying drug delivery systems. *J Pharm Sci,* 102**,** 4406-13.

GRAINGER, C. I., GREENWELL, L. L., MARTIN, G. P. & FORBES, B. 2009. The permeability of large molecular weight solutes following particle delivery to air-interfaced cells that model the respiratory mucosa. *Eur J Pharm Biopharm,* 71**,** 318-24.

GRIFFITHS, P. C., OCCHIPINTI, P., MORRIS, C., HEENAN, R. K., KING, S. M. & GUMBLETON, M. 2009. PGSE-NMR and SANS studies of the interaction of model polymer therapeutics with mucin. *Biomacromolecules,* 11**,** 120-125.

GROO, A.-C., SAULNIER, P., GIMEL, J.-C., GRAVIER, J., AILHAS, C., BENOIT, J.-P. & LAGARCE, F. 2013. Fate of paclitaxel lipid

nanocapsules in intestinal mucus in view of their oral delivery. *International journal of nanomedicine,* 8**,** 4291.

GRUBEL, P. & CAVE, D. 1998. Factors affecting solubility and penetration of clarithromycin through gastric mucus. *Alimentary Pharmacology and Therapeutics,* 12**,** 569-576.

HANANI, M. 2012. Lucifer yellow - an angel rather than the devil. *J Cell Mol Med,* 16**,** 22-31.

HIDA, K., LAI, S. K., SUK, J. S., WON, S. Y., BOYLE, M. P. & HANES, J. 2011. Common gene therapy viral vectors do not efficiently penetrate sputum from cystic fibrosis patients. *PloS one,* 6**,** e19919.

KARARLI, T. T. 1995. Comparison of the gastrointestinal anatomy, physiology, and biochemistry of humans and commonly used laboratory animals. *Biopharmaceutics & drug disposition,* 16**,** 351-380.

KARLSSON, J., WIKMAN, A. & ARTURSSON, P. 1993. The mucus layer as a barrier to drug absorption in monolayers of human intestinal epithelial HT29-H goblet cells. *International journal of pharmaceutics,* 99**,** 209-218.

KESIMER, M. & SHEEHAN, J. K. 2012. Mass spectrometric analysis of mucin core proteins. *Mucins.* Springer.

KHANVILKAR, K., DONOVAN, M. D. & FLANAGAN, D. R. 2001. Drug transfer through mucus. *Adv Drug Deliv Rev,* 48**,** 173-93.

KIRCH, J., SCHNEIDER, A., ABOU, B., HOPF, A., SCHAEFER, U. F., SCHNEIDER, M., SCHALL, C., WAGNER, C. & LEHR, C. M. 2012. Optical tweezers reveal relationship between microstructure and

nanoparticle penetration of pulmonary mucus. *Proc Natl Acad Sci U S A,* 109**,** 18355-60.

LAI, S. K., SUK, J. S., PACE, A., WANG, Y.-Y., YANG, M., MERT, O., CHEN, J., KIM, J. & HANES, J. 2011. Drug carrier nanoparticles that penetrate human chronic rhinosinusitis mucus. *Biomaterials,* 32**,** 6285-6290.

LAI, S. K., WANG, Y.-Y. & HANES, J. 2009a. Mucus-penetrating nanoparticles for drug and gene delivery to mucosal tissues. *Advanced drug delivery reviews,* 61**,** 158-171.

LAI, S. K., WANG, Y.-Y., HIDA, K., CONE, R. & HANES, J. 2010. Nanoparticles reveal that human cervicovaginal mucus is riddled with pores larger than viruses. *Proceedings of the National Academy of Sciences of the United States of America,* 107**,** 598-603.

LAI, S. K., WANG, Y.-Y., WIRTZ, D. & HANES, J. 2009b. Micro-and macrorheology of mucus. *Advanced drug delivery reviews,* 61**,** 86-100.

LARHED, A. W., ARTURSSON, P. & BJÖRK, E. 1998. The influence of intestinal mucus components on the diffusion of drugs. *Pharmaceutical research,* 15**,** 66-71.

LARHED, A. W., ARTURSSON, P., GRÅSJÖ, J. & BJÖRK, E. 1997. Diffusion of drugs in native and purified gastrointestinal mucus. *Journal of pharmaceutical sciences,* 86**,** 660-665.

LI, X., CHEN, D., LE, C., ZHU, C., GAN, Y., HOVGAARD, L. & YANG, M. 2011a. Novel mucus-penetrating liposomes as a potential oral drug delivery system: preparation, in vitro characterization, and enhanced cellular uptake. *Int J Nanomedicine,* 6**,** 151-62.

LI, X., CHEN, D., LE, C., ZHU, C., GAN, Y., HOVGAARD, L. & YANG, M. 2011b. Novel mucus-penetrating liposomes as a potential oral drug delivery system: preparation, in vitro characterization, and enhanced cellular uptake. *International journal of nanomedicine,* 6**,** 3151.

LILLEHOJ, E. R. & KIM, K. C. 2002. Airway mucus: its components and function. *Arch Pharm Res,* 25**,** 770-80.

MCGILL, S. L. & SMYTH, H. D. 2010. Disruption of the mucus barrier by topically applied exogenous particles. *Molecular pharmaceutics,* 7**,** 2280-2288.

MÜLLER, C., PERERA, G., KÖNIG, V. & BERNKOP-SCHNÜRCH, A. 2014. Development and in vivo evaluation of papain-functionalized nanoparticles. *European Journal of Pharmaceutics and Biopharmaceutics,* 87**,** 125-131.

NORRIS, D. A. & SINKO, P. J. 1997. Effect of size, surface charge, and hydrophobicity on the translocation of polystyrene microspheres through gastrointestinal mucin. *Journal of applied polymer science,* 63**,** 1481-1492.

PARISH, C. R. 1999. Fluorescent dyes for lymphocyte migration and proliferation studies. *Immunol Cell Biol,* 77**,** 499-508.

PATEL, A., KEIR, S. D., BROWN, M. B., HIDER, R., JONES, S. A. & PAGE, C. P. 2016. Using Salt Counterions to Modify β2-Agonist Behavior in Vivo. *Molecular pharmaceutics,* 13**,** 3439-3448.

PETIT, B., BOUCHEMAL, K., VAUTHIER, C., DJABOUROV, M. & PONCHEL, G. 2012. The counterbalanced effect of size and surface properties of chitosan-coated poly (isobutylcyanoacrylate) nanoparticles

on mucoadhesion due to pluronic F68 addition. *Pharmaceutical research,* 29**,** 943-952.

PONCHEL, G. & IRACHE, J. 1998. Specific and non-specific bioadhesive particulate systems for oral delivery to the gastrointestinal tract. *Adv Drug Deliv Rev,* 34**,** 191-219.

POQUET, L., CLIFFORD, M. N. & WILLIAMSON, G. 2008. Transport and metabolism of ferulic acid through the colonic epithelium. *Drug Metabolism and Disposition,* 36**,** 190-197.

RAMAKRISHNAN, S. & SULOCHANA, K. 2012. *Manual of Medical laboratory techniques*, JP Medical Ltd.

ROSELLI, R. J. & DILLER, K. R. 2011. *Biotransport: principles and applications*, Springer Science & Business Media.

ROUND, A. N., BERRY, M., MCMASTER, T. J., STOLL, S., GOWERS, D., CORFIELD, A. P. & MILES, M. J. 2002. Heterogeneity and persistence length in human ocular mucins. *Biophys J,* 83**,** 1661-70.

SANDERS, N. N., DE SMEDT, S. C., VAN ROMPAEY, E., SIMOENS, P., DE BAETS, F. & DEMEESTER, J. 2000. Cystic fibrosis sputum: a barrier to the transport of nanospheres. *American journal of respiratory and critical care medicine,* 162**,** 1905-1911.

SCHUSTER, B. S., SUK, J. S., WOODWORTH, G. F. & HANES, J. 2013. Nanoparticle diffusion in respiratory mucus from humans without lung disease. *Biomaterials,* 34**,** 3439-3446.

SHAW, L. R., IRWIN, W. J., GRATTAN, T. J. & CONWAY, B. R. 2005. The influence of excipients on the diffusion of ibuprofen and paracetamol in gastric mucus. *International journal of pharmaceutics,* 290**,** 145-154.

SHEEHAN, J. K., OATES, K. & CARLSTEDT, I. 1986. Electron microscopy of cervical, gastric and bronchial mucus glycoproteins. *Biochemical Journal,* 239**,** 147-153.

STENTEBJERG-ANDERSEN, A., NOTLEVSEN, I. V., BRODIN, B. & NIELSEN, C. U. 2011. Calu-3 cells grown under AIC and LCC conditions: implications for dipeptide uptake and transepithelial transport of substances. *Eur J Pharm Biopharm,* 78**,** 19-26.

STEWART, W. W. 1978. Functional connections between cells as revealed by dye-coupling with a highly fluorescent naphthalimide tracer. *Cell,* 14**,** 741-759.

STEWART, W. W. 1981. Lucifer dyes[mdash]highly fluorescent dyes for biological tracing. *Nature,* 292**,** 17-21.

SUK, J. S., LAI, S. K., WANG, Y.-Y., ENSIGN, L. M., ZEITLIN, P. L., BOYLE, M. P. & HANES, J. 2009. The penetration of fresh undiluted sputum expectorated by cystic fibrosis patients by non-adhesive polymer nanoparticles. *Biomaterials,* 30**,** 2591-2597.

TAKATSUKA, S., KITAZAWA, T., MORITA, T., HORIKIRI, Y. & YOSHINO, H. 2006. Enhancement of intestinal absorption of poorly absorbed hydrophilic compounds by simultaneous use of mucolytic agent and non-ionic surfactant. *European journal of pharmaceutics and biopharmaceutics,* 62**,** 52-58.

TANG, B. C., DAWSON, M., LAI, S. K., WANG, Y.-Y., SUK, J. S., YANG, M., ZEITLIN, P., BOYLE, M. P., FU, J. & HANES, J. 2009. Biodegradable polymer nanoparticles that rapidly penetrate the human

mucus barrier. *Proceedings of the National Academy of Sciences,* 106**,** 19268-19273.

THE FOOD DATABASE, F. 2017. Rose Bengal. [online] foodb.ca/compounds. *Available at: http://foodb.ca/compounds/FDB015530.*

THE UNITED STATES ENVIRONMENTAL PROTECTION AGENCY, U. S. E. 2017. *Lucifer yellow. [online] https://comptox.epa.gov/dashboard* [Online]. [Accessed].

VLLASALIU, D., FOWLER, R., GARNETT, M., EATON, M. & STOLNIK, S. 2011. Barrier characteristics of epithelial cultures modelling the airway and intestinal mucosa: a comparison. *Biochemical and biophysical research communications,* 415**,** 579-585.

WOODLEY, J. 2001. Bioadhesion: new possibilities for drug administration? *Clin Pharmacokinet,* 40**,** 77-84.

Chapter 3 - Untargeted metabolomics analysis of the *in-vitro* mucus model

3.1. Introduction

The suffix '-omics' refers to gene product discovery (transcript, protein, and metabolites) in biological systems. Recently established, metabolomics is the analysis of small molecules present in a specific biological system (Saito and Matsuda, 2010). These small molecules or metabolites are generated by genomic interactions with the environment and are not merely gene expression end products, but are components of a biological systems metabolic status (Maier et al., 2013). Hence, metabolomics includes the comprehensive analysis of biological systems through studying biofluids (such as cerebrospinal fluid, mucus, plasma, and saliva) or cell extracts originating from *in-vitro* cell cultures and tissues *in-vivo*. Thus, it provides a better understanding of biological dynamics, e.g. cellular response to gene, mRNA, protein, and metabolite function which can be investigated and assessed by combining metabolomics with other "omics" groups (Figure 3.1.1) (Reo, 2002).

Metabolomics as a tool can be applied to several distinct research areas, e.g. integrative systems biology, biomarker discovery, and environmental and biological stress studies (Malmendal et al., 2013, Sabidó et al., 2012, Wang et al., 2012). These disciplines are metabolically relevant as they involve biological perturbations resulting from metabolite mutation and/or perturbation (Khoo and Al-Rubeai, 2007, Goodacre et al., 2004). Within these disciplines, regulated metabolites can be studied either by targeting specific metabolites, or by a more global metabolic profiling approach.
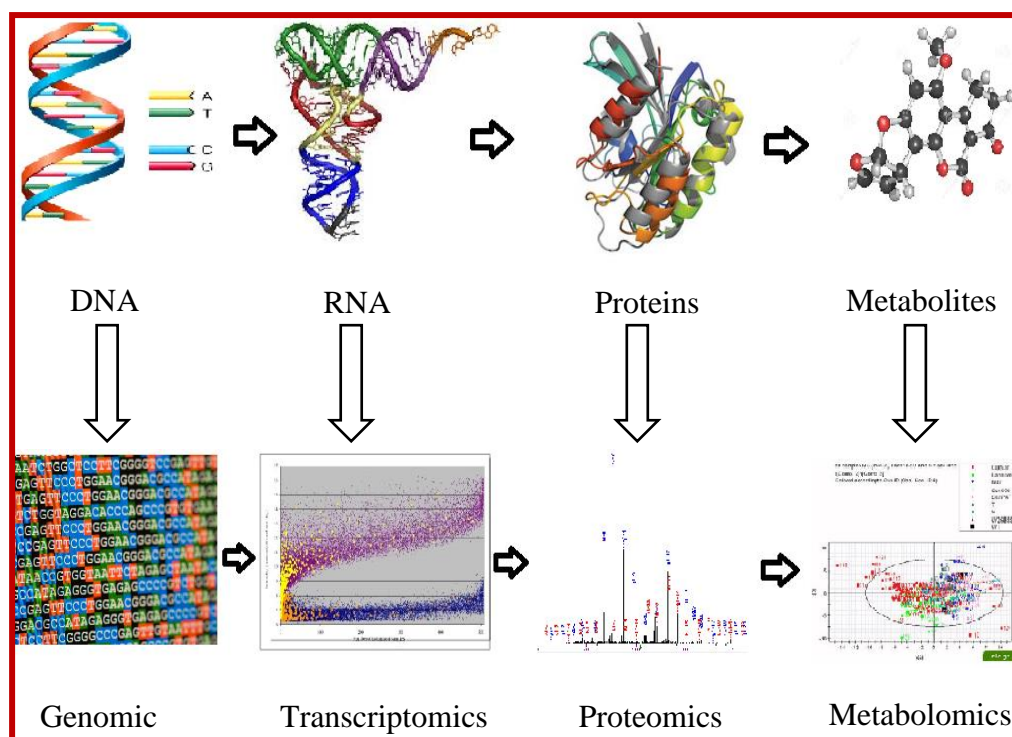
Figure 3.1.1. Different '-omics' research areas (genomics, transcriptomics, proteomics or metabolomics). The related suffix '-ome' is used to indicate the objects of study of such fields as in the genome, transcriptome, proteome, or metabolome respectively.

3.1.1. Targeted metabolomics

Targeted metabolomics analyses specific classes of metabolites or a single well characterised metabolite on a particular pathway (Wishart, 2005) (Roberts et al., 2012). Authenticated analytical standards, which provide absolute quantification, give accurate quantifiable data when using this approach (Roberts et al., 2012). Furthermore, relative quantification can be used to identify specific biomarkers (Chapman et al., 2012). Targeted metabolomics takes into account the function of well-known metabolic enzymes, well characterised biochemical pathways and their end products (Roberts et al., 2012).

Differentiating targeted metabolites from other metabolites is a prerequisite for this approach. This can be achieved in three ways; 1) analysing chemical shifts in nuclear magnetic resonance (NMR) spectra, 2) a mass to charge ratio on a mass spectrometer (MS) and 3) by chromatography retention time (Lu et al., 2008).

3.1.2. Non-targeted metabolomics

Under certain conditions, non-targeted metabolomics focusses on analysing all small molecule metabolites in a specific biological system from a representative set of samples (Naz et al., 2014). It is an influential tool for biological studies as it can be used in the discovery of functional metabolites, i.e. biomarker discovery (Jain et al., 2012, Gowda et al., 2008, van der Greef et al., 2006, Nicholson, 2005). However, since it is a measure of all metabolites in a given biological sample, the generated metabolome is highly complex and difficult to analyse. Analytical platforms pose a challenge for researchers in this field since concentrations of metabolites in the biological sample range over more than 12 orders of magnitude while the dynamic range of current instruments give magnitudes of about four to five orders (Yin and Xu, 2014).

Non targeted metabolomics can be used for cells extracts, tissues, organs or organisms. For cell extracts, non-targeted cellular endogenous metabolite analysis provides phenotypic information or information on pathophysiology mechanisms (Nicholson et al., 1999, Nicholson et al., 2011, Kinross et al., 2011, Griffin and Nicholls, 2006, Weiss and Kim, 2012, Evans et al., 2014).

3.1.3. Sample preparation in metabolomics

Analytical studies require correct sample preparation to obtain good quality robust data (Figure 3.1.2). To reduce potential problems from cell matrix interference, it is essential to use an extraction procedure which selectively separates metabolites of interest from unwanted biological matrix components. If extracted metabolite concentrations are low, pre-concentration of the sample ensures improved detection limits (Dettmer et al., 2007).
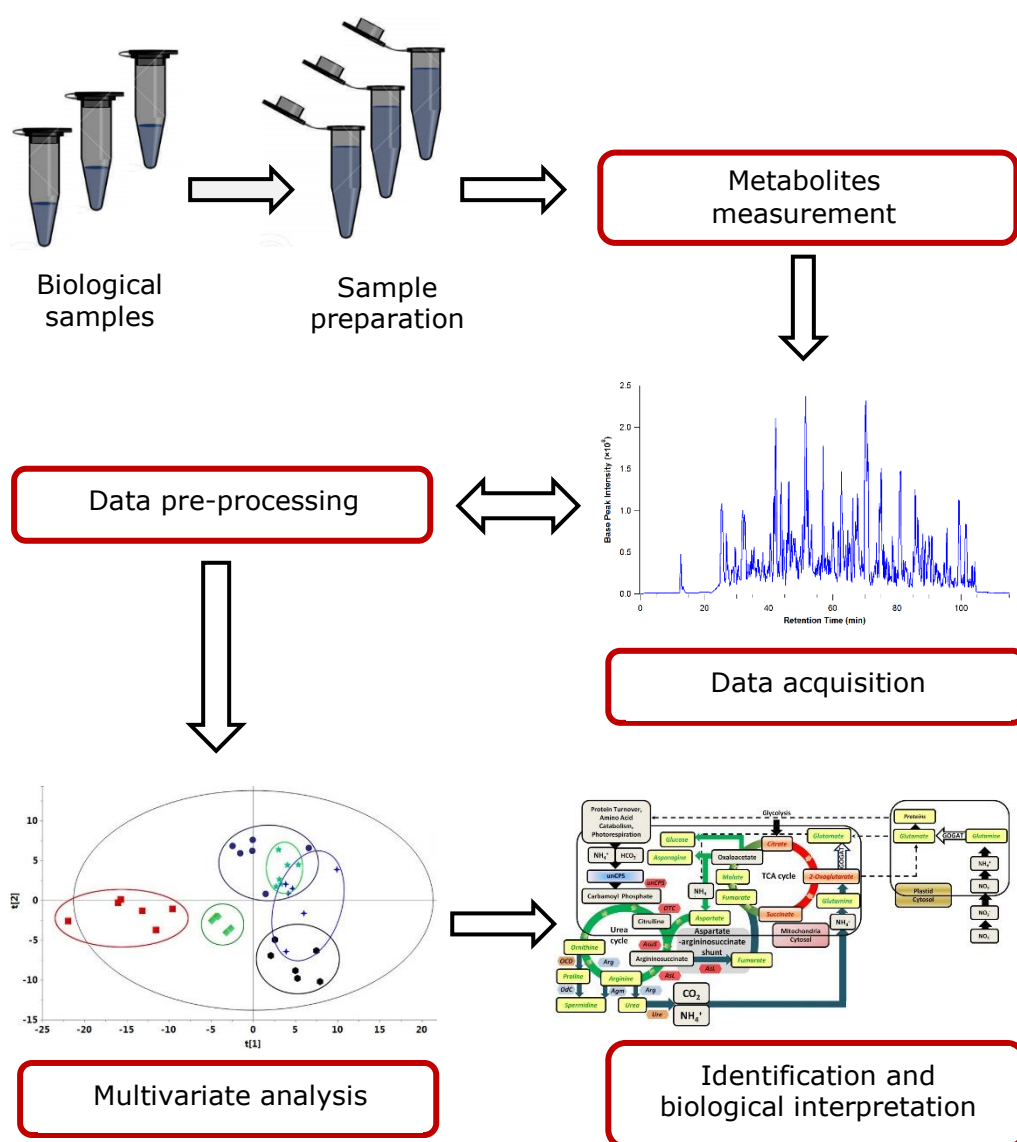
Figure 3.1.2. Typical workflow for untargeted metabolomics.

3.1.3.1.   Solid-phase extraction (SPE)

The most popular extraction technique in the preparation of biological samples is solid phase extraction (SPE) (Mitra, 2004). Targeted metabolomics generally incorporates this separation technique to remove matrix interference and to obtain high analyte concentrations. Analytes from liquid samples are retained on a solid stationary phase called a solid sorbent. Selection of different solid sorbent phases is based on analyte chemistry. Elution buffers, using a mixture of solvents, elutes the analyte from the sorbent phase (Mitra, 2004). SPE effectively removes protein contaminants enhancing the detection of non-lipidic analytes (David et al., 2014).

3.1.3.2.   Liquid-liquid extraction

Biological fluids can be extracted using the liquid-liquid extraction technique, which is considered the best method for extracting frozen samples from liquid nitrogen (Dettmer et al., 2007). From frozen, the sample is ground to a fine homogeneous powder using a mortar and pestle (Weckwerth et al., 2004), blended with a solvent (Roessner et al., 2000b), mixed with inert beads (Colebatch et al., 2004), and inserted into a grinding mill (Jonsson et al., 2004). Vortexing with organic solvents also extracts metabolites. The ideal way to produce biphasic metabolite extracts is to separate polar from non-polar metabolites. Using a combination of water and methanol with ethyl acetate or chloroform to generate aqueous and organic phases makes the analysis of two separate phases possible (Fiehn et al., 2000, Colebatch et al., 2004).

3.1.4. Analytical techniques used in metabolomics

Recently, several metabolomics analytical platforms have been promoted as rapid and sensitive techniques; NMR and Fourier transform infrared (FT-IR) spectroscopy and more importantly MS, when coupled to gas chromatography (GC), liquid chromatography (LC), direct injection (DI), and capillary electrophoresis (CE). These latter techniques are combined as they increase metabolite detection which might be difficult to achieve when using a single instrumentation for analysis (Zhang et al., 2012). The low signal intensity from some metabolites makes data collection and analysis difficult; processing software which restricts metabolomics studies due to very low biological sample concentration or insufficient ionisation of the ionisation source (Werner et al., 2008).

When high sensitivity and high resolution are required, MS is the best analytical platform for these purposes (Han et al., 2009). To reduce the loss of analytical signal, matrix effect, and to overcome biological sample complexity, separation techniques are combined with MS to optimise performance, e.g. chromatography techniques.

3.1.4.1. Liquid chromatography-mass spectrometry (LC-MS)

In terms of accuracy and reproducibility, MS is highly effective in the metabolic profiling of a broad range of metabolites from biological samples (Gika et al., 2008, Want et al., 2006, Michopoulos et al., 2009, Zelena et al., 2009). The collection of large datasets from metabolomes can be achieved using liquid chromatography-MS (LC-MS)(Zhou et al., 2012, Yin and Xu, 2013, Becker et al., 2012).

3. Untargeted metabolomics analysis of the in-vitro mucus model

LC-MS is a combination system separating metabolites through liquid chromatography (LC) and ionising the sample by atmospheric pressure chemical ionisation (APCI) or more commonly, by electrospray ionisation source (ESI). ESI, developed by Fenn and Tanaka to give ion source characterised by its robustness that are interfere to liquid chromatography which can be applied to a wide range of biological molecule classes (Figure 3.1.3) (Fenn et al., 1989). ESI is considered a good choice for polar compounds such as metabolites. Liquid samples are converted to droplets through a metal capillary and nebulised as charged droplets. Similar to ESI, but with a different ionisation technique, APCI pumps the liquid sample into the capillary with the ionising gas to react the analyte with these ions. This technique is a good choice for small stable molecules that cannot be ionised via ESI (Byrdwell, 2001, Rosenberg, 2003).
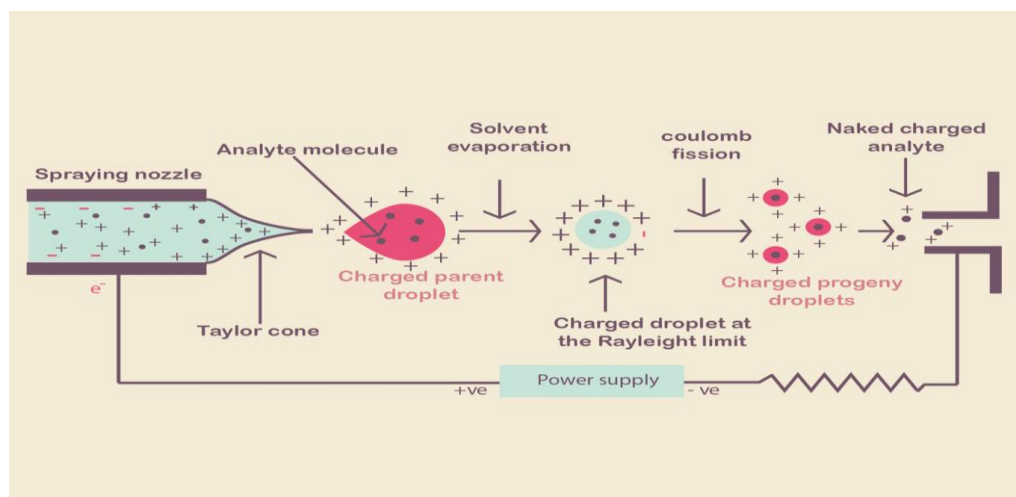
Figure 3.1.3. Schematic representation of Electrospray Ionisation Source (ESI). Reproduced from (Banerjee and Mazumdar, 2012).

After ionisation, the molecules are passed to the mass analyser for analysis and detection. Several mass analysers can be used; 1) quadrupole, 2) time-of-flight (TOF), and 3) Orbitrap analysers that are coupled to different techniques to

enhance the mass spectrum coverage and produce a good separation (Figure 3.1.4).
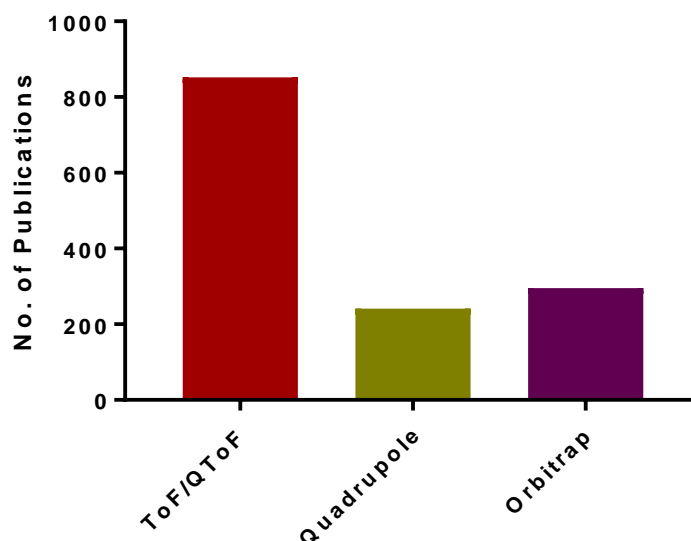
Figure 3.1.4. Frequency of published metabolomics studies using different mass spectrometry techniques. Key terms were 'Metabolomics', 'time-of-flight/ToF/QToF', 'Quadrupole', and 'Orbitrap'.

1. Quadrupole analysers consist of four parallel rods. Mass spectrum of the quadrupole results from voltage variation with time that scans m/z values. It operates <4000 m/z with a speed of 1000 m/z per sec (Chen et al., 2008). This kind of analyser is mainly used in clinical LC-MC applications due to ease of scanning and the generation of high quality quantitative data (Jansen et al., 2005).

2. TOF uses high voltage to accelerate ions (Williamson and Bartlett, 2007). m/z values control ion velocity and the time between the flight tube and detector. TOF records rapid spectra with high sensitivity and high accuracy facilitating small molecule analysis (Bristow, 2006).

3. Orbitrap is a high performance technique required for complex samples. It provides high mass accuracy, resolving power and sensitivity through electrostatic fields to confine and analyse injected ions (Perry et al., 2008).

Different mass analysers can be combined to generate tandem mass spectrometers. For instance, a TOF analyser takes the place of the third quadrupole of a triple quadrupole MS to generate a hybrid QTOF mass analyser (Figure 3.1.5) (Chernushevich et al., 2001, Ens and Standing, 2005).
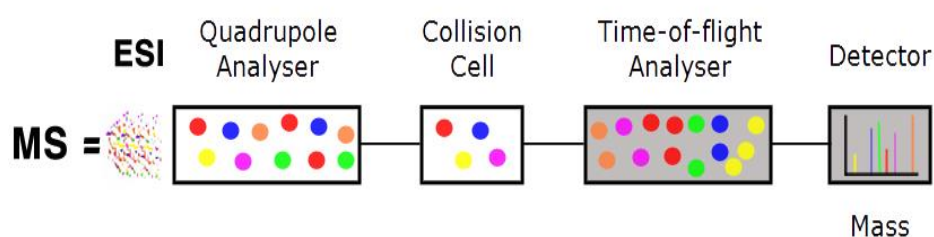
Figure 3.1.5. Schematic of a QTOF mass spectrometer. Reproduced from (Banerjee and Mazumdar, 2012).

3.1.4.2. Other MS-based techniques

Other MS-based techniques can be used in metabolomics studies such as GC-MS which separates volatile compounds in the GC section then elutes them in the MS section to be detected through an energetic ionisation source, relying on the removal of electrons; 'Electron Impact'. Volatile and stable compounds in terms of thermal state can be analysed through GC-MS directly (Deng et al., 2004, Perera et al., 2002). Hence, metabolite chemical derivatisation is required to produce stable compounds, which can be achieved at room or higher temperatures (Roessner et al., 2000a).

Direct-injection mass spectrometry (DIMS) is a technique that reduces the analysis period by omitting the separation component (chromatography) through

high throughput analysis by introducing the samples to the MS directly (Kayser and Warzecha, 2012). Research using the DIMS system are mainly focussed on microbes (Castrillo et al., 2003). *Saccharomyces cerevisiae* mutants have been investigated by differentiating external from internal cellular metabolites (metabolic footprinting) using DIMS (Allen et al., 2003). Similarly, it has been used in analysing secondary metabolites from fungal extracts as metabolic fingerprinting (Smedsgaard and Frisvad, 1996).

Capillary Electrophoresis (CE) is another MS-based instrument that is used less frequently. However, CE has been shown to produce high resolution separation when combined with MS (which is known for its high sensitivity) (Soga et al., 2003).

Laser desorption ionisation (LDI) is a growing field of interest in ionising metabolites directly on the application plate which requires fewer preparation procedures (Ernst et al., 2015).

3.1.5. Column techniques

3.1.5.1. Hydrophilic interaction liquid chromatography (HILIC)

In 1950, the first stationary phase comprising anion exchange resin, to separate monosaccharides was introduced (Gabrielson and Samuelson, 1950). HILIC, developed by Alpert in 1990, comprises a column of silica coated with an organic cation-exchange polymer (Alpert, 1990b). Nowadays, modern HILIC stationary phases have hydrophilic functional groups covalently attached to silica (Hemström and Irgum, 2006).

For effective separation, HILIC requires two essential elements; first, analytes should be separated in a hydrophilic atmosphere and second, low

chromatographically electrostatic interactions should be present (Alpert, 1990a, Alpert et al., 1994). HILIC provides an alternative chromatography approach to reversed phase, especially for polar metabolites which are poorly retained by reversed-phase (Dunn and Ellis, 2005).

3.1.5.2. Reversed-phase chromatography (RPC)

Reversed-phase columns have been used in metabolomics to generate high quantities of non-polar compounds. Nevertheless, the technique causes ion suppression for hydrophilic compounds and limited metabolite mass spectral due to limited retainable capacity for polar metabolites coverage (Haggarty et al., 2015). Hydrophobic interactions play important roles in RPC since the retention and separation of metabolites are dependent on these conditions. Highly polar metabolites are eluted close to the dead time point since polar compounds, such as amino acids and organic acids are not retained under RPC hydrophobic conditions (Danielsson et al., 2011, Guy et al., 2008, Hodson et al., 2009, Issaq et al., 2008). Hence, reagents such as ion pairing may be used to separate polar and ionic compounds in RPC (Haggarty et al., 2015). Recent studies have shown good separation of a broad range of polar metabolites such as carboxylic acids, nucleotides, and sugar phosphates on reversed phase chromatography using an amine ion-pairing agent (Huck et al., 2003, Luo et al., 2007, Tuytten et al., 2002). A C18 column with an ion pairing agent (tributylamine) coupled with an orbitrap mass analyser has been used successfully in metabolite profiling of *Saccharomyces cerevisiae* (Lu et al., 2010).

3.1.6. Aim

The main aim of this study was to characterise the small molecular weight components of pig tracheal mucus using an untargeted metabolomics approach. To this end, an LC method was first validated using 268 authentic standards in MassLynx software with the following objectives: 1) evaluate peak area reproducibility for each authentic standard in positive and negative LC-MS modes. 2) Evaluate the retention time reproducibility for each authentic standard in positive and negative LC-MS modes. 3) Evaluate the mass accuracy (mass error) in parts per million (ppm).

After validation of the method, this was applied to profile the small components of pig tracheal mucus and compare it with the composition of human pulmonary mucus that is described in the literature. Moreover, to evaluate potential differences in the composition of raw and cleaned mucus samples, multivariate data analysis was used. To this end, principal component analysis (PCA) and orthogonal partial least square-discriminant analysis (OPLS-DA) were applied using the Simca P +14 software. The difference in composition between raw and cleaned pig tracheal mucus was determined using IDEOM software.

3.2. Materials and methods

3.2.1. Materials

Pig tracheal mucus was sourced as detailed in chapter 2. Chemicals and reagents were used without purification, and they were of LC-MS, HPLC, and analytical grades. Sigma-Aldrich Chemie-GmbH, Germany, was the supplier for ammonium carbonate ($\geq$30% NH_3 basis, HPLC grade), leucine enkephalin (2 mg/mL stock solution, stored at 4ºC), formic acid (98% formic acid for MS), sodium hydroxide (97% NaOH), and methanol (LC-MS grade). Water was supplied by ELGA LabWater, Veolia Water Solutions and Technologies, UK (distilled and deionised water (18.2 MΩ) was prepared using a Purelab Ultra water purification system). Acetonitrile (99.99% HPLC gradient grade for QTOF and 100% LC-MS grade for Exactive) and 2-propanol (99.96% HPLC grade) were provided by Fisher Scientific, UK. Authentic standards (268 metabolites) of HPLC grade were purchased from Sigma-Aldrich (UK). Table 3.2.1 outlines the standards based on Human Metabolome Database (HMDB) classification. The Appendix II contains a full list of all authentic standards with their formulae and molecular weights (Tables A-1 – A-5).

Table 3.2.1. Authentic HPLC-grade standards (268 metabolites)

Metabolite class	Number of authentic standards
Alkaloids	2
Benzenoids	26
Homogeneous non-metal compounds	2
Lipids	22
Nucleosides and nucleotides	40
Organic acids	78
Organoheterocyclic compounds	36
Organonitrogen compounds	14
Organooxygen compounds	36
Organophosphorus compounds	5
Organosulfur compounds	2
Phenylpropanoids	5
Total number of metabolites	268

3.2.2. Preparation of authentic standards and samples

3.2.2.1. Preparation of authentic standards

Each authentic standard was prepared as a stock solution at 100 µM in water and stored at –20°C. The standards were then diluted five times using acetonitrile to achieve a 20 µM working solution. This solution was distributed into five groups to segregate similar molecular weights in different mixture groups. The five working solution groups were stored at –20°C and brought to room temperature before analysis.

3.2.2.2. Raw and cleaned mucus preparation

Generation of a suitable amount of mucus was required to characterise pig tracheal mucus using untargeted metabolomics approach. Due to the minimal amount of raw mucus produced per trachea (150-200 µL), 108 pig tracheae were used for this study. These tracheae were classified into six groups (18 tracheae per group) (please refer to Figure 2.2.1. for the mucus collection and cleaning procedures). Each group produced ac. 3.2 mL of raw mucus. A total of 500 µL was withdrawn from each group, representing raw mucus. This was transferred into an Eppendorf vial (1.5 mL), while the remaining volume (approximately 2.7 mL) was cleaned to yield 500 µL of cleaned mucus and then transferred into an Eppendorf vial. Following the generation of six raw and six cleaned biological mucus replicates of similar volume (500 µL per vial), methanol was added to each sample at a ratio of 1:1 then vortexed for 1 min and centrifuged at 14,000 rpm at 4 °C for 15 min (Eppendorf® Refrigerated Microcentrifuge, Model 5417R). Then, 200 µL of the supernatant was placed into an LC-MS vial containing an insert to facilitate the LC injection. The vials were then stored at

–20°C and brought to room temperature prior to shipping to Glasgow Polyomics, University of Glasgow, Glasgow, UK.

3.2.3. Instruments and software

3.2.3.1. Quadrupole-time of flight (QTOF) mass spectrometry

Accurate mass measurements were obtained via this mass spectrometer which allows the acquisition of high-resolution full-range spectra (Gross, 2004). The geometry of the ion optics determines the resolution, which varies between 10,000–17,500.

Sodium formate was used as an external instrumental calibration for accurate mass measurements (0.05 M sodium hydroxide, 0.5% formic acid in 90:10 ratio of 2-propanol:water) and continuous lockspray calibration against leucine enkephalin solution (556.2773 Da in positive mode and 554.2615 in negative mode, 2 μg/mL) was carried out.

The MS system was controlled by MassLynx® software (Waters Corp.), while the Shimadzu LC system was controlled manually.

The electrospray source temperature was set to 120 °C with a desolvation gas flow rate of 400 L/h at 300°C. The capillary voltage was set at 3000 V with a sampling cone voltage of 40 V and a cone gas flow of 60 L/h.

Data were collected from *m/z* 50–1000 with an acquisition rate of 1 spectrum per second. The Lockspray syringe pump was 5 mL with a diameter of 10.3 mm, and the flow rate of the leucine enkephalin calibration solution was adjusted to 5.0 μL/min.

Data acquisition and processing of the validation done on QTOF were performed using the MassLynx® software, where data were exported into a secure online

data storage and backup server (kingfisher.pharm.nottingham.ac.uk). Offline data analyses were performed using MarkerLynx® software (Waters, USA). The software is mostly dedicated for processing the LC-MS-acquired data in centroid mode which are generated by MassLynx®.

3.2.3.2. Orbitrap Exactive mass spectrometer

Orbitrap Exactive mass spectrometer coupled with an Accela Autosampler high performance liquid chromatography (ThermoScientific, Hemel Hempstead, UK) was used to characterise pig tracheal mucus using untargeted metabolomics approach. The CalMix solution was used for instrumental calibration. The capillary temperature was set at 275°C while the heater temperature was 150°C. The sheath gas, desolvation, and sweep gas were set at 40, 5, and 1 units, respectively, for both positive and negative modes. The acquisition range was from *m/z* 70–1400. Table 3.2.2 shows the differences in switching modes between positive and negative modes.

Table 3.2.2. Differences in positive and negative switching modes in an Orbitrap Exactive instrument

Parameter	Positive mode	Negative mode
Spray voltage (v)	4500	3500
Capillary voltage (v)	40	30
Tube lens voltage (v)	70	70
Skimmer voltage (v)	20	18

3.2.4. LC-MS methodology

3.2.4.1. Validation of the QTOF LC-MS method using authentic standards

LC-MS analysis of six replicates in six different days of each authentic standards mixture were performed on a QTOF system using 150 mm × 4.6 mm × 5 μm p-HILIC column (Merck, Germany). The column was maintained at 40°C, and the mobile phase was prepared as 20 mM ammonium carbonate in water (1.92 g ammonium carbonate in 1000 mL of deionized water (18.2 MΩ); mobile phase A) and 1000 mL of acetonitrile HPLC grade (mobile phase B). The gradient started at 80% (B) and decreased to 5% over 15 min and increased back up to 80% at 17 min until the end of the run time (24 min). The flow rate was 300 μL/min and the injection volume was 10 μL. A guard metal-free column was used (p-HILIC, 20 x 2.1 mm, 5 μm, Merck, Germany) to protect the column and minimize expected contaminations. A solvent blank used in the preparation of the authentic standard mixtures (acetonitrile) was injected six times and between each authentic standard mixture group (once) to eliminate the effect of the blank from the analysed authentic standards.

3.2.4.1.1. Leucine enkephalin (QTOF lockspray calibration compound)

Leucine enkephalin stock solution (2 mg/mL) was added at a volume of 20 μL into a mixture of 9.99 mL of 0.1% formic acid in water and 9.99 ml of 0.1% formic acid in acetonitrile to prepare 2 μg/mL of LockSpray calibration solution.

3.2.4.1.2. Sodium formate (QTOF external calibration compound)

Formic acid (1.0 mL) was added to 9.0 mL of water to produce 10% formic acid. Then, 500 μL of this solution and 500 μL of 0.1 M sodium hydroxide were added

to 9.0 mL of 2-propanol:water at a ratio of 90:10 to produce the final external calibration solution.

3.2.4.2. Orbitrap Exactive mass spectrometer for mucus samples analysis

LC-MS analysis of six biological replicates of the raw and cleaned mucus groups were performed on an Exactive system on a p-HILIC column (150 mm × 4.6 mm × 5 μm; Merck, Germany). The column was maintained at 40°C and the mobile phase was 20 mM ammonium carbonate in water (mobile phase A) and LC-MS grade acetonitrile (mobile phase B). The same gradient and run time used for the QTOF method were used in Exactive. The flow rate was 300 μL/min and the injection volume was 10 μL. A metal-free guard column was used to protect the column and minimize expected contaminations (p-HILIC, 20 x 2.1 mm, 5 μm, Merck, Germany). A blank of the solvent (methanol) used in the preparation of authentic standard mixtures (water) was injected six times to eliminate the effect of the blank from the analysed authentic standards.

3.2.5. Statistical analysis and identification of the pig tracheal mucus metabolome

Raw data from the Orbitrab Exactive LC-MS were acquired and visualized with Xcalibur v2.1 software (Thermo Scientific, US). Multivariate data analysis using principal component analysis (PCA) and orthogonal partial least squares-discriminant analysis (OPLS-DA) were used to study the ability of the validated LC-MS method to differentiate between raw and cleaned mucus and to investigate the metabolite differences between the two groups datasets using

3. *Untargeted metabolomics analysis of the in-vitro mucus model*

Simca P +14 software (Umetrics AB, Sweden). The OPLS-DA model was validated using cross-validation and permutation test using the R^2X, R^2Y, and Q^2 (cum) parameters that represent the explanation, fitness, and prediction power, respectively. R^2X is the percentage of all LC-MS response variables explained by the model. R^2Y is the percentage of all observation or sample variables explained by the model. Q^2 is the percentage of all observation or sample variables predicted by the model. The ions responsible for the class separation in the OPLS-DA model of raw and cleaned mucus were selected using variable importance for the projection (VIP). The Student's *t* test was performed to test the significant difference in the selected ions between the two groups. The p values were then adjusted using the false discovery rate (FDR) for the multiple testing problem (Figure 3.2.1). Full raw and cleaned mucus data were imported, pre-processed, and processed using IDEOM software. IDEOM is a bioanalytics program developed by a group of scientists at the Wellcome Trust Centre for Molecular Parasitology, College of Medical, Veterinary and Life Sciences, University of Glasgow, UK (Creek et al., 2012b). LC-Exactive data were pre-processed with XCMS for untargeted peak-picking while peak matching and annotation of related peaks was carried out by mzMatch (Kim et al., 2015). IDEOM was used for putative metabolite identification and noise filtering using default parameters (Creek et al., 2012a). Authentic standard retention times and accurate masses were matched with the identified metabolites (level 1 metabolite identification) (Sumner et al., 2007, Sumner et al., 2014). Predicted retention times were used in case standards were unavailable, hence those metabolites are considered putative (level 2 metabolite identification). High

identification confidence levels for metabolites were produced in graphical and

pie charts.
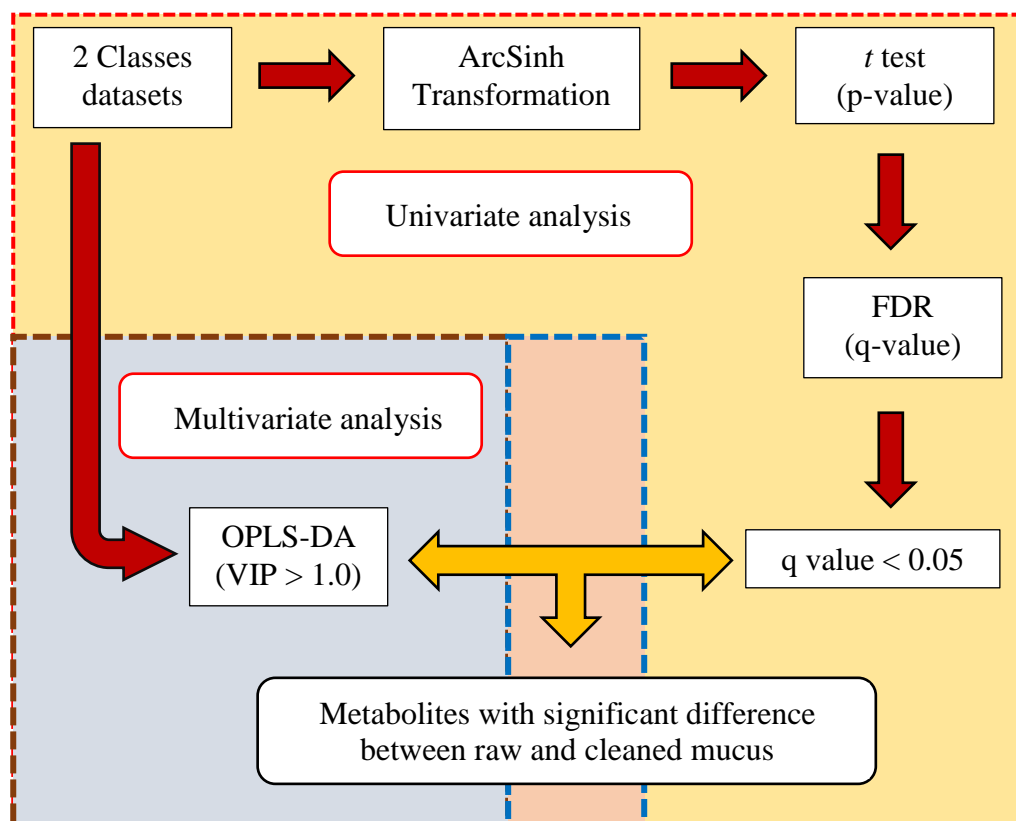
Figure 3.2.1. Workflow depicting the selection of the potential mucus metabolites. Parallel univariate and multivariate analyses were performed to extract metabolites with significant differences between raw and cleaned mucus. The q value is the adjusted p value using FDR.

3.3. Results and discussion

3.3.1. LC-MS method validation

The LC-MS method was tested for its sensitivity and effectiveness by verifying its reproducibility in QTOF. It was verified by six consecutive inter-day analytical replicates containing the five standard mixtures. A solvent blank (acetonitrile) was also run after six replicates of each standard mixture. A total ion chromatogram (TIC) of the five standard mixtures in both modes (positive and negative) was generated (Figure 3.3.1 and Figure 3.3.2).
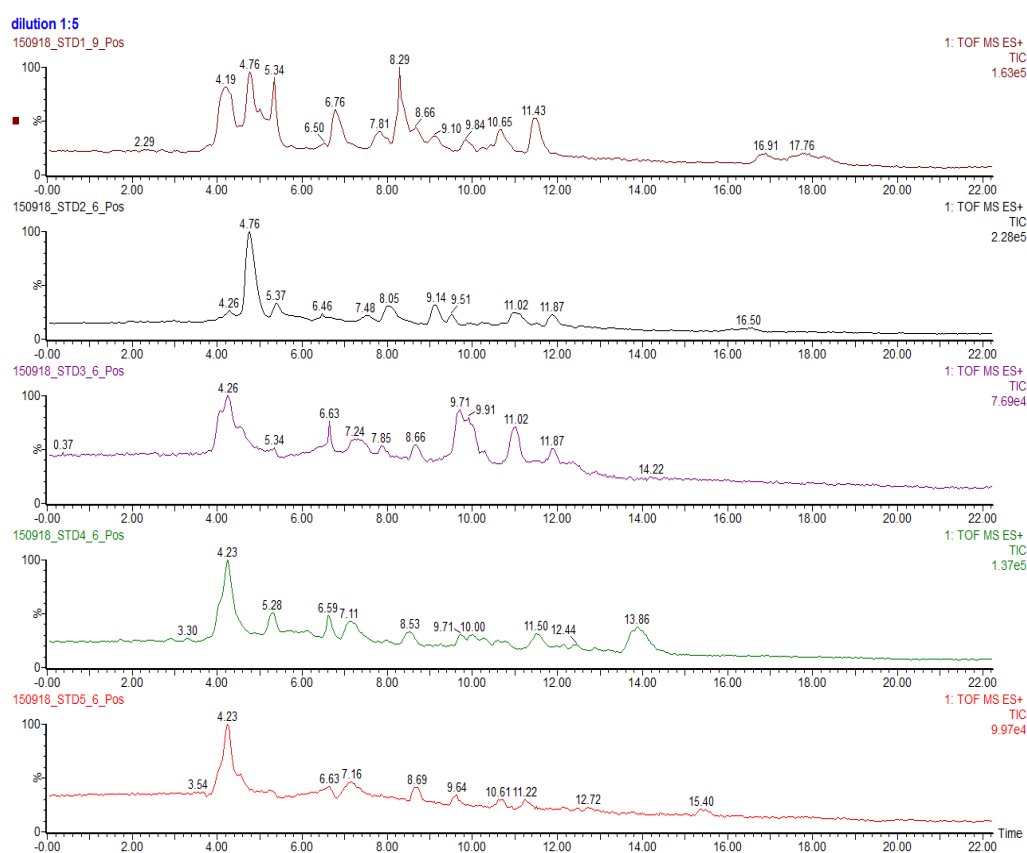
Figure 3.3.1. TICs of five authentic standard mixtures under the validated LC condition in positive mode using QTOF. From top to bottom, the TIC of the authentic standard mixture group 1, 2, 3, 4, and 5.

3. Untargeted metabolomics analysis of the in-vitro mucus model
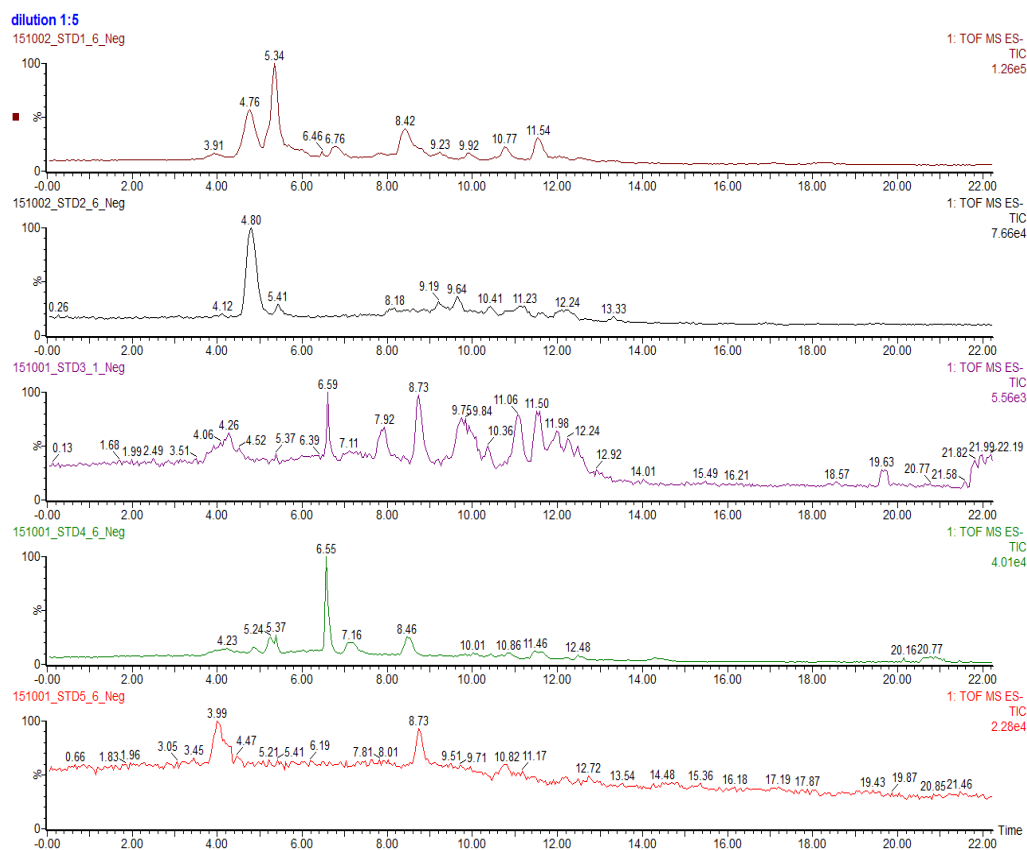
Figure 3.3.2. TICs of five authentic standard mixtures under the validated LC conditions in negative mode using QTOF. From top to bottom, TICs of authentic standard mixture group 1, 2, 3, 4, and 5.

Raw data obtained from LC-MS/QTOF were processed with MarkerLynx. Across the replicates (n = 6), the percentage of coefficient of variation (%CV) of peak areas and retention times were used to investigate the inter-day variation for all detected metabolites.

Figure 3.3.3 to Figure 3.3.6 show the peak area and retention time reproducibility. For a full list of results including the mass error, see Appendix II (Tables A-6 and A-7).

3. Untargeted metabolomics analysis of the in-vitro mucus model
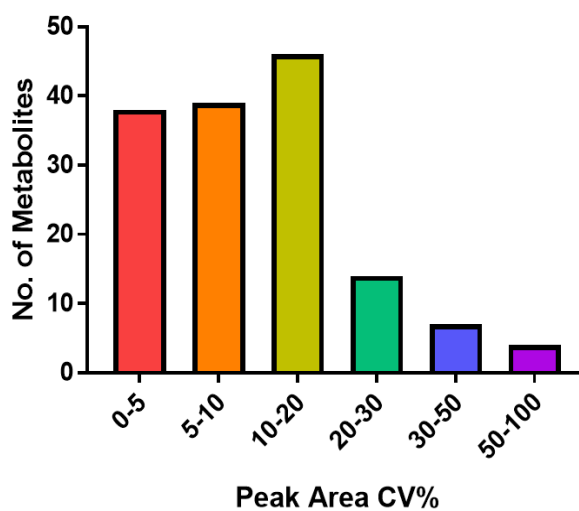
Figure 3.3.3. Distribution bar graph showing the peak area CV% and the number of metabolites in the positive mode using QTOF.
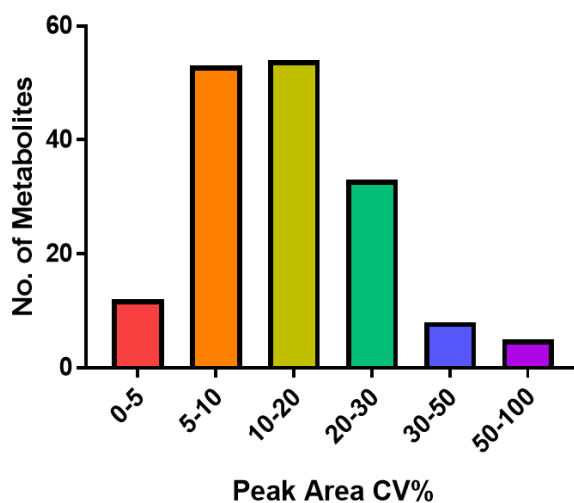
Figure 3.3.4. Distribution bar graph showing peak area CV% and the number of metabolites in the negative mode using QTOF.

Figure 3.3.5. Distribution bar graph showing retention time CV% and the number of metabolites in the positive mode using QTOF.
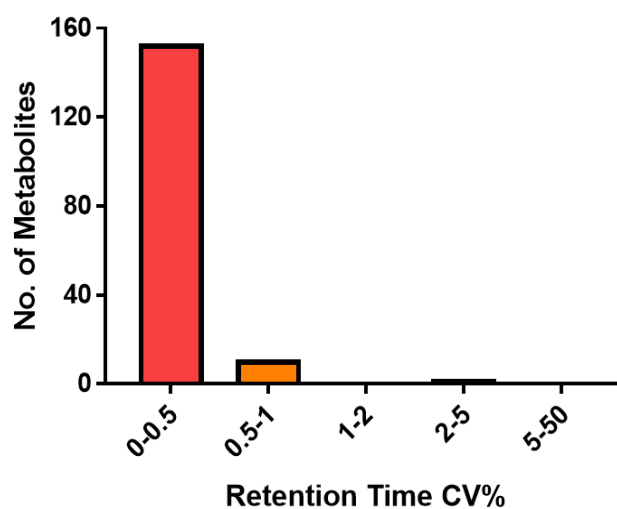
Figure 3.3.6. Distribution bar graph showing retention time CV% and the number of metabolites in the negative mode using QTOF.

3. Untargeted metabolomics analysis of the in-vitro mucus model

Based on these results, the LC-MS method detected the most metabolites using the negative and positive electrospray ionization modes (ESI- and ESI+) with QTOF. This method displayed good reproducibility, and the coefficient of variation (CV%) of peak area and retention time were less than 20% and 0.5% in the most of detected compounds, respectively.

Variations between the peak shape for a replicated standard was the main cause of the deviation from the mean, which resulted in high CV% for some compounds.

For inter-day reproducibility, most of the detected metabolites were less than 20%. These results indicated that the LC-MS method is reproducible. The Food and Drug Administration (FDA) considers conventional bioanalysis as an acceptable method if at least five determinations of the analyte do not exceed 20% of the CV% while those near the lower limit of quantification (LLOQ) are accepted if the CV% is ≤25% (Food and Drug Administration (FDA), 2013). With regard to metabolite identification, an upper limit of 30% can be considered adequate validation (Gika et al., 2007). The mass error should be less than 5 ppm as stated in Waters Micromass QTOF Premier Mass Spectrometer Operator's Guide, which is comparable with the obtained data (Figure 3.3.7 and Figure 3.3.8).

3. Untargeted metabolomics analysis of the in-vitro mucus model
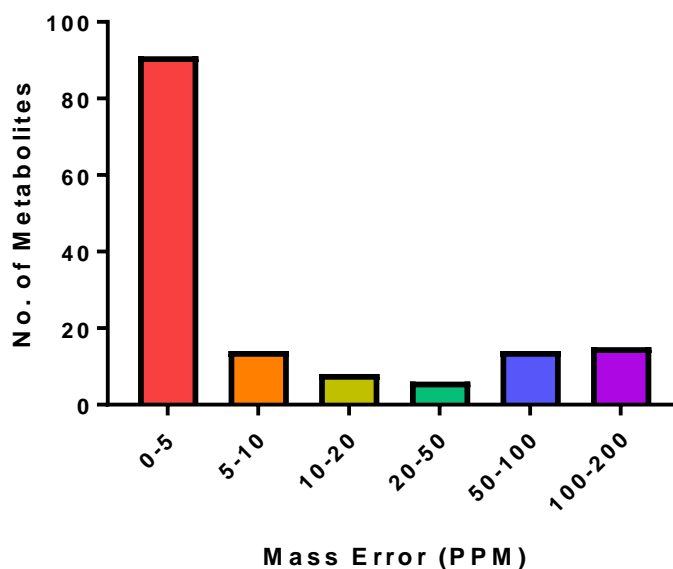
Figure 3.3.7. Distribution bar graph showing mass error in ppm and the number of metabolites in the positive mode using QTOF.
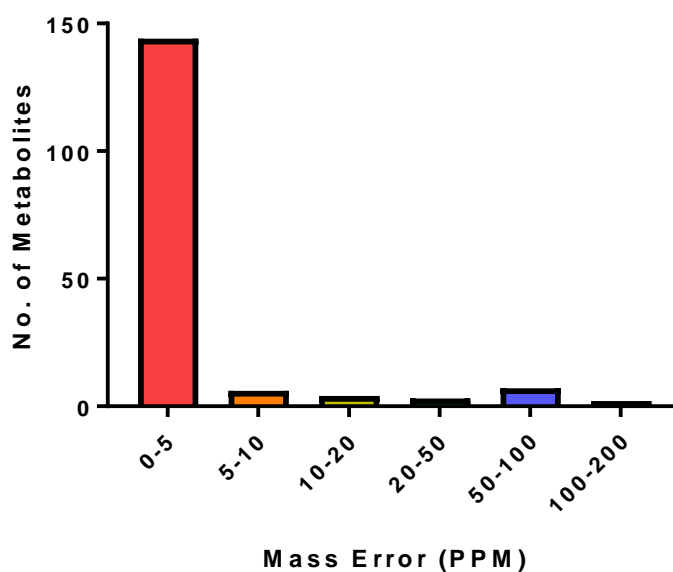
Figure 3.3.8. Distribution bar graph showing mass error in ppm and the number of metabolites in the negative mode using QTOF.

The instrumental sensitivity for the detected compounds was accepted on the basis of the operator's guidance. Therefore, the difference between the theoretical and measured mass below 5 ppm was considered reliable.

3. *Untargeted metabolomics analysis of the in-vitro mucus model*

Good and poor performances were used to classify metabolite signatures. "Good" performances were observed when authentic standards gave symmetric narrow peaks.

Some phosphates, organoheterocyclic compounds, lipids, and other standards performed well using p-HILIC. Hence, a good assessment was attributed to these compounds (Figure 3.3.9 and Figure 3.3.10).
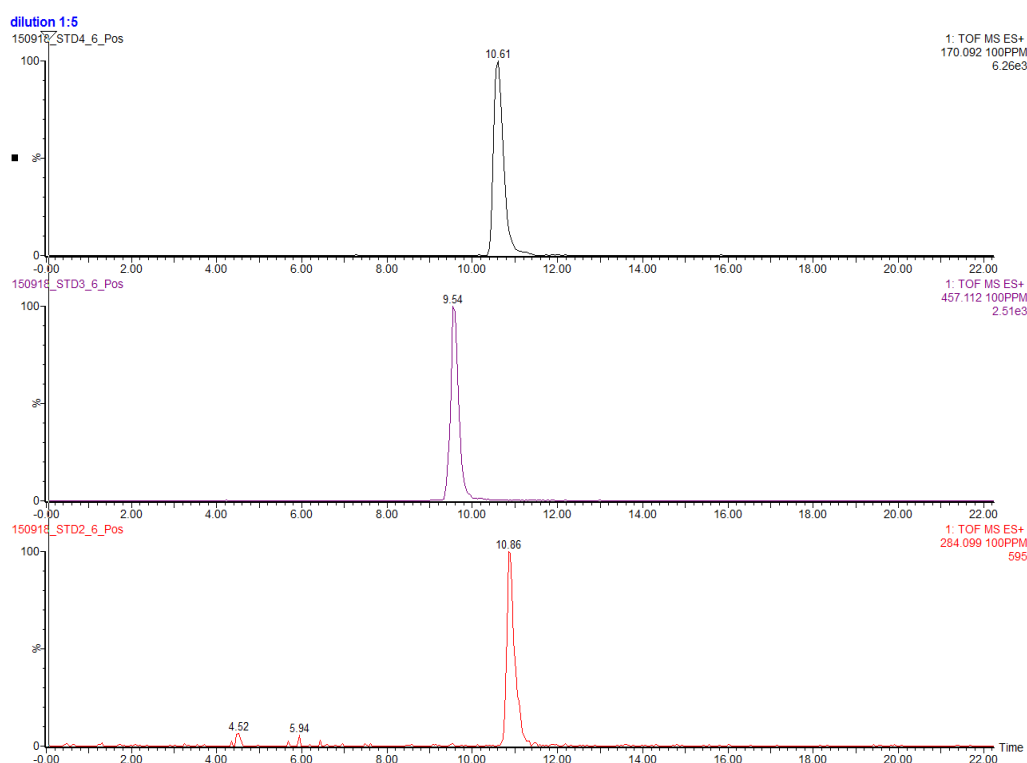
Figure 3.3.9. Examples of 'good' extracted ion chromatographs (EICs). From top to bottom, choline phosphate, isonicotinic acid, and deoxyadenosine under the validated LC condition in the positive mode using QTOF. Those EICs show symmetric narrow peaks due to electrostatic interactions and hydrophilic partitioning of those compounds between p-HILIC and the gradient mobile phase.

3. Untargeted metabolomics analysis of the in-vitro mucus model
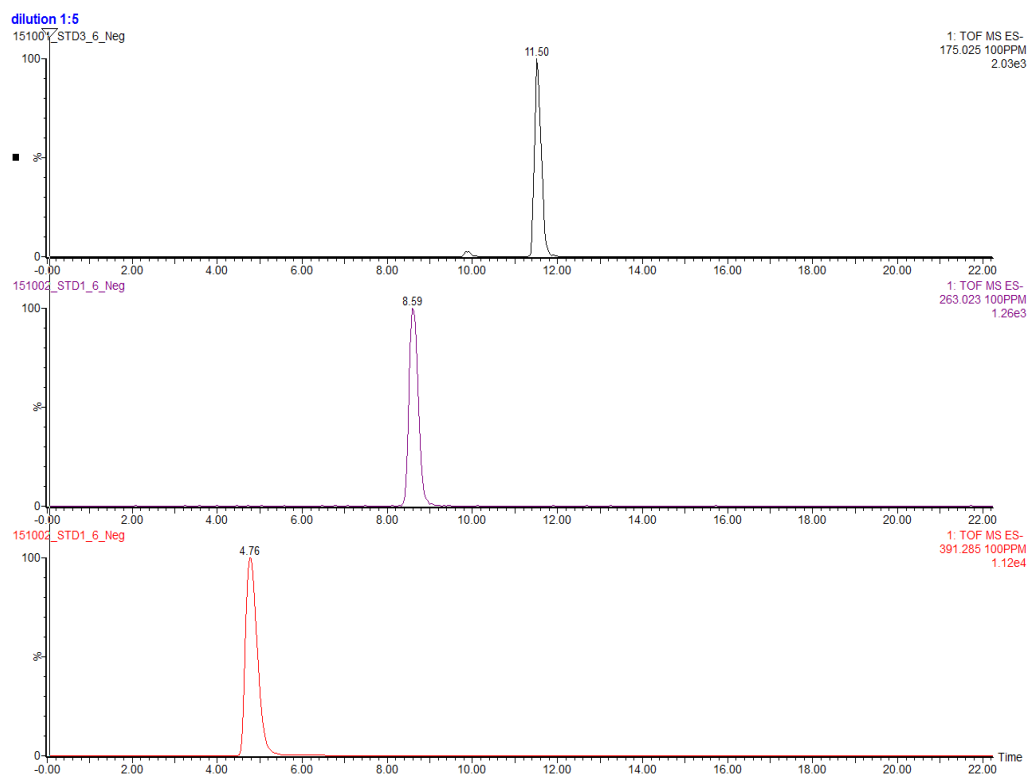
Figure 3.3.10. Examples of 'good' extracted ion chromatographs (EICs). From top to bottom, ascorbate, 3-methoxy-4-hydroxyphenylglycol sulfate, and chenodeoxycholic acid under the validated LC condition in the negative mode using QTOF. Those EICs show symmetric narrow peaks due to electrostatic interactions and hydrophilic partitioning of the compounds between p-HILIC and the gradient mobile phase.

Therefore, it can be concluded that two main factors led to the retention of polar authentic standards on p-HILIC: electrostatic interaction and hydrophilic partitioning of polar compounds between the water-rich stationary phase and the mobile phase. Hence, the poor peak shape was mainly due to electrostatic and hydrophilic interactions between incompletely ionized standards. Some amines displayed poor performances under the given LC conditions due to pH stability of the column, which could not tolerate high basic compounds (Figure 3.3.11).

3. Untargeted metabolomics analysis of the in-vitro mucus model
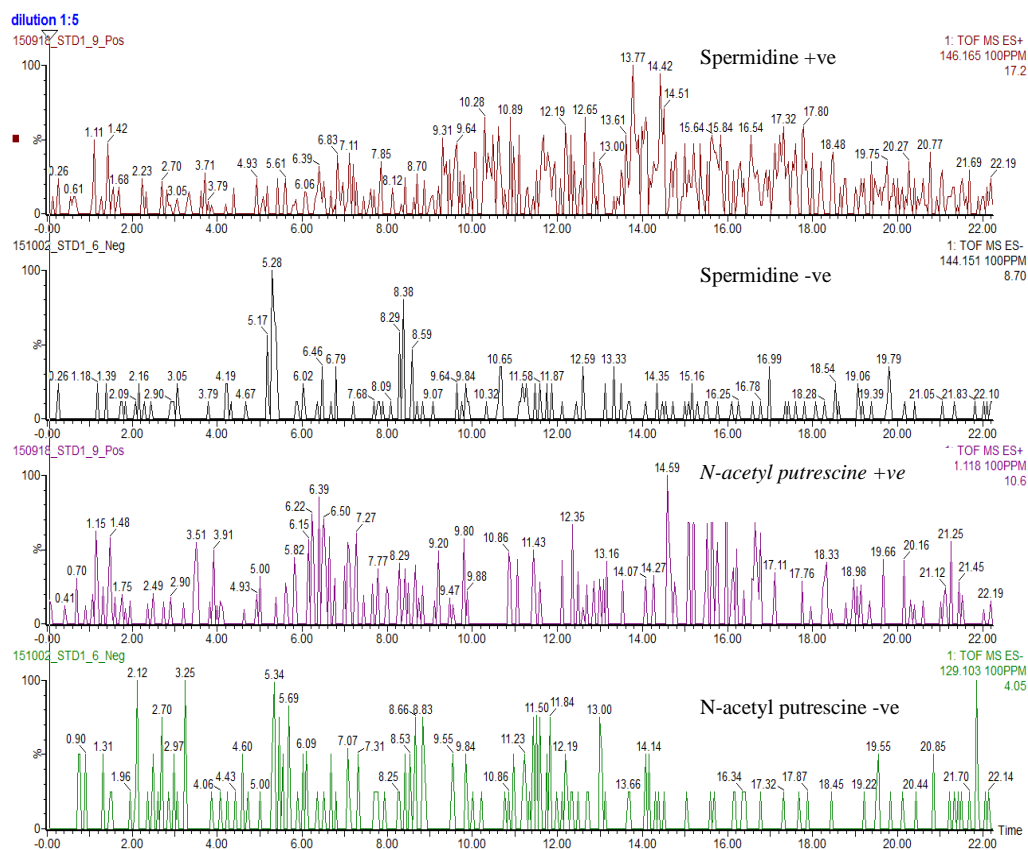
Figure 3.3.11. Examples of poor extracted ion chromatographs (EICs). From top to bottom, spermidine (positive and negative modes) and N-acetyl putrescine (positive and negative modes) under the validated LC condition using QTOF.

However, LC conditions and methodology have proven to be powerful tools in identifying the majority of standards used in this validation. Therefore, this methodology can be useful in identifying mammalian metabolomes and exploring the composition of pig tracheal mucus.

3.3.2. Mucus metabolomics of raw and cleaned pig tracheal mucus

PCA and OPLS-DA are considered powerful statistical analytical tools that offer insights into separations between experimental datasets based on high-dimensional spectral measurements from MS, NMR, and other analytical instruments (Worley and Powers, 2016). From our obtained data, there was a clear separation between the raw and cleaned pig tracheal mucus samples in the PCA score plots (Figure 3.3.12). Although PCA showed a clear separation, OPLS-DA was also applied with rigorous validation to provide a better understanding and to detect the potential metabolites showing prominent changes in levels between the two datasets. VIP statistics (VIP > 1.0) were primarily used to pre-select detected mass ions to identify the detected ions that could account for such a significant separation. Then, in order to decrease the risk of false positives in the selection of significantly altered mass ions, FDR (ANOVA) < 0.05 selection was carried out from those detected mass ions that showed the most correlation with the OPLS-DA discriminant scores. Figure 3.3.13 reveals segregated groups that showed differential metabolite compositions and levels between raw and cleaned pig tracheal mucus. The quality of the resulting discriminant models are $R^2X = 0.673$, $R^2Y = 0.986$, and $Q^2 = 0.985$. These three parameters are > 0.50, indicating all the models were robust and had good explanation, fitness, and prediction power, respectively (Pohjanen et al., 2006).

3. Untargeted metabolomics analysis of the in-vitro mucus model
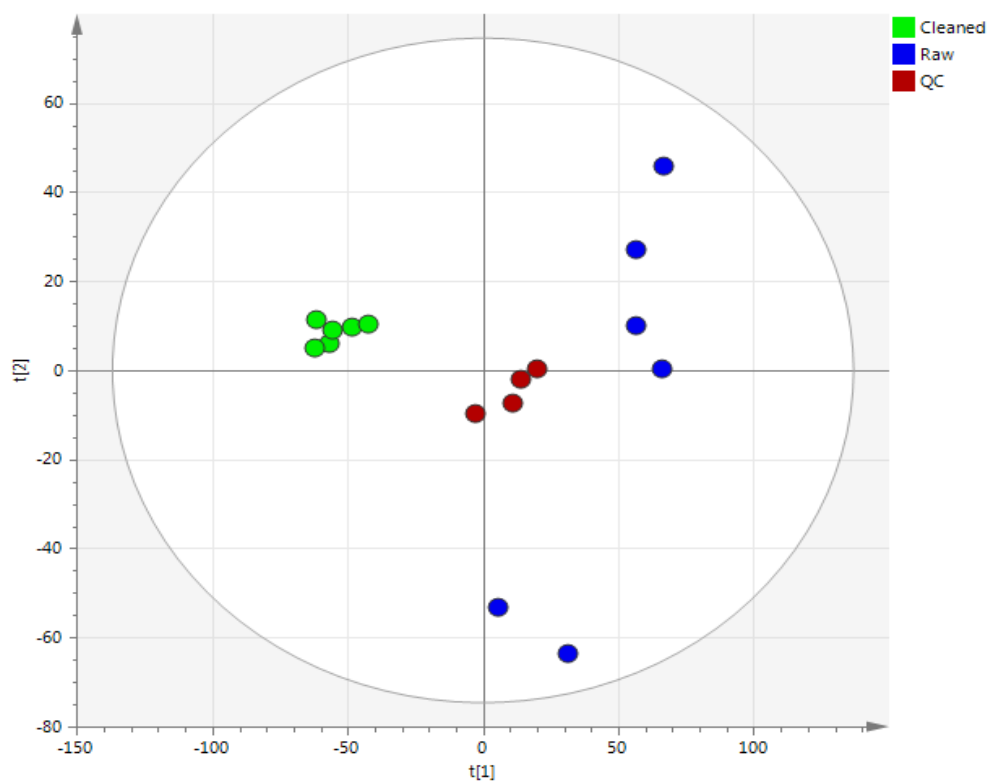
Figure 3.3.12. PCA score plot of untargeted metabolomics of raw (blue) and cleaned (green) pig tracheal mucus. QC samples are presented in red colour.
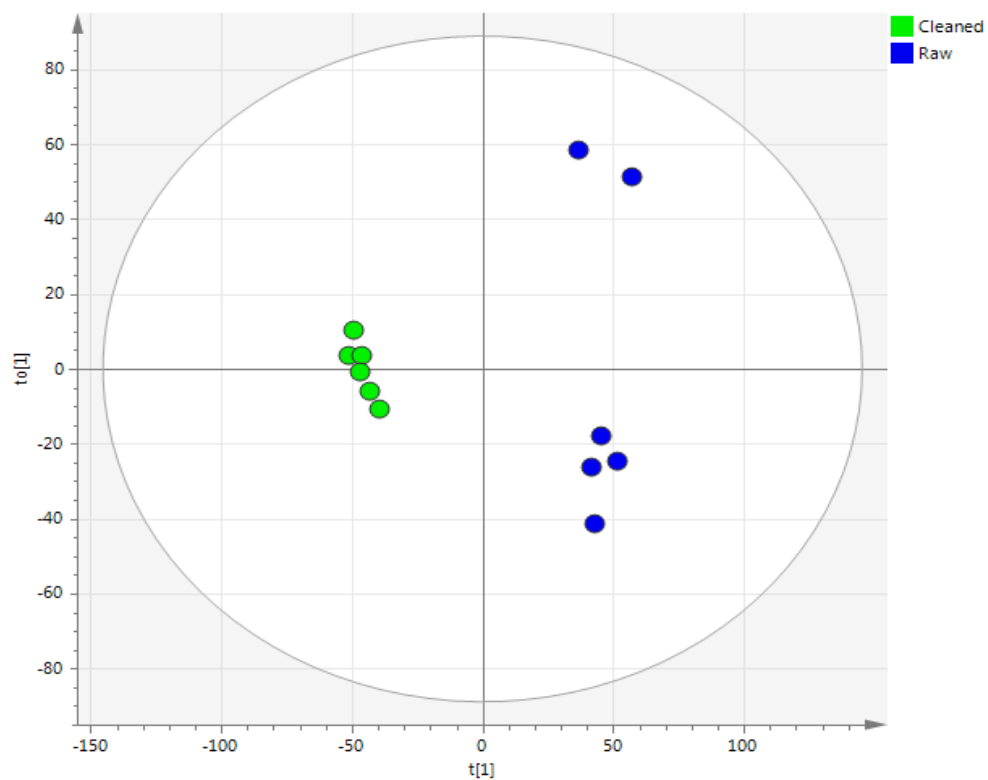
Figure 3.3.13. OPLS-DA score plot of untargeted metabolomics of raw (blue) and cleaned (green) pig tracheal mucus.

3. Untargeted metabolomics analysis of the in-vitro mucus model

To assess the instrument function, pooled samples were assessed for reproducibility. Pooled (QC) samples are run throughout the sample analysis, every 5th sample. Figure 3.3.14 and Figure 3.3.15 show the minimum and maximum signals seen in the pooled samples in both the positive and negative ionization modes, and the interquartile range, which shows the spread of the samples. This shows the high reproducibility of the instrument over time.
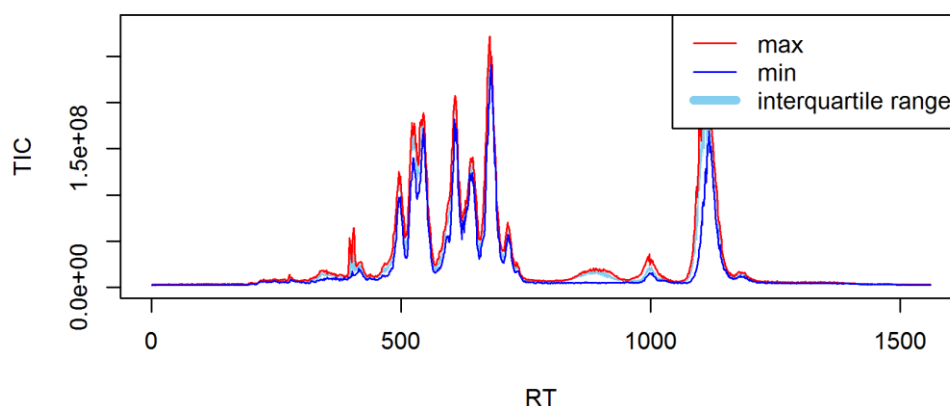
Figure 3.3.14. Minimum/maximum and interquartile ranges for the pooled samples in positive ionization mode showing high reproducibility of the instrument over time. TIC; total ion chromatogram, RT; retention time on the column in seconds.
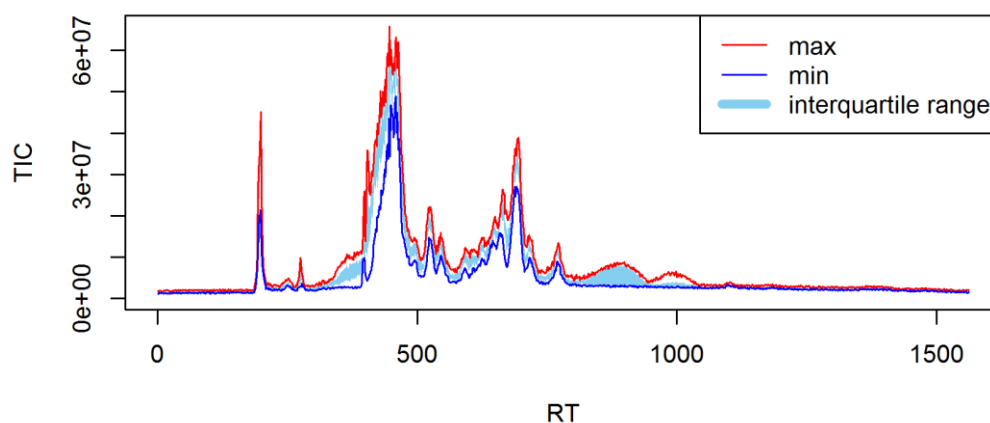
Figure 3.3.15. Minimum/maximum and interquartile ranges for the pooled samples in negative ionization mode showing high reproducibility of the instrument over time. TIC; total ion chromatogram, RT; retention time on the column in seconds.

3.3.3. Tentative identification of metabolites in pig tracheal mucus

A total of 816 metabolites were common to both sets of mucus, which are listed in detail in the Appendix II, Table A-8. Figure 3.3.16 shows the distribution of metabolites based on their chemical classes. Hence, it can be concluded that raw and cleaned mucus share the same metabolite profile , at the exception of nine compounds that were not present or were at the LLOQ following the cleaning process (Table 3.3.1).
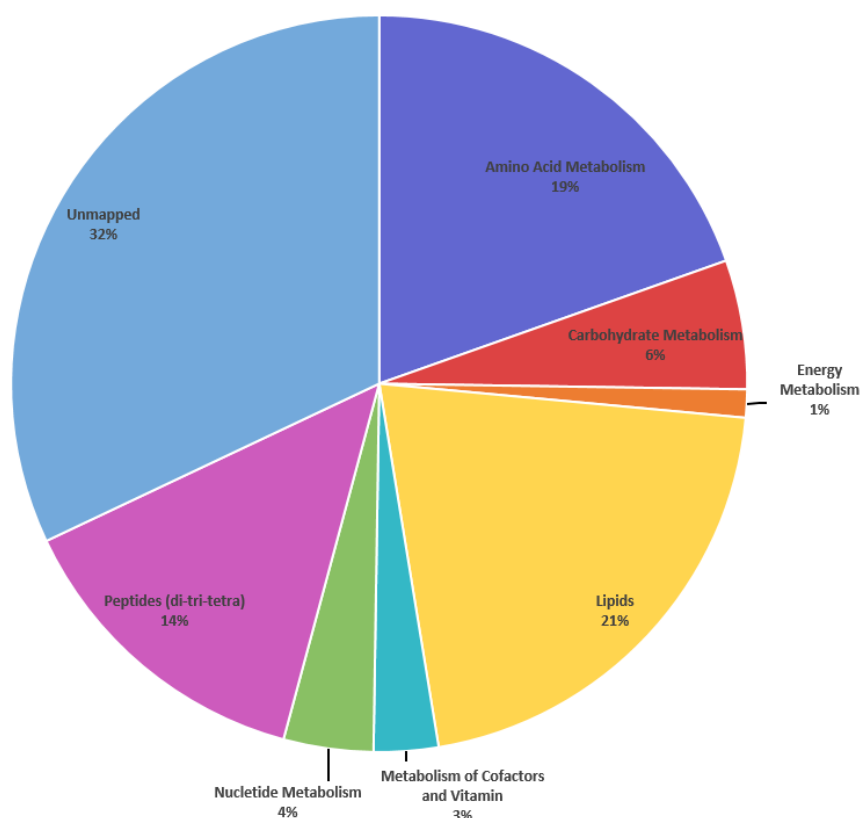
Figure 3.3.16. Chemical composition of pig tracheal mucus (raw and cleaned) where metabolites are categorised by biochemical class.

As shown in the pie chart (Figure 3.3.16), approximately 50% of pig tracheal mucus is composed of lipids or products of amino acid metabolism, and carbohydrate metabolism. These results are in accordance with the previously reported composition of human bronchial mucus (Esther et al., 2016, Nobakht M. Gh et al., 2015, SLAYTER et al., 1984).

3. Untargeted metabolomics analysis of the in-vitro mucus model

Table 3.3.1. Metabolites that were not present in cleaned pig tracheal mucus

Mass	Retention Time	Formula	Putative metabolite	Class
189.0637	6.648	$C_7H_{11}NO_5$	Glutarylglycine	Fatty Acid Metabolism
243.1041	7.85	$C_{10}H_{17}N_3O_2S$	Biotinamide	Metabolism of Cofactors and Vitamins
253.0949	6.705	$C_{12}H_{15}NO_5$	*N*-Acetylvanilalanine	Amino Acid Metabolism
233.0357	6.598	$C_8H_{11}NO_5S$	Dopamine 3-*O*-sulfate	Amino Acid Metabolism
251.1156	3.659	$C_{13}H_{17}NO_4$	*N*-Acetyl-L-tyrosine ethyl ester	Amino Acid Metabolism
120.0436	6.832	$C_5H_4N_4$	Purine	Nucleotide Metabolism
264.1109	3.982	$C_{13}H_{16}N2O_4$	Formyl-*N*-acetyl-5-methoxykynurenamine	Amino Acid Metabolism
301.2252	4.562	$C_{16}H_{31}NO_4$	2-6-dimethylheptanoylcarnitine	Amino Acid Metabolism
313.2253	4.549	$C_{17}H_{31}NO_4$	9-Decenoylcarnitine	Amino Acid Metabolism

3. Untargeted metabolomics analysis of the in-vitro mucus model

The metabolites described in Table 3.3.1 were those missing in cleaned mucus. These are mainly blood components associated with raw mucus. For instance, dopamine 3-*O*-sulfate is a sulfonated form of dopamine predominant in human plasma, while purines are found both on endothelial and hematopoietic cells, which play a crucial role in blood vessels (Fu et al., 2017, Yegutkin et al., 2003). Furthermore, formyl-*N*-acetyl-5-methoxykynurenamine is the main oxidation product of melatonin, the hormone which participates in blood pressure regulation (Hardeland et al., 2003). In addition, 2-6-dimethylheptanoylcarnitine, which is a derivative of carnitine, and 9-decenoylcarnitine, which is also a member of the acyl carnitines, are found in human serum: http://www.ebi.ac.uk/chebi/chebiOntology.do?chebiId=CHEBI:85234&treeView=true#vizualisation.

However, according to the statistical validation applied, 20 identified metabolites were significantly concentrated in cleaned mucus as compared to raw mucus. These metabolites are summarised in Table 3.3.2 while Figure 3.3.17 shows the changes in levels of the 10 most concentrated identified metabolites.

3. *Untargeted metabolomics analysis of the in-vitro mucus model*

Table 3.3.2. Tentative identification of components of pig tracheal mucus showing a higher concentration in cleaned vs raw mucus

Mass	RT	Formula	Putative metabolite	Class	Maximum intensity	Fold Change Cleaned mucus	Raw mucus
217.1425	12.03	$C_9H_{19}N_3O_3$	gamma-L-Glutamylputrescine	Amino Acid Metabolism	438771	234.11	1.00
245.1487	12.14	$C_9H_{19}N_5O_3$	beta-Alanyl-L-arginine	Amino Acid Metabolism	225560	109.66	1.00
176.0797	6.719	$C_6H_{12}N_2O_4$	N5-Formyl-N5-hydroxy-L-ornithine	Amino Acid Metabolism	122172	48.75	1.00
220.1059	8.105	$C_8H_{16}N_2O_5$	N-Acetyl-beta-D-glucosaminylamine	Unmapped	31291	23.77	1.00
276.1068	10.34	$C_9H_{16}N_4O_6$	4-(1-D-Ribitylamino)-5-amino-2,6-dihydroxypyrimidine	Metabolism of Cofactors and Vitamins	19179	14.49	0.00
229.2405	4.142	$C_{14}H_{31}NO$	[SP (14:0)] 1-deoxy-tetradecasphinganine	Lipids (SP, sphingolipids)	192525	7.32	1.00
204.1110	7.103	$C_8H_{16}N_2O_4$	N6-Acetyl-N6-hydroxy-L-lysine	Amino Acid Metabolism	77829	5.85	1.00
190.0953	8.11	$C_7H_{14}N_2O_4$	N5-Acetyl-N5-hydroxy-L-ornithine	Amino Acid Metabolism	62462	5.83	1.00
240.0238	11.5	$C_6H_{12}N_2O_4S_2$	L-Cystine	Amino Acid Metabolism	126564	5.46	1.00
113.0477	5.351	$C_5H_7NO_2$	1-Pyrroline-2-carboxylate	Amino Acid Metabolism	402920	5.45	1.00
188.1161	6.674	$C_8H_{16}N_2O_3$	N6-Acetyl-L-lysine	Amino Acid Metabolism	1042135	4.56	1.00
113.0477	7.343	$C_5H_7NO_2$	(S)-1-Pyrroline-5-carboxylate	Amino Acid Metabolism	792406	4.46	1.00
302.2246	3.301	$C_{20}H_{30}O_2$	FA (20:5)	Lipids (FA, Fatty Acyls)	128674	3.76	1.00

3. *Untargeted metabolomics analysis of the in-vitro mucus model*

Mass	RT	Formula	Putative metabolite	Class	Maximum intensity	Fold Change Cleaned mucus	Raw mucus
322.2508	3.294	$C_{20}H_{34}O_3$	FA hydroxy (20:3)	Lipids (FA, Fatty Acyls)	44464	2.76	1.00
294.2195	3.313	$C_{18}H_{30}O_3$	FA oxo (18:1)	Lipids (FA, Fatty Acyls)	297595	2.69	1.00
154.0031	8.784	$C_3H_7O_5P$	Propanoyl phosphate	Carbohydrate metabolism	20397	2.53	1.00
330.2558	3.273	$C_{22}H_{34}O_2$	Taxa-4(20),11(12)-dien-5alpha-yl acetate	Biosynthesis of secondary metabolites	20242	2.41	1.00
276.2090	3.423	$C_{18}H_{28}O_2$	FA (18:4)	Lipids (FA, Fatty Acyls)	126041	2.17	1.00
292.2040	3.451	$C_{18}H_{28}O_3$	FA oxo (18:3)	Lipids (FA, Fatty Acyls)	20241	2.12	1.00
295.1281	6.667	$C_{12}H_{17}N_5O_4$	N6,N6-Dimethyladenosine	Nucleotide metabolism	34308	2.04	1.00
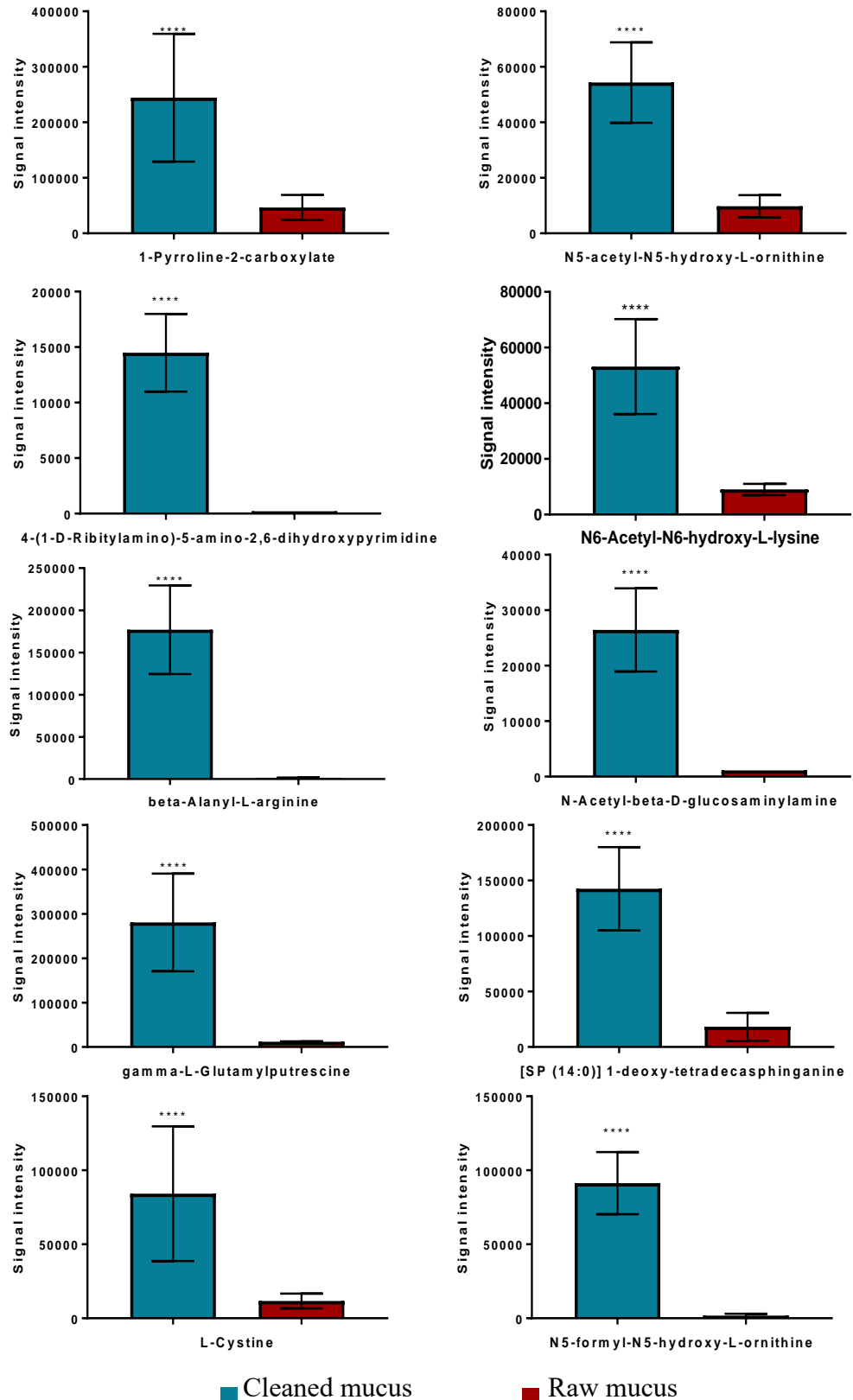
Figure 3.3.17. Changes in the levels of the ten metabolites with the most significant higher concentration in clean vs raw mucus samples. Data are presented as mean of six biological replicates ± SD.

3. *Untargeted metabolomics analysis of the in-vitro mucus model*

Amongst the significantly concentrated metabolites in cleaned mucus, *N*-acetyl-beta-D-glucosaminylamine, has been found to result from the catalysis of N4-(b-*N*-acetyl-D-glucosaminyl)-L-asparagine hydrolysis that is released from mucin via N4-(b-N-acetylglucosaminyl)-L-asparaginase (Atwood et al., 2006). Another example is 4-(1-D-Ribitylamino)-5-amino-2,6-dihydroxypyrimidine, was investigated previously and has been shown to be a major metabolite of riboflavin, which is considered to be an essential vitamin for the respiratory system as it aids in the maintenance of the mucus layer lining the respiratory tract (Atwood et al., 2006, Wacker et al., 1964). In addition, N5-acetyl-N5-hydroxy-L-ornithineis a metabolite of L-ornithine, which is distributed throughout human tissues and in most biofluids, including blood, cerebrospinal fluid (CSF), urine, saliva, sweat, mucus, and feces. This amino acid is a known biomarker that is upregulated in bronchitis (Esther et al., 2016). Furthermore, 1-pyrroline-2-carboxylate, a terminal product of proline metabolism, and its stereoisomer, (S)-1-pyrroline-2-carboxylate, is an intermediate in proline biosynthesis and degradation. Proline has been investigated previously and was shown to be a major amino acid component in human tracheobronchial secretions (Woodward et al., 1982).

3.4. Conclusion

In the present chapter, an LC-MS method was validated for the comprehensive analysis of global metabolic profiles in biofluids and applied for characterizing the composition of pig tracheal mucus samples before and after the cleaning procedure

The metabolomics profile of cleaned mucus and raw mucus shared approximately 99% of the components. The missing metabolites after cleaning were mainly blood components. Approximately 50% of the metabolites identified in the mucus samples consisted of lipids and products of amino acid or carbohydrate metabolism.

The metabolomics profile obtained reflected the previously reported composition of human bronchial mucus and gave confidence in the suitability of the developed in-vitro model for studying inhaled airway mucus-drug interactions.

3.5. References

ALLEN, J., DAVEY, H. M., BROADHURST, D., HEALD, J. K., ROWLAND, J. J., OLIVER, S. G. & KELL, D. B. 2003. High-throughput classification of yeast mutants for functional genomics using metabolic footprinting. *Nat Biotech,* 21**,** 692-696.

ALPERT, A. J. 1990a. Hydrophilic-interaction chromatography for the separation of peptides, nucleic acids and other polar compounds. *Journal of chromatography A,* 499**,** 177-196.

ALPERT, A. J. 1990b. Hydrophilic-interaction chromatography for the separation of peptides, nucleic acids and other polar compounds. *J Chromatogr,* 499**,** 177-96.

ALPERT, A. J., SHUKLA, M., SHUKLA, A. K., ZIESKE, L. R., YUEN, S. W., FERGUSON, M. A., MEHLERT, A., PAULY, M. & ORLANDO, R. 1994. Hydrophilic-interaction chromatography of complex carbohydrates. *Journal of Chromatography A,* 676**,** 191-202.

ATWOOD, T., CAMPBELL, P., PARISH, H., SMITH, T., STIRLING, J., VELLA, F. & CAMMACK, C. 2006. Oxford Dictionary of Biochemistry and Molecular Biology. Oxford Univ. Press, Oxford.

BANERJEE, S. & MAZUMDAR, S. 2012. Electrospray ionization mass spectrometry: a technique to access the information beyond the molecular weight of the analyte. *International journal of analytical chemistry,* 2012.

BECKER, S., KORTZ, L., HELMSCHRODT, C., THIERY, J. & CEGLAREK, U. 2012. LC-MS-based metabolomics in the clinical laboratory. *J Chromatogr B Analyt Technol Biomed Life Sci,* 883-884**,** 68-75.

BRISTOW, A. W. 2006. Accurate mass measurement for the determination of elemental formula--a tutorial. *Mass Spectrom Rev,* 25**,** 99-111.

BYRDWELL, W. C. 2001. Atmospheric pressure chemical ionization mass spectrometry for analysis of lipids. *Lipids,* 36**,** 327-46.

CASTRILLO, J. I., HAYES, A., MOHAMMED, S., GASKELL, S. J. & OLIVER, S. G. 2003. An optimized protocol for metabolome analysis in yeast using direct infusion electrospray mass spectrometry. *Phytochemistry,* 62**,** 929-937.

CHAPMAN, H. M., SCHUTT, K. L., DIETER, E. M. & LAMOS, S. M. 2012. Relative quantification of biomarkers using mixed-isotope labeling coupled with MS. *Bioanalysis,* 4**,** 2525-2541.

CHEN, H., MCCOY, L. F., SCHLEICHER, R. L. & PFEIFFER, C. M. 2008. Measurement of 25-hydroxyvitamin D3 (25OHD3) and 25-hydroxyvitamin D2 (25OHD2) in human serum using liquid chromatography-tandem mass spectrometry and its comparison to a radioimmunoassay method. *Clin Chim Acta,* 391**,** 6-12.

CHERNUSHEVICH, I. V., LOBODA, A. V. & THOMSON, B. A. 2001. An introduction to quadrupole-time-of-flight mass spectrometry. *J Mass Spectrom,* 36**,** 849-65.

COLEBATCH, G., DESBROSSES, G., OTT, T., KRUSELL, L., MONTANARI, O., KLOSKA, S., KOPKA, J. & UDVARDI, M. K. 2004. Global changes in transcription orchestrate metabolic differentiation during symbiotic nitrogen fixation in Lotus japonicus. *Plant J,* 39**,** 487-512.

CREEK, D. J., CHOKKATHUKALAM, A., JANKEVICS, A., BURGESS, K. E., BREITLING, R. & BARRETT, M. P. 2012a. Stable isotope-assisted metabolomics for network-wide metabolic pathway elucidation. *Analytical chemistry,* 84**,** 8442-8447.

CREEK, D. J., JANKEVICS, A., BURGESS, K. E., BREITLING, R. & BARRETT, M. P. 2012b. IDEOM: an Excel interface for analysis of LC-MS-based metabolomics data. *Bioinformatics,* 28**,** 1048-9.

DANIELSSON, R., ALLARD, E., SJÖBERG, P. J. R. & BERGQUIST, J. 2011. Exploring liquid chromatography–mass spectrometry fingerprints of urine samples from patients with prostate or urinary bladder cancer. *Chemometrics and Intelligent Laboratory Systems,* 108**,** 33-48.

DAVID, A., ABDUL-SADA, A., LANGE, A., TYLER, C. R. & HILL, E. M. 2014. A new approach for plasma (xeno)metabolomics based on solid-phase extraction and nanoflow liquid chromatography-nanoelectrospray ionisation mass spectrometry. *Journal of Chromatography A,* 1365**,** 72-85.

DENG, C., ZHANG, J., YU, X., ZHANG, W. & ZHANG, X. 2004. Determination of acetone in human breath by gas chromatography–mass spectrometry and solid-phase microextraction with on-fiber derivatization. *Journal of Chromatography B,* 810**,** 269-275.

DETTMER, K., ARONOV, P. A. & HAMMOCK, B. D. 2007. MASS SPECTROMETRY-BASED METABOLOMICS. *Mass spectrometry reviews,* 26**,** 51-78.

DUNN, W. B. & ELLIS, D. I. 2005. Metabolomics: current analytical platforms and methodologies. *TrAC Trends in Analytical Chemistry,* 24**,** 285-294.

ENS, W. & STANDING, K. G. 2005. Hybrid quadrupole/time-of-flight mass spectrometers for analysis of biomolecules. *Methods Enzymol,* 402**,** 49-78.

ERNST, M., SILVA, D. B., SILVA, R., MONGE, M., SEMIR, J., VÊNCIO, R. Z. N. & LOPES, N. P. 2015. A metabolomic protocol for plant systematics by matrix-assisted laser-desorption/ionization time-of flight mass spectrometry. *Analytica Chimica Acta,* 859**,** 46-58.

ESTHER, C. R., TURKOVIC, L., ROSENOW, T., MUHLEBACH, M. S., BOUCHER, R. C., RANGANATHAN, S. & STICK, S. M. 2016. Metabolomic biomarkers predictive of early structural lung disease in cystic fibrosis. *European Respiratory Journal,* 48**,** 1612-1621.

EVANS, C. R., KARNOVSKY, A., KOVACH, M. A., STANDIFORD, T. J., BURANT, C. F. & STRINGER, K. A. 2014. Untargeted LC-MS metabolomics of bronchoalveolar lavage fluid differentiates acute respiratory distress syndrome from health. *J Proteome Res,* 13**,** 640-9.

FENN, J. B., MANN, M., MENG, C. K., WONG, S. F. & WHITEHOUSE, C. M. 1989. Electrospray ionization for mass spectrometry of large biomolecules. *Science,* 246**,** 64-71.

FIEHN, O., KOPKA, J., TRETHEWEY, R. N. & WILLMITZER, L. 2000. Identification of uncommon plant metabolites based on calculation of elemental compositions using gas chromatography and quadrupole mass spectrometry. *Anal Chem,* 72**,** 3573-80.

FOOD AND DRUG ADMINISTRATION (FDA), C. 2013. Guidance for Industry, Bioanalytical Method Validation. *FDA guidelines*.

3. Untargeted metabolomics analysis of the in-vitro mucus model

FU, H., MEADOWS, A. S., PINEDA, R. J., MOHNEY, R. P., STIRDIVANT, S. & MCCARTY, D. M. 2017. Serum global metabolomics profiling reveals profound metabolic impairments in patients with MPS IIIA and MPS IIIB. *Metab Brain Dis,* 32**,** 1403-1415.

GABRIELSON, G. & SAMUELSON, O. 1950. Utilization of ion exchangers in analytical chemistry. *XVI: Adsorption of aldehydes and ketones. Sven Kem Tidskr,* 62**,** 214-223.

GIKA, H. G., THEODORIDIS, G. A. & WILSON, I. D. 2008. Liquid chromatography and ultra-performance liquid chromatography–mass spectrometry fingerprinting of human urine: Sample stability under different handling and storage conditions for metabonomics studies. *Journal of Chromatography A,* 1189**,** 314-322.

GIKA, H. G., THEODORIDIS, G. A., WINGATE, J. E. & WILSON, I. D. 2007. Within-day reproducibility of an HPLC-MS-based method for metabonomic analysis: application to human urine. *Journal of proteome research,* 6**,** 3291-3303.

GOODACRE, R., VAIDYANATHAN, S., DUNN, W. B., HARRIGAN, G. G. & KELL, D. B. 2004. Metabolomics by numbers: acquiring and understanding global metabolite data. *Trends Biotechnol,* 22**,** 245-52.

GOWDA, G. N., ZHANG, S., GU, H., ASIAGO, V., SHANAIAH, N. & RAFTERY, D. 2008. Metabolomics-based methods for early disease diagnostics. *Expert Review of Molecular Diagnostics,* 8**,** 617-633.

GRIFFIN, J. L. & NICHOLLS, A. W. 2006. Metabolomics as a functional genomic tool for understanding lipid dysfunction in diabetes, obesity and related disorders. *Pharmacogenomics,* 7**,** 1095-107.

GROSS, J. H. 2004. *Mass spectrometry: a textbook*, Springer Science & Business Media.

GUY, P. A., TAVAZZI, I., BRUCE, S. J., RAMADAN, Z. & KOCHHAR, S. 2008. Global metabolic profiling analysis on human urine by UPLC– TOFMS: Issues and method validation in nutritional metabolomics. *Journal of Chromatography B,* 871**,** 253-260.

HAGGARTY, J., OPPERMANN, M., DALBY, M., BURCHMORE, R., COOK, K., WEIDT, S. & BURGESS, K. V. 2015. Serially coupling hydrophobic interaction and reversed-phase chromatography with simultaneous gradients provides greater coverage of the metabolome. *Metabolomics***,** 1-6.

HAN, J., DATLA, R., CHAN, S. & BORCHERS, C. H. 2009. Mass spectrometry-based technologies for high-throughput metabolomics. *Bioanalysis,* 1**,** 1665-84.

HARDELAND, R., POEGGELER, B., NIEBERGALL, R. & ZELOSKO, V. 2003. Oxidation of melatonin by carbonate radicals and chemiluminescence emitted during pyrrole ring cleavage. *Journal of pineal research,* 34**,** 17-25.

HEMSTRÖM, P. & IRGUM, K. 2006. Hydrophilic interaction chromatography. *Journal of separation science,* 29**,** 1784-1821.

HODSON, M., DEAR, G., GRIFFIN, J. & HASELDEN, J. 2009. An approach for the development and selection of chromatographic methods for high- throughput metabolomic screening of urine by ultra pressure LC-ESI- ToF-MS. *Metabolomics,* 5**,** 166-182.

3. Untargeted metabolomics analysis of the in-vitro mucus model

HUCK, J. H., STRUYS, E. A., VERHOEVEN, N. M., JAKOBS, C. & VAN DER KNAAP, M. S. 2003. Profiling of pentose phosphate pathway intermediates in blood spots by tandem mass spectrometry: application to transaldolase deficiency. *Clinical chemistry,* 49**,** 1375-1380.

ISSAQ, H. J., NATIV, O., WAYBRIGHT, T., LUKE, B., VEENSTRA, T. D., ISSAQ, E. J., KRAVSTOV, A. & MULLERAD, M. 2008. Detection of bladder cancer in human urine by metabolomic profiling using high performance liquid chromatography/mass spectrometry. *J Urol,* 179**,** 2422-6.

JAIN, M., NILSSON, R., SHARMA, S., MADHUSUDHAN, N., KITAMI, T., SOUZA, A. L., KAFRI, R., KIRSCHNER, M. W., CLISH, C. B. & MOOTHA, V. K. 2012. Metabolite profiling identifies a key role for glycine in rapid cancer cell proliferation. *Science,* 336**,** 1040-4.

JANSEN, R., LACHATRE, G. & MARQUET, P. 2005. LC-MS/MS systematic toxicological analysis: comparison of MS/MS spectra obtained with different instruments and settings. *Clin Biochem,* 38**,** 362-72.

JONSSON, P., GULLBERG, J., NORDSTROM, A., KUSANO, M., KOWALCZYK, M., SJOSTROM, M. & MORITZ, T. 2004. A strategy for identifying differences in large series of metabolomic samples analyzed by GC/MS. *Anal Chem,* 76**,** 1738-45.

KAYSER, O. & WARZECHA, H. 2012. *Pharmaceutical biotechnology : drug discovery and clinical applications,* Weinheim; Chichester, Wiley-VCH ; John Wiley [distributor].

KHOO, S. H. & AL-RUBEAI, M. 2007. Metabolomics as a complementary tool in cell culture. *Biotechnol Appl Biochem,* 47**,** 71-84.

3. Untargeted metabolomics analysis of the in-vitro mucus model

KIM, D.-H., ACHCAR, F., BREITLING, R., BURGESS, K. E. & BARRETT, M. P. 2015. LC–MS-based absolute metabolite quantification: application to metabolic flux measurement in trypanosomes. *Metabolomics,* 11**,** 1721-1732.

KINROSS, J. M., HOLMES, E., DARZI, A. W. & NICHOLSON, J. K. 2011. Metabolic phenotyping for monitoring surgical patients. *Lancet,* 377**,** 1817-9.

LU, W., BENNETT, B. D. & RABINOWITZ, J. D. 2008. Analytical strategies for LC-MS-based targeted metabolomics. *J Chromatogr B Analyt Technol Biomed Life Sci,* 871**,** 236-42.

LU, W., CLASQUIN, M. F., MELAMUD, E., AMADOR-NOGUEZ, D., CAUDY, A. A. & RABINOWITZ, J. D. 2010. Metabolomic analysis via reversed-phase ion-pairing liquid chromatography coupled to a stand alone orbitrap mass spectrometer. *Anal Chem,* 82**,** 3212-21.

LUO, B., GROENKE, K., TAKORS, R., WANDREY, C. & OLDIGES, M. 2007. Simultaneous determination of multiple intracellular metabolites in glycolysis, pentose phosphate pathway and tricarboxylic acid cycle by liquid chromatography-mass spectrometry. *J Chromatogr A,* 1147**,** 153-64.

MAIER, T., MARCOS, J., WODKE, J. A., PAETZOLD, B., LIEBEKE, M., GUTIÉRREZ-GALLEGO, R. & SERRANO, L. 2013. Large-scale metabolome analysis and quantitative integration with genomics and proteomics data in Mycoplasma pneumoniae. *Molecular BioSystems,* 9**,** 1743-1755.

MALMENDAL, A., SØRENSEN, J. G., OVERGAARD, J., HOLMSTRUP, M., NIELSEN, N. C. & LOESCHCKE, V. 2013. Metabolomic analysis of the selection response of Drosophila melanogaster to environmental stress: are there links to gene expression and phenotypic traits? *Naturwissenschaften,* 100**,** 417-427.

MICHOPOULOS, F., LAI, L., GIKA, H., THEODORIDIS, G. & WILSON, I. 2009. UPLC-MS-based analysis of human plasma for metabonomics using solvent precipitation or solid phase extraction. *J Proteome Res,* 8**,** 2114-21.

MITRA, S. 2004. *Sample preparation techniques in analytical chemistry*, John Wiley & Sons.

NAZ, S., VALLEJO, M., GARCIA, A. & BARBAS, C. 2014. Method validation strategies involved in non-targeted metabolomics. *J Chromatogr A,* 1353**,** 99-105.

NICHOLSON, G., RANTALAINEN, M., MAHER, A. D., LI, J. V., MALMODIN, D., AHMADI, K. R., FABER, J. H., HALLGRIMSDOTTIR, I. B., BARRETT, A., TOFT, H., KRESTYANINOVA, M., VIKSNA, J., NEOGI, S. G., DUMAS, M. E., SARKANS, U., THE MOLPAGE, C., SILVERMAN, B. W., DONNELLY, P., NICHOLSON, J. K., ALLEN, M., ZONDERVAN, K. T., LINDON, J. C., SPECTOR, T. D., MCCARTHY, M. I., HOLMES, E., BAUNSGAARD, D. & HOLMES, C. C. 2011. Human metabolic profiles are stably controlled by genetic and environmental variation. *Mol Syst Biol,* 7**,** 525.

NICHOLSON, J. 2005. Metabonomics and global systems biology approaches to molecular diagnostics. *Drug Metabolism Reviews,* 37**,** 10-10.

NICHOLSON, J. K., LINDON, J. C. & HOLMES, E. 1999. 'Metabonomics': understanding the metabolic responses of living systems to pathophysiological stimuli via multivariate statistical analysis of biological NMR spectroscopic data. *Xenobiotica,* 29**,** 1181-9.

NOBAKHT M. GH, B. F., ALIANNEJAD, R., REZAEI-TAVIRANI, M., TAHERI, S. & OSKOUIE, A. A. 2015. The metabolomics of airway diseases, including COPD, asthma and cystic fibrosis. *Biomarkers,* 20**,** 5-16.

PERERA, R. M., MARRIOTT, P. J. & GALBALLY, I. E. 2002. Headspace solid-phase microextraction—comprehensive two-dimensional gas chromatography of wound induced plant volatile organic compound emissions. *Analyst,* 127**,** 1601-1607.

PERRY, R. H., COOKS, R. G. & NOLL, R. J. 2008. Orbitrap mass spectrometry: instrumentation, ion motion and applications. *Mass spectrometry reviews,* 27**,** 661-699.

POHJANEN, E., THYSELL, E., LINDBERG, J., SCHUPPE-KOISTINEN, I., MORITZ, T., JONSSON, P. & ANTTI, H. 2006. Statistical multivariate metabolite profiling for aiding biomarker pattern detection and mechanistic interpretations in GC/MS based metabolomics. *Metabolomics,* 2**,** 257-268.

REO, N. V. 2002. NMR-BASED METABOLOMICS. *Drug and Chemical Toxicology,* 25**,** 375-382.

ROBERTS, L. D., SOUZA, A. L., GERSZTEN, R. E. & CLISH, C. B. 2012. Targeted Metabolomics. *Current Protocols in Molecular Biology,* CHAPTER**,** Unit30.2-Unit30.2.

ROESSNER, U., WAGNER, C., KOPKA, J., TRETHEWEY, R. N. & WILLMITZER, L. 2000a. Simultaneous analysis of metabolites in potato tuber by gas chromatography–mass spectrometry. *The Plant Journal,* 23**,** 131-142.

ROESSNER, U., WAGNER, C., KOPKA, J., TRETHEWEY, R. N. & WILLMITZER, L. 2000b. Technical advance: simultaneous analysis of metabolites in potato tuber by gas chromatography-mass spectrometry. *Plant J,* 23**,** 131-42.

ROSENBERG, E. 2003. The potential of organic (electrospray- and atmospheric pressure chemical ionisation) mass spectrometric techniques coupled to liquid-phase separation for speciation analysis. *J Chromatogr A,* 1000**,** 841-89.

SABIDÓ, E., QUEHENBERGER, O., SHEN, Q., CHANG, C.-Y., SHAH, I., ARMANDO, A. M., ANDREYEV, A., VITEK, O., DENNIS, E. A. & AEBERSOLD, R. 2012. Targeted proteomics of the eicosanoid biosynthetic pathway completes an integrated genomics-proteomics-metabolomics picture of cellular metabolism. *Molecular & Cellular Proteomics,* 11**,** M111. 014746.

SAITO, K. & MATSUDA, F. 2010. Metabolomics for functional genomics, systems biology, and biotechnology. *Annu Rev Plant Biol,* 61**,** 463-89.

SLAYTER, H. S., LAMBLIN, G., TREUT, A. L., GALABERT, C., HOUDRET, N., DEGAND, P. & ROUSSEL, P. 1984. Complex

structure of human bronchial mucus glycoprotein. *European journal of biochemistry,* 142**,** 209-218.

SMEDSGAARD, J. & FRISVAD, J. C. 1996. Using direct electrospray mass spectrometry in taxonomy and secondary metabolite profiling of crude fungal extracts. *Journal of Microbiological Methods,* 25**,** 5-17.

SOGA, T., OHASHI, Y., UENO, Y., NARAOKA, H., TOMITA, M. & NISHIOKA, T. 2003. Quantitative metabolome analysis using capillary electrophoresis mass spectrometry. *Journal of proteome research,* 2**,** 488-494.

SUMNER, L. W., AMBERG, A., BARRETT, D., BEALE, M. H., BEGER, R., DAYKIN, C. A., FAN, T. W. M., FIEHN, O., GOODACRE, R., GRIFFIN, J. L., HANKEMEIER, T., HARDY, N., HARNLY, J., HIGASHI, R., KOPKA, J., LANE, A. N., LINDON, J. C., MARRIOTT, P., NICHOLLS, A. W., REILY, M. D., THADEN, J. J. & VIANT, M. R. 2007. Proposed minimum reporting standards for chemical analysis Chemical Analysis Working Group (CAWG) Metabolomics Standards Initiative (MSI). *Metabolomics : Official journal of the Metabolomic Society,* 3**,** 211-221.

SUMNER, L. W., LEI, Z., NIKOLAU, B. J., SAITO, K., ROESSNER, U. & TRENGOVE, R. 2014. Proposed quantitative and alphanumeric metabolite identification metrics. *Metabolomics,* 10**,** 1047-1049.

TUYTTEN, R., LEMIERE, F., DONGEN, W. V., ESMANS, E. L. & SLEGERS, H. 2002. Short capillary ion-pair high-performance liquid chromatography coupled to electrospray (tandem) mass spectrometry for

the simultaneous analysis of nucleoside mono-, di- and triphosphates. *Rapid Commun Mass Spectrom,* 16**,** 1205-15.

VAN DER GREEF, J., HANKEMEIER, T. & MCBURNEY, R. N. 2006. Metabolomics-based systems biology and personalized medicine: moving towards n = 1 clinical trials? *Pharmacogenomics,* 7**,** 1087-94.

WACKER, H., HARVEY, R., WINESTOCK, C. & PLAUT, G. 1964. the Second Product of the Riboflavin Synthetase Reaction. *The Journal of biological chemistry,* 239.

WANG, X., ZHANG, A., HAN, Y., WANG, P., SUN, H., SONG, G., DONG, T., YUAN, Y., YUAN, X. & ZHANG, M. 2012. Urine metabolomics analysis for biomarker discovery and detection of jaundice syndrome in patients with liver disease. *Molecular & Cellular Proteomics,* 11**,** 370-380.

WANT, E. J., O'MAILLE, G., SMITH, C. A., BRANDON, T. R., URITBOONTHAI, W., QIN, C., TRAUGER, S. A. & SIUZDAK, G. 2006. Solvent-dependent metabolite distribution, clustering, and protein extraction for serum profiling with mass spectrometry. *Analytical Chemistry,* 78**,** 743-752.

WECKWERTH, W., WENZEL, K. & FIEHN, O. 2004. Process for the integrated extraction, identification and quantification of metabolites, proteins and RNA to reveal their co-regulation in biochemical networks. *Proteomics,* 4**,** 78-83.

WEISS, R. H. & KIM, K. 2012. Metabolomics in the study of kidney diseases. *Nat Rev Nephrol,* 8**,** 22-33.

WERNER, E., HEILIER, J.-F., DUCRUIX, C., EZAN, E., JUNOT, C. & TABET, J.-C. 2008. Mass spectrometry for the identification of the discriminating signals from metabolomics: Current status and future trends. *Journal of Chromatography B,* 871**,** 143-163.

WILLIAMSON, L. N. & BARTLETT, M. G. 2007. Quantitative liquid chromatography/time-of-flight mass spectrometry. *Biomed Chromatogr,* 21**,** 567-76.

WISHART, D. S. 2005. Metabolomics: the principles and potential applications to transplantation. *Am J Transplant,* 5**,** 2814-20.

WOODWARD, H., HORSEY, B., BHAVANANDAN, V. & DAVIDSON, E. A. 1982. Isolation, purification, and properties of respiratory mucus glycoproteins. *Biochemistry,* 21**,** 694-701.

WORLEY, B. & POWERS, R. 2016. PCA as a practical indicator of OPLS-DA model reliability. *Current metabolomics,* 4**,** 97-103.

YEGUTKIN, G. G., SAMBURSKI, S. S. & JALKANEN, S. 2003. Soluble purine-converting enzymes circulate in human blood and regulate extracellular ATP level via counteracting pyrophosphatase and phosphotransfer reactions. *Faseb j,* 17**,** 1328-30.

YIN, P. & XU, G. 2013. Metabolomics for tumor marker discovery and identification based on chromatography-mass spectrometry. *Expert Rev Mol Diagn,* 13**,** 339-48.

YIN, P. & XU, G. 2014. Current state-of-the-art of nontargeted metabolomics based on liquid chromatography-mass spectrometry with special emphasis in clinical applications. *J Chromatogr A,* 1374**,** 1-13.

ZELENA, E., DUNN, W. B., BROADHURST, D., FRANCIS-MCINTYRE, S., CARROLL, K. M., BEGLEY, P., O'HAGAN, S., KNOWLES, J. D., HALSALL, A., WILSON, I. D. & KELL, D. B. 2009. Development of a robust and repeatable UPLC-MS method for the long-term metabolomic study of human serum. *Anal Chem,* 81**,** 1357-64.

ZHANG, A., SUN, H., WANG, P., HAN, Y. & WANG, X. 2012. Modern analytical techniques in metabolomics analysis. *Analyst,* 137**,** 293-300.

ZHOU, B., XIAO, J. F., TULI, L. & RESSOM, H. W. 2012. LC-MS-based metabolomics. *Mol Biosyst,* 8**,** 470-81.

Chapter 4 - Development of the MicroSprayer® based aerosol deposition system

4.1. Introduction

Traditionally, the development of new active pharmaceutical ingredients (APIs) from the R&D stages until the production of the final medicine requires that pre-clinical/toxicological studies be performed on animals prior to their evaluation in the clinical situation (humans) (Chapman et al., 2013). The testing of inhaled medicinal products often involves intratracheal administration or forced inhalation followed by tissue or blood analysis for the purpose of obtaining pharmacokinetic data. Unfortunately, it is very difficult to translate the outcomes obtained from respiratory animal tests into humans. This can be mainly attributed to inter-species differences in terms of the mechanisms of drug deposition, absorption and disposition as well as aerosol administration (Hein et al., 2010).

Moreover, scientists are being encouraged to develop alternative *in-vitro* systems to study medicinal efficacy after administration which would circumvent the need for animal involvement, which is in line with investigational ethics and animal rights, and supports the "Three Rs principles"; 1) Replacement, 2) Reduction, and 3) Refinement of animal use (Russell et al., 1959).

4.1.1. *In-vitro* methods for aerosols exposure

Regional particle deposition in the respiratory system can be predicted and simulated with a number of *in vitro* devices which reproduce the lung

organisation such as the Andersen cascade impactor (ACI), the multistage liquid impinger (MSLI), the glass twin stage impinger (TSI), and the next generation impactor (NGI). However, operationally, these systems exclusively depend on inertial impaction. Moreover, they do not assess particle dissolution or drug transportation through the airway epithelium.

Thus, in recent years, significant efforts have been made to modify and amend these different *in-vitro* apparatuses in order to investigate the transport of administrated molecules and/or study particle dissolution following deposition onto epithelial cell layers. In environmental toxicology, test systems that facilitate both absorption and deposition studies are extensively used (Aufderheide et al., 2013, Bitterle et al., 2006, Kim et al., 2013, Tang et al., 2012) and have, for instance, been applied to investigate the effects of cigarette smoke on bronchial cells (Phillips et al., 2005). Nevertheless, these systems are only useful for testing low-dose and long exposure of test air or particles. Therefore, these systems cannot be practically applied to test inhalation aerosols used for therapeutic purposes. Furthermore, the aims and objectives in inhalation testing are focused on inhaled aerosol-cell interaction, quite different from those of toxicological and environmental studies.

The major drawback of current *in-vitro* systems is the lack of a properly designed cell layer – exogenous agent exposure unit. Several pharmaceutical and engineering scientists have modified and amended established *in-vitro* systems to incorporate biological tissues/cell layers into the devices and expose them to the test air flow. The Astra-type liquid impinger is a representative example where the cells are placed under a nozzle conducting the test aerosol (Figure 4.1.1) (Fiegel et al., 2003). It is also called MSLI and comprises five

stages maintained in moist conditions that separate aerosolised particles/droplets according to their size. The cut-off diameters of stages 1, 2, 3 and 4 are 13, 6.8, 3.1 and 1.7 µm, respectively. The fifth stage comprises an integral paper filter to capture the remaining fraction of aerosols less than 1.7 µm.
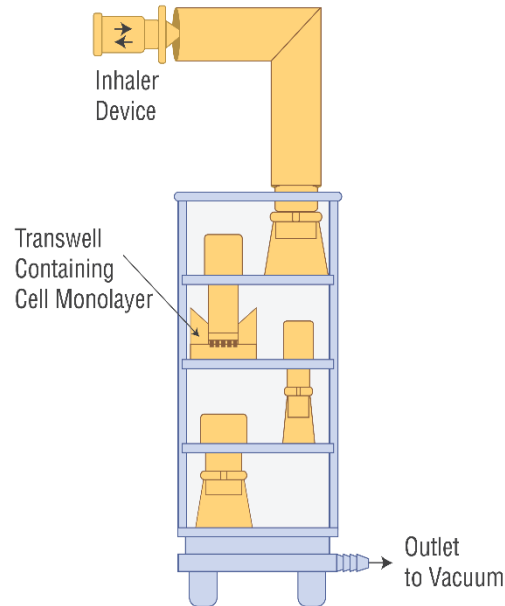
Figure 4.1.1. Schematic representation of the Astra-type liquid impinger. Reproduced from (Fiegel et al., 2003).

This operational setup causes turbulence resulting in low deposition efficacy due to the wall of the Transwell® insert. However, a study has improved this setup by cultivating cells on the underside of the Transwell® inserts, making holes through the selected stage surface of the impinger and then inserting the Transwell® inserts (Figure 4.1.2) (Bur et al., 2009). This approach resulted in better deposition efficacy and significantly reduced turbulence.

Calu3- Cell
Fluid Layer On Stage
Filter Insert
Stainless Steel Capsulae
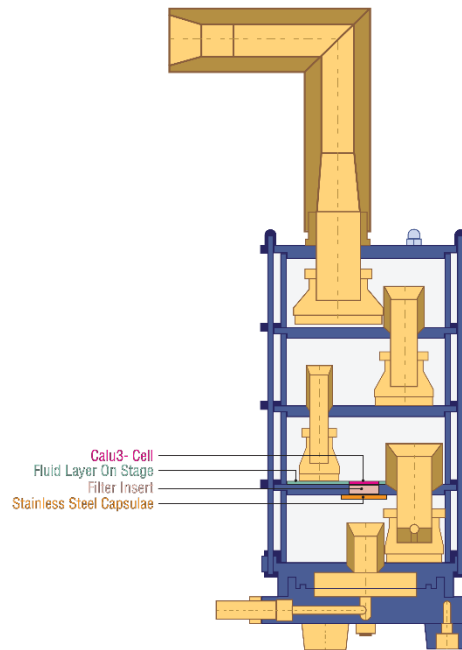
Figure 4.1.2. Schematic representation of modified MSLI. Reproduced from (Bur et al., 2009).

The cascade centripeter (CC), also called a fractionating sampler, consists of three impaction stages (phase 1, 2, and 3) and a backup filter (phase 4). The size separation is acquired through directing the aerosol flow against a nozzle. Larger aerosols will enter the nozzle and deposit on a filter, smaller aerosols will follow the main air flow around the nozzle to the next stage. The last impactor stage will confine aerosols with 1 µm size. CC was adapted to deposit microparticles onto a Transwell® insert covered with cell layers (Figure 4.1.3) (Sadler et al., 2011). In this impactor, the particles are collected at the collection cone entrance.
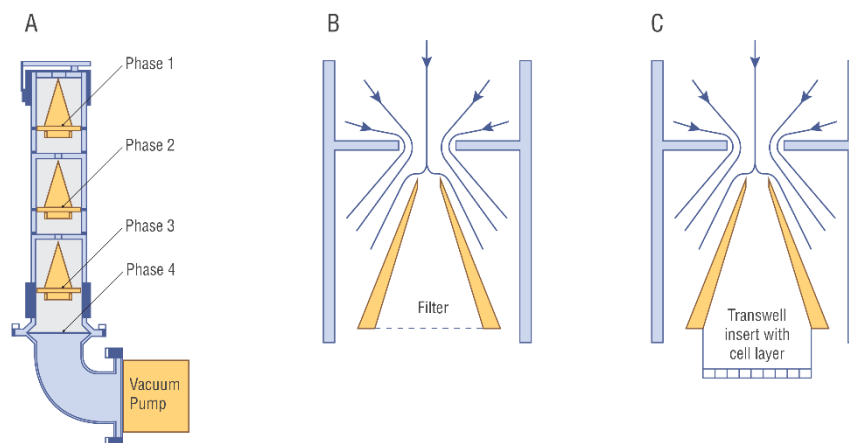
Figure 4.1.3. Schematic representation of the cascade centripeter. A) the cascade centripeter; B) impaction cone and airflow around it; C) application of a Transwell® insert. Reproduced from (Sadler et al., 2011).

The ACI design was also amended to investigate molecule transport across cell layers and study particle dissolution. Each stage of the impactor contains a series of jets or nozzles through which the aerosol is drawn, directing aerosols toward the collection plate surface for that particular stage. Aerosolised particles impact on a particular stage is dependent on its aerodynamic diameter. Aerosols having sufficient inertia impact on that particular stage collection plate, whilst smaller aerosols remain entrained in the air stream and pass to the next stage. The Andersen cascade impactor set-up was modified by removing impaction plate number 4 and placing Transwell® inserts on plate number 5. This was used to deposit a nebulized aerosol of FITC-dextran of different molecular weights on the cell layers (Cooney et al., 2004).
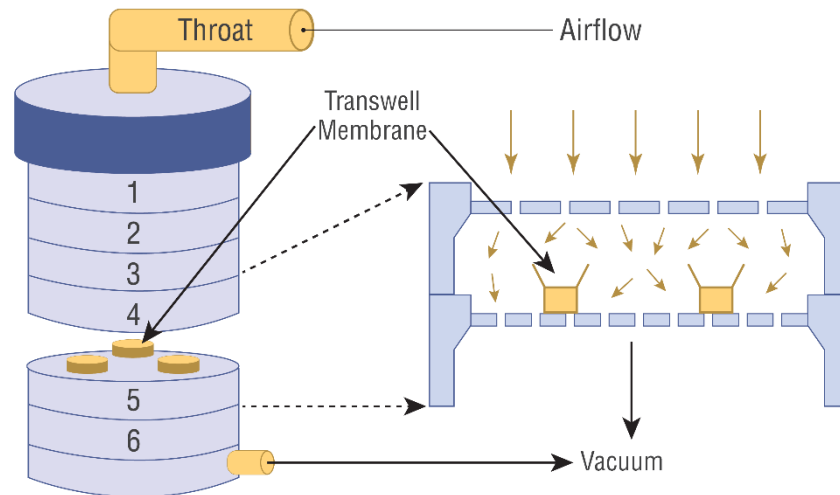
Figure 4.1.4. Schematic representation of a modified ACI where several Transwell® inserts are placed on one collection plate. Reproduced from (Cooney et al., 2004).

This method improved the reproducibility of aerosol deposition since multiple Transwell® inserts could be placed on a specific stage. However, it must be mentioned that this design required a standard Transwell® insert to be placed between two ACI stages with the intermediate impaction plate being omitted. Consequently, this set-up may affect the cut-off diameter of the collecting stage, as observed in the study. Moreover, this modified model increases both the distance between the jet and the plate and the flow through the system. A modified model using Snapwell® instead of Transwell® inserts allowed for a small change in the distance between the nozzle and the plate (Figure 4.1.5) (Haghi et al., 2014).
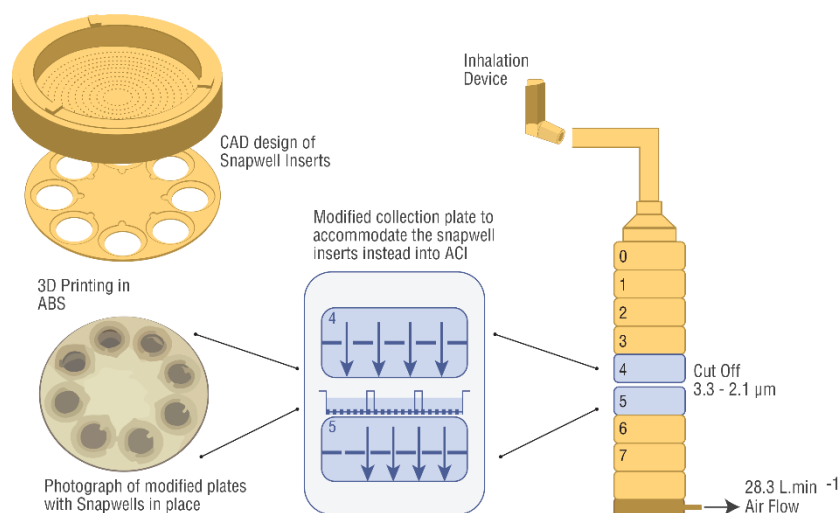
Figure 4.1.5. Schematic representation of an ACI modified to accommodate several Snapwells inserts. Reproduced from (Haghi et al., 2014).

The twin-stage impinger (TSI or glass twin impinger) is a system (Figure 4.1.6) which was developed by GlaxoSmithKline (GSK) for the assessment of nebulizers, MDIs and DPIs. It is relatively easy to assemble and use. It is operated using the principle of liquid impingement that divides the inhaler-emitted dose into respirable and non-respirable fractions. The impaction of non-respirable fraction occurs at the back of the glass throat and the upper impingement chamber. The remaining respirable fraction (dose) that would penetrate the lungs is collected in the lower impingement chamber.

TSI has been adapted to host a Transwell® insert (Grainger et al., 2009, Ong et al., 2012, Saunders et al., 2008). However, its main limitation is that only one Transwell® insert can be exposed to the puff at a time, which leads to variability in the amount of drug deposited between replicates as well as a time-consuming procedure.
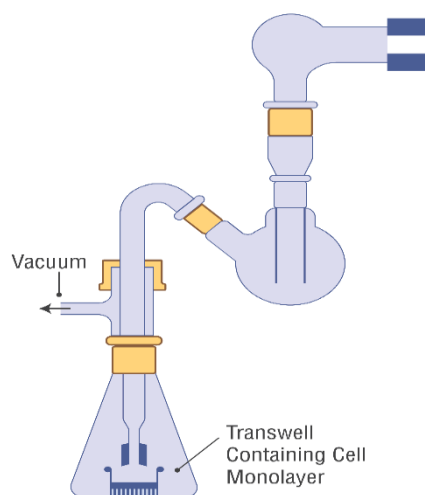
Figure 4.1.6. Schematic representation of a TSI hosting a Transwell® insert. Reproduced from (Grainger et al., 2009).

4.1.2. *In-vitro* applications of the PennCentury MicroSprayer®

Alternative methods for exposing biological layers to a test aerosol include the use of microsprayers or insufflators. The most commonly used models of these types are those produced by PennCentury Inc. (Philadelphia, PA, USA). The PennCentury™ MicroSprayer and dry powder insufflator™ were originally developed for facilitating the intratracheal administration of inhalation therapy formulations in laboratory animals during *in-vivo* studies.

Due to its ease of operation and low cost in comparison to the impactors/impingers described previously, the MicroSprayer® system has been used in some studies to spray aerosols onto biological layers. For instance, a suspension of polystyrene fluorescent particles was sprayed onto A549 cells using a MicroSprayer® (Blank et al., 2006). This study aimed to investigate particle transport across the respiratory epithelium after the cells had been exposed first to air, then to the aerosols in order to realistically mimic a clinical environment. To produce a homogeneous distribution of the particles, the

4. Development of the MicroSprayer® based aerosol deposition system

MicroSprayer® was connected to a tube that was mounted on a rack with vertically moveable clamps (Figure 4.1.7).
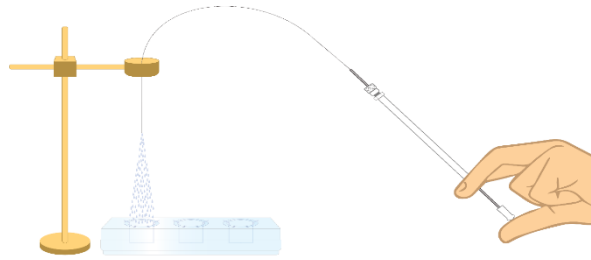
Figure 4.1.7. Penn-Century MicroSprayer® used to deposit particles on A549 cell cultures. Each Transwell® insert was placed under the tip of the MicroSprayer® and separately exposed to the particle sprays.

Fluorescent polystyrene particles were also used in a study that compared the coupled VITROCELL/PARI BOY (VITROCELL Systems GmbH/Pari GmbH) and MicroSprayer® in terms of deposition onto A549 cultures (Fröhlich et al., 2013). The deposition rates of the aerosolized particles were about 700 times higher from the MicroSprayer® than from the VITROCELL/PARI BOY system (Figure 4.1.8).
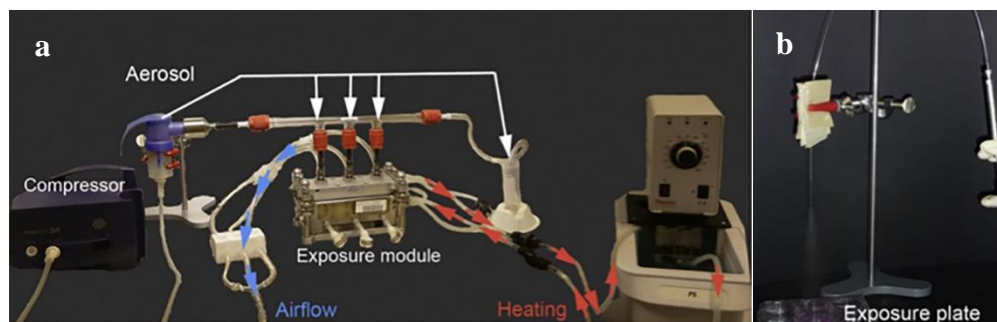
Figure 4.1.8. Exposure systems used to compare the deposition of polystyrene aerosols onto A549 cells cultured on Transwell® inserts. (a): The main components of the VITROCELL/PARI BOY exposure system. (b): a MicroSprayer® aerosolizer connected to a tube attached to a stand with a clamp and whose tip is positioned at a distance of 11 cm above the cells.

4. Development of the MicroSprayer® based aerosol deposition system

Fluorescein and rhodamine 123 were used as model compounds to be sprayed as solutions or dry powders on Calu-3 cultures using a MicroSprayer® and a DP-4 dry powder insufflator®, respectively. Notably, aerosols generated from the fluorescent solutions and sprayed from the MicroSprayer® were deposited with an efficacy of 27 ± 3%. In contrast, the DP-4 dry powder insufflator® that delivered fluorescent micronized powder showed considerable variations in terms of delivery to the cells, with an efficiency of 13.7 ± 4.4%. Variations observed with the DP-4 dry powder insufflator® can be attributed to the properties of the aerosolized powders and are also observed with dry-powder inhalers. For instance, surface texture, particle size, shape, surface energy, contact area, hygroscopy, electrical properties, and relative humidity are known to affect the rate of delivery (Zeng et al., 2003). Therefore, the observed differences between the two systems were expected.

Nevertheless, although the MicroSprayer® is technically less demanding and achieves higher relative depositions compared to the systems mentioned above, its main drawback is that it generates droplets in the 16-22 μm size range which would not be inhaled in a clinical scenario.

4.1.3. Aim

The pulmonary system is a complex system with bifurcations which narrow the airway gradually towards the alveoli. It is now well-known that the generation of prominent fine aerosols is not always sufficient to achieve effective pulmonary delivery. Important questions such as what happens to the aerosols after landing on the epithelium, how molecules are transported across the airway epithelium and how they are degraded remain incompletely answered and need to be addressed. To partly fill such voids in knowledge, this body of work focuses on investigating the interactions of inhaled aerosolised drugs with airway mucus. Hence, in this experimental chapter, we aimed to develop and validate a low-cost, simple deposition system based on the MicroSprayer® to reproducibly deposit spray aerosols onto multiple Transwell® inserts, with a view to exploit it later to deliver fine sprays onto layers of pig tracheal mucus described in the second chapter and eventually improve our understanding of how aerosols interact with the mucus in the lungs.

4.2. Materials and methods

4.2.1. Materials

Pig tracheal mucus was sourced from RB Elloitt and Son Ltd., Stud Farm abattoir, Calow, Chesterfield, Derbyshire, UK. Transwell® inserts (0.4 µm pore size, polyester membrane, 1.2 mm inserts, sterile), 12-well plates, 48-well plates and black 96-well plates were purchased from Corning Inc. – Life Science (NY, USA). Water was supplied by ELGA LabWater, Veolia Water Solutions and Technologies, UK (Distilled and deionised water (18.2 MΩ) was prepared using a Purelab Ultra water purification system). HBSS, sodium chloride and Lucifer yellow CH dipotassium were purchased from Sigma-Aldrich, St. Louis, USA.

4.2.2. Development of the deposition system

The deposition system developed and validated in this experimental chapter used an opaque high-pressure syringe (FMJ-250) (Penn-Century. Inc. Wyndmoor, PA) (Figure 4.2.1 a), which operates at pressures of up to 3000 psi with a maximum volume capacity of 250 µL. Dose volume "spacers" could be incorporated to facilitate precise delivery of 25 or 50 µL sprays. Spacers could also be combined to allow for larger volume dosing when attached to a plunger (Figure 4.2.1 b and c. The high pressure syringe system was connected to a unique air-free atomiser (MicroSprayer® Aerosoliser Model IA-1C) with a 120-degree bend (Penn-Century. Inc. Wyndmoor, PA; Figure 4.2.1 d). Solution pass at the very tip through the aerosol components. The inner diameter of the passageway is approximately 60 µm.

To withdraw the sample using the FMJ-250® syringe and MicroSprayer® Aerosoliser, the aerosoliser was removed from the syringe and the syringe was immersed in the sample solution to be sprayed. The plunger was then pulled back and the syringe was connected to the aerosoliser. To ensure the production of a uniform aerosol spray, the plunger was pushed forward in a sharp, firm, quick motion (Figure 4.2.1 f).

4. Development of the MicroSprayer® based aerosol deposition system
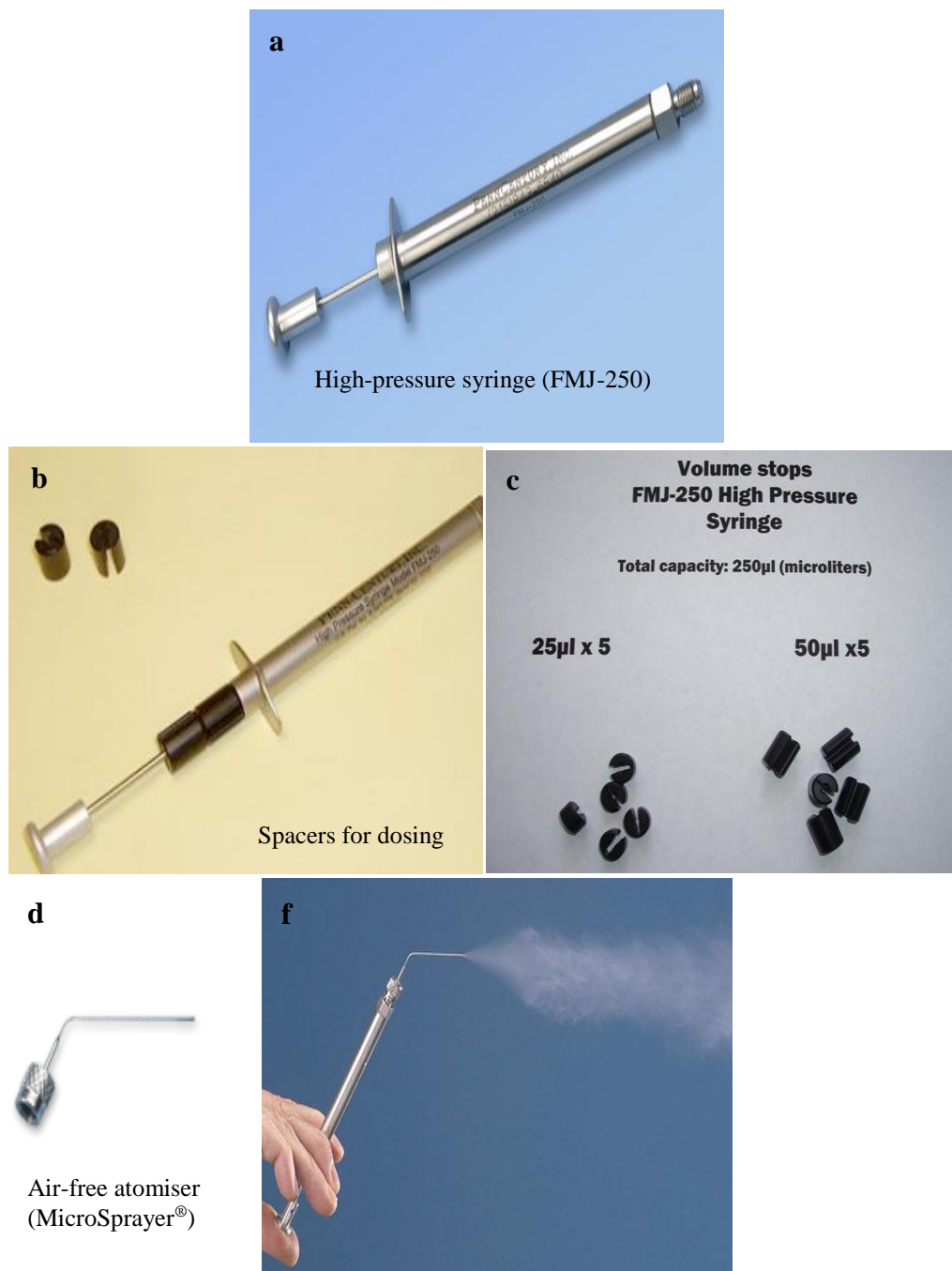
Figure 4.2.1. Penn-Century aerosoliser system (a) high-pressure syringe (FMJ-250) which is made of stainless steel with a white Teflon® plunger tip. (b) and (c) a set of five 50-µl and five 25-µl spacers for dosing the syringe precisely. (d) The MicroSprayer® Aerosoliser (IA-1C) contains tiny components in its tip that help to generate an aerosol from the loaded sample. (f) Aerosols produced by a Penn-Century high-pressure syringe (FMJ-250) connected to a MicroSprayer® Aerosoliser (IA-1C).

4. *Development of the MicroSprayer® based aerosol deposition system*

The Penn-Century aerosoliser system was mounted into a holder glass desiccator to further refine the accuracy of the deposition and protect the operator from aerosol exposure. The vacuum glass desiccator featured an internal flat surface and an external custom-made stand which held the Penn-Century aerosoliser system in position to ensure a consistent spraying point at the centre of the vacuum glass desiccator (Figure 4.2.2).

Figure 4.2.2. The deposition system. (a) The vacuum glass desiccator. (b) The stand which ensures the consistency of the spraying point (c) The final deposition system, assembled as a Penn-Century MicroSprayer® Aerosoliser (IA-1C) connected to the high-pressure syringe (FMJ-250) and held in position by the stand. Sample solutions are sprayed inside the holder glass desiccator system.

4. *Development of the MicroSprayer® based aerosol deposition system*

The neck of the stand was inclined at 60 degrees which ensured that the bent MicroSprayer® was held at a vertical position (90-degree) facing the centre of the internal glass desiccator surface. The distance between the desiccator port entrance and the surface for aerosol deposition was 20.0 cm. Figure 4.2.3 shows the detailed dimensions of the design.
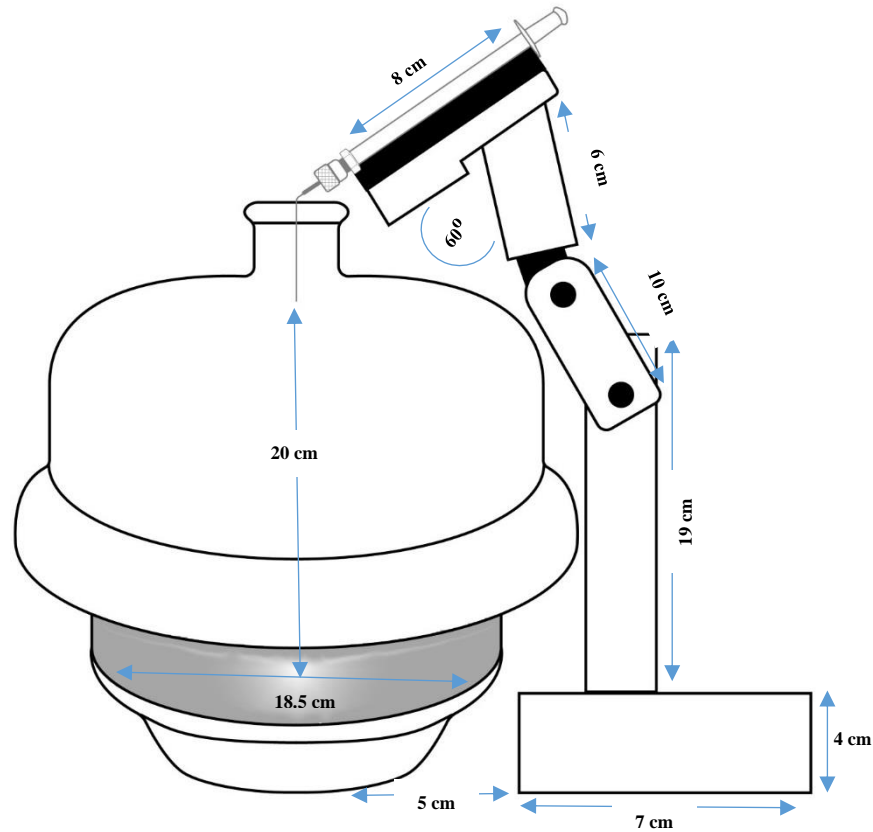
Figure 4.2.3. Schematic representation of the deposition system showing the dimensions of the different components of the assembly.

4.2.3. Validation of the deposition system

The deposition system was designed to be used with mucus covering the Transwell® inserts. Hence, it was necessary to have a reproducible deposition area on the internal glass desiccator. In order to optimise the deposition, three key parameters were varied; 1) the distance between the MicroSprayer® and the

4. Development of the MicroSprayer® based aerosol deposition system

Transwell® inserts, 2) the spray volume, and 3) the geometrical arrangement of the Transwell® inserts. Three distances between the MicroSprayer® nozzle tip and the inserts were tested: 20, 8, and 10 cm. Twenty cm represented the distance separating the sprayer from the internal surface of the glass desiccator. In order to shorten that distance, custom-made platforms were introduced inside the dessicator (Figure 4.2.4).
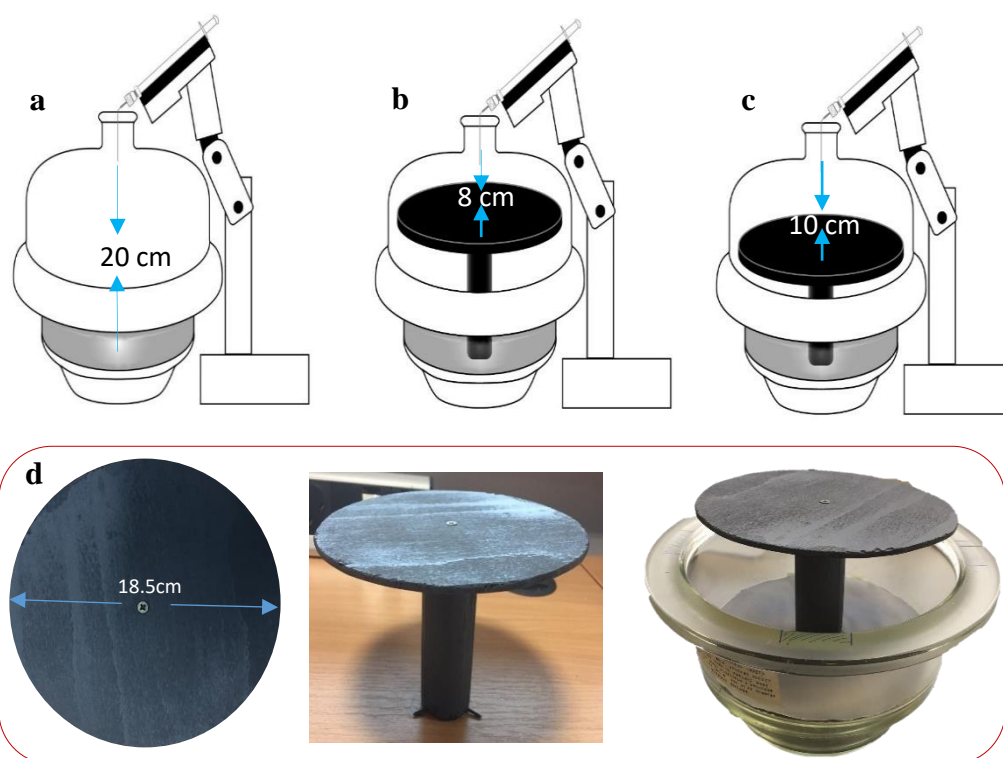
Figure 4.2.4. Representation of the deposition system modified to optimise the distance between the MicroSprayer® and the Transwell® inserts (a-c). (d) shows the internal platforms introduced to the deposition system to adjust the spraying distance.

4.2.3.1. Distance between the MicroSprayer® and the internal surface; 20 cm

The geometrical arrangement for optimising deposition on the internal glass desiccator surface was based on the assumption that if the aerosol droplets were

sprayed uniformly from the desiccator port entrance to the internal glass desiccator surface, this should result in similar droplet distribution across every circle line of the internal glass desiccator surface.

Three different square with increasing surface areas from 20 to 100 cm^2 were plotted and four Transwell® inserts were placed on each of the four square corners; namely, A, B, C, and D, so that they were equidistant from the centre of the dessicator internal surface, as shown in Figure 4.2.5.
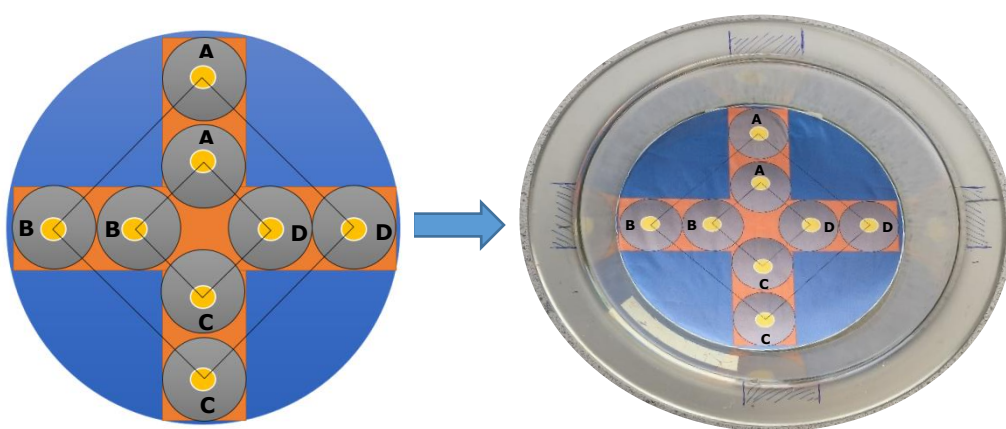
Figure 4.2.5. Schematic representation of the geometrical arrangement of the Transwell® inserts inside the dessicator. The grey circles represent the Petri dishes, and the small yellow circles represent the Transwell® inserts. The distance between each Transwell® insert was 4.5 or 10 cm in the 20 or 100 cm^2 arrangement, respectively.

To enhance the volume that was sprayed in the deposition system, a third geometrical arrangement intermediate in size between the 20 and 100 cm^2 arrangement was tested. To this end, a 50 cm^2 area was introduced onto the internal glass dessicator surface with four corners; namely, A, B, C, and D. The four Transwell® inserts were covered with clean glass coverslips (1.2 cm in diameter, VWR, Germany), to block the semipermeable polyester membrane of the Transwell® inserts. These were placed at the centre of Petri dish lids on the

internal glass desiccator surface. The Transwell® inserts were filled with 100 µL HBSS to collect the fluorescent marker droplets when they were sprayed on the internal glass desiccator surface.

Various volumes (50, 100, and 200 µL) of fluorescent marker (1mM Lucifer yellow) were loaded into the Penn-Century high-pressure syringe (FMJ-250)®, which was connected to the MicroSprayer® Aerosoliser (IA-1C). The solution was then sprayed, as described above. After spraying, 70 µL was collected from each Transwell® insert and transferred to a black 96 well plate (Nunc F96, Scientific Laboratory Supplies, Nottingham, UK). The concentration of Lucifer yellow in each sample was quantified using a Tecan (SPARK 10M) plate-reader and the fluorescence intensity was measured at $\lambda_{em} = 427$ nm and $\lambda_{ex} = 535$ nm. Experiments were performed in triplicate for each volume and each geometrical arrangement (N = 3).

A calibration curve was obtained from the measurement of standard solutions of Lucifer yellow in HBSS at various concentrations, and this was used to quantify the amount of Lucifer yellow from each Transwell® insert (see Appendix I, Figure A-5).

4.2.3.2. Distance between the MicroSprayer® and the internal surface; 8 cm

Using a platform stand within the glass desiccator, as schematically depicted in Figure 4.2.4 (d), the distance between the MicroSprayer® and the internal surface was adjusted to 8 cm, with a view to increasing aerosol deposition.

The geometrical arrangements previously described were again tested (20, 50, and 100 cm^2) Additionally, to enhance the reproducibility of the aerosol

deposition, the Petri dishes (3.9 cm diameter) used as Transwell® insert holders in the previous arrangement were replaced by inverted scintillation vial caps with a diameter of 1.6 cm, so that the Transwell® inserts sat closer to each other (Figure 4.2.6).
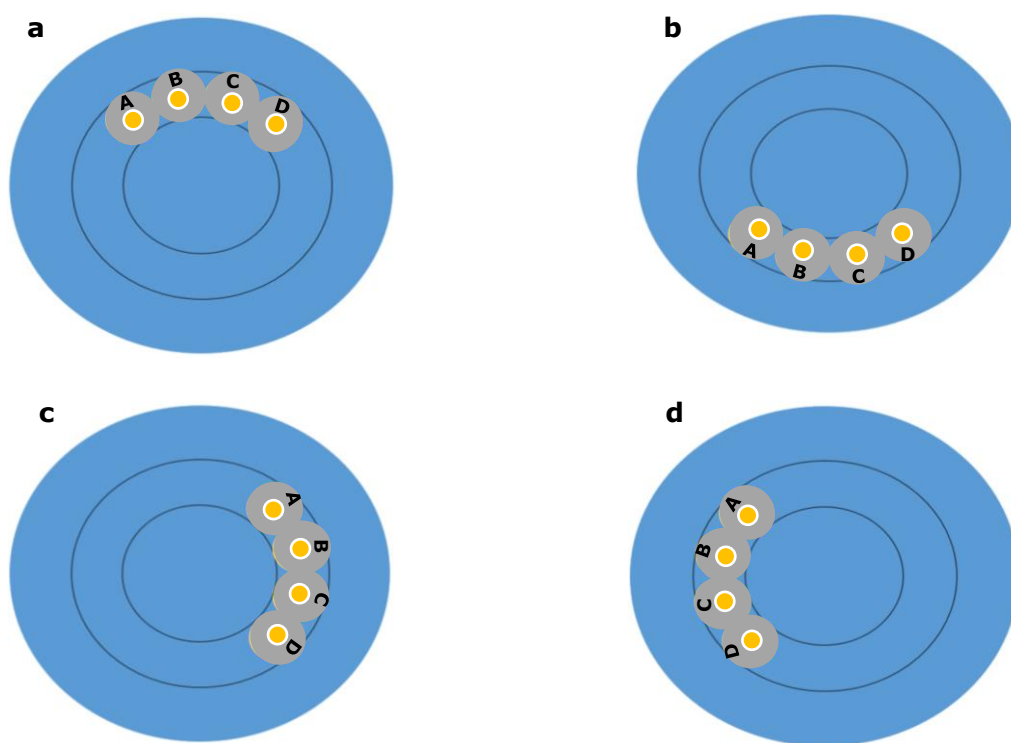
Figure 4.2.6. Geometrical arrangement of Transwell® inserts using scintillation vial caps instead of Petri dishes as insert holders. Up, down, right, and left crescent shapes were used, (a), (b), (c), and (d) respectively. The grey circles represent the scintillation vial caps and the yellow circles represent the Transwell® inserts.

The method described in 4.2.3.1 was again followed except that the spray volume was increased to 150, 200, and 250 µL.

A calibration curve was used to quantify the amount of Lucifer yellow from each Transwell® insert from the standard solutions of Lucifer yellow in HBSS at various concentrations (see Appendix I, Figure A-6).

4.2.3.3. Distance between the MicroSprayer® and the internal surface; 10 cm

A platform with a shorter leg was created, as depicted in Figure 4.2.4 c, to allow for the testing of an additional MicroSprayer® to internal surface distance of 10 cm with a view to further enhancing aerosol deposition.

Similarly to the experiments described above, 20, 100, and 50 cm² geometrical arrangements were used (Figure 4.2.5) and the spraying method described in section 4.2.3.1 was followed but the spray volume was increased to 150, 200, and 250 µL.

The calibration curve used to quantify the amount of Lucifer yellow from each Transwell® insert from the standard solutions of Lucifer yellow in HBSS at various concentrations is presented in Appendix I, Figure A-7.

4.2.4. Optimisation of the sampling time intervals

To estimate the time required for complete permeation of test compounds across mucus layers, two Lucifer yellow permeation experiments were carried out using mucus covered Transwell® inserts, as described previously in chapter 2, placed inside the dessicator according to the 50 cm² geometrical arrangement previously described (A, B, C, and D) (section 4.2.3).

Lucifer yellow (200 µL; 1 mM) was dissolved in HBSS and then sprayed over the mucus covered Transwell® inserts using the MicroSprayer®. The dye that permeated through the mucus covered inserts was collected in a 12-well plate filled with 500 µL/well of HBSS. Samples (200 µL) were withdrawn from the basolateral side after 1, 2, 3, 4, and 5 h in the first experiment and 10, 15, 20, 30,

60, 90, and 120 mins in the second one. Fresh pre-warmed HBSS (200 µL) was used to maintain the initial basolateral volume after each sampling time point. Following the last sampling time point, the mucus layer in the apical chamber was washed using 200 µL of HBSS to measure the remaining amount of Lucifer yellow. This was then added to the cumulative amount recovered in the basolateral chamber to calculate the total amount of Lucifer yellow that had landed on the mucus layer. Then, 100 µL of each withdrawn sample was transferred to a black 96 well plate (Nunc F96, Scientific Laboratory Supplies, Nottingham, UK). The concentration of Lucifer yellow in the samples was measured using a Tecan (SPARK 10M) plate-reader and the fluorescence intensity was measured at $\lambda_{em} = 427$ nm and $\lambda_{ex} = 535$ nm.

The calibration curve used to quantify the amount of Lucifer yellow from the samples produced in each test interval was drawn from standard solutions of Lucifer yellow in HBSS at various concentrations (see Appendix I, Figure A-8). In order to verify the reproducibility of the deposition system, three pig trachea batches were used to prepare mucus layers on Transwell® inserts, four per batch. Mucus covered Transwell® inserts were placed in the 50 cm^2 geometrical arrangement as previously described (A, B, C, and D). Lucifer yellow permeation (1 mM) over time was used as an indicator of the repeatability of the study. The apical to basolateral (A→B) permeability of the fluorescent marker was monitored over two hours according to the methodology described above. The calibration curve used to quantify the amount of Lucifer yellow from the samples produced in each test interval was drawn from standard solutions of Lucifer yellow in HBSS at various concentrations (see Appendix I, Figure A-9).

4.2.5. Statistical analysis

Statistical analysis was performed using GraphPad Prism 6.02. The unpaired *t*-test (multiple comparisons) and ANOVA two-way analysis (with Tukey's multiple comparison test) were used to compare results between two groups or more than two groups, respectively. Differences between experimental groups were considered significant when the p-value was lower than 0.05.

4.3. Results and discussion

4.3.1. Deposition system development and validation

Respiratory mucus is not an impermeable barrier that clears and entraps all inhaled particles. To be clinically effective, an aerosol formulation must be deposited efficiently in the airway and then diffuse across the mucus layer while retaining bioactivity (Rubin, 1996). The testing of aerosols on mucus layers is necessary to investigate the effect of mucus against the penetration of such nebulised aerosol formulations and to elucidate the mechanism by which aerosols permeate through the mucus gel. *In vivo* systems have some limitations that might lead to misleading conclusions against clinical comparisons due to interspecies differences in the morphology and physiology of the respiratory tract. Moreover, a lack of well-established *in vitro* systems and difficulties in working with these models make it difficult to evaluate such aerosols in a way that is truly satisfactory (Fröhlich et al., 2013). Some *in vitro* systems have been developed and have been discussed in detail in section 4.1.1, such as the Minucell, Cultex, and Vitrocell systems (Aufderheide et al., 2013, Bitterle et al., 2006, Fröhlich et al., 2013).

In this work, we evaluated a system based on the Penn-Century® high pressure syringe and aerosoliser needle (FMJ-250®_MicroSprayer®) connected to a holder glass desiccator system, by assessing the deposition of a fluorescent marker (Lucifer yellow) onto Transwell® inserts covered with clean glass coverslips using different spray aerosol volumes.

Three parameters were varied and assessed to optimise the deposition of the aerosols; 1) the distance between the MicroSprayer® and the internal deposition

surface; 2) the spray volume; and 3) the geometrical arrangements of the inserts on the internal surface.

4.3.1.1. Distance between the microSprayer® and the internal surface; 20 cm

Four Transwell® inserts were placed on each corner of virtual 20, 100, and 50 cm² squares centred on the middle of the internal glass desiccator surface. Then, 50, 100 or 200 µL of Lucifer yellow solution was sprayed inside the developed deposition system. Each experiment was performed in triplicate. The resulting deposition patterns are shown in Figure 4.3.1.

4. Development of the MicroSprayer® based aerosol deposition system
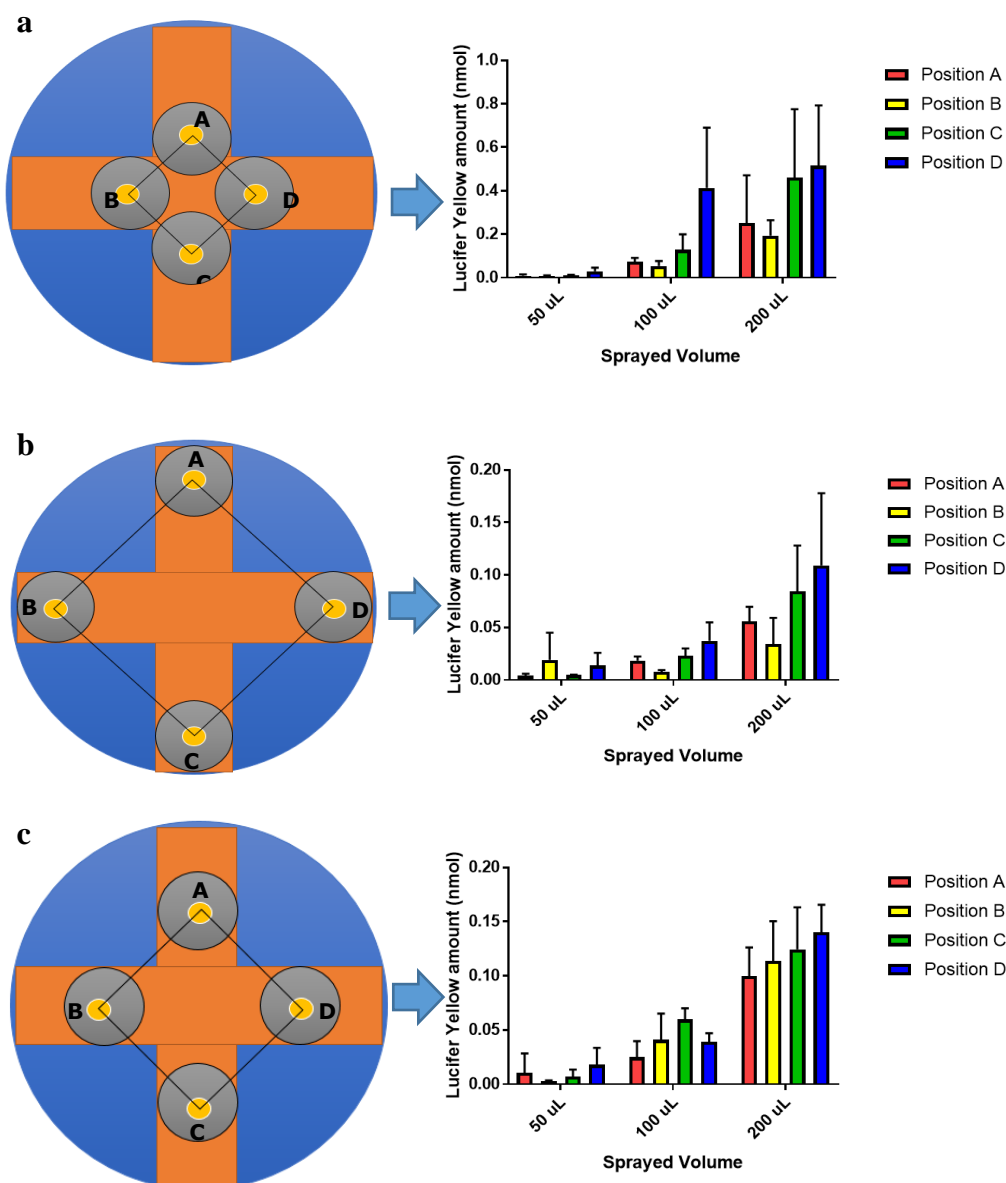
Figure 4.3.1. Lucifer yellow deposition on Transwell® inserts when sprayed from a distance of 20 cm between the MicroSprayer® and the internal deposition surface. Inserts were arranged in a 20, 100, and 50 cm² square, as shown in a, b, and c, respectively. Three volumes (50, 100, and 200 µL) were sprayed inside the developed deposition system. Data are presented as mean ± SD (n = 3).

In Figure 4.3.1 a, as expected, the highest spray volume (200 µL) resulted in the highest relative amount of fluorescent molecules delivered to the Transwell® inserts with an average of 0.36 nmol, corresponding to a volume of 360 nL. In

contrast, the 50 µL spray was shown to be only covering the 0.008 to 0.03 nmol range. Notably, there were high SD for all three spray volume tests when the 20 cm^2 geometrical arrangement was used, which can be attributed to the close distance between the four Transwell® inserts (4.5 cm). Additionally, significant differences between amounts deposited onto the four inserts were also observed with this geometrical arrangement, ($p < 0.05$).

Therefore, a wider geometrical arrangement (100 cm^2) was introduced and placed in the centre of the internal glass desiccator surface. It was hypothesised that this arrangement would lower the CV% that was associated with the 20 cm^2 arrangement (72%), Figure 4.3.1 b.

As can be seen from Figure 4.3.1 b, a lower quantity of Lucifer yellow was deposited on the Transwell® inserts for all three volumes tested compared to the 20 cm^2 geometrical arrangement. This was expected due to the farther distance the spray had to travel from the centre of the internal glass desiccator surface to reach the Transwell® inserts. However, less variability was noted, notably after the 100 µL spray that resulted in no significant difference between the amount of dye collected from the four Transwell® inserts, ($p > 0.05$), in contrast to the differences observed for the 50 and 200 µL applied volumes.

As mentioned above, spraying onto the 20 cm^2 geometrical arrangement resulted in a higher deposited amount than in the 100 cm^2 arrangement, though it was associated with a higher level of variations in the dose deposited. Hence, with a view to finding a balance between high deposition and reproducibility, a third geometrical arrangement with a dimensional square between 20 and 100 cm^2 was introduced.

A 50 cm^2 geometrical arrangement (Figure 4.3.1 c) was therefore evaluated. As shown in the associated graph, the 50 µL spray volume resulted in highly variable deposition quantities between inserts, likely due to the very low amount of dye collected (~ 0.01 nmol in each Transwell® insert). By increasing the spray volume to 100 µL, a noticeable increase in the deposition (up to 0.04 nmol) was observed, though still with high variability between samples. However, a spray volume of 200 µL provided the highest deposition (~ 0.12 nmol in each Transwell® insert) with the lowest average CV% among all the sprayed volumes (27%). No significant differences between positions (A, B, C, and D) were observed with the 200 µL spray volume ($p > 0.05$).

While the geometrical arrangement and sprayed volume had been optimised, a hypothesis was developed that these results may be improved upon if the internal surface was closer to the MicroSprayer® nozzle, which should reduce the quantity of aerosol wasted inside the desiccator and thus an increase amount of aerosol deposited onto Transwell® inserts may be achieved.

4.3.1.2. Distance between the MicroSprayer® and the internal surface; 8 cm

A new internal surface was introduced to the system with a view to improving the deposition accuracy by decreasing the distance between the MicroSprayer® and the Transwell® inserts to 8 cm. The geometric arrangements and the corresponding deposition results for Lucifer yellow are detailed in Figure 4.3.2 and Figure 4.3.3.
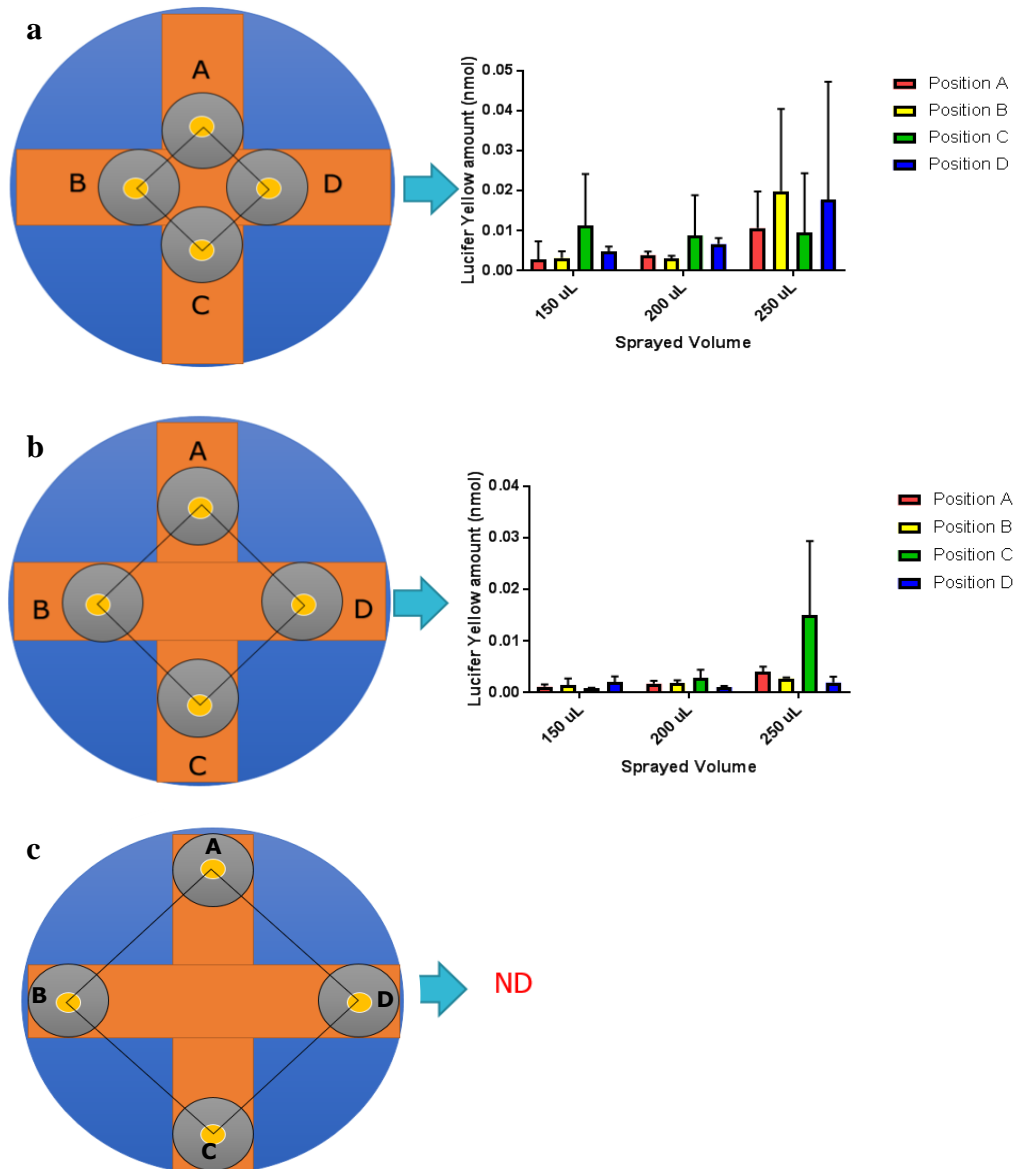
Figure 4.3.2. Lucifer yellow deposition in the Transwell® inserts after the distance between the MicroSprayer® and the internal surface was reduced to 8 cm. Inserts were placed in the 20, 50, and 100 cm² area geometrical arrangements (a, b, and c, respectively). Three Lucifer yellow solution volumes (150, 200, and 250 µL) were sprayed insideg the developed deposition system. ND stands for not detected. Data are presented as mean ± SD (n = 3).
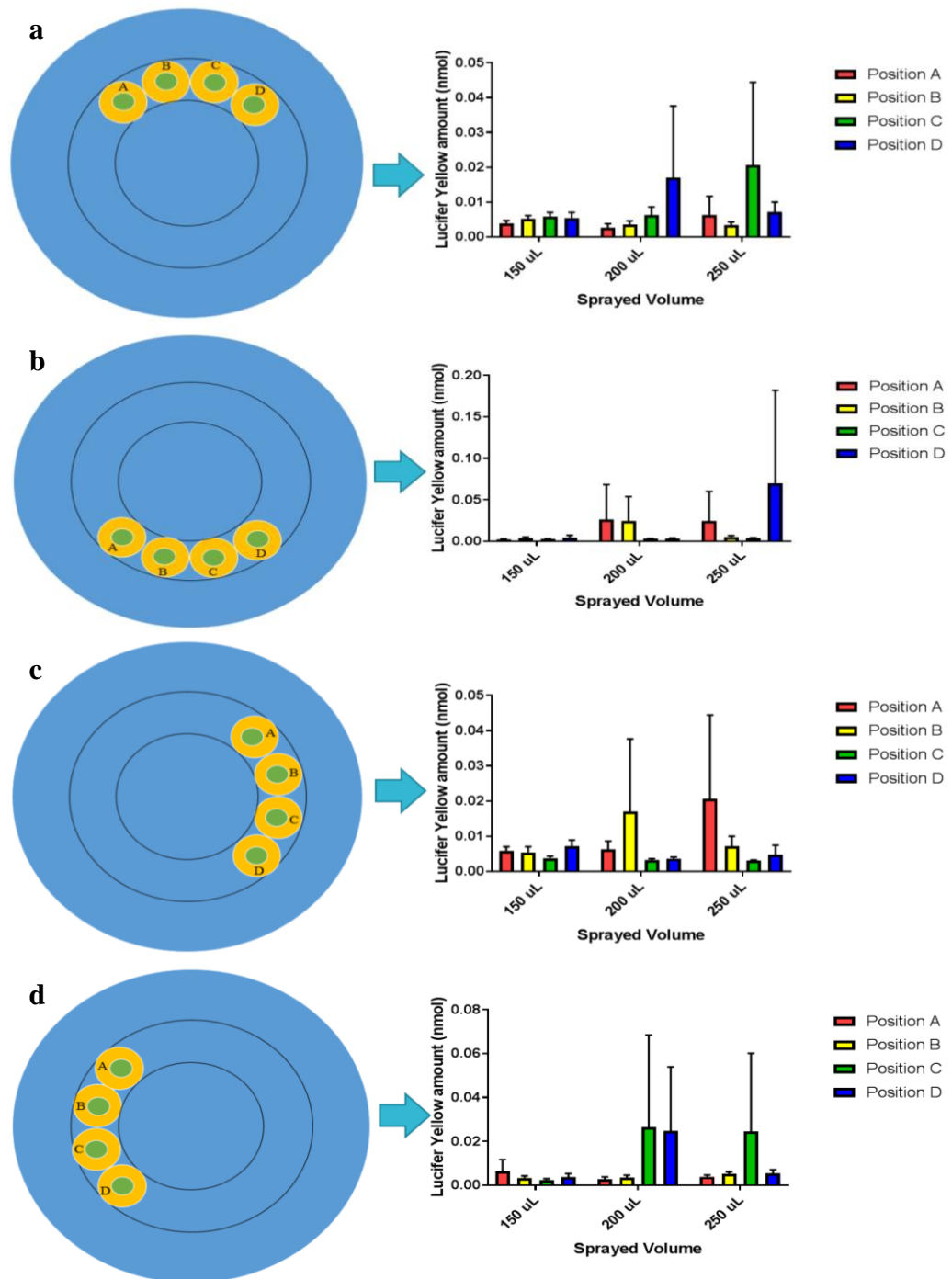
Figure 4.3.3. Lucifer yellow deposition in the Transwell® inserts after the distance between the MicroSprayer® and the internal surface was reduced to 8 cm. Inserts were arranged in an up, down, right, and left crescent shape (a, b, c, and d, respectively). Three volumes (150, 200, and 250 µL) were sprayed inside the developed deposition system. Data are presented as mean ± SD (n = 3).

Notably, the deposition results for all the geometrical arrangements for this 8 cm spraying distance, as detailed in Figure 4.3.2 and Figure 4.3.3, were poor compared to the 20 cm^2 experimental analogues, with < 0.05 nmol Lucifer yellow deposited recorded in all cases for all Transwell® inserts. Significant differences were shown between all test samples placed at A, B, C, and D positions for all geometrical arrangements. These poorer results than we had predicted were attributed to a narrow spray angle which led to a more centralised spray. Hence and in light of these results, a longer distance, between the 8 cm and 20 cm spraying distances was tested.

4.3.1.3.   Distance between the MicroSprayer® and the internal surface; 10 cm

It was hypothesised that an intermediate spraying distance between 8 cm and 20 cm may in fact strike a balance to achieve enhanced and more reproducible deposition. Therefore, a stand that set the spray distance at10 cm was introduced within the desiccator system, as previously described in the methods. The geometrical arrangements tested and the associated results in terms of Lucifer yellow deposition are detailed in Figure 4.3.4.

4. Development of the MicroSprayer® based aerosol deposition system
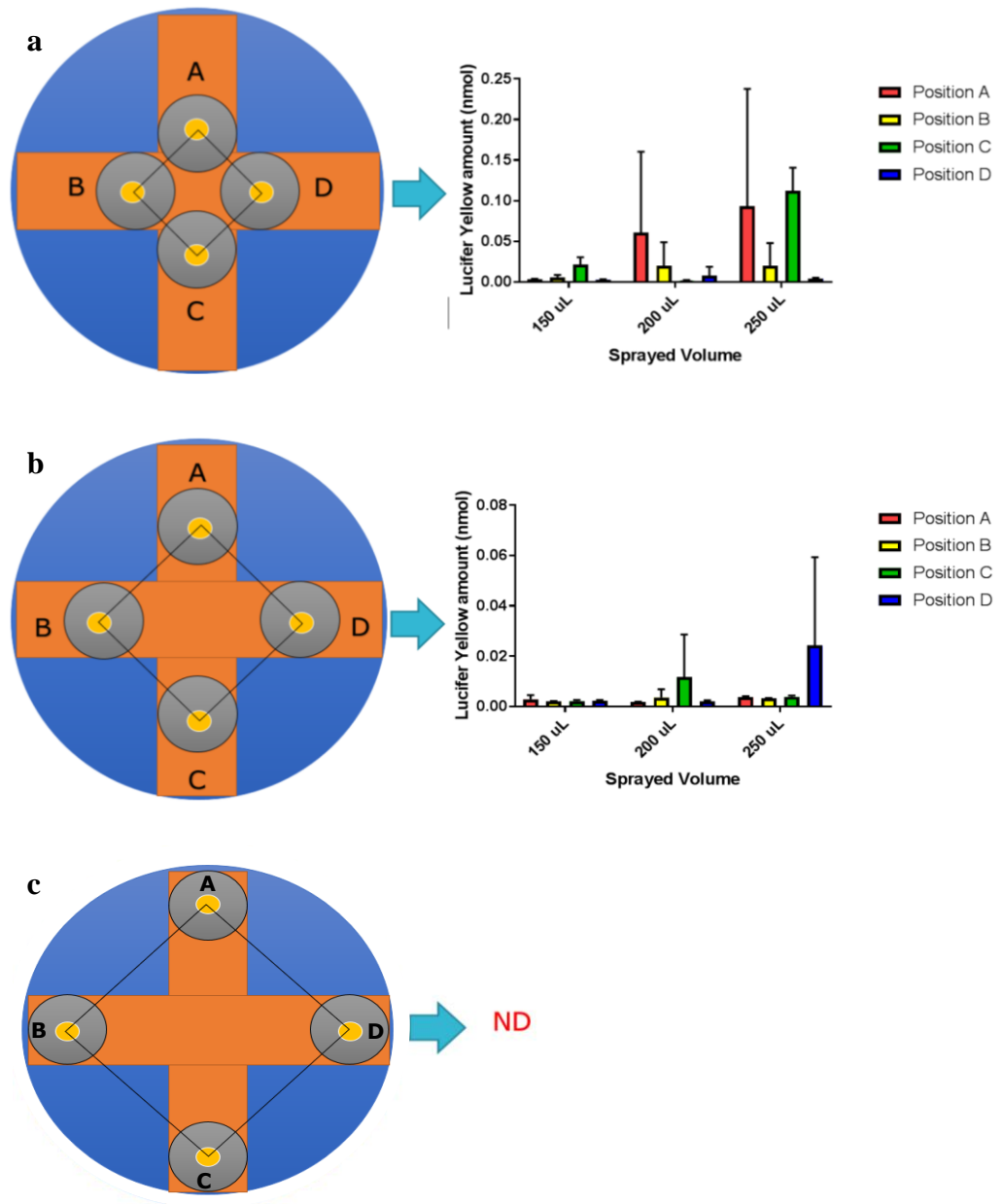
Figure 4.3.4. Lucifer yellow deposition on Transwell® inserts when the distance between the MicroSprayer® and the internal deposition surface was set at 10 cm The inserts were placed in a 20, 50, and 100 cm² area geometrical arrangement (a, b, and c, respectively). Three volumes (150, 200, and 250 µL) were sprayed inside the developed deposition system. ND stands for not detected. Data are presented as mean ± SD (n = 3).

Enhanced deposition of Lucifer yellow was noted in the 10 cm configuration compared to the 8 cm one, with approximately 0.1 nmol deposited on each insert. However, this was lower than obtained previously with a spraying distance of 20 cm. Additionally, significant differences were evident between the A, B, C, and D positions in all geometrical arrangements.

In light of the above results, subsequent experiments were performed setting the distance between the MicroSprayer® and the internal surface at 20 cm, placing the Transwell® inserts in the 50 cm^2 geometrical arrangement and spraying a volume of 200 µL.

4.3.2. Optimisation of sampling time intervals

In order to optimise the sampling intervals when assessing the permeability of aerosolised compounds across the mucus layers, 200 µL of 1 mM Lucifer yellow solution was sprayed onto mucus covered Transwell® inserts and clean Transwell® inserts, and the concentration of Lucifer Yellow that permeated through was initially evaluated over five hours. Figure 4.3.5. illustrates the permeation profile obtained.
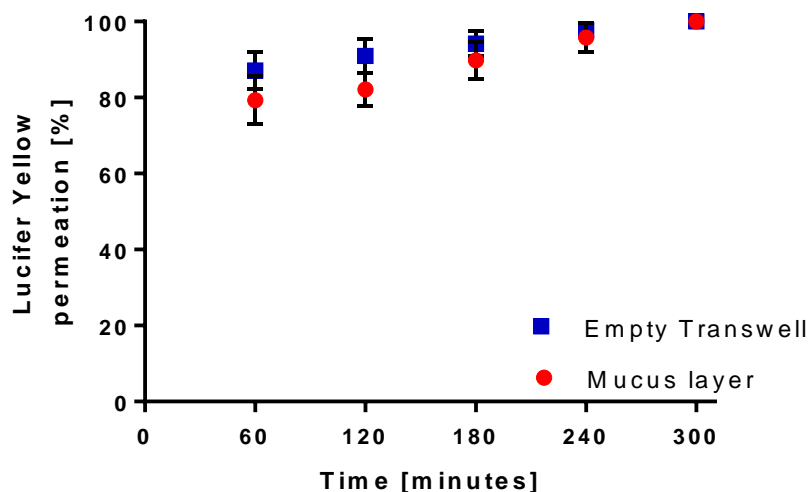
Figure 4.3.5. Apical to basolateral (A→B) permeation profile of Lucifer yellow (1 mM) over a five-hour period after spraying of 200 µL onto the mucus layer and clean Transwell® insert membranes. For collection, 500 µL of HBSS buffer was present in the basal compartment. Data are presented in percentage of the initial dose applied as mean ± SD (n = 4).

An insignificant difference was observed between the two permeation profiles (multiple t-test, $p > 0.05$). As can be observed from Figure 4.3.5, after one hour 79% of the Lucifer yellow had permeated though the mucus layer. No Lucifer yellow remained in the apical side in both experimental set-ups by the end of the five-hour sampling time point. Considering these results, decreasing the duration of the experiment and increasing the frequency of sampling time points was deemed necessary for a more accurate permeation assessment.

To this end, samples were then taken from the basolateral compartments over two hours. Figure 4.3.6 shows the permeation profile obtained.
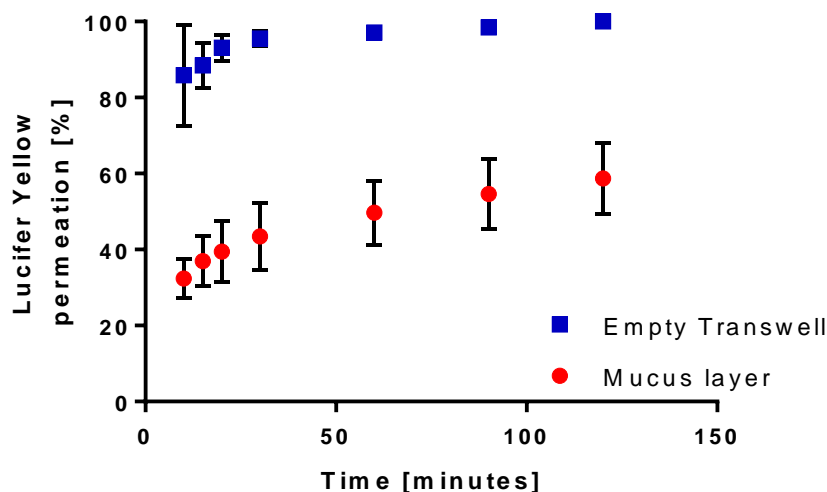
Figure 4.3.6. Apical to basolateral (A→B) permeation profile of Lucifer Yellow (1 mM) over a two-hour period sprayed after a 200 µL solution was sprayed onto the mucus covered Transwell® inserts or clean Transwell® insert membranes. For collection, 500 µL of HBSS buffer was present in the basal compartment. Data are presented in percentage of the initial dose applied as mean ± SD (n = 4).

As shown in Figure 4.3.6, after 10 min, a significantly higher quantity of Lucifer yellow had crossed the bare semipermeable Transwell® (~86%) than the mucus covered inserts, where ~ 68% was confined in the mucus layer inserts at the same time point. After 30 min, the permeation through the bare Transwell® inserts plateaued out, while permeation through the mucus layer increased steadily by about 5% every subsequent 30 min. The permeation profile reveals that mucus acts as a barrier for the fluorescent dye. This study indeed showed that the permeation of Lucifer yellow across the mucus layer was significantly lower than across empty Transwell® inserts (t-test, $p < 0.05$). Hence, a sampling period of two hours was chosen in the subsequent experiments.

4. Development of the MicroSprayer® based aerosol deposition system

A Lucifer yellow solution was then sprayed onto mucus layers obtained from three different batches on three different days to assess the reproducibility of the mucus barrier in the developed deposition system (Figure 4.3.7).
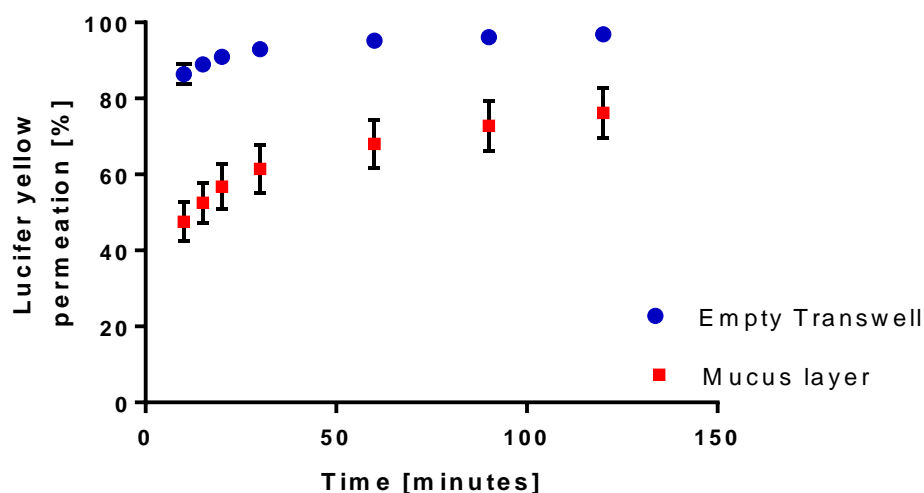
Figure 4.3.7. Apical to basolateral (A→B) permeation profile of Lucifer yellow (1mM) sprayed as 200 µL solution onto the mucus layer and clean Transwell® insert membranes. For collection, 500 µL of HBSS buffer was present in the basal compartment. Data are presented as mean ± SEM (N = 3, n = 4).

Permeation of Lucifer yellow through the clean semipermeable Transwell® inserts reached 90% in the first 30 mins and plateaued afterward. Permeation across the mucus layer revealed a slower diffusional rate, with only 76% of the deposited dose reaching the basolateral compartment at the end of the testing period (120 min). Permeation of Lucifer yellow across the empty Transwell® inserts was significantly higher than across the mucus layer (t-test, $p < 0.05$), indicating the mucus offers a resistance to the diffusion of the dye.

The sampling intervals of this experiment followed those of the study when 50 µL of the same fluorescent marker (Lucifer yellow) was pipetted on the apical side of the mucus layer discussed in section 2.3.3. However, comparing the

results obtained in both sets of experiments, the pipetting methodology resulted in a higher permeation profile compared to the deposition system described in this chapter. This may be due to the high volume that was placed over the mucus layer (50 µL solution vs 12 µL of mucus) which may have diluted the mucus layer and facilitated fast permeation of the dye.

4.4. Conclusion

The aim of the work described in this chapter was to develop and validate a simple and low cost *in-vitro* system to spray aerosols onto a mucus layer.

The developed system was used to investigate factors that influence the permeation of aerosolised compounds across a pulmonary mucus layer.

We successfully assembled and validated a system based on the PennCentury FMJ-250® high pressure syringe and a MicroSprayer® Aerosoliser needle attached to a holder glass desiccator system. Three essential parameters were optimised; 1) the distance between the MicroSprayer® and the internal deposition surface, 2) the aerosol spray volume, and 3) the geometrical arrangement of the mucus layers on the deposition surface. The best and most reproducible results were achieved when 200 µL of the model aerosol were sprayed from a distance of 20 cm onto the Transwell® inserts that were arranged around a 50 cm^2 area.

4.5.   References

AUFDERHEIDE, M., HALTER, B., MÖHLE, N. & HOCHRAINER, D. 2013. The CULTEX RFS: a comprehensive technical approach for the in vitro exposure of airway epithelial cells to the particulate matter at the air-liquid interface. *BioMed research international,* 2013.

BITTERLE, E., KARG, E., SCHROEPPEL, A., KREYLING, W., TIPPE, A., FERRON, G., SCHMID, O., HEYDER, J., MAIER, K. & HOFER, T. 2006. Dose-controlled exposure of A549 epithelial cells at the air–liquid interface to airborne ultrafine carbonaceous particles. *Chemosphere,* 65**,** 1784-1790.

BLANK, F., ROTHEN-RUTISHAUSER, B. M., SCHURCH, S. & GEHR, P. 2006. An optimized in vitro model of the respiratory tract wall to study particle cell interactions. *Journal of aerosol medicine,* 19**,** 392-405.

BUR, M., ROTHEN-RUTISHAUSER, B., HUWER, H. & LEHR, C.-M. 2009. A novel cell compatible impingement system to study in vitro drug absorption from dry powder aerosol formulations. *European Journal of Pharmaceutics and Biopharmaceutics,* 72**,** 350-357.

CHAPMAN, K. L., HOLZGREFE, H., BLACK, L. E., BROWN, M., CHELLMAN, G., COPEMAN, C., COUCH, J., CRETON, S., GEHEN, S. & HOBERMAN, A. 2013. Pharmaceutical toxicology: designing studies to reduce animal use, while maximizing human translation. *Regulatory Toxicology and Pharmacology,* 66**,** 88-103.

COONEY, D., KAZANTSEVA, M. & HICKEY, A. J. 2004. Development of a size-dependent aerosol deposition model utilising human airway

epithelial cells for evaluating aerosol drug delivery. *Alternatives to laboratory animals: ATLA,* 32**,** 581-590.

FIEGEL, J., EHRHARDT, C., SCHAEFER, U. F., LEHR, C.-M. & HANES, J. 2003. Large porous particle impingement on lung epithelial cell monolayers—toward improved particle characterization in the lung. *Pharmaceutical research,* 20**,** 788-796.

FRÖHLICH, E., BONSTINGL, G., HÖFLER, A., MEINDL, C., LEITINGER, G., PIEBER, T. R. & ROBLEGG, E. 2013. Comparison of two in vitro systems to assess cellular effects of nanoparticles-containing aerosols. *Toxicology in vitro,* 27**,** 409-417.

GRAINGER, C., GREENWELL, L., MARTIN, G. & FORBES, B. 2009. The permeability of large molecular weight solutes following particle delivery to air-interfaced cells that model the respiratory mucosa. *European Journal of Pharmaceutics and Biopharmaceutics,* 71**,** 318-324.

HAGHI, M., TRAINI, D. & YOUNG, P. 2014. In vitro cell integrated impactor deposition methodology for the study of aerodynamically relevant size fractions from commercial pressurised metered dose inhalers. *Pharmaceutical research,* 31**,** 1779-1787.

HEIN, S., BUR, M., KOLB, T., MUELLINGER, B., SCHAEFER, U. F. & LEHR, C.-M. 2010. The Pharmaceutical Aerosol Deposition Device on Cell Cultures (PADDOCC) in vitro system: design and experimental protocol. *Alternatives to laboratory animals: ATLA,* 38**,** 285-295.

KIM, J. S., PETERS, T. M., O'SHAUGHNESSY, P. T., ADAMCAKOVA-DODD, A. & THORNE, P. S. 2013. Validation of an in vitro exposure

system for toxicity assessment of air-delivered nanomaterials. *Toxicology in Vitro,* 27**,** 164-173.

ONG, H. X., TRAINI, D., CIPOLLA, D., GONDA, I., BEBAWY, M., AGUS, H. & YOUNG, P. M. 2012. Liposomal nanoparticles control the uptake of ciprofloxacin across respiratory epithelia. *Pharmaceutical research,* 29**,** 3335-3346.

PHILLIPS, J., KLUSS, B., RICHTER, A. & MASSEY, E. 2005. Exposure of bronchial epithelial cells to whole cigarette smoke: assessment of cellular responses. *Altern Lab Anim,* 33**,** 239-48.

RUBIN, B. K. 1996. Therapeutic aerosols and airway secretions. *J Aerosol Med,* 9**,** 123-30.

RUSSELL, W. M. S., BURCH, R. L. & HUME, C. W. 1959. *The principles of humane experimental technique*, Methuen London.

SADLER, R., PRIME, D., BURNELL, P., MARTIN, G. & FORBES, B. 2011. Integrated in vitro experimental modelling of inhaled drug delivery: deposition, dissolution and absorption. *Journal of Drug Delivery Science and Technology,* 21**,** 331-338.

SAUNDERS, M., BUTTINI, F., GRAINGER, C., FORBES, B., ROYALL, P. G., LINCOLN, P. & JONES, S. A. 2008. Characterisation of Particles Emitted from Beclomethasone Dipropionate Solution Metered Dose Inhalers. *19th, Drug delivery to the lungs.* Edinburgh: Aerosol Society.

TANG, T., GMINSKI, R., KÖNCZÖL, M., MODEST, C., ARMBRUSTER, B. & MERSCH-SUNDERMANN, V. 2012. Investigations on cytotoxic and genotoxic effects of laser printer emissions in human epithelial A549

4. *Development of the MicroSprayer® based aerosol deposition system*

lung cells using an air/liquid exposure system. *Environmental and molecular mutagenesis,* 53**,** 125-135.

ZENG, X. M., MARTIN, G. P. & MARRIOTT, C. 2003. *Particulate Interactions in Dry Powder Formulation for Inhalation*, CRC Press.

Chapter 5 - Impact of the mucus barrier on the permeation of various bronchodilators

5.1. Introduction

The two obstructive pulmonary diseases asthma and COPD represent major causes of disability and death globally, and it is estimated that COPD will be the third most common cause of death by 2020 (Agusti, 2018). Although asthma and COPD are both chronic inflammatory respiratory disorders, the most important difference between them might be the nature of the inflammation that occurs. In asthma, eosinophils are mainly the reason behind the inflammation, whereas in COPD neutrophils are involved (Barnes, 2004). This is an important distinction feature as this affects the response to pulmonary agents. For instance, corticosteroids are effective against eosinophilic inflammation but largely ineffective against neutrophilic inflammation. However, bronchodilators are effective in both asthma and COPD and serve to decrease respiratory airway resistance and increase airflow to the lungs when applied. These bronchodilators can be endogenous or may be synthesised as drugs to alleviate the symptoms of obstructive airway disease.

5.1.1. Bronchodilators

Bronchodilators relax constricted airway smooth muscles and when bronchodilator drugs are administered to asthmatic patients, an immediate reversal of airway obstruction is usually observed (Goldie et al., 1991). They also prevent bronchoconstriction and thus can be considered bronchoprotectors.

5. Impact of the mucus barrier on the permeation of various bronchodilators

Current bronchodilators can be divided into three main classes: 1) β_2 adrenergic agonists, 2) muscarinic receptor antagonists and 3) methylxanthines (theophylline).

5.1.1.1. β_2 adrenergic agonists

Inhaled β_2 agonists are generally used to treat asthma due to their high efficacy and minimal side effects, when used correctly (Santus et al., 2015).

The development of β_2 agonists was based on substitutions of norepinephrine and epinephrine catecholamine structures. Within these structures, the catechol ring presents with hydroxyl groups in the 3 and 4 positions of the benzene ring and norepinephrine differs from epinephrine only in the terminal amine group (Figure 5.1.1).
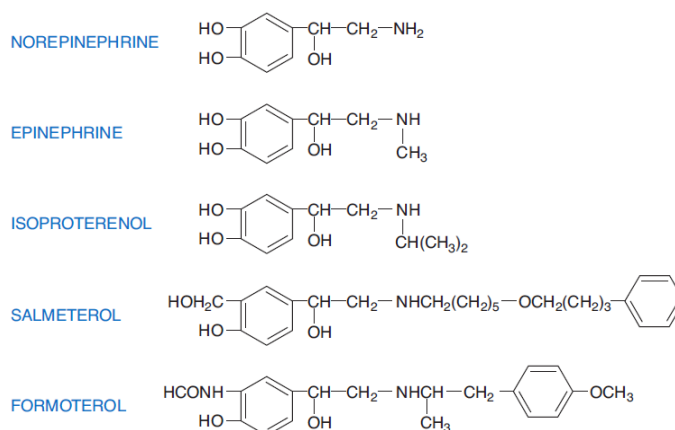
Figure 5.1.1.Representitive adrenergic agonist chemical structures; the molecules were developed from catecholamines through substitution on the catechol nucleus and side chain.

Many β_2 selective agonists are now in clinical use. Although there might be differences in their potency, they show no clinically significant differences with

regard to selectivity (Karampitsakos et al., 2017). Inhaled β_2-selective drugs such as salbutamol sulphate and terbutaline sulphate, which are currently in wide-spread clinical use, have a similar therapeutic duration of action (3–6 h), and are referred to as short-acting β_2 agonists due to their rapid absorbance and the lack of retention in respiratory system (Table 5.1.1). Long-acting β_2 agonists act over a longer duration due to their higher retention in the lung and sustained release where the molecule is constantly partitioned between the membrane and the surrounding aqueous phase depending on their degree of lipophilicity, the cell membrane acting as a reservoir for the long-acting β_2 agonists. For instance, formoterol contains a bulky group in the aliphatic chain and is moderately lipophilic, which ensures that the drug molecules sit in the cell membrane close to the receptor and is slowly released (Brunton, 2014). It is assumed that it is continuously released from the lipid bilayer reservoir into the aqueous phase to interact with the active site of the β_2 receptor, providing bronchodilation and bronchoprotection effects for over 12 h (Montuschi and Ciabattoni, 2015).

Indacaterol is a novel ultra-long-acting β_2 agonist (therapeutic efficacy of 24 h) with a rapid onset of five minutes. Indacaterol was developed by Novartis for the once-daily treatment of asthma and COPD. It is marketed in a salt form (maleate salt) and its molecule is a chiral molecule, but only the R-enantiomer is marketed. It was approved by the European Medicines Agency (EMA) in 2009 under the trade name Onbrez® and by the FDA in 2011 under the trade name Arcapta®.

The ultra-long duration mechanism of indacaterol is still unknown. However, indacaterol is more lipophilic than formoterol and, hence, would bind more strongly to the cell membrane (Montuschi and Ciabattoni, 2015).

5. *Impact of the mucus barrier on the permeation of various bronchodilators*

Table 5.1.1. Pharmacodynamics/kinetics of some β_2 agonists, summarised from UpToDate software

Drug	Onset of action	Duration	Protein binding	Metabolism	Half-life elimination	Excretion
Salbutamol sulphate	-Nebulization/oral inhalation: 0.5 to 2 hours -CFC-propelled salbutamol: 10 minutes (peak plasma concentration) -Inhalation powder: 30 minutes (peak plasma concentration) -HFA inhalers: 25 minutes (peak plasma concentration); ~56 minutes (peak forced expiratory volume in 1 second (FEV$_1$) effect)	-Nebulization/oral inhalation: 2 to 6 hours; -Oral: Immediate release: 4 to 6 hours; extended release tablets: Up to 12 hours	10%	Hepatic to an inactive sulfate	-Inhalation: 3.8 to ~5 hours; -Oral: 3.7 to 5 hours	-Urine (30% as unchanged drug); -feces (<20%)

5. *Impact of the mucus barrier on the permeation of various bronchodilators*

Drug	Onset of action	Duration	Protein binding	Metabolism	Half-life elimination	Excretion
Formoterol	**Powder for inhalation: Within 3 minutes**	**Improvement in FEV$_1$ observed for 12 hours in most patients**	**61% to 64% *in vitro* at higher concentrations than achieved with usual dosing**	**Hepatic via direct glucuronidation and O-demethylation; CYP2D6, CYP2C8/9, CYP2C19, CYP2A6 involved in O-demethylation**	**Powder: ~10-14 hours; Nebulized solution: ~7 hours**	**Children 5-12 years: Urine (7% to 9% as direct glucuronide metabolites, 6% as unchanged drug) Adults: Urine (15% to 18% as direct glucuronide metabolites, 2% to 10% as unchanged drug)**
Indacaterol maleate	**5 minutes**	**24 hours**	**~95%**	**Hepatic; hydroxylated via CYP3A4, CYP2D6, and CYP1A1**	**40-56 hours**	**Feces (>90%; 54% as unchanged drug [after oral**

5. *Impact of the mucus barrier on the permeation of various bronchodilators*

Mechanism of action

β_2 receptors that are occupied by agonists activate the G_s-adenylyl cyclase-cAMP-PKA pathway, which results in phosphorylative events that lead to the relaxation of bronchial smooth muscles (Brunton, 2014).

In vivo, β_2 agonists may cause bronchodilation not only through direct action on airway smooth muscles, but also through indirect inhibition of the release of bronchoconstrictor mediators from inflammatory cells and bronchoconstrictor neurotransmitters from airway nerves (Cuevas, 2018). It has also been reported that β_2 agonists prevent mediator release from isolated human lung mast cells and encourage the secretion of mucus from the submucosal glands, which may improve mucociliary clearance (Sharma et al., 2017).

Clinical Use

Short-acting β_2 agonists are the most widely used and effective bronchodilator inhalers in asthma therapy due to their rapid antagonistic effect against bronchoconstriction compared to other bronchodilators (Santus et al., 2015). They provide rapid relief of asthma symptoms. They can also be administered before exercising in order to prevent exercise-induced bronchoconstriction. (Smith and Parry-Billings, 2003).

Long-acting β_2 agonists, such as formoterol, salmeterol and arformoterol and ultra-long-acting β_2 agonists, such as indacaterol, represent significant therapeutic advances in the treatment of asthma and COPD. Their therapeutic bronchodilation efficacy endures for more than 12 hours and they play a protective antagonistic bronchoconstriction role over the same period (Cazzola et al., 2015). Unlike the short-acting β_2 agonists, long-acting β_2 agonists are only

administered in a daily single dose, which provides a better control of the respiratory condition.

Side Effects

Undesired affects associated with common inhaler use is the extrapulmonary stimulation of β receptors. However, those adverse reactions are commonly observed with oral and intravenous administrations and are notably known to be less common in the case of inhaled administration (Travers et al., 2012).

5.1.1.2. Muscarinic cholinergic antagonists

The treatment of asthma using the chemical antagonism of acetylcholine is not a new idea. Two centuries ago, it was discovered that *Datura stramonium* (jimson weed) and species related to the nightshade family presented an intrinsic therapeutic muscarinic antagonism due to atropine, hyoscyamine and scopolamine components and were smoked by asthmatic patients (Devi et al., 2011). Consequently, atropine, the purified plant alkaloid, was therapeutically introduced for asthma treatment. An intact ester of tropic acid and tropine is crucial for antimuscarinic activity (Figure 5.1.2) (Nair and Hunter, 2004). Notably, due to the atropine's significant adverse reactions, particularly excessive dry mouth, quaternary compounds with less solubility have been developed (e.g.; atropine methylnitrate and ipratropium bromide) (Bonini and Usmani, 2016).
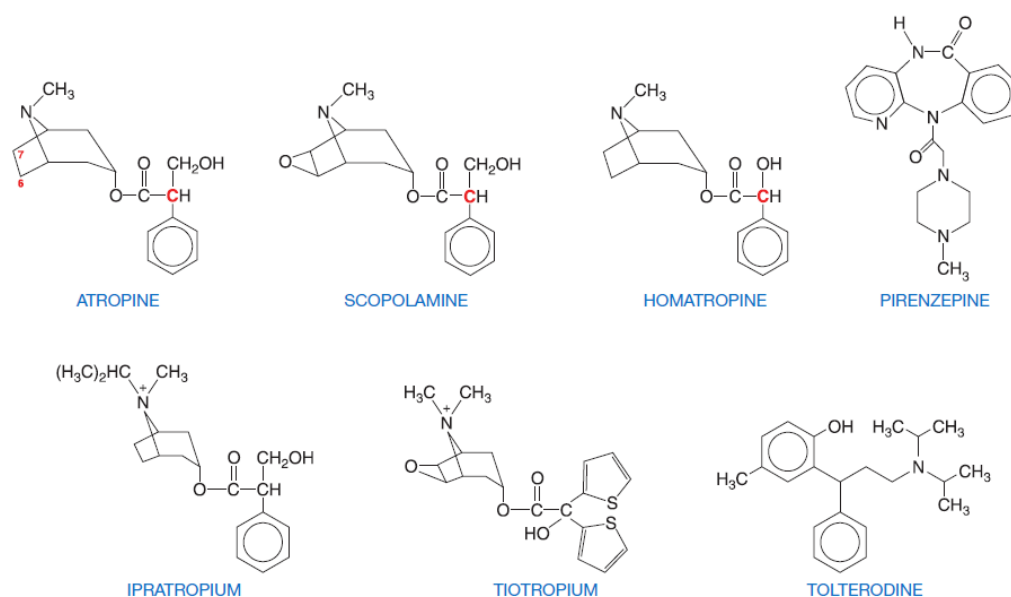
Figure 5.1.2. Belladonna alkaloids structural formulas and semisynthetic and synthetic analogues. The red C indicates an asymmetric carbon atom.

Similarly to β_2 agonists, pulmonary antimuscarinic agents are classified into two groups; short-acting and long-acting. Short-acting muscarinic antagonists include ipratropium and oxitropium. They increase FEV_1 with an onset of action of 10 to 15 minutes and a duration of action of 4 to 6 hours due to their rapid absorption and lack of retention within the respiratory system. Long-acting muscarinic antagonists include tiotropium, glycopyrronium, and aclidinium which are slower in onset than ipratropium, but last longer, with bronchodilation lasting at least 12 hours after aclidinium and more than 24 hours after tiotropium and glycopyrronium due to their bind to the M_3 receptors for a longer period of time (Table 5.1.2).

Mechanism of action

These antimuscarinic agents are considered competitive antagonists of acetylcholine that binds to muscarinic cholinergic receptors. Consequently, these drugs block the endogenous acetylcholine influence at muscarinic

cholinergic receptors, including the direct bronchial smooth muscle constriction mediated via its muscarinic receptor (M_3 receptors) (Prakash et al., 2015). Theoretically, antimuscarinic agents may reduce airway mucus secretion and mucus clearance (Bateman et al., 2009). However, this has not been generally observed in *in vivo* studies, though it has been reported that oxitropium bromide in high doses lowers mucus hypersecretion levels in patients with COPD (Tamaoki et al., 1994).

Clinical Use

Antimuscarinic drugs are less effective than β_2 agonists as bronchodilators and provide a less efficient protection against bronchial challenges in asthmatic patients (Santus et al., 2015). However, these agents are reported to be more effective in the treatment of elderly patients with asthma who suffer from a fixed airway obstruction (Mathur, 2010). Antimuscarinic agents are currently used in bronchodilator polypharmacy approaches, particularly, with β_2 agonists where asthma cannot be controlled with only β_2 agonists (Barnes, 2012). In the treatment of acute severe asthma, nebulised antimuscarinic agents are effective, but less so than β_2 agonists. However, for acute and chronic asthma treatment, an additive antimuscarinic agent and β_2 agonist effect has been observed and therefore should be considered when asthma control is inadequate through nebulised β_2 agonists alone.

5. *Impact of the mucus barrier on the permeation of various bronchodilators*

Table 5.1.2. Pharmacodynamics/Kinetics of some M₃ antagonists, summarised from UpToDate software system

Drug	Onset of action	Duration	Protein binding	Metabolism	Half-life elimination	Excretion
Ipratropium bromide	Within 15 minutes	-pMDI: 2 to 4 hours; -Nebulization solution: 4 to 5 hours, up to 7 to 8 hours in some patients	≤ 9%	Partially metabolized to inactive ester hydrolysis products	2 hours	Urine (50%)
Glycopyrronium bromide	Within 30 minutes	24 hours	38% to 41%	Hepatic	33 to 53 hours	-Urine; -Bile
Tiotropium bromide	Within 30 minutes	24 hours	72%	Hepatic, via CYP2D6 and CYP3A4	-DPI: COPD: ~25 hours -pMDI: Asthma: 44 hours COPD: 25 hours	-Urine (7% of an inhaled dose [DPI]; 18.6% of an inhaled dose (COPD) or 12.8% (asthma) [pMDI])

Side Effects

Inhaled antimuscarinic drugs are usually well tolerated. However, upon cessation, airway responsiveness has shown a small rebound increase, though the clinical data on this is inconsistent (Salahudeen and Nishtala, 2016). Whether discontinuing anticholinergic medicines can improve cognition is uncertain and randomised clinical trials (RCTs) are needed to address these uncertainties; until then, physicians will be reluctant to discontinue these medicines.

Systemic adverse reactions after ipratropium bromide and tiotropium bromide inhalation are rare in normal clinical use due to minimal systemic absorption (Gray, 2017).

Due to mucus secretion stimulation initiated by the administration of muscarinic agonists, it is of concern that antimuscarinics may lower mucus secretion levels and lead to more viscous mucus (Agusti, 2005). Nevertheless, even high doses of ipratropium bromide have been reported to have no noticeable effect on mucociliary clearance in either normal patients or in subjects with lung disease. Indeed, an investigation based on a randomised, double-blind, controlled trial could not find any evidence of pulmonary mucus clearance retardation in COPD subjects who had been treated with tiotropium bromide (Hasani et al., 2004).

5.1.1.3. Methylxanthines

Methylxanthines, particularly theophylline, which are structurally related to caffeine, have been used since the 1930's in asthma therapy. Indeed, theophylline is still extensively used in developing countries due to its low economic burden. Its rapid onset of action and long treatment duration time have made it a viable therapy against asthma (Gray, 2017). Nevertheless, the

associated side-effects and relative low efficacy of theophylline have led to its minimal usage in many countries due to the considered superior option to select inhaled $\beta 2$ agonists, which are known to be far more effective than methylxanthines (Barnes, 2013). However, theophylline still remains a very useful drug for the treatment of severe asthmatic and COPD patients (Barnes, 2013).

5.1.2. Target-sites of bronchodilator aerosols in the lungs

If a suboptimal dose of a bronchodilator aerosol is delivered to a part of the lung devoid of the targeted receptor, the therapy's effectiveness may be compromised. β_2 and M_3 receptors are not distributed throughout the lung in a uniform fashion.

Autoradiographic investigations have demonstrated β_2 receptors are present in high density in the airway tract epithelium from the bronchi to the terminal bronchioles. Lower densities of β_2 receptors have been found in airway smooth muscle in the bronchioles than in the bronchi (Carstairs et al., 1985). Nevertheless, more than 90% of all β receptors are present in the alveolar wall, an area with no airway smooth muscle and whose functional significance is unidentified.

Another autoradiographic investigation has shown M_3 receptors in high density within airway submucosal glands, with a moderate density located in airway smooth muscles, bronchi and alveolar walls (Mak and Barnes, 1990).

Therefore, β_2 receptors and M_3 receptors are located in different pulmonary cell types including in the luminal epithelium cells and not only the airway smooth muscle cells. Consequently, other cell types might be involved in the therapeutic

5. *Impact of the mucus barrier on the permeation of various bronchodilators*

activity of the current bronchodilators. Nevertheless, the bronchodilator effect is likely to occur principally in the upper airways. Those are coated with a mucus layer that could act as a major barrier to the aerosolised drug journey towards the targeted receptors.

5.1.3. Aim

The effects of direct interactions between the mucus and inhaled bronchodilators have been largely ignored so far. With this in mind, the aim of the study described in this chapter was to investigate the impact of pulmonary mucus on the diffusion of ipratropium bromide, glycopyrronium bromide, salbutamol sulphate, formoterol, and indacaterol maleate, using the in vitro approaches described in Chapters 2 & 4. The investigated drugs were selected to cover a range of lipophilicity and present different physicochemical properties.

Ipratropium bromide and glycopyrronium bromide are quaternary ammonium compounds with permanent positive charge while salbutamol sulphate and formoterol possess a secondary aliphatic amine with high pKa values; 10.3 and 9.8, respectively. Indacaterol maleate exists in solution at physiologic pH as a zwitterionic molecule. Hence, all molecules were expected to bind electrostatically with the negatively charged mucin fibers.

5.2. Materials and methods

5.2.1. Materials

Pig tracheae were sourced as described in chapter 2. Transwell® inserts of two different membrane types; polyester (0.4 and 3.0 μm pore sizes and 1.2 mm inserts, sterile), and polycarbonate (3.0 μm pore size and 1.2 mm inserts, sterile), 12-well plates, and black 96-well plates were purchased from Corning Inc. – Life Science, New York, USA. Water was supplied by ELGA LabWater, Veolia Water Solutions and Technologies, UK (Distilled and deionised water (18.2 MΩ) was prepared using a Purelab Ultra water purification system). Hank's balanced salt solution (HBSS), sodium chloride, dimethyl sulfoxide (DMSO) $\geq$ 99%, fluorescein isothiocyanate isomer I (FITC), salbutamol sulphate, formoterol, ipratropium bromide, and glycopyrronium bromide were purchased from Sigma-Aldrich, St. Louis, USA. Indacaterol maleate was purchased from MedChemExpress (MEC), New Jersey, USA.

5.2.2. Impact of the mucus barrier on the permeation of various bronchodilators

The permeation of five drugs (the M_3 antagonists ipratropium bromide and glycopyrronium bromide, and β_2 the agonists; salbutamol sulphate, formoterol, and indacaterol maleate, Table 5.2.1.) across mucus layer coated polyester Transwell® inserts with 0.4 μm pores was initially measured.

Furthermore, indacaterol maleate permeation measurements across mucus layers spread onto Transwell® polyester or polycarbonate membranes with a pore size of 3.0 µm were undertaken to assess the effect of the substrate pore size and chemical composition of the membrane on drug diffusion. The four

other drugs were then tested after aerosolization onto mucus coated polyester Transwell® inserts with 3.0 µm pores.

Mucus layers were prepared as described in section 2.2.2. Transwell® inserts coated with mucus were transferred the following day to position A, B, C and D of the deposition chamber in the deposition system described in chapter 4. Ipratropium bromide, glycopyrronium bromide and salbutamol sulphate were dissolved in HBSS to be sprayed at a concentration of 10 mM, formoterol and indacaterol maleate were dissolved in HBSS (10% of DMSO) to be sprayed at a concentration of 1 mM.
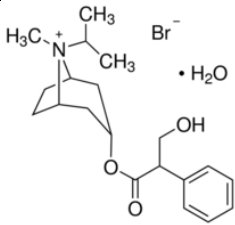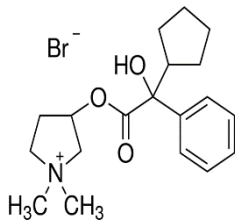
The PennCentury™ MicroSprayer® was loaded with the drug of interest, and 200 µL of the solutions were aerosolised onto the mucus layers from a distance of 20 cm. The same validated protocol as described in section 4.2.3. was followed to conduct the drug permeation study where 500 µL of either HBSS or HBSS-10% DMSO were placed in the basolateral chamber, depending on the solubility of the investigated compound.

Two hours after aerosol application, the mucus layers were washed with 200 µL of HBSS or HBSS-10% DMSO, depending on the drug solvent used and removed from the insert for analysis.
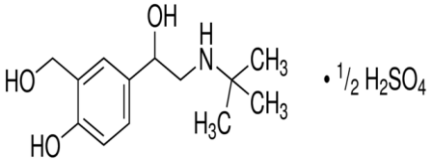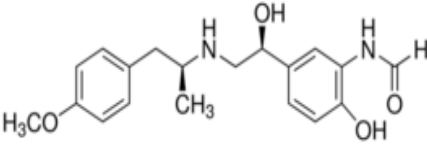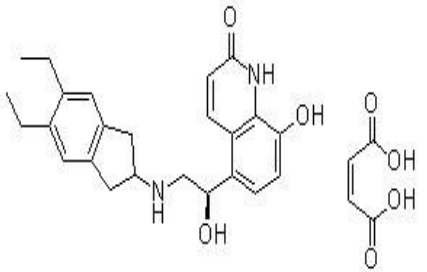
The suspension obtained from the washed apical side was vortexed for one minute and then centrifuged for five minutes at 14,000 rpm. The collected supernatant was used for quantification of the residual non-permeated drug.

5. *Impact of the mucus barrier on the permeation of various bronchodilators*

Table 5.2.1. Characteristics of the various bronchodilators used in the mucus permeation studies.

Name	Structure	Form	logP	Pharmacological Classification	Mass Spectra Specifications
Ipratropium Bromide		Base in a salt form	-1.8	M_3 antagonist	MS/MS: 332.16>165.89 Cone Voltage: 40 Collision Energy: 28
Glycopyrronium Bromide		Base in a salt form	-1.4	M_3 antagonist	MS/MS: 318.09>115.84 Cone Voltage: 34 Collision Energy: 28

5. *Impact of the mucus barrier on the permeation of various bronchodilators*

Name	Structure	Form	logP	Pharmacological Classification	Mass Spectra Specifications
Salbutamol Sulphate		Base in a salt form	1.4	B$_2$ agonist	MS/MS: 240.1>148.1 Cone Voltage: 35 Collision Energy: 20
Formoterol		Free base	2.2	B$_2$ agonist	345>148.9 Cone Voltage: 45 Collision Energy: 18
Indacaterol Maleate		Base in a salt form	4.05	B$_2$ agonist	393>173 Cone Voltage: 35 Collision Energy: 30

A similar method was used to examine the permeation of each investigated bronchodilator across empty Transwell® inserts.

All samples were processed for LC-MS/MS analysis following the protocols described in section 5.2.4. where four replicates were carried out for each drug studied.

5.2.3. Influence of DMSO on the permeation of a fluorescent dye across the mucus layers

In order to assess if high concentrations of DMSO affected the barrier properties of mucus, the permeation of FITC across the mucus layers was studied in presence of different concentrations of DMSO in HBSS (0.1, 1.0, and 10%). Fifty µL of 10 µM FITC and these different concentrations of DMSO in HBSS was pipetted onto the donor compartment. A volume of 500 µL of HBSS containing 0.1, 1.0, or 10% of DMSO (was added to the basolateral compartment. To this end, the optimised protocol described in section 2.2.7. was followed.

The calibration curve used to quantify the amount of FITC with different concentrations of DMSO in HBSS was drawn from standard solutions of FITC at various concentrations (see Appendix, Figure A-15).

5.2.4. LC-MS/MS methodology

Samples obtained from the mucus layer drug permeation experiments were analysed for drug content by LCMS-MS.

5. Impact of the mucus barrier on the permeation of various bronchodilators

The LC system was comprised of an Agilent Hewlett Packard series 1100 coupled with a Micromass Quattro Ultima Pt mass spectrometer (Waters, Milford, USA) equipped with an electrospray ion source operated in positive mode. An ACE3 C18 (3μm, 150 mm x i.d. 2.1 mm) column fitted with a C18 guard cartridge was used for all analysis.

Ipratropium bromide, glycopyrronium bromide, formoterol and indacaterol maleate were processed similarly. All samples were diluted 1:3 with cold MeOH containing 5 nM of the internal standard (glycopyrronium bromide, Ipratropium bromide, indacaterol maleate, and formoterol, respectively) before being housed in a freezer (-20 ºC) overnight. The following day, the samples were vortexed for one minute and centrifuged at 5,000 rpm for five minutes at 4° C. The supernatant was diluted (1:1) with 0.1% formic acid in water, transferred to LC-MS vials and stored in a refrigerator until analysis.

On the day of the LC-MS/MS analysis, a 10 μL volume was injected into the LC-MS system. Samples were run at 0.2 mL/min in gradient phases, where phase A was MilliQ water containing 0.1% formic acid and phase B was MeOH (HPLC grade) containing 0.1% formic acid. The gradient started with 45% (B) and increased to 90% over two minutes then decreased back to 45% for 3.5 minutes until the end of the run time (8.5 minutes). The LC-MS/MS parameters that are described in Table 5.2.1 were followed. In addition, a source temperature of 125 °C, a desolvation temperature of 350°C and a collision energy of 20 kV were operationally applied.

Salbutamol sulphate samples were diluted 1:1 with MeOH and then vortexed for a minute and centrifuged at 5,000 rpm for five minutes at 4 °C. The supernatant was diluted 1:1 with phase A which was an aqueous solution containing 0.1%

v/v formic acid, ammonium formate 20 mM (pH 3.8). Then, 50 µL of the resulting solution was injected into the LC-MS/MS system for quantification. Samples were run at 0.2 mL min^{-1} isocratically using a mixture of phase A and MeOH (HPLC grade, phase B; 50:50) as the mobile phase. The MS/MS parameters are detailed in Table 5.2.1, the source temperature was set to 125 °C, while the desolvation temperature was fixed at 350 °C.

The calibration curve used to quantify the amount of ipratropium bromide, glycopyrronium bromide, and salbutamol sulphate in the samples using polyester Transwell® inserts with 0.4 µm pores was drawn from standard solutions of each drug in HBSSs (see Appendix I, Figure A-10 – A-12). Formoterol and indacaterol maleate curves were obtained from standard solutions of each drug in HBSS with 10% DMSO (see Appendix I, Figure A-13 and A-14 and A-16 – A-20).

5.2.5. Statistical analysis

Statistical analysis was performed using GraphPad Prism 6.02. Unpaired t-test (multiple comparisons) to compare two groups and ANOVA one-way and two-way analysis (with Tukey's multiple comparison test) were used to compare more than two groups. Differences between experimental groups were considered significant when the p-value was lower than 0.05.

5.3. Results and discussion

Mucus is a central feature of respiratory defences and fulfils its protective role through various mechanisms. Despite acting as a barrier to the penetration of foreign molecules, the mucus layer also enables the diffusion of other molecules from the surface towards the epithelial cell layer (Round et al., 2002). Previous studies suggested that the extent and rate of permeation across mucus depends on the physiochemical properties of the drugs to which it is exposed (Khanvilkar et al., 2001).

With this in mind, we investigated the penetration of five aerosolised drugs with different physicochemical properties across the mucus layers.

Notably, and to our knowledge, this is the first attempt to study inhaled drug-mucus interactions following drug aerosolisation at the surface of a mucus layer *in-vitro.*

5.3.1. Impact of the mucus barrier on the permeation of various bronchodilators using Transwell® inserts with a 0.4 μm pore size

The ability of the test bronchodilators to permeate across mucus layer was first investigated using mucus layers formed on 0.4 μM pore size polyester inserts, Figure 5.3.1.
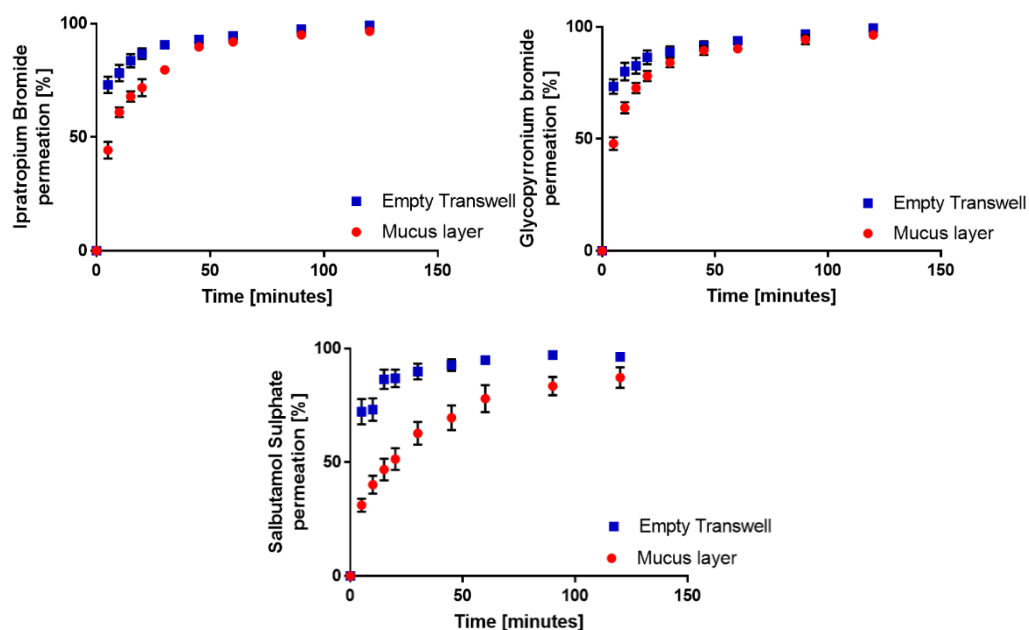
Figure 5.3.1. Apical to basolateral (A→B) permeation profile of ipratropium bromide, glycopyrronium bromide, and salbutamol sulphate across mucus layers mounted on polyester 0.4 μm pore size Transwell® and corresponding empty inserts. Drugs were dissolved in HBSS (10 mM). Drugs were sprayed as a 200 μL bolus at a distance of 20 cm. Data are presented as mean ± SEM (N = 4, n = 4).

The above figure reveals a significant difference in the permeation of ipratropium bromide and glycopyrronium bromide across the mucus layer and empty Transwell® inserts within the first 30 minutes ($p < 0.05$). A permeation value of 44% ± 4% (SEM) and 48% ± 3% (SEM) of the applied dose of ipratropium bromide and glycopyrronium bromide, respectively, had crossed the mucus layer within the first five minutes before the permeation profile of both drugs reached a plateau after 45 minutes, when a plateau was similarly observed for their diffusion across the empty Transwell® inserts. However, no significant differences in the permeation profile of both drugs were observed ($p < 0.05$). This trend can be attributed to the fact that they share similar physicochemical properties. Specifically, they are both hydrophilic compounds with logP values

of -1.8 and -1.4, respectively, with a quaternary amine functional group with a base salt form (bromide).

The permeation of the short acting β_2 agonist salbutamol sulphate was significantly lower across the mucus layer than across empty Transwell® inserts over all tested time points ($p < 0.05$). Only 31% $\pm$ 3% (SEM) of the initial dose had permeated within the first five minutes. Salbutamol sulphate exhibits a logP of 1.4, higher than those of ipratropium bromide and glycopyrronium bromide. This may account for the longer retention of salbutamol sulphate in the mucus layer than the M_3 antagonists.

To assess the diffusion of the long-acting β_2 agents, formoterol and indacaterol maleate through the mucus barrier, those needed to be dissolved in HBSS containing 10% DMSO since they are poorly soluble in HBSS alone, However, the influence of DMSO in high concentration on the integrity of the mucus layers also had to be considered. Hence, FITC was used in this experiment as it was the fluorescent dye that was the most retained in the mucus in Chapter 2. Therefore, any damaging effect of DMSO on the mucus layers would be more clearly observed. FITC transport across mucus was examined in HBSS containing increasing DMSO concentrations (0.1%, 1.0%, and 10%) (Figure 5.3.2).

5. *Impact of the mucus barrier on the permeation of various bronchodilators*
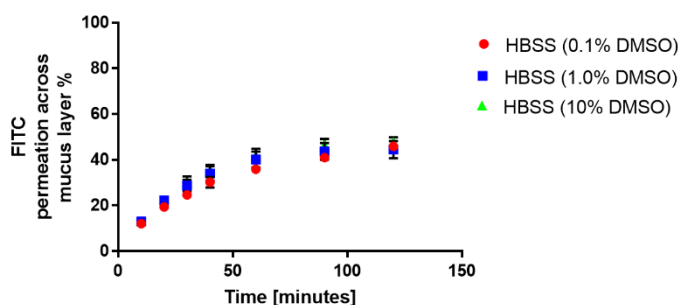
Figure 5.3.2. Apical to basolateral (A→B) permeation profile of FITC (10 µM) dissolved in HBSS with different concentrations of DMSO (0.1%, 1.0%, and 10%) delivered as a 50 µL solution in the apical compartment across the mucus layer while 500 µL of the buffer (HBSS (0.1%, 1.0%, and 10%, respectively) was added to the basal compartment. Data are presented as mean ± SD (n = 4).

Only ~ 20% of the FITC permeated through the layer within 20 minutes with insignificant differences between the three DMSO concentrations tested. Hence, subsequent experiments with formoterol and indacaterol maleate were performed using HBSS with 10% DMSO as the solvent (Figure 5.3.3). Nevertheless, it is worth mentioning that a limitation of this experiment is that, due to solubility issues, FITC permeation could not be investigated in the absence of DMSO. Therefore, comparing the permeation profile of a hydrophilic molecule in the presence or absence of DMSO would be necessary, although the rapid permeation across mucus of such compounds may be an issue.

5. Impact of the mucus barrier on the permeation of various bronchodilators
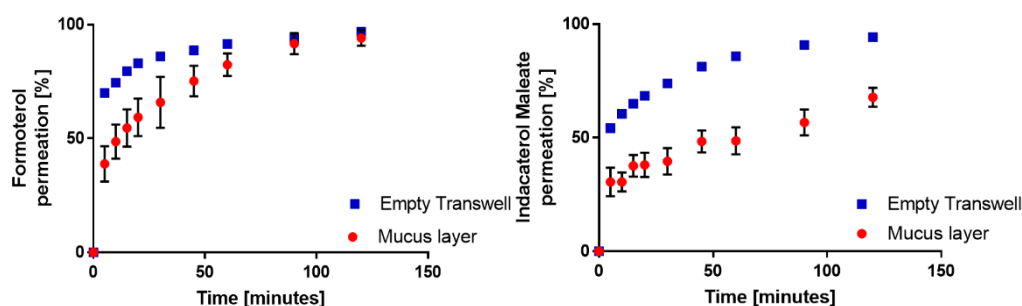
Figure 5.3.3. *Apical to basolateral (A→B) permeation profile of formoterol and indacaterol maleate across mucus layers mounted on polyester 0.4 μm pore size Transwell® and corresponding empty inserts. Drugs (1 mM) were dissolved in HBSS (10% DMSO). Drugs were sprayed as a 200 μL bolus at a distance of 20 cm. Data are presented as mean ± SEM (N = 4, n = 4).*

Formoterol permeation profile was comparatively fast, with 39% ± 8% (SEM) of the dose recovered in the basolateral chamber five minutes post-application and 82% ± 5% (SEM) after the first hour (p < 0.05). Insignificant differences between the fraction that had permeated through the mucus layer samples and the empty Transwell® inserts were observed over the following hour and formoterol permeation plateaued (94% ± 3% SEM) by the end of the experiment. A slower permeation profile across mucus was evident for indacaterol maleate, with 31% ± 6% (SEM) of the applied dose found basolaterally five minutes post-application. Indacaterol maleate is a lipophilic drug with a logP value of 4.05, which may explain its comparative mucus layer retention compared to formoterol, which is less lipophilic with a logP of 2.2.

Interestingly, it was observed that the empty Transwell® inserts acted as a barrier to all five drugs that were tested against the mucus layer. For instance, about a third of the M_3 antagonists dose was hindered by the 0.4 μm pore polyester semipermeable membrane within the first five minutes. A similar trend was observed for salbutamol sulphate and formoterol. An even higher retardation

was noted in the case of the ultra-long-acting β_2 agonist Indacaterol Maleate, with only 54% $\pm$ 2% (SEM) of the drug applied crossing the empty Transwell® inserts over the first five minutes.

Hence, it was assumed that either a chemical or physical hindrance (or possibly both) of the compound diffusion occurred in the 0.4 µm polyester semipermeable pore Transwell® inserts. For instance, chemical retardation may be caused by binding to the hydrophobic polyester membrane. Hence, a less lipophilic polycarbonate membrane may reduce the hindrance caused by polyester membrane. In addition, physical retardation may arise from the aerosolised droplet size being 50 times larger than the pore size of the Transwell® inserts.

5.3.2. Influence of two different 3.0 µm pore Transwell® insert membranes on the permeation of indacaterol maleate across the mucus layer

Transwell® inserts with either a polyester or polycarbonate semipermeable membrane were used in diffusion experiments to assess the impact of the polymeric component on the diffusion of molecules. Moreover, the investigated membranes had a pore size of 3.0 µm instead of 0.4 µm, with a view to investigating whether the pore size affected drug diffusion. Indacaterol maleate was used as the model drug for this experiment as previous observations had shown it was comparatively the most retained of the drugs tested within the inserts (Figure 5.3.4).

5. Impact of the mucus barrier on the permeation of various bronchodilators
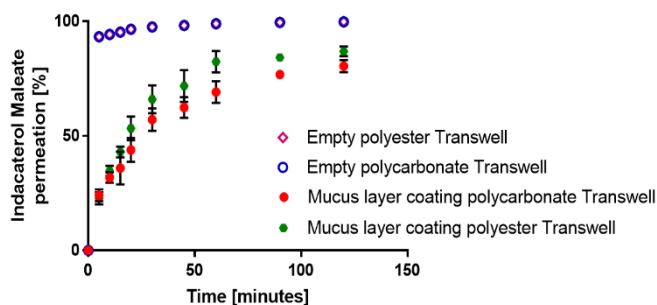
Figure 5.3.4. *Apical to basolateral (A→B) permeation profile of indacaterol maleate across mucus layers mounted on polyester and polycarbonate 3.0 μm pore size Transwell® and corresponding empty inserts. Indacaterol maleate (1 mM) was dissolved in HBSS (10% DMSO). Drugs were sprayed as a 200 μL bolus at a distance of 20 cm. Data are presented as mean ± SEM (N = 4, n = 4).*

Drug permeation through the two types of empty Transwell® inserts exceeded 90% at the first time point (five minutes), with insignificant differences recorded between the two different polymeric membranes ($p > 0.05$) indicating that the chemical nature of the polymer membrane does not affect the barrier properties of the Transwell® inserts. When the membranes were covered by a mucus layer, a slightly higher percentage permeated (2%) was observed for the polyester membrane by the end of experiment ($p < 0.05$). However, inserts with a polycarbonate membrane were not used in subsequent experiments due to several reasons; 1) the drug permeation profile was similar between the two membranes covered by mucus within the first hour ($p > 0.05$), 2) at the last experimental time point, the fraction that had permeated through the mucus layer was only 2% higher with a polyester membrane, and 3) to allow comparison between the drug permeation profile across 3.0 μm and 0.4 μm pore size membranes as previous diffusion studies were conducted using polyester membranes.

227

5. *Impact of the mucus barrier on the permeation of various bronchodilators*

The faster permeation profile through the 3.0 μm pore size empty Transwell®
inserts can be mainly attributed to the width of the transport channel (pore size).
The impact of Transwell® inserts on molecular diffusion has been studied
previously. Drug permeability across polyester Transwell® membranes with 0.4
μm pores has been compared with that across modified Transwell® inserts
(Rohrschneider et al., 2015). This modification was performed by removing the
polyester membrane and applying mild heat to form notches that would support
a replacement membrane made of a glass microfiber filter with a 1.6 μm pore
size (Figure 5.3.5).
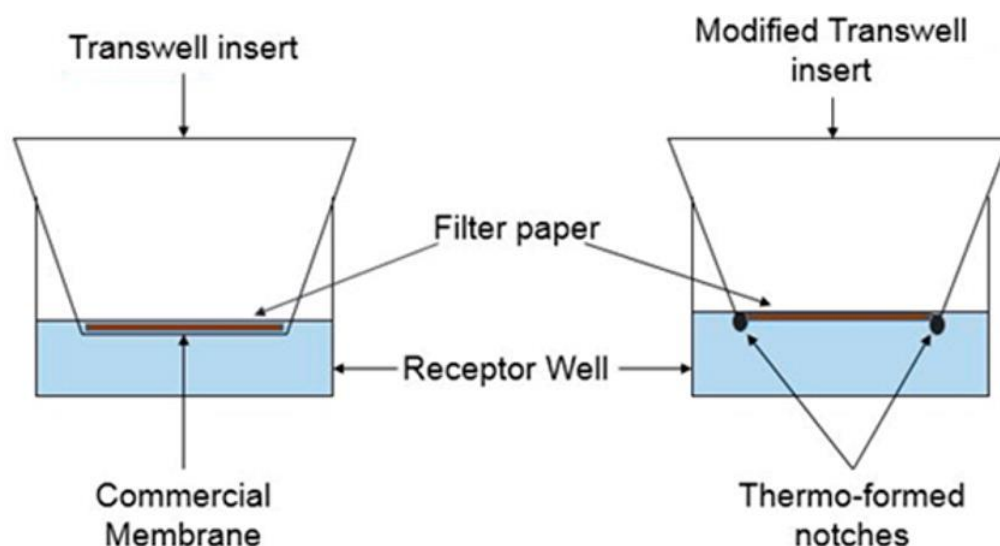
*Figure 5.3.5.Commercially available Transwell® inserts with a polyester
membrane (left), and Transwell® inserts modified by replacing the polyester
membrane with a glass microfiber filter (right), reproduced from
(Rohrschneider et al., 2015).*

 A faster transfer rate of the model drug ciclesonide was observed when the drug
was applied over the modified setup. However, control experiments to discard
any leakage from the placed glass microfiber filter during the experiments were

not reported. However, this study suggested that polyester 0.4 μm pore Transwell® inserts were by themselves a barrier for molecular diffusion.

From our obtained data, we believe that the immersed base of an aerosolised droplet over the membrane pores might play an important role in the permeation of molecules. Figure 5.3.6 illustrates how the surface area of the immersed base of an aerosolised droplet can be measured.
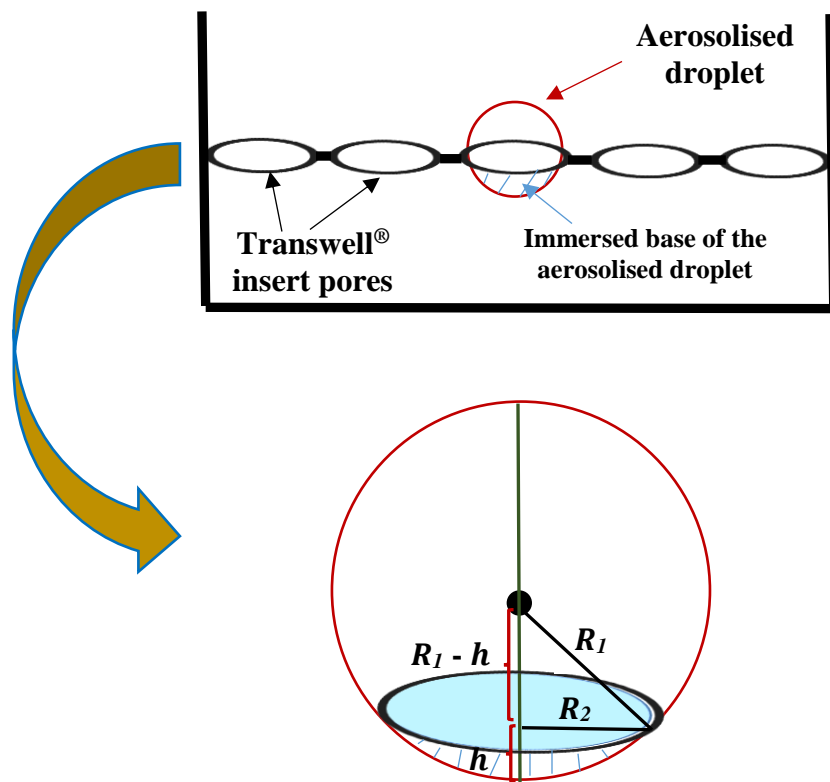
Figure 5.3.6. Representation of the aerosolised droplet on a 0.4 μm pore Transwell® polyester semipermeable membrane. (a) Represents a landed droplet on a pore of the Transwell® insert. (b) Represents a larger view of the droplet size on a pore of the Transwell® insert, where R_1 represents the radius of the aerosolised droplet, R_2 represents the radius of the pore, and h represents the height of the immersed base of the aerosolised droplet.

5. *Impact of the mucus barrier on the permeation of various bronchodilators*

To measure the surface area of the aerosolised droplet immersed base, definition of the immersed base h was required. $R_1 - h$ was calculated by applying Pythagoras' theorem, cognisant of the 20 µm bubble diameter and the 0.4 µm pore Transwell® insert.

$$((R_1 - h)^2 + (R_2)^2 = (R_1)^2$$

$$R_1 - h = \sqrt{(10)^2 - (0.2)^2} = 9.9979 \text{ µm}$$

$$h = R_1 - (R_1 - h) = 10 - 9.9979 = 0.002 \text{ µm}$$

Hence, the surface area of a spherical immersed base is given by $2\pi R_1 h$

$$2\pi R_1 h = 2\pi(10)(0.002) = 0.126 \text{ µm}^2$$

Therefore, only a height of 2 nm of the aerosolised droplet was immersed, with a total surface area of 0.126 µm^2 in the 0.4 pore membranes. This also indicates that when the pore size was increased to 3.0 µm, an increased height of 113 nm of the aerosolised droplet was immersed with a 60-fold larger total surface area (7.109 µm^2) for the pore membranes. This would increase the probability of faster diffusion through the empty Transwell® insert.

This may be because the aerosolised droplets applied to the 0.4 µm pore size are too large to wet the inside of the channel and remain above the channel for a longer period of time. In contrast, wetting of the inside of the channel can occur with a 3.0 µm width, which causes the droplet to protrude into the pore via a wetting phenomenon, Figure 5.3.7.
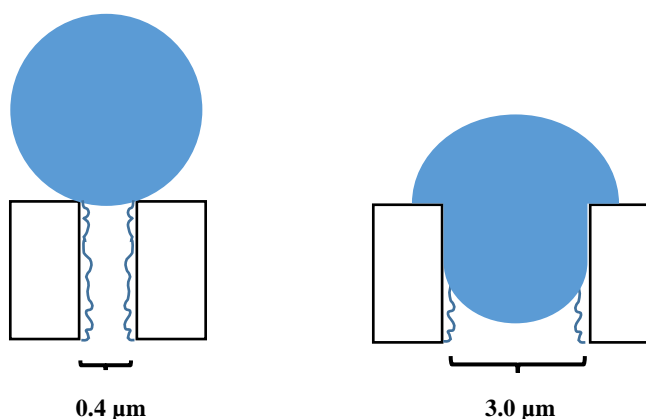
Figure 5.3.7. Theoretical hypothesis of how the aerosolised droplets behave above 0.4 µm (left) or 3.0 µm pores (right).

Despite extensive literature research, a study that measured the contact angle of a buffer like HBSS with the polyester membrane could not be found. This would have allowed an estimation of the surface energy (surface tension) of the aerosolised droplets and the capillary forces dragging them to the basal compartment.

With this in mind, we considered that measuring the capillary forces of HBSS within a polyester membrane (0.4 µm) would be informative. After consideration, a way to measure how fast the buffer penetrates in the pores of the membrane might be via confocal microscopy imaging, although the thickness of the membrane and its intrinsic fluorescence may be issues.

5.3.3. Impact of the mucus barrier on the permeation of various bronchodilators using Transwell® inserts with 3.0 µm pore size

The impact of mucus on the diffusion of the drugs tested in section 5.3.1 was investigated again using a similar set up but using inserts with a 3.0 µm pore size. Glycopyrronium bromide was omitted from this study as it exhibited a

similar permeation profile across the mucus layer as ipratropium bromide when 0.4 µm pore Transwell® inserts were used (Figure 5.3.1) and both drugs share many physicochemical properties (Table 5.3.1).

The permeation profiles of ipratropium bromide, salbutamol sulphate, formoterol, and indacaterol maleate across the mucus layer are shown in Figure 5.3.8.
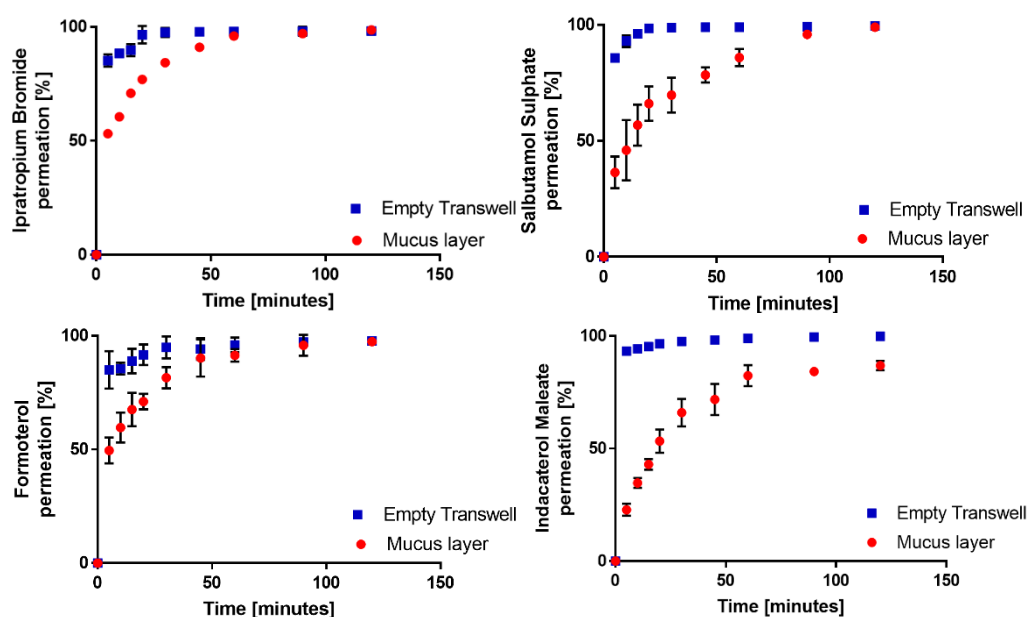
Figure 5.3.8. Apical to basolateral (A→B) permeation profile of ipratropium bromide, salbutamol sulphate, formoterol, and indacaterol maleate across mucus layers mounted on polyester 3.0 µm pore size Transwell® and corresponding empty inserts. Ipratropium bromide and salbutamol sulphate (10 mM) were dissolved in HBSS while formoterol and indacaterol maleate (1 mM) were dissolved in HBSS (10%DMSO). Drugs were sprayed as a 200 µL bolus at a distance of 20 cm. Data are presented as mean ± SEM (N = 4, n = 4).

Ipratropium bromide rapidly permeated across the mucus layer, with more than 50% of the drug molecule transferred into the basolateral chamber within the first five minutes. In addition, more than 85% of the dose applied crossed the empty Transwell® inserts in that period of time. The drug diffusion through the

mucus layer was slower than through the uncoated inserts during the first hour of the experiment ($p < 0.05$). After one hour, both permeation profile plateaued at ~ 95%.

In the case of salbutamol sulphate, 5 min were needed for about one third (36% ± 7%, SEM) of the deposited dose to diffuse across the mucus layer. A significant differences between the drug permeation profile across empty and mucus covered Transwell® inserts was observed during the first 60 min post-application ($p < 0.05$), before both plateaued at 98% ± 1% (SEM) on the last two time points (90 and 120 min, $p > 0.05$).

In the first five minutes, 50% ± 6% (SEM) of formoterol had diffused across the mucus layer ($p < 0.05$). This gap decreased over time between formoterol permeation profile across mucus layer and empty Transwell® inserts until it reached an insignificant difference 45 minutes post-application when a plateau at 90% ± 8% (SEM) was reached.

Indacaterol maleate was the only compound to exhibit a different permeation profile over all of the tested time intervals in presence or absence of mucus on the inserts ($p < 0.05$). In addition, more than 75% of the applied dose was still retained in the mucus layer at the first sampling time point. A plateau was observed from 90 minutes with 84% ± 1% (SEM) of the dose recovered on the opposite side of the mucus layers. Notably, more than 90% of this inhaled medicine was transferred to the basal compartment of the empty Transwell® inserts within the first five minutes.

5. *Impact of the mucus barrier on the permeation of various bronchodilators*

The drugs investigated were sprayed at different concentrations due to the fact that the poorly soluble compounds (formoterol and indacaterol maleate) could not be dissolved at a concentration above 1 mM. Furthermore, the soluble compounds (ipratropium bromide and salbutamol sulphate) could not be sprayed at a concentration of 1 mM due to analytical quantification issues. It is worth mentioning that the amount of drug deposited on the mucus layers varied in the nanogram range, where ipratropium bromide, salbutamol sulphate, formoterol, and indacaterol maleate showed a deposition of 442 ng ± 76 ng SEM, 687 ng ± 116 ng SEM, 216 ng ± 46 ng SEM, 232 ng ± 61 ng SEM, respectively. However, this variation in the deposition was not linked to the drug concentrations sprayed. It might instead be related to the different viscosity of the sprayed solutions as well as the different physicochemical properties of the investigated compounds. If the clinical situation is considered, the amount of inhaled drug depositing in the airways is no more than 10-20% of the dose emitted from the inhaler device (Newman and Clarke, 1983, Newman et al., 1981, O'Callaghan and Barry, 1997). Taking into consideration the surface area of the airways ($\sim$ 5 m^2, excluding the alveoli) and the non-homogenous distribution of the delivered dose (Haughney et al., 2010, Pavelka and Roth, 2010, Rohrschneider et al., 2015), this might lead to a very low deposited dose. However, it is impossible to experimentally mimic such a deposited quantity due to the quantification limits of the analytical instruments.

5. *Impact of the mucus barrier on the permeation of various bronchodilators*

To make a proper comparison between the four drugs investigated, the % of the dose deposited retained in the mucus layer after 20 min was plotted for each of them (Figure 5.3.9). Indeed, at this time, all investigated compounds had permeated across the empty Transwell® inserts. Furthermore, the mucus turnover in the respiratory system has been reported to be 10 to 20 minutes (Sarmento, 2018). This high rate of pulmonary mucus turnover might limit the contact pulmonary agents with the respiratory system. Drug molecules trapped in the mucus would be cleared by the muco-ciliary escalator and swallowed
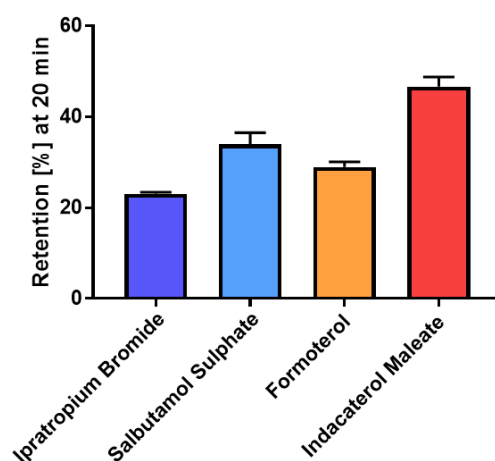
Figure 5.3.9. Percentage of deposited dose retained in mucus layers covering 3.0 µm pore sized Transwells 20 minutes post-application. Ipratropium Bromide and salbutamol sulphate (10 mM) were dissolved in HBSS, and Formoterol and Indacaterol Maleate (1 mM) were dissolved in HBSS (10% DMSO). Drugs were sprayed as a 200 µL bolus at a distance of 20 cm. Data are presented as mean ± SEM (N = 4, n = 4).

Ipratropium bromide showed the lowest retention among the investigated agents, with only 23% ± 1% (SEM) still trapped inside the mucus layer after 20 minutes, which was significantly different from the value obtained with the other three compounds ($p < 0.05$). In contrast, indacaterol maleate was the most retained molecule with 47% ± 4% (SEM) of the molecules confined in the mucus

after 20 minutes. This was significantly higher than for the other three test molecules ($p < 0.05$). The level of retention of salbutamol sulphate and formoterol were similar, with 34% ± 4% (SEM) and 29% ± 2% (SEM) of the delivered amount retained apically 20 minutes post-application, respectively, ($p > 0.05$).

In order to determine which physicochemical properties drive drug interactions with mucus, relationships were drawn between their retention 20 min post application and their logP, molecular weight (MW), H-acceptor count, H-donor count, polar surface area (PSA), heavy atom count, covalently-bonded unit count, and rotatable bond count (Table 5.3.1). Figure 5.3.10 visually represents those trends.

Table 5.3.1. Physicochemical properties of the investigated inhaler compounds; logP, PSA, MW, covalently-bonded unit, heavy atom, H donor, H acceptor, and rotatable bonds were extracted from the PubChem database of chemical molecules.

Drug	logP (o/w)	PSA (Å²)	MW (g/mol)	Covalently-Bonded Unit Count	Heavy Atom Count	H donor Count	H acceptor Count	Rotable Bonds Count
Ipratropium Bromide	-1.8	46.5	412.368	2	25	1	4	6
Glycopyrronium Bromide	-1.4	46.5	398.341	2	24	1	4	5
Salbutamol Sulphate	1.4	228	576.702	3	39	10	12	10
Formoterol	2.2	90.8	344.411	1	25	4	5	8
Indacaterol Maleate	4.05	156	508.571	2	37	6	8	8
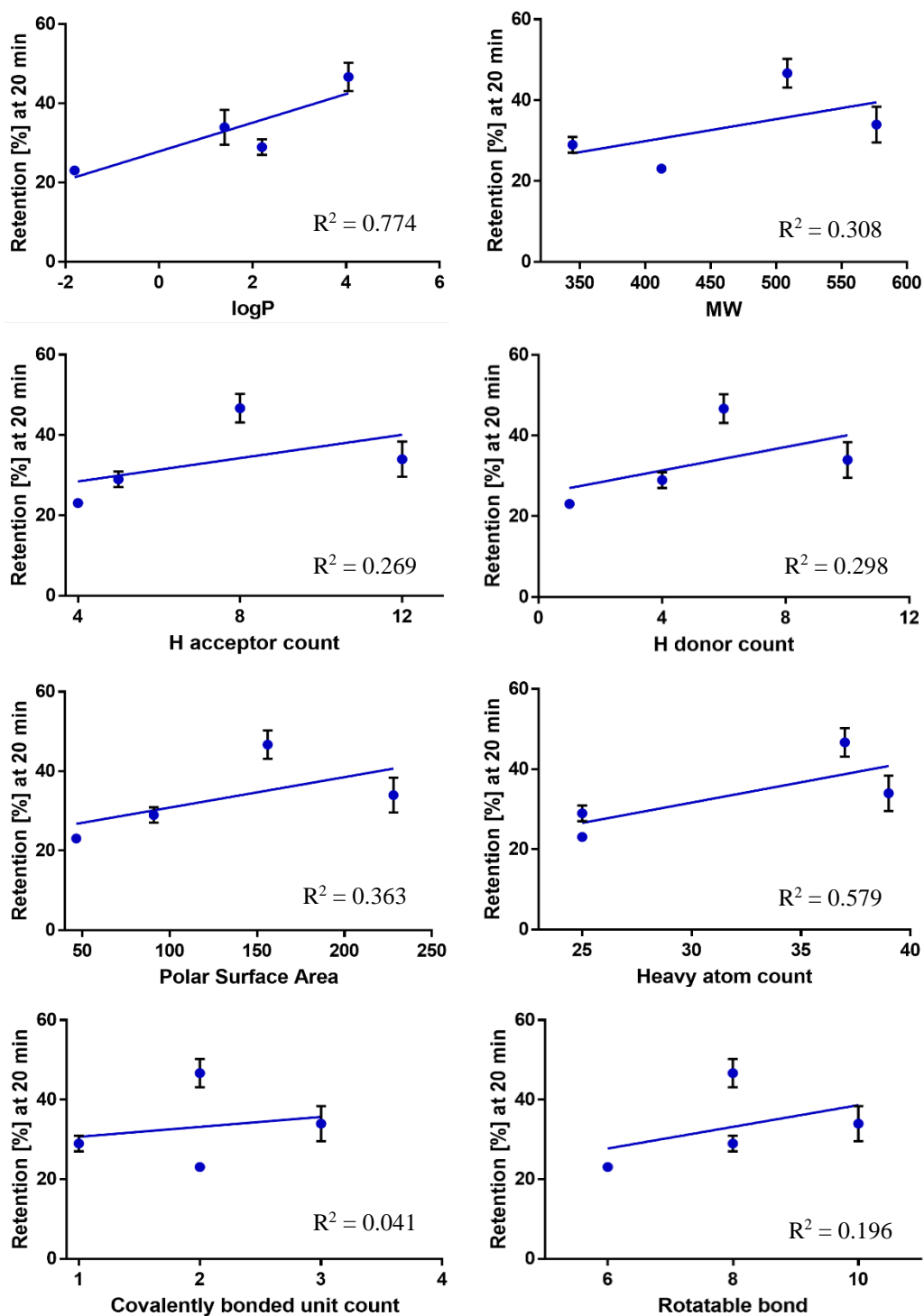
Figure 5.3.10. Relationship between the % of drug retained in the mucus layer 20 minutes post-application and different physicochemical parameters. Data are presented as mean ± SEM (N = 4, n = 4).

5. *Impact of the mucus barrier on the permeation of various bronchodilators*

Considering that only four commonly used inhaled drugs were tested, none of the correlations was statistically significant. Therefore, this study can only give a thumbnail sketch of the parameters that might promote drug retention in airway mucus. For instance, it seems that the logP is the most important factor that influences mucus-drug interaction ($R^2 = 0.774$). Weaker relationships between mucus retention and PSA ($R^2 = 0.363$), molecular weight ($R^2 = 0.308$), H acceptor ($R^2 = 0.270$), and H donor ($R^2 = 0.230$) were obtained.

No relationship was observed with the heavy atom count, rotatable bond count, and covalently-bonded unit count but two of the investigated agents were characterised by the same number of heavy atoms, rotatable bond count, and covalently-bonded unit count.

Although logP was shown to affect drug permeation through airway mucus, a more extended range of molecules with highly variable physicochemical properties should be studied to establish stronger links between drug physicochemical properties and their interactions with pulmonary mucus.

Associations between logP and permeation through mucus has been reported previously for similar compounds. The barrier effect of pig gastric mucin against 12 amiloride analogues with different physicochemical properties was recently investigated (Giorgetti, 2016). The investigated compounds were split into two groups, including quaternary amine and non-quaternary amine compounds. Considering their different physicochemical properties, a strong positive correlation was observed between retained compounds and LogP for both quaternary and non-quaternary amine compounds ($R^2 = 0.899$ and $R^2 = 0.952$, respectively).

5. *Impact of the mucus barrier on the permeation of various bronchodilators*

For quaternary amine compounds, a weaker but positive correlation was observed with the number of rotatable bonds ($R^2 = 0.838$), PSA ($R^2 = 0.613$), molecular weight ($R2 = 0.758$), and number of H acceptor sites ($R2 = 0.730$). No correlation could be drawn with the number of H donor sites as four compounds were characterized by the same value. Strong correlations were prohibited in the case of non-quaternary amine compounds due to a small sample set of four compounds. However, the level of statistical significance (p-value) of the correlation coefficients was not reported in that study.

Another investigation showed that mucus binding of seven steroids with a logP in the range of 1.53 to 3.99 following rat intestinal perfusion, may be due to interactions with hydrophobic regions of mucin (Komiya et al., 1980).

Bhat and colleagues studied the extent of binding to pig gastric mucus for several compounds with a logP ranging from -1.23 to 2.85 (Bhat et al., 1995) and proposed that hydrophobic interactions with mucus could explain the binding phenomenon.

An important limitation of this study is that none of the investigated compounds was negatively charged or neutral, hence, the impact of electrostatic interactions on molecule retention in the mucus layers could not be investigated. Indeed, several studies have suggested that electrostatic binding with mucin is, in some cases, significant. For instance, the diffusion of positively and negatively charged particles within pig gastric mucins was more hindered and less mobile at acidic pH 3 (Lieleg et al., 2010). In comparison, at neutral pH 7, charged particles diffused almost freely in mucus. Indeed, the mobility at low pH was reduced compared to neutral pH suggesting that pH-dependent structural rearrangements of the mucin hydrogel might partly be responsible for the

decrease in particle mobility. Lieleg and colleagues suggested that changes in pH can alter the conformation of mucus by promoting the exposure of hydrophobic domains of the mucins, changing electrostatic charges of their glycosylated regions, influencing non-covalent mucin–mucin interactions thereby increasing the viscoelasticity.

Moreover, an additional study showed that a negatively charged virus was trapped in low pH human cervicovaginal mucus, but not at neutral pH 7 (Lai et al., 2009). Collectively, these studies suggest that electrostatic binding with mucin is pH sensitive, and mainly binds electrostatically to acidic mucus environment; in contrast to the pulmonary mucus pH which is neutral.

5.4. Conclusion

The *in-vitro* methodology developed previously to apply pulmonary agents onto a mucus layer lung model was exploited to investigate the interactions of current inhaled drugs with airway mucus. Five drugs were tested (ipratropium bromide, glycopyrronium bromide, salbutamol sulphate, formoterol, and indacaterol maleate) and showed different rates of diffusion across the mucus layers. Indacaterol was retained the longest within the mucus layer while ipratropium bromide and glycopyrronium bromide were the fastest drugs in terms of mucus layer penetration. The effect of varied physicochemical properties on drug permeation through the mucus layer was investigated. Although not statistically significant, the strongest relationship observed in this study was between logP and the percentage of drugs retained within the mucus layer. However, a wider range of compounds with highly variable physicochemical properties is required to better understand inhaled drug-mucus interactions.

5.5. References

AGUSTI, A. 2005. COPD, a multicomponent disease: implications for management. *Respiratory medicine,* 99**,** 670-682.

AGUSTI, A. 2018. Filling the gaps in COPD: the TRIBUTE study. *The Lancet,* 391**,** 1004-1006.

BARNES, P. J. 2004. Alveolar macrophages as orchestrators of COPD. *COPD: Journal of Chronic Obstructive Pulmonary Disease,* 1**,** 59-70.

BARNES, P. J. 2012. Severe asthma: advances in current management and future therapy. *Journal of Allergy and Clinical Immunology,* 129**,** 48-59.

BARNES, P. J. 2013. Theophylline. *American journal of respiratory and critical care medicine,* 188**,** 901-906.

BATEMAN, E., RENNARD, S., BARNES, P., DICPINIGAITIS, P., GOSENS, R., GROSS, N., NADEL, J., PFEIFER, M., RACKÉ, K. & RABE, K. 2009. Alternative mechanisms for tiotropium. *Pulmonary pharmacology & therapeutics,* 22**,** 533-542.

BHAT, P. G., FLANAGAN, D. R. & DONOVAN, M. D. 1995. The limiting role of mucus in drug absorption: Drug permeation through mucus solution. *International journal of pharmaceutics,* 126**,** 179-187.

BONINI, M. & USMANI, O. S. 2016. Drugs for airway disease. *Medicine,* 44**,** 271-280.

BRUNTON, L. L. 2014. *Goodman and Gilman's manual of pharmacology and therapeutics*, McGraw-Hill New York.

CARSTAIRS, J., NIMMO, A. & BARNES, P. J. 1985. Autoradiographic visualization of beta-adrenoceptor subtypes in human lung. *American review of respiratory disease,* 132**,** 541-547.

5. *Impact of the mucus barrier on the permeation of various bronchodilators*

CAZZOLA, M., BEEH, K. M., PRICE, D. & ROCHE, N. 2015. Assessing the clinical value of fast onset and sustained duration of action of long-acting bronchodilators for COPD. *Pulmonary pharmacology & therapeutics,* 31**,** 68-78.

CUEVAS, J. 2018. Adrenergic Agonists and Their Clinical Uses. *Brody's Human Pharmacology E-Book***,** 89.

DEVI, M. R., BAWARI, M., PAUL, S. & SHARMA, G. 2011. Neurotoxic and medicinal properties of Datura stramonium L.–review. *Assam University Journal of Science and Technology,* 7**,** 139-144.

GIORGETTI, M. 2016. *Studies on the interaction between inhaled drug molecules and mucin.* University of East Anglia.

GOLDIE, R., PATERSON, J. & LULICH, K. 1991. Pharmacology and therapeutics of β-adrenoceptor agonists. *Pharmacology of Asthma.* Springer.

GRAY, C. The treatment of asthma. The Specialist Forum, 2017. New Media Publishing, 12-17.

HASANI, A., TOMS, N., AGNEW, J. E., SARNO, M., HARRISON, A. J. & DILWORTH, P. 2004. The effect of inhaled tiotropium bromide on lung mucociliary clearance in patients with COPD. *Chest,* 125**,** 1726-1734.

HAUGHNEY, J., PRICE, D., BARNES, N. C., VIRCHOW, J. C., ROCHE, N. & CHRYSTYN, H. 2010. Choosing inhaler devices for people with asthma: current knowledge and outstanding research needs. *Respiratory Medicine CME,* 3**,** 125-131.

KARAMPITSAKOS, T., PROTOPAPAS, A., GIANOLOUDI, M., PAPADOPOULOS, V. P., BOUROS, D., CHATZIMICHAEL, A. &

5. Impact of the mucus barrier on the permeation of various bronchodilators

PARASKAKIS, E. 2017. The effect of bronchodilation and spirometry on fractional exhaled nitric oxide (FeNO50), bronchial NO flux (JawNO) and alveolar NO concentration (CANO) in children and young adults. *Journal of Asthma*, 1-8.

KHANVILKAR, K., DONOVAN, M. D. & FLANAGAN, D. R. 2001. Drug transfer through mucus. *Adv Drug Deliv Rev,* 48, 173-93.

KOMIYA, I., PARK, J., KAMANI, A., HO, N. & HIGUCHI, W. 1980. Quantitative mechanistic studies in simultaneous fluid flow and intestinal absorption using steroids as model solutes. *International Journal of Pharmaceutics,* 4, 249-262.

LAI, S. K., HIDA, K., SHUKAIR, S., WANG, Y.-Y., FIGUEIREDO, A., CONE, R., HOPE, T. J. & HANES, J. 2009. Human immunodeficiency virus type 1 is trapped by acidic but not by neutralized human cervicovaginal mucus. *Journal of virology,* 83, 11196-11200.

LIELEG, O., VLADESCU, I. & RIBBECK, K. 2010. Characterization of particle translocation through mucin hydrogels. *Biophysical journal,* 98, 1782-1789.

MAK, J. & BARNES, P. J. 1990. Autoradiographic visualization of muscarinic receptor subtypes in human and guinea pig lung. *Am Rev Respir Dis,* 141, 1559-1568.

MATHUR, S. K. Allergy and asthma in the elderly. Seminars in respiratory and critical care medicine, 2010. NIH Public Access, 587.

MONTUSCHI, P. & CIABATTONI, G. 2015. Bronchodilating drugs for chronic obstructive pulmonary disease: current status and future trends. *Journal of medicinal chemistry,* 58, 4131-4164.

NAIR, V. P. & HUNTER, J. M. 2004. Anticholinesterases and anticholinergic drugs. *Continuing Education in Anaesthesia, Critical Care & Pain,* 4**,** 164-168.

NEWMAN, S. & CLARKE, S. 1983. Therapeutic aerosols 1--physical and practical considerations. *Thorax,* 38**,** 881.

NEWMAN, S. P., PAVIA, D., MORÉN, F., SHEAHAN, N. & CLARKE, S. W. 1981. Deposition of pressurised aerosols in the human respiratory tract. *Thorax,* 36**,** 52-55.

O'CALLAGHAN, C. & BARRY, P. W. 1997. The science of nebulised drug delivery. *Thorax,* 52 Suppl 2**,** S31-S44.

PAVELKA, M. & ROTH, J. 2010. Alveoli: Gas Exchange and Host Defense. *Functional Ultrastructure.* Springer.

PRAKASH, A., BABU, K. S. & MORJARIA, J. B. 2015. Profile of inhaled glycopyrronium bromide as monotherapy and in fixed-dose combination with indacaterol maleate for the treatment of COPD. *International journal of chronic obstructive pulmonary disease,* 10**,** 111.

ROHRSCHNEIDER, M., BHAGWAT, S., KRAMPE, R., MICHLER, V., BREITKREUTZ, J. & HOCHHAUS, G. 2015. Evaluation of the Transwell System for Characterization of Dissolution Behavior of Inhalation Drugs: Effects of Membrane and Surfactant. *Mol Pharm,* 12**,** 2618-24.

ROUND, A. N., BERRY, M., MCMASTER, T. J., STOLL, S., GOWERS, D., CORFIELD, A. P. & MILES, M. J. 2002. Heterogeneity and persistence length in human ocular mucins. *Biophys J,* 83**,** 1661-70.

SALAHUDEEN, M. S. & NISHTALA, P. S. 2016. Examination and estimation of anticholinergic burden: current trends and implications for future research. *Drugs & aging,* 33**,** 305-313.

SANTUS, P., RADOVANOVIC, D., PAGGIARO, P., PAPI, A., SANDUZZI, A., SCICHILONE, N. & BRAIDO, F. 2015. Why use long acting bronchodilators in chronic obstructive lung diseases? An extensive review on formoterol and salmeterol. *European journal of internal medicine,* 26**,** 379-384.

SARMENTO, B. A. N., J. 2018. *Biomedical applications of functionalized nanomaterials*.

SHARMA, R., SOOD, M., SHARMA, R., AGARWAL, S., VASHIST, H., SISODIA, S. & GUPTA, A. 2017. WORLD JOURNAL OF PHARMACY AND PHARMACEUTICAL SCIENCES.

SMITH, I. J. & PARRY-BILLINGS, M. 2003. The inhalers of the future? A review of dry powder devices on the market today. *Pulmonary pharmacology & therapeutics,* 16**,** 79-95.

TAMAOKI, J., CHIYOTANI, A., TAGAYA, E., SAKAI, N. & KONNO, K. 1994. Effect of long term treatment with oxitropium bromide on airway secretion in chronic bronchitis and diffuse panbronchiolitis. *Thorax,* 49**,** 545-548.

TRAVERS, A. H., MILAN, S. J., JONES, A. P., CAMARGO JR, C. A. & ROWE, B. H. 2012. Addition of intravenous beta (2)-agonists to inhaled beta (2)-agonists for acute asthma. *Cochrane Database Syst Rev,* 12.

Chapter 6 - General discussion and future work

Pulmonary drug delivery is a growing market that offers a variety of options for systemic or local drug delivery. The Grand View Research Institution estimated that the pulmonary drug delivery market in 2016 was worth approximately USD 36.5 billion globally, with expected growth in-line with the Compound Annual Growth Rate (CAGR) of 4.7% over the forecast period (Patil and Deshpande, 2018). Unfortunately, incidence rates of respiratory diseases are expected to increase, thus the demand for novel performant pulmonary drug delivery systems are expected to correspondingly increase, concomitantly with interests into improving patient outcomes in the area.

The primary focus in the field of pulmonary drug delivery has mainly been on improving device technologies to enhance the deposition of the aerosols in the lungs. Although expanded progresses have been made in this area, there is still a knowledge-gap in relation to the detailed events that follow drug deposition in the lung. This is mainly due to the insufficient available tools to investigate drug disposition mechanisms post-inhalation. The inhalation route is considered an optimal option for treating patients with airflow obstruction through the administration of drugs such as β-agonists and corticosteroids, whereas antibiotics are more commonly used against *P. aeruginosa* in cystic fibrosis patients (Hewer and Smyth, 2017).

Successful drug delivery by aerosolisation must overcome the supra-epithelial mucus barrier to ensure effective drug transportation to the affected area. Similarly, sufficient penetration into the mucus barrier is essential for inhaled

antibiotics to target bacterial colonies located in airway secretions (Worlitzsch et al., 2002).

Mucus-molecular interactions have been previously studied using toxic compounds such as polycyclic aromatic hydrocarbons (PAHs), generally exposed to humans through tobacco smoke and pollution sources. During the late 80's and early 90's, the retention of lipophilic PAHs within the pulmonary mucus layer was investigated using dog models (Gerde et al., 1993, Gerde and Scholander, 1987). The studies measured the tissue concentrations of two known candidate markers of PAHs, benzo[a]pyrene (BaP) and phenanthrene. Approximately 35% of the lipophilic toxicant BaP (logP = 6) was detected in the mucus layer after 1 min of exposure, while only 3% of phenanthrene (logP = 4) was retained under the same conditions. The authors suggested that the differences observed were due to lipid components of the mucus layer, however, no concrete proof was shown for this hypothesis.

In spite of the clear interactions between airway mucus and inhaled toxins, very minor attention has been given to pulmonary mucus-drug interactions. In contrast, for oral delivery, which is the primary administrative route of choice for a large number of important drugs, numerous studies have been conducted to evaluate drug-mucus interactions and suggested that those may result in limited drug bioavailability (Barry and Braybrooks, 1974, Bhat et al., 1995, Kearney and Marriott, 1986). For instance, in a study using the HT29-H cell line, a mucus-producing cell model, the diffusion rate of the lipophilic steroid testosterone significantly increased by ~ 50% following mucus removal from the apical side of the cells (Karlsson et al., 1993).

6. *General discussion and future work*

Similar investigations on pulmonary mucus-drug interactions are still lacking and was a motivation for this body of work.

In order to study those interactions in vitro, Transwell® inserts were successfully coated with 12 µL of pig tracheal mucus. Although the thickness of the mucus layer formed is higher than the pulmonary mucus layer in a clinical setting, most respiratory diseases are associated with excessive secretion of mucus..

This mucus layer was physically characterised following the different preparation stages which were shown not to have an effect of the internal structure of the final mucus layer.

Measurements of fluorescent dye permeability across the mucus layers revealed lipophilic compounds were retarded, likely due to hydrophobic interactions. However, it was deemed that other interactions such as electrostatic interactions might be important for hydrophilic solutes. However, insignificant effects were observed with the hydrophilic compound examined; Rhodamine 123.

The LC-MS method used was validated for the analysis of simultaneous authentic standards to profile pig tracheal mucus. Following the validation, the composition of pig tracheal mucus samples (raw and cleaned) was investigated by applying a global metabolomics approach using this method. Lipids and products of amino acid and carbohydrate metabolism represented, approximately, 50% of the small molecular weight constituents of the pig tracheal mucus, which was in line with the previously reported composition of human bronchial mucus (Esther et al., 2016, Nobakht M. Gh et al., 2015, SLAYTER et al., 1984). This gave us more confidence about using the mucus model since it reflected the human bronchial mucus composition.

6. *General discussion and future work*

However, some metabolites were diluted after cleaning the raw mucus. Nevertheless, the cleaning procedure was a crucial stage in the preparation of mucus model to remove blood components from the mucus layers. Other metabolites were significantly concentrated after the cleaning process, which potentially play important roles in mucus barrier protection.

It is worth mentioning that a limitation of this work is the lack of metabolite profiling in the final stage of the mucus layer covering Transwell® inserts. However, this would be time-consuming as this would require thousands of pig tracheal batches to extract the required amount of mucus for coating Transwell® inserts. Moreover, the metabolomics approach would be more powerful if the pig tracheal mucus model developed could be characterised alongside mucus removed from the surface of Calu-3 broncho-epithelial cell layers grown at an air-liquid interface, mucus from healthy human subjects and mucus from cystic fibrosis subjects. This would give us insight into how the composition of our mucus model compares with human mucus either in healthy or diseased conditions. However, the low amount of mucus produced from Calu-3 cells would imply culturing very large batches to collect sufficient amount for analysis whereas obtaining mucus samples from human subjects requires an ethical approval and we were limited by time in this project.

Following this, we successfully assembled and validated a deposition system based on a Penn-Century FMJ-250® high pressure syringe and MicroSprayer® aerosoliser needle attached to a glass-holder desiccator system. The test results demonstrated that our system was able to consistently deposit aerosols when delivered over a mucus layer. Compared to other tested systems such as TSI (Grainger et al., 2009) or VITROCELL (Kim et al., 2013), which have a

maximum capacity of three inserts, it is more convenient as it allows more room for a higher number of inserts to be positioned over the internal surface. Moreover, compared to the aforementioned deposition systems, this deposition system boasts easier and more cost-effective operation. It would be capable of facilitating fast screening of candidate compounds in the early stages of development with minimal consumed amount (200 µL) which would be financially advantageous.

Finally, once the test-mucus layer was characterised and the deposition system was developed and optimised, drug permeability through the mucus layers was measured in conditions simulating the lung environment.

Five drugs (ipratropium bromide, glycopyrronium bromide, salbutamol sulphate, formoterol, and indacaterol maleate) were investigated using the developed *in-vitro* approaches and were all shown to be retained within the mucus layers through different rates of diffusion.

The investigated pulmonary agents exhibited different physicochemical properties and the strongest observed relationship was between logP and their retention in the mucus layer. A limitation of this body of work is the lack of negatively charged molecules to examine different ionisation states and their charge binding to the mucus layer. However, some previous studies excludes the theory of electrostatic binding between ionised molecules and mucus; for example, six different molecules with different states of ionisation have been investigated across pig gastric mucin (Bhat et al., 1995, Bhat et al., 1996). All the molecules showed affinities of the same magnitude order to mucin regardless of their ionization state and chemical structure. It was suggested that the forces involved in the binding of molecules to mucin are hydrophobic interaction but

6. *General discussion and future work*

not electrostatic interaction. Nevertheless such conclusion would be in contrast to other investigations that have reported that electrostatic interactions are important (Niibuchi et al., 1986, Kearney and Marriott, 1987). It is expected that positively charged drugs bind electrostatically to the negatively charged components in mucus (Crater and Carrier, 2010, Lieleg et al., 2010).

The research groups of Wikman–Larhed examined the diffusion of several compounds with different log*P* values in pig intestinal mucus and also in individual mucus components like mucin and lipids (Karlsson et al., 1993, Larhed et al., 1998, Larhed et al., 1997, Wikman et al., 1993). They proposed that also the lipid component in the mucus are responsible for decreasing lipophilic molecular diffusion not only mucin. Diffusion of hydrophilic molecules showed no change upon increased concentration of mucin or lipid components.

Legen and Kristl investigated the diffusion of four acyclovir analogues across pig gastric mucus and used phosphate buffer for comparison (Legen and Kristl, 2001). All compounds chosen were relatively hydrophilic analogues (log*P* ranges from −1.57 to −1.08). Only Acyclovir (logP −1.57) showed significantly lower permeation across pig gastric mucus compared to buffer ($P < .05$). The shown data might indicate that the analogues chosen were not lipophilic enough to be involved in hydrophobic interactions. The authors concluded that some evidence existed for mucin interaction with polar or ionized groups of the compounds being tested.

Although previous investigation of mucus-drug interaction supports our findings, a wide range of compounds with varied physicochemical properties is deemed necessary to better understand aerosolised drug-mucus interactions.

6. *General discussion and future work*

In our future work, one of the main ideas is to carry on the same developed/optimised in-vitro approaches but with a large number of molecules to include molecules with varied physicochemical properties,.

Moreover, development on this portfolio would be considered to include future pulmonary –omics investigation in the area, through comparing healthy and diseased pulmonary mucus, such as cystic fibrosis mucus, or to compare cystic fibrosis mucus treated with a pulmonary agent with a similar mucus but with no treatment, control mucus. This would give us a better understanding on the mucus-drug interactions by monitoring concentration changes in a broad range of metabolites (Zhang et al., 2016). Also, it would help us in developing more specific in vitro models to include individual components that are believed to be the main constitution of cystic fibrosis mucus.

Considering that this PhD thesis focused on the understanding of the impact of the mucus layer on drug permeability in the lung using *in vitro* systems; it would be an idea to take a somewhat diametric approach, in which we will investigate the effect of aerosolised drugs on mucus characteristics. Mucus water content, internal structure, and rheological characteristics should be probed before and after the deposition of pulmonary aerosols. Furthermore, drugs such as aspirin, some anticholinergics, and benzodiazepines have been shown to depress the pulmonary mucociliary transport system (Houtmeyers et al., 1999). As such, since many lung disease sufferers often suffer from more than a single medical health issue, and thus are administered more than one therapeutic application to treat these multiple cases, a combinatory approach, to at least one or more commonly encountered simultaneously administered drugs in the case of lung diseases, deserves more attention.

6. *General discussion and future work*

To improve the permeation of poorly diffused drugs across mucus layers, as demonstrated herein with indacaterol maleate, different ratios of some mucolytic agents could be investigated as a combinatory formulation with poor permeation candidate drugs across mucus layers taking into consideration drug-drug interaction and insignificant side effects. This would be undertaken with a view to enhancing the transport of these drugs by inhibiting the nitric oxide dependent activation of the soluble guanylate cyclase gene, which is responsible for mucus secretion.

The findings described in this PhD thesis should provide valuable insights into the impact of the mucus layer on drug permeability in the lung. In particular, they suggest that the physicochemical properties of inhaled aerosols might affect their permeation across airway mucus. This could aid in the design of therapeutic agents taking into account the importance of pulmonary mucus-drug interaction, which has thus-far been under-reported in the literature.

6.1. **References**

BARRY, B. & BRAYBROOKS, M. 1974. Effect of mucin on the bioavailability of tetracycline from the gastro-intestinal tract: in vivo, in vitro correlations. *Journal of Pharmacy and Pharmacology,* 26**,** 64P-65P.

BHAT, P. G., FLANAGAN, D. R. & DONOVAN, M. D. 1995. The limiting role of mucus in drug absorption: Drug permeation through mucus solution. *International journal of pharmaceutics,* 126**,** 179-187.

BHAT, P. G., FLANAGAN, D. R. & DONOVAN, M. D. 1996. Drug binding to gastric mucus glycoproteins. *International journal of pharmaceutics,* 134**,** 15-25.

CRATER, J. S. & CARRIER, R. L. 2010. Barrier properties of gastrointestinal mucus to nanoparticle transport. *Macromolecular bioscience,* 10**,** 1473-1483.

ESTHER, C. R., TURKOVIC, L., ROSENOW, T., MUHLEBACH, M. S., BOUCHER, R. C., RANGANATHAN, S. & STICK, S. M. 2016. Metabolomic biomarkers predictive of early structural lung disease in cystic fibrosis. *European Respiratory Journal,* 48**,** 1612-1621.

GERDE, P., MUGGENBURG, B. A., SABOURIN, P. J., HARKEMA, J. R., HOTCHKISS, J. A., HOOVER, M. & HENDERSON, R. 1993. Disposition of polycyclic aromatic hydrocarbons in the respiratory tract of the Beagle dog: II. The conducting airways. *Toxicology and applied pharmacology,* 121**,** 319-327.

GERDE, P. & SCHOLANDER, P. 1987. A mathematical model of the penetration of polycyclic aromatic hydrocarbons through the bronchial lining layer. *Environmental research,* 44**,** 321-334.

GRAINGER, C., GREENWELL, L., MARTIN, G. & FORBES, B. 2009. The permeability of large molecular weight solutes following particle delivery to air-interfaced cells that model the respiratory mucosa. *European Journal of Pharmaceutics and Biopharmaceutics,* 71**,** 318-324.

HEWER, S. C. L. & SMYTH, A. R. 2017. Antibiotic strategies for eradicating Pseudomonas aeruginosa in people with cystic fibrosis. *Cochrane Database of Systematic Reviews*.

HOUTMEYERS, E., GOSSELINK, R., GAYAN-RAMIREZ, G. & DECRAMER, M. 1999. Effects of drugs on mucus clearance. *European Respiratory Journal,* 14**,** 452-467.

KARLSSON, J., WIKMAN, A. & ARTURSSON, P. 1993. The mucus layer as a barrier to drug absorption in monolayers of human intestinal epithelial HT29-H goblet cells. *International journal of pharmaceutics,* 99**,** 209-218.

KEARNEY, P. & MARRIOTT, C. 1986. The effects of mucus glycoproteins on the bioavailability of tetracycline. I. Dissolution rate. *International journal of pharmaceutics,* 28**,** 33-40.

KEARNEY, P. & MARRIOTT, C. 1987. The effects of mucus glycoproteins on the bioavailability of tetracycline. III. Everted gut studies. *International journal of pharmaceutics,* 38**,** 211-220.

KIM, J. S., PETERS, T. M., O'SHAUGHNESSY, P. T., ADAMCAKOVA-DODD, A. & THORNE, P. S. 2013. Validation of an in vitro exposure system for toxicity assessment of air-delivered nanomaterials. *Toxicology in Vitro,* 27**,** 164-173.

LARHED, A. W., ARTURSSON, P. & BJÖRK, E. 1998. The influence of intestinal mucus components on the diffusion of drugs. *Pharmaceutical research,* 15**,** 66-71.

LARHED, A. W., ARTURSSON, P., GRÅSJÖ, J. & BJÖRK, E. 1997. Diffusion of drugs in native and purified gastrointestinal mucus. *Journal of pharmaceutical sciences,* 86**,** 660-665.

LEGEN, I. & KRISTL, A. 2001. Comparative permeability of some acyclovir derivatives through native mucus and crude mucin dispersions. *Drug development and industrial pharmacy,* 27**,** 669-674.

LIELEG, O., VLADESCU, I. & RIBBECK, K. 2010. Characterization of particle translocation through mucin hydrogels. *Biophysical journal,* 98**,** 1782-1789.

NIIBUCHI, J.-J., ARAMAKI, Y. & TSUCHIYA, S. 1986. Binding of antibiotics to rat intestinal mucin. *International journal of pharmaceutics,* 30**,** 181-187.

NOBAKHT M. GH, B. F., ALIANNEJAD, R., REZAEI-TAVIRANI, M., TAHERI, S. & OSKOUIE, A. A. 2015. The metabolomics of airway diseases, including COPD, asthma and cystic fibrosis. *Biomarkers,* 20**,** 5-16.

PATIL, T. S. & DESHPANDE, A. S. 2018. Nanostructured lipid carriers-based drug delivery for treating various lung diseases: A State-of-the-Art Review. *International journal of pharmaceutics*.

SLAYTER, H. S., LAMBLIN, G., TREUT, A. L., GALABERT, C., HOUDRET, N., DEGAND, P. & ROUSSEL, P. 1984. Complex

structure of human bronchial mucus glycoprotein. *European journal of biochemistry,* 142**,** 209-218.

WIKMAN, A., KARLSSON, J., CARLSTEDT, I. & ARTURSSON, P. 1993. A drug absorption model based on the mucus layer producing human intestinal goblet cell line HT29-H. *Pharmaceutical research,* 10**,** 843-852.

WORLITZSCH, D., TARRAN, R., ULRICH, M., SCHWAB, U., CEKICI, A., MEYER, K. C., BIRRER, P., BELLON, G., BERGER, J. & WEISS, T. 2002. Effects of reduced mucus oxygen concentration in airway Pseudomonas infections of cystic fibrosis patients. *The Journal of clinical investigation,* 109**,** 317-325.

ZHANG, A., SUN, H., YAN, G., WANG, P. & WANG, X. 2016. Mass spectrometry-based metabolomics: applications to biomarker and metabolic pathway research. *Biomedical Chromatography,* 30**,** 7-12.

Appendix I

Calibration curves
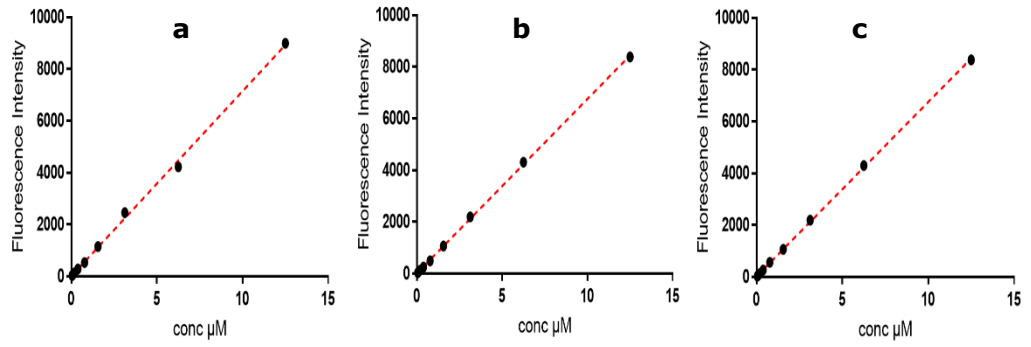
Figure A-1. Calibration curve of Lucifer yellow CH dipotassium used in the three volumetric designs. a :500/1500 μl, b: 250/1000 μl, and c: 50/500 μl, a: Y = 713.19 x + 13.44; R^2 = 0.9984, b: Y = 674.11 x + 14.35; R^2 = 0.9997, c: Y = 672.57 x + 27.71; R^2 = 0.9998.
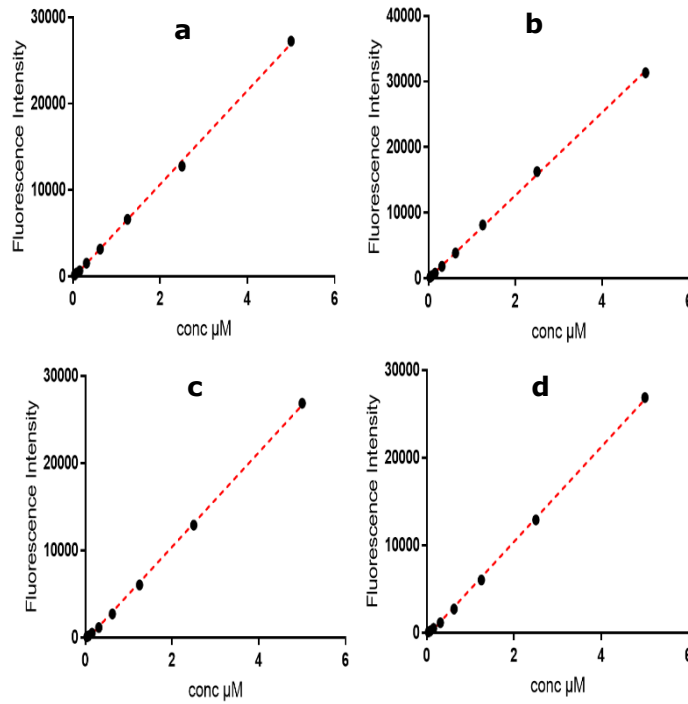
Figure A-2. Calibration curve of FITC used in the four mucus batch reproducibility experiments. a: Y = 5423.8 x - 186.5; R^2 = 0.9994, b: Y = 6328.4 x – 8.0994; R^2 = 0.9995, c: Y = 5412.2 x – 411.36; R^2 = 0.9993, and d: Y = 7066.9 x – 101.85; R^2 = 0.9994.
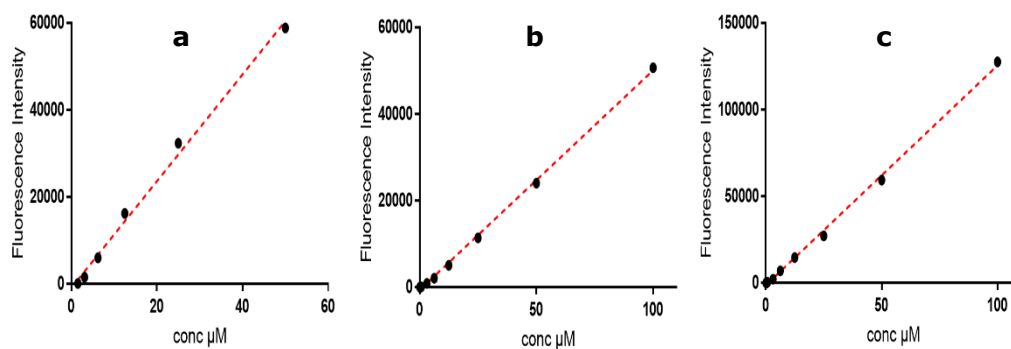
Figure A-3. Calibration Curve of a: Rhodamine B base, b: Rhodamine 123, and c: Rose Bengal standard solutions dissolved in HBSS. a: $Y = 1226.5\,x - 935.07$; $R^2 = 0.994$, b: $Y = 506.8\,x - 615.96$; $R^2 = 0.9988$, c: $Y = 1267.3\,x - 1293.3$; $R^2 = 0.9982$.
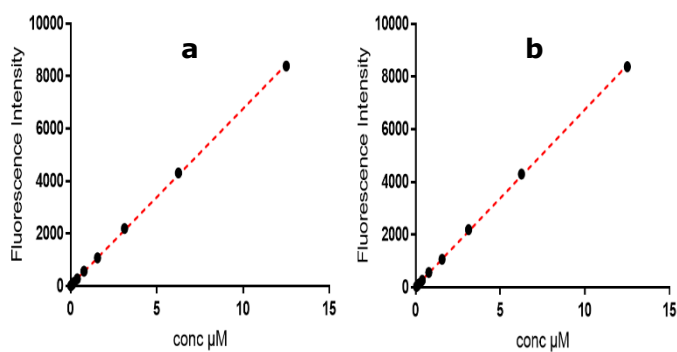
Figure A-4. Calibration Curve of Lucifer yellow CH a: dilithium salt; b: dipotassium salt dissolved in HBSS. a: $Y = 545.75\,x - 600.63$; $R^2 = 0.9925$, b: $Y = 672.57\,x + 27.71$; $R^2 = 0.9998$.
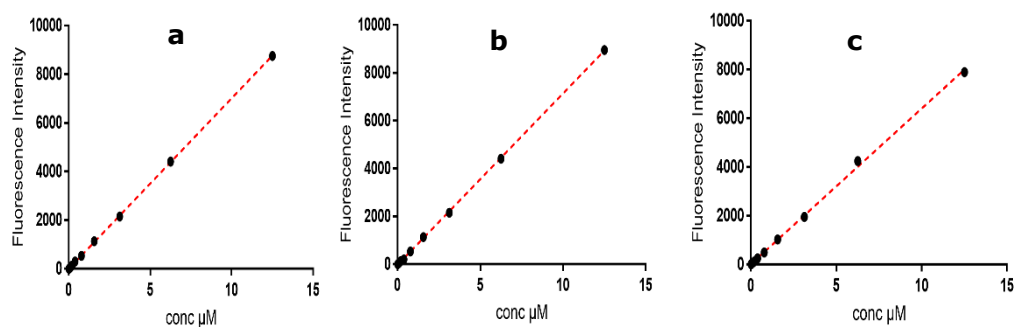
Figure A-5. Calibration curve of Lucifer yellow sprayed from a distance of 20 cm on 20 (a), 100 (b), and 50 (c) cm2 geometrical arrangements for deposition system validation. a: Y = 701.23 x + 0.9844; R^2 = 0.9999, b: Y = 715.96 x + 23.403; R^2 = 0.9998, and c: Y = 638.36 x + 19.666; R^2 = 0.9989.
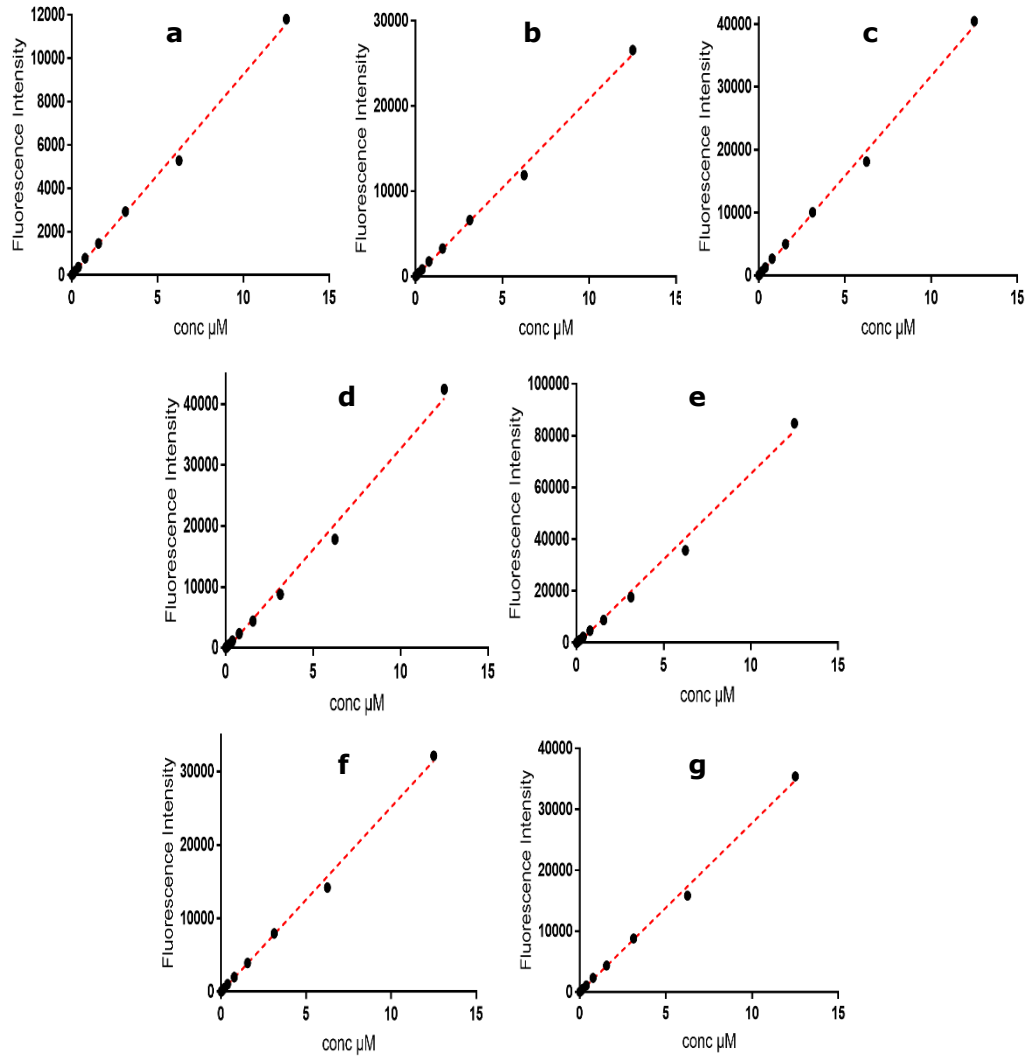
Figure A-6. Calibration curve of Lucifer yellow sprayed from a distance of 8 cm on 20 (a), 100 (b), and 50 (c) cm2 geometrical arrangements and up (d), down (e), right (f), and left (g) crescent shapes for the deposition system validation.a: $Y = 927.13\ x - 13.367$; $R^2 = 0.9967$, b: $Y = 2086\ x + 29.992$; $R^2 = 0.9976$, c: $Y = 3178.8\ x - 45.44$; $R^2 = 0.9976$, d: $Y = 3306.2\ x - 431.61$; $R^2 = 0.9938$, e: $Y = 6612.5\ x - 841.23$; $R^2 = 0.9938$, f: $Y = 2519.9\ x - 64.092$; $R^2 = 0.9970$, g: $Y = 2781.4\ x - 39.508$; $R^2 = 0.9976$.
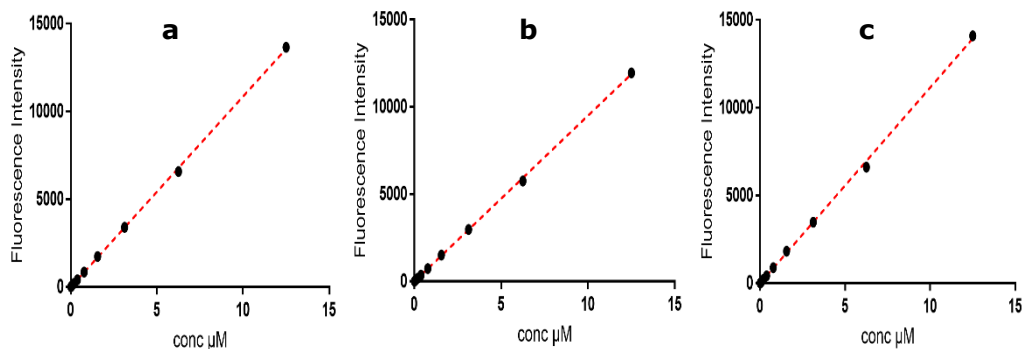
Figure A-7. Calibration curve of Lucifer yellow sprayed from a distance of 10 cm on 20 (a), 100 (b), and 50 (c) cm2 geometrical arrangements for the deposition system validation. a: Y = 1084.9 x + 0.5264; R^2 = 0.9997, b: Y = 949.27 x + 0.0584; R^2 = 0.9997, c: Y = 1114.9 x – 3.9996; R^2 = 0.9992.
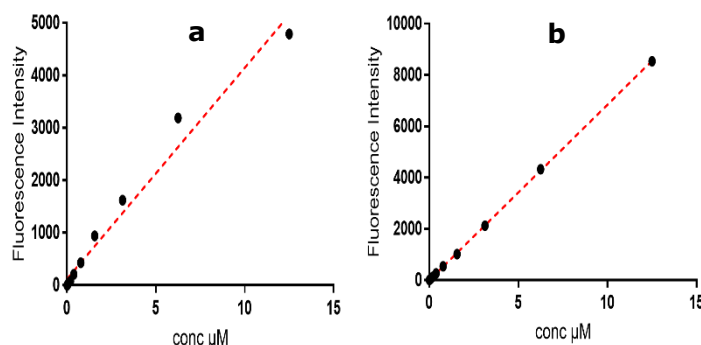
Figure A-8. Calibration curve of Lucifer yellow in the deposition system using mucus covered Transwell® inserts over five (a) and two (b) hour sampling time intervals.Figure. a: Y = 502.79 x – 146.69; R^2 = 0.9957, b: Y = 684.24 x – 6351; R^2 = 0.9999.
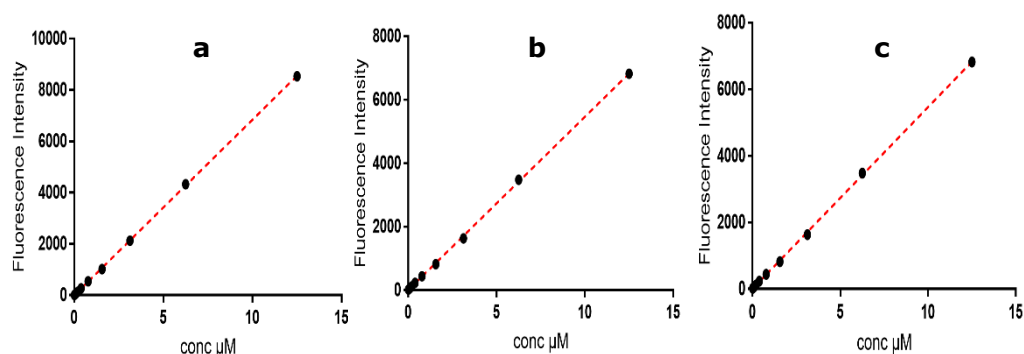
Figure A-9. Calibration curve of Lucifer yellow in the deposition system validation, reproducibility of the optimised system using three different mucus batches (a, b, and c). a: Y = 684.24 x – 6351; R^2 = 0.9999, b: Y = 545.91 x + 6.0196; R^2 = 0.9997, c: Y = 787.52 x + 1.8284; R^2 = 0.9999.
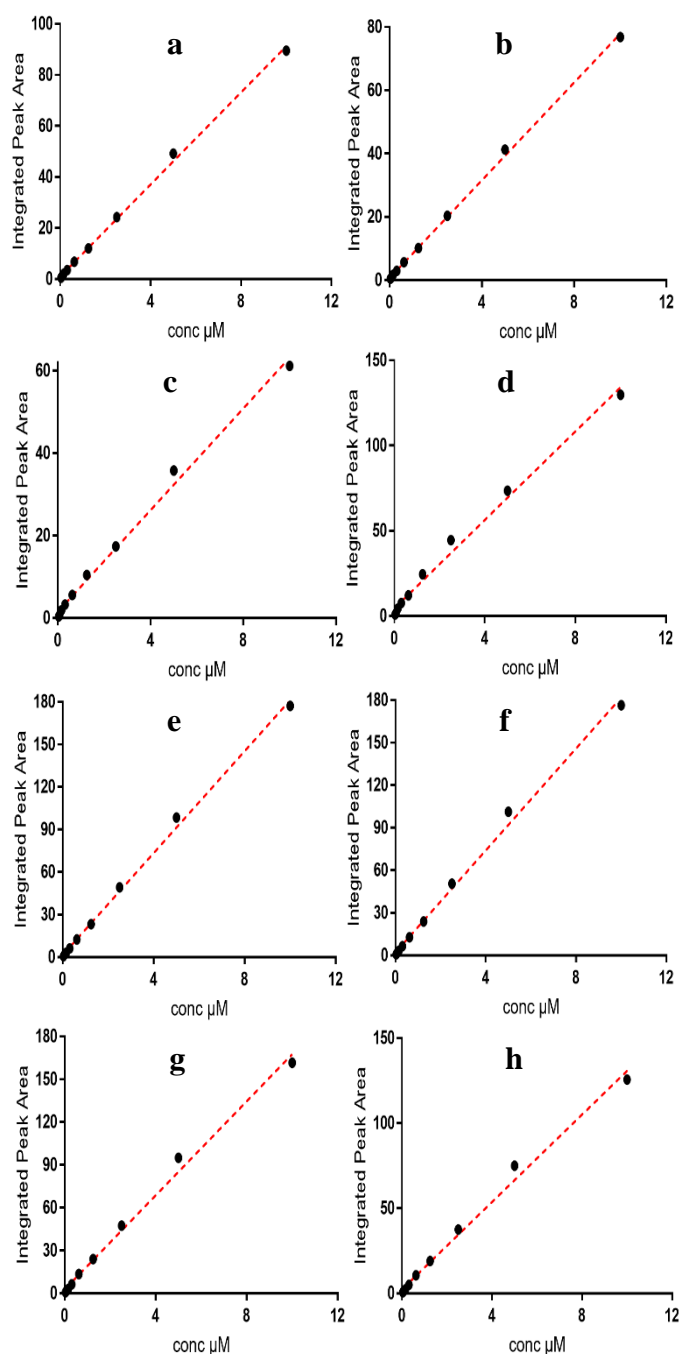
Figure A-10. Calibration curve of ipratropium bromide standard solutions dissolved in HBSS for the two spraying experiments using polyester Transwell® inserts with 0.4 µm sized pores. The two experimental results detailed are; 1) mucus covered Transwell® inserts; four replicates; (a), (b), (c), and (d) and 2) empty Transwell® inserts; four replicates; (e), (f), (g), and (h). a: Y = 9.0234 x + 1.0002; R² = 0.9981, b: Y = 7.7194 x + 0.7079; R² = 0.9989, c: Y = 6.1622 x + 1.5144; R² = 0.9937, d: Y = 12.966 x + 4.5234; R² = 0.9907, e: Y = 17.969 x + 1.5427; R² = 0.9972, f: Y = 17.984 x + 2.085; R² = 0.9951, g: Y = 16.473 x + 2.7945; R² = 0.9932, h: Y = 12.839 x + 2.373; R² = 0.9917.
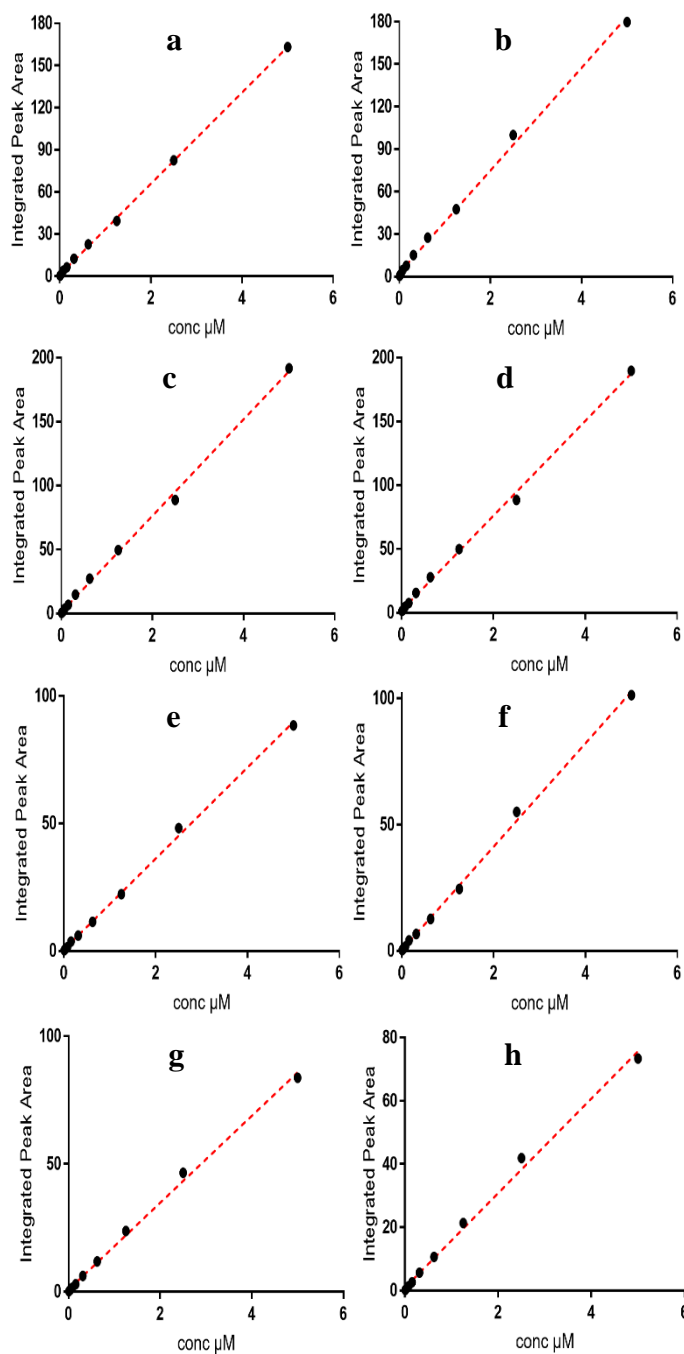
Figure A-11. Calibration curve of glycopyrronium bromide standard solutions dissolved in HBSS for the two spraying experiments using polyester Transwell® inserts with 0.4 μm sized pores. The two experiments are; 1) mucus covered Transwell® inserts; four replicates; (a), (b), (c), and (d) and 2) empty Transwell® inserts; four replicates; (e), (f), (g), and (h). a: Y = 32.47 x + 0.9431; R² = 0.9995, b: Y = 36.23 x + 2.4228; R² = 0.9973, c: Y = 37.705 x + 0.858; R² = 0.9981, d: Y = 37.14 x + 1.8451; R² = 0.9981, e: Y = 17.863 x + 0.5022; R² = 0.9984, f: Y = 20.463 x + 0.3393; R² = 0.9983, g: Y = 16.999 x + 0.8109; R² = 0.997, h: Y = 14.956 x + 0.8721; R² = 0.9953.
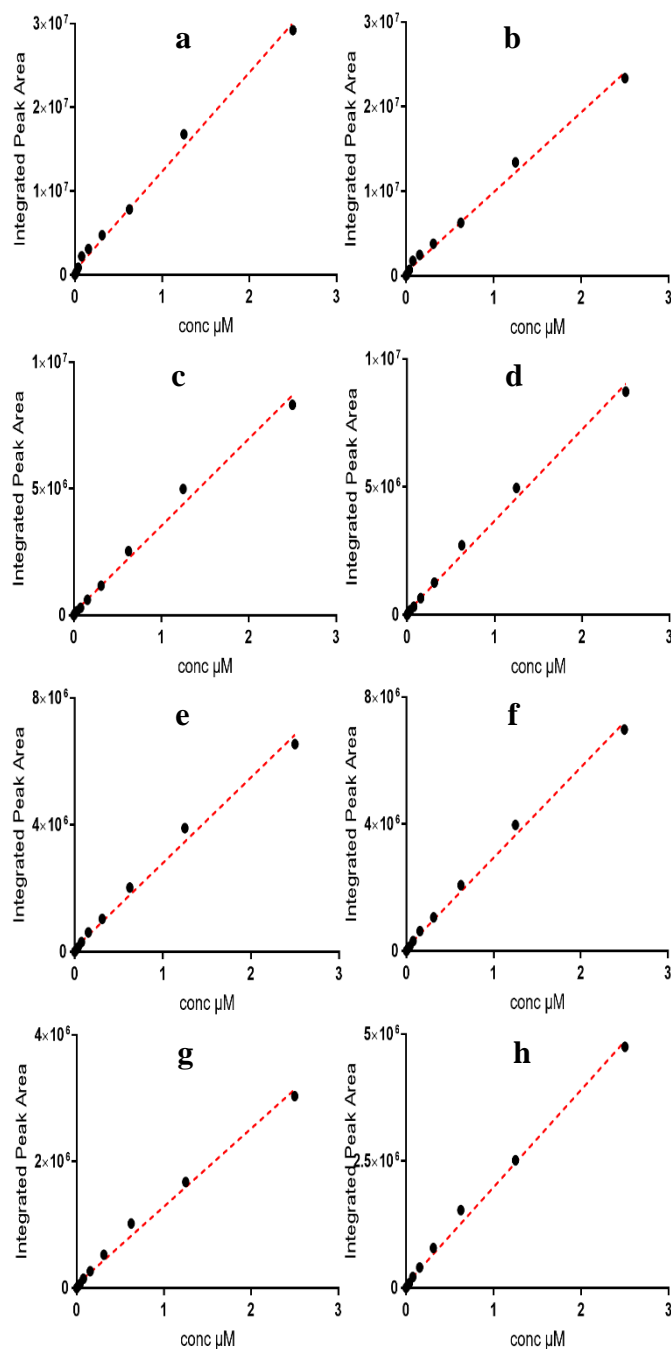
Figure A-12. Calibration curve of salbutamol sulphate standard solutions dissolved in HBSS for the two spraying experiments using polyester Transwell® inserts with 0.4 μm sized pores. The two experiments were; 1) mucus covered Transwell® inserts; four replicates; (a), (b), (c), and (d) and 2) empty Transwell® inserts; four replicates; (e), (f), (g), and (h). a: Y = (1×10⁷) x + 550325; R² = 0.9938, b: Y = (9×10⁶) x + 440680; R² = 0.9938, c: Y = (3×10⁶) x + 93458; R² = 0.9915, d: Y = (4×10⁶) x + 100947; R² = 0.9944, e: Y = (3×10⁶) x + 108113; R² = 0.9914, f: Y = (3×10⁶) x + 93623; R² = 0.9951, g: Y = (1×10⁶) x + 53957; R² = 0.9918, h: Y = (2×10⁶) x + 69834; R² = 0.9946.
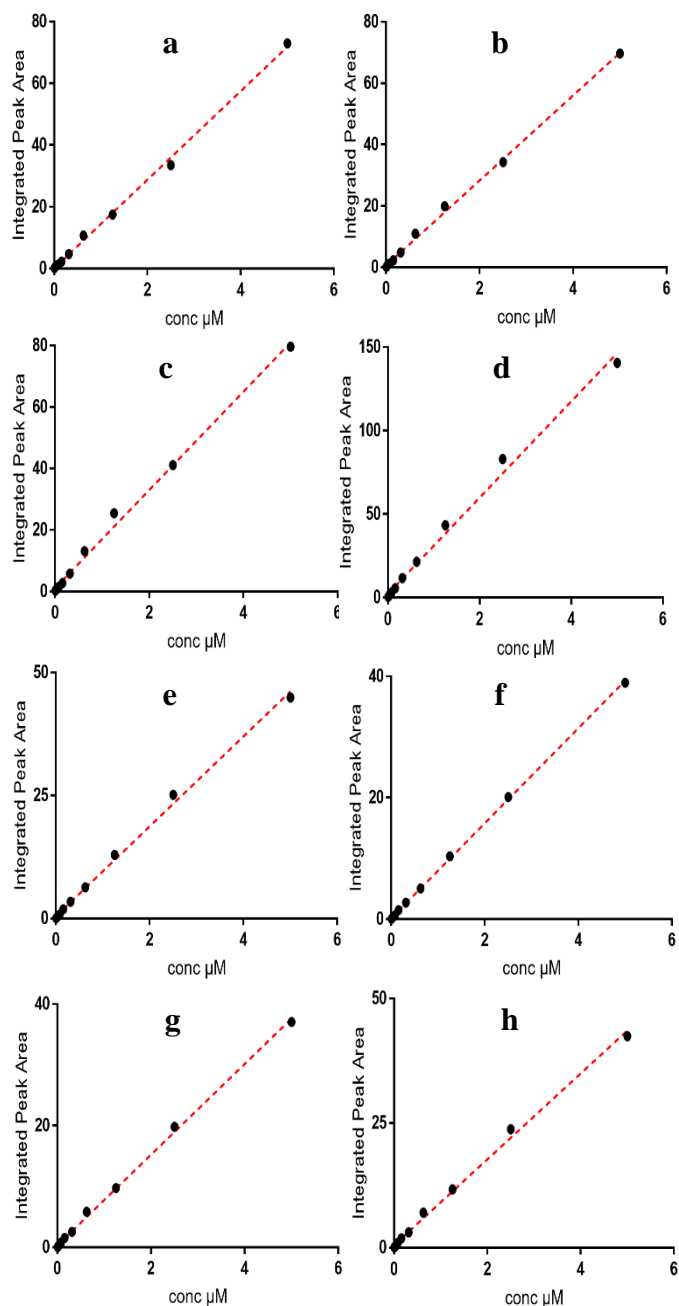
Figure A-13. Calibration curve of formoterol standard solutions dissolved in HBSS containing 10% of DMSO for the two spraying experiments using polyester Transwell® inserts with 0.4 µm sized pores. The two experiments were; 1) mucus covered Transwell® inserts; four replicates; (a), (b), (c), and (d) and 2) empty Transwell® inserts; four replicates; (e), (f), (g), and (h). a: Y = 14.34 x + 0.1057; R^2 = 0.9979, b: Y = 13.862 x + 0.5763; R^2 = 0.9981, c: Y = 15.982 x + 1.0661; R^2 = 0.9952, d: Y = 28.804 x + 2.2493; R^2 = 0.9927, e: Y = 9.1441 x + 0.4379; R^2 = 0.9966, f: Y = 7.8214 x + 0.1632; R^2 = 0.9996, g: Y = 7.4568 x + 0.3165; R^2 = 0.9984, h: Y = 8.6108 x + 0.5046; R^2 = 0.9963.
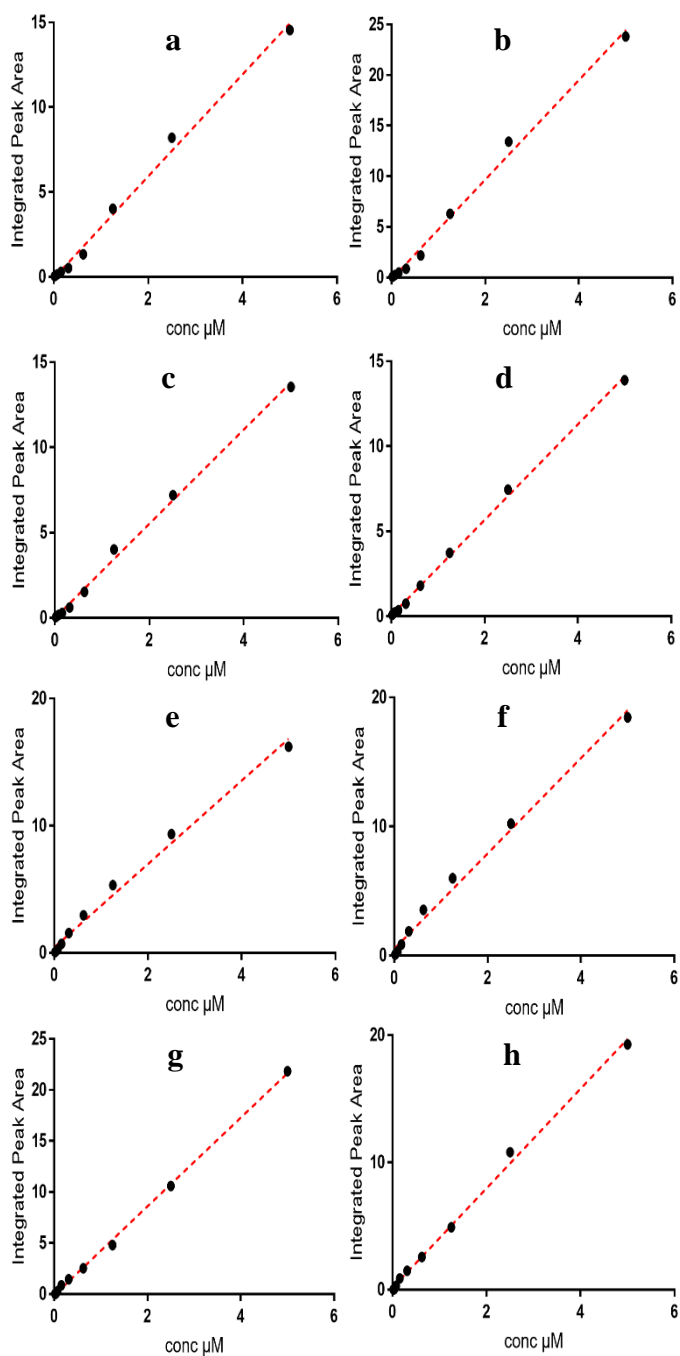
Figure A-14. Calibration curve of indacaterol maleate standard solutions dissolved in HBSS containing 10% of DMSO for the two spraying experiments using polyester Transwell® inserts with 0.4 µm sized pores. The two experiments are; 1) mucus covered Transwell® inserts; four replicates; (a), (b), (c), and (d) and 2) empty Transwell® inserts; four replicates; (e), (f), (g), and (h). a: Y = 3.0089 x – 0..0903; R² = 0.994, b: Y = 4.921 x – 0.1761; R² = 0.9945, c: Y = 7.7621 x – 0.0619; R² = 0.9965, d: Y = 2.8141 x + 0.0382; R² = 0.9985, e: Y = 3.2789 x + 0.4297; R² = 0.9902, f: Y = 3.695 x + 0.5149; R² = 0.9915, g: Y = 4.348 x – 0.1029; R² = 0.9988, h: Y = 3.9107 x + 0.1431; R² = 0.9967.
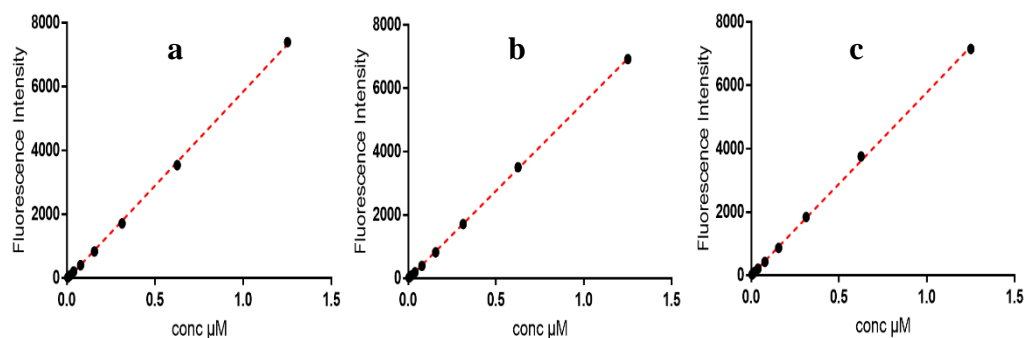
Figure A-15. Calibration curve of FITC standard solutions dissolved in HBSS with different DMSO concentrations were as follows; 0.1%, 1.0%, and 10% DMSO for (a), (b) and (c), respectively. a: Y = 5901.2 x –50.489; R^2 = 0.9994, b: Y = 5561.8 x – 17.717; R^2 = 0.9999, c: Y = 5776.9 x + 4.5613; R^2 = 0.9994.
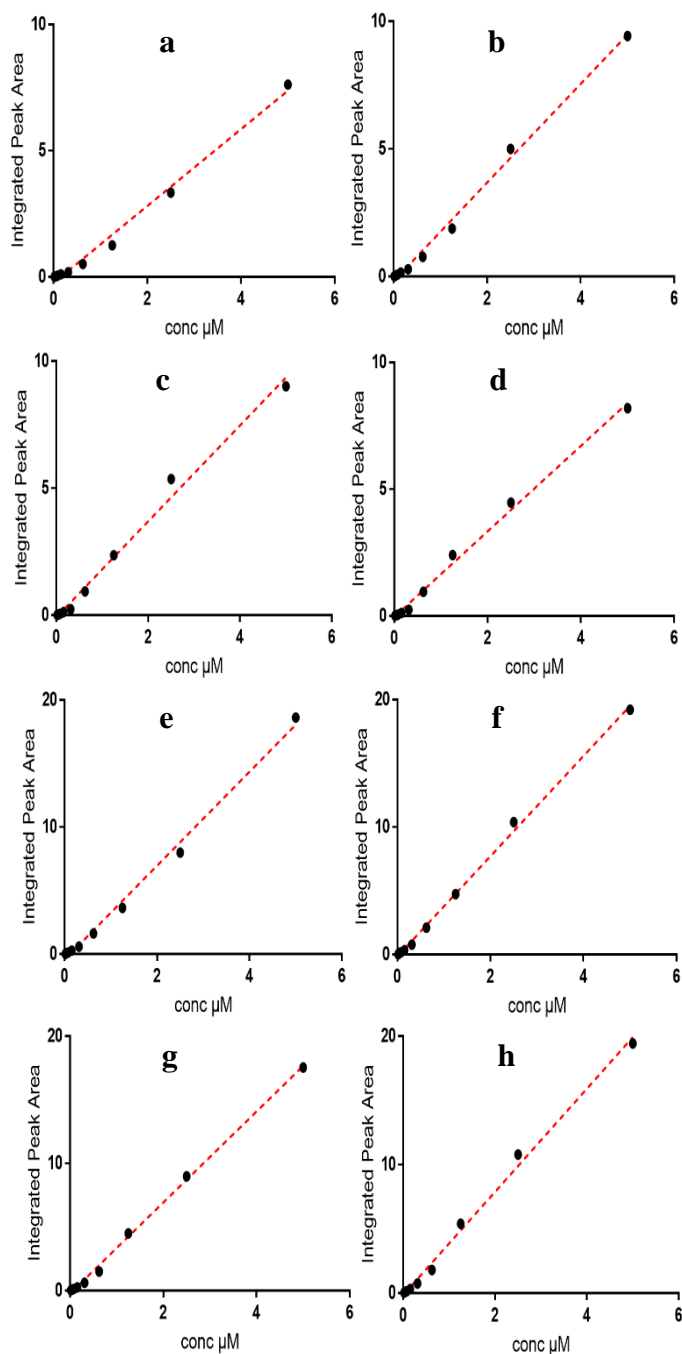
Figure A-16. Calibration curve of indacaterol maleate standard solutions dissolved in HBSS containing 10% of DMSO for the two spraying experiments using polyester Transwell® inserts 3.0 μm sized pores. The two experiments were; 1) mucus covered Transwell® inserts; four replicates; (a), (b), (c), and (d) and 2) empty Transwell® inserts; four replicates; (e), (f), (g), and (h). a: Y = 1.5218 x – 0.2323; R² = 0.9913, b: Y = 1.9331 x – 0.183; R² = 0.9953, c: Y = 1.8863 x – 0.0766; R² = 0.9904, d: Y = 1.6868 x – 0.0766; R² = 0.9904, e: Y = 3.6973 x – 0.4353; R² = 0.9943, f: Y = 3.9327 x – 0.1525; R² = 0.9978, g: Y = 3.5765 x – 0.2238; R² = 0.998, h: Y = 4.0122 x – 0.1363; R² = 0.995.
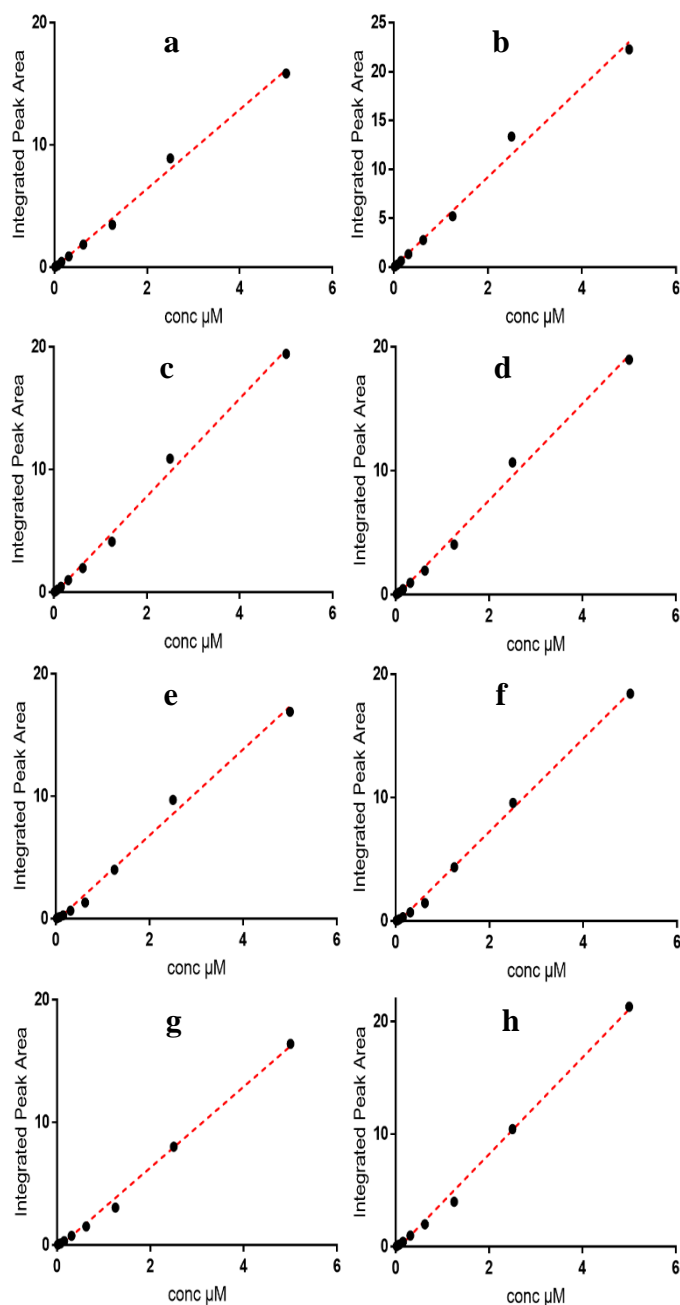
Figure A-17. Calibration curve of indacaterol maleate standard solutions dissolved in HBSS containing 10% of DMSO for the two spraying experiments using polycarbonate Transwell® inserts with 3.0 μm sized pores. The two experiments were; 1) mucus covered Transwell® inserts; four replicates; (a), (b), (c), and (d) and 2) empty Transwell® inserts; four replicates; (e), (f), (g), and(h). a: Y = 3.2431 x – 0.0668; R² = 0.9953, b: Y = 4.6025 x – 0.0238; R² = 0.991, c: Y = 3.9923 x – 0.1829; R² = 0.9946, d: Y = 3.8985 x – 0.1726; R² = 0.9944, e: Y = 3.5112 x – 0.2121; R² = 0.9925, f: Y = 3.7648 x – 0.273; R² = 0.9976, g: Y = 3.2998 x – 0.2839; R² = 0.9964, h: Y = 4.2898 x – 0.3691; R² = 0.9964.
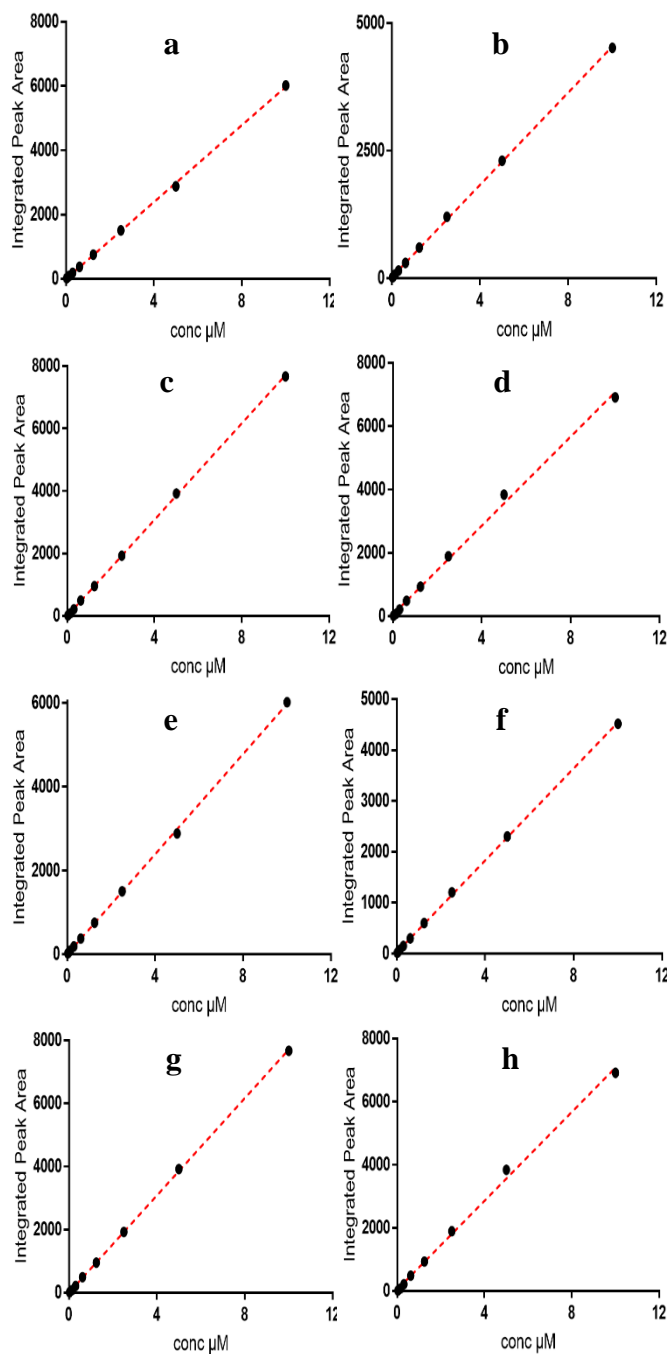
Figure A-18. Calibration curve of ipratropium bromide standard solutions dissolved in HBSS for the two spraying experiments using polyester Transwell®️ inserts with 3.0 μm sized pores. The two experiments were; 1) mucus covered Transwell®️ inserts; four replicates; (a), (b), (c), and (d) and 2) empty Transwell®️ inserts; four replicates; (e), (f), (g), and (h). a: Y = 598.39 x – 5.045; R² = 0.9996, b: Y = 452.5 x + 20.77; R² = 0.997, c: Y = 771.31 x – 3.9052; R² = 0.9998, d: Y = 703.46 x + 45.784; R² = 0.9971, e: Y = 396.05 x – 26.739; R² = 0.9994, f: Y = 245.66 x – 0.8377; R² = 0.9976, g: Y = 194.93 x + 13.663; R² = 0.9989, h: Y = 185.35 x + 8.0739; R² = 0.9972.
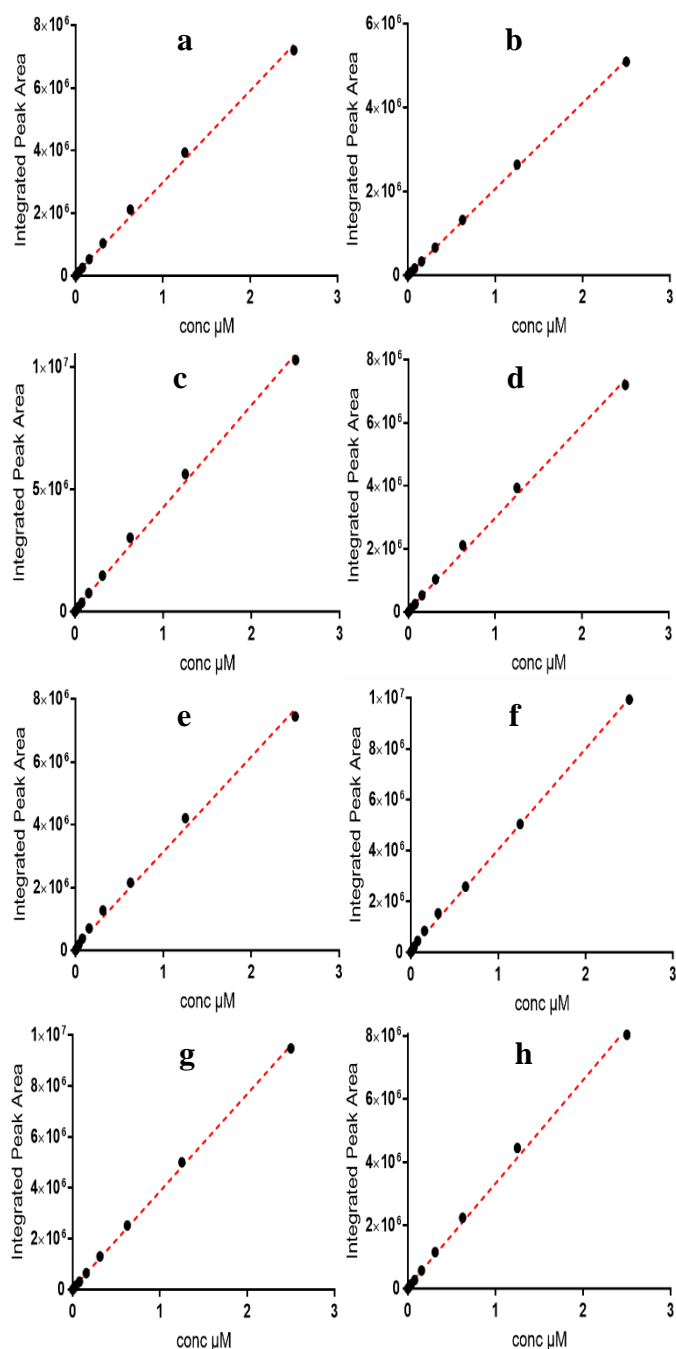
Figure A-19. Calibration curve of salbutamol sulphate standard solutions dissolved in HBSS for the two spraying experiments using polyester Transwell® inserts with 3.0 μm sized pores. The two experiments were; 1) mucus covered Transwell® inserts; four replicates; (a), (b), (c), and (d) and 2) empty Transwell® inserts; four replicates; (e), (f), (g), and (h). a: Y = (3×10⁶) x + 30925; R² = 0.9986, b: Y = (2×10⁶) x + 10546; R² = 0.9997, c: Y = (4×10⁶) x + 121369; R² = 0.9971, d: Y = (3×10⁶) x + 57327; R² = 0.9971, e: Y = (3×10⁶) x + 108113; R² = 0.995, f: Y = (4×10⁶) x + 90137; R² = 0.999, g: Y = (4×10⁶) x + 38257; R² = 0.9992, h: Y = (3×10⁶) x + 56251; R² = 0.9973.
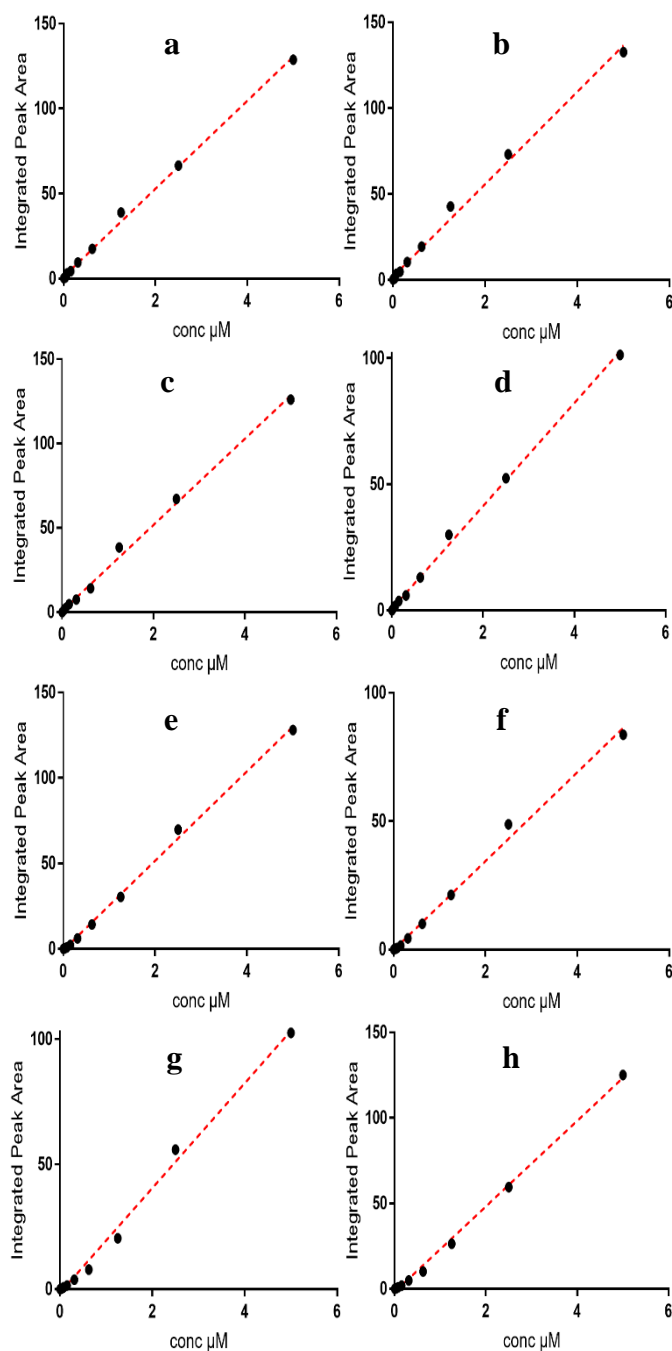
Figure A-20. Calibration curve of formoterol standard solutions dissolved in HBSS containing 10% of DMSO for the two spraying experiments using polyester Transwell® inserts with 3.0 µm sized pores. The two experiments were; 1) mucus covered Transwell® inserts; four replicates; (a), (b), (c), and (d) and 2) empty Transwell® inserts; four replicates; (e), (f), (g), and (h). a: Y = 25.868 x + 1.1566; R² = 0.9979, b: Y = 29.937 x + 1.8377; R² = 0.9944, c: Y = 25.56 x + 0.6245; R² = 0.9965, d: Y = 20.419 x + 0.503; R² = 0.998, e: Y = 26.17 x – 0.7982; R² = 0.9977, f: Y = 17.307 x – 0.1844; R² = 0.9942, g: Y = 20.963 x – 1.4941; R² = 0.9938, h: Y = 25.049 x – 1.8499; R² = 0.9974.

Appendix II

Metabolomics data

Table A-1. List of authentic standards mixture (group 1)

Metabolite	Formula	Molecular weight
2-Ethylhexyl phthalate	C16H22O4	278.1518
Menadione	C11H8O2	172.0524
Melatonin	C13H16N2O2	232.1212
N-Acetyl-L-phenylalanine	C11H13NO3	207.0895
4-Aminobenzoate	C7H7NO2	165.079
Glutarate	C5H8O4	132.0423
4-Aminohippuricacid	C9H10N2O3	194.0691
3-Methoxytyramine	C9H13NO2	167.0946
Deoxyuridine	C9H12N2O5	228.0746
5-Hydroxyindoleacetate	C10H9NO3	191.0582
O-Butanoylcarnitine	C11H21NO4	231.1471
Inosine	C10H12N4O5	268.0808
[FA (10:0)] O-decanoyl-R-carnitine	C17H33NO4	315.241
5'-Methylthioadenosine	C11H15N5O3S	297.0896
Dopamine	C9H11NO4	197.0688
Biopterin	C9H11N5O3	237.0862
L-Rhamnose	C6H12O5	164.0685
Hexanoylcarnitine	C13H25NO4	259.1784
Adenosine	C10H13N5O4	267.0968
1H-Imidazole-4-ethanamine	C5H9N3	111.0796
Imidazole	C3H4N2	68.03745
L-Leucine	C6H13NO2	131.0946
L-Methionine	C5H11NO2S	149.051
Guanine	C5H5N5O	151.0494
5-Methoxytryptamine	C11H14N2O	190.1106
L-Proline	C5H9NO2	115.0633
L-Lysine	C6H15N2O2	146.1055
sn-Glycero-3-Phosphocholine	C8H20NO6P	257.1028
Imidazole-4-acetate	C5H6N2O2	126.0429
Glycine	C2H5NO2	75.03203
Serotonin	C10H12N2O	176.095
Creatinine	C4H7N3O	113.0589
Guanidinoacetate	C3H7N3O2	117.0538
Cytidine	C9H13N3O5	243.0855
L-Cystathionine	C7H14N2O4S	222.0674
Cadaverine	C5H14N2	102.1157
Putrescine	C4H12N2	88.10005
D-Glucosamine	C6H13NO5	179.0794
L-Arginine	C6H14N4O2	174.1117
L-Methionine sulfone	C4H9NO5S	181.0409

Table A-1. (Cont.) List of authentic standards mixture (group 1)

Metabolite	Formula	Molecular weight
Methylglyoxal	C3H4O2	72.02113
N-Acetylputrescine	C6H14N2O	130.1106
Phenylhydrazine	C6H8N2	108.0687
Spermidine	C7H19N3	145.1579
Thiamine	C12H17N4OS	265.1123
Phenolsulfonphthalein	C19H14O5S	354.0562
[ST hydrox] 3alpha,7alpha-Dihydroxy-5beta-cholan-24-oic Acid	C24H40O4	392.2927
1-Naphthylacetic acid	C12H10O2	186.0681
3-Methyl-2-oxobutanoic acid	C5H8O3	116.11520
3-Hydroxyphenylacetate	C8H8O3	152.0473
3-(4-Hydroxyphenyl)pyruvate	C9H8O4	180.0423
Acetylcysteine	C5H9NO3S	163.0303
Fumarate	C4H4O4	116.011
3-(3-Hydroxy-phenyl)-propanoic acid	C9H10O3	166.063
(R)-Lactate	C3H6O3	90.03169
3,4-Dihydroxyphenylacetate	C8H8O4	168.0423
3-Methoxy-4-Hydroxyphenylglycolsulfate	C9H12O7S	264.0304
Malonate	C3H4O4	104.011
(R)-2-Hydroxyglutarate	C5H8O5	148.0372
2-Oxoglutarate	C5H6O5	146.0215
Glycolate	C2H4O3	76.01604
Orotate	C5H4N2O4	156.0171
Pyrazinoate	C5H4N2O2	124.0273
Uridine	C9H12N2O6	244.0695
D-Glycerate	C3H6O4	106.0266
Gallate	C7H6O5	170.0215
3,4-Dihydroxymandelate	C8H8O5	184.0372
2-Methylcitrate	C7H10O7	206.0427
N-Acetyl-D-glucosamine	C8H15NO6	221.0899
D-Erythrose	C4H8O4	120.0423
Glyoxylate	C2H2O3	74.00039
Mannitol	C6H14O6	182.079
MOPS	C7H15NO4S	209.0722
Pyridoxal phosphate	C8H10NO6P	247.0246
D-Gluconic acid	C6H12O7	196.0583
D-Ribose 5-phosphate	C5H11O8P	230.0192
D-Galactarate	C6H10O8	210.0376
Taurine	C2H7NO3S	125.0147
N6-Acetyl-L-lysine	C8H16N2O3	188.1161
Adenine	C5H5N5	135.0545

Table A-1. (Cont.) List of authentic standards mixture (group 1)

Metabolite	Formula	Molecular weight
L-Glutamate	C5H9NO4	147.0532
Pyridoxine	C8H11NO3	169.0739
Ethanolamine phosphate	C2H8NO4P	141.0191
L-Citrulline	C6H13N3O3	175.0957
L-2-Aminoadipate	C6H11NO4	161.0688
L-Histidine	C6H9N3O2	155.0695
L-2,4-Diaminobutanoate	C4H10N2O2	118.0742
L-2,3-Diaminopropanoate	C3H8N2O2	104.0586
L-Threonine	C4H9NO3	119.0582
2,3-Bisphospho-D-glycerate	C3H8O10P2	265.9593
2-Oxoadipate	C6H8O5	160.0372
3-Phospho-D-glycerate	C3H7O7P	185.9929
4-Hydroxybutanoic acid	C4H7O3	103.0395
ATP	C10H16N5O13P3	506.9957
CoA	C21H36N7O16P3S	767.1152
Glycerol	C3H8O3	92.04734
GTP	C10H16N5O14P3	522.9907
Indoxylsulfate	C8H7NO4S	213.0096
(S)-Malate	C4H6O5	134.0215
NAD+	C21H27N7O14P2	664.1169
Phosphate	O4P	94.95342
Phosphoenolpyruvate	C3H5O6P	167.9824
Sorbitol 6-phosphate	C6H15O9P	262.0454

Table A-2. List of authentic standards mixture (group 2)

Metabolite	Formula	Molecular weight
Picolinic acid	C6H5NO2	123.032
Hypoxanthine	C5H4N4O	136.0385
Deoxyguanosine	C10H13N5O4	267.0968
Deoxyadenosine	C10H13N5O3	251.1018
Guanosine	C10H13N5O5	283.0917
5-Methoxytryptamine	C11H14N2O	190.1106
L-Tyrosine	C9H11NO3	181.0739
L-Valine	C5H11NO2	117.079
1,3-Diaminopropane	C3H10N2	74.0844
L-Homoserine	C4H9NO3	119.0582
L-Metanephrine	C10H15NO3	197.1052
1-Aminocyclopropane-1-carboxylate	C4H7NO2	101.0477
L-Asparagine	C4H8N2O3	132.0535
L-Serine	C3H7NO3	105.0426
4-Trimethylammoniobutanoate	C7H15NO2	146.1181
N-Acetylornithine	C7H14N2O3	174.1004
Methylguanidine	C2H7N3	73.064
D-Glucosamine 6-phosphate	C6H14NO8P	259.0457
L-Cystine	C6H12N2O4S2	240.0238
1-Aminopropan-2-ol	C3H9NO	75.06841
Cytosine	C4H5N3O	111.0433
HEPES	C8H18N2O4S	238.0987
meso-2,6-Diaminoheptanedioate	C7H14N2O4	190.0954
L-Ornithine	C5H12N2O2	132.0899
Deoxycarnitine	C7H16NO2	146.1181
FAD	C27H33N9O15P2	785.1571
Guanidine	CH5N3	59.04835
Spermine	C10H26N4	202.2157
Taurocholate	C26H45NO7S	515.2917
[ST hydrox] 3alpha,12alpha-Dihydroxy-5beta-cholan-24-oic Acid	C24H40O4	392.2927
Lipoate	C8H14O2S2	206.0435
Mesaconate	C5H6O4	130.0266
Succinate	C4H6O4	118.0266
Thymine	C5H6N2O2	126.0429
5-Oxoproline	C5H7NO3	129.0426
N-Acetylglutamine	C7H12N2O4	188.0797
Folate	C19H19N7O6	441.1397
Orotidine	C10H12N2O8	288.0594
Uracil	C4H4N2O2	112.0273
2-Deoxy-D-glucose	C6H12O5	164.0685

Table A-2. (Cont.) List of authentic standards mixture (group 2)

Metabolite	Formula	Molecular weight
4-Hydroxyphenylacetate	C8H8O3	152.0473
Acetyl-CoA	C23H38N7O17P3S	809.1258
ADP	C10H15N5O10P2	427.0294
Biotin	C10H16N2O3S	244.0882
CTP	C9H16N3O14P3	482.9845
D-Fructose 1,6-bisphosphate	C6H14O12P2	339.996
Glyceraldehyde	C3H6O3	90.03169
IDP	C10H14N4O11P2	428.0134
L-Gulono-1,4-lactone	C6H10O6	178.0477
N6-Methyl-L-lysine	C7H16N2O2	160.1212
myo-Inositol	C6H12O6	180.0634
Oxalate	C2H2O4	89.99531
Oxaloacetate	C4H4O5	132.0059
Phenylacetylglycine	C10H11NO3	193.0739
UDP-Glucose	C15H24N2O17P2	566.055

Table A-3. List of authentic standards mixture (group 3)

Metabolite	Formula	Molecular weight
2-hydroxyethyldisulfide	C4H10O2S2	154.0122
O-Acetyl-L-serine	C5H9NO4	147.0532
dGMP	C10H14N5O7P	347.0631
dAMP	C10H14N5O6P	331.0682
Betaine	C5H11NO2	117.079
L-Homocysteine	C4H9NO2S	268.0551
L-Cysteine	C3H7NO2S	121.0197
O-Acetylcarnitine	C9H17NO4	203.1158
L-Glutamine	C5H10N2O3	146.0691
L-Alanine	C3H7NO2	89.04768
L-Carnitine	C7H15NO3	161.1052
5-Aminolevulinate	C5H9NO3	131.0582
S-Adenosyl-L-homocysteine	C14H20N6O5S	384.1216
L-Noradrenaline	C8H11NO3	169.0739
S-Adenosylmethioninamine	C14H22N6O3S	355.1552
Benzoate	C7H6O2	122.0368
Maleic acid	C4H4O4	116.011
4-Coumarate	C9H8O3	164.0473
2-Oxobutanoate	C4H6O3	102.0317
Itaconate	C5H6O4	130.0266
Pyruvate	C3H4O3	88.01604
N-Acetyl-L-glutamate	C7H11NO5	189.0637
Isonicotinic acid	C6H5NO2	123.032
FMN	C17H21N4O9P	456.1046
L-Dehydroascorbate	C6H6O6	174.0164
Ascorbate	C6H8O6	176.0321
D-Fructose	C6H12O6	180.0634
3',5'-Cyclic AMP	C10H12N5O6P	329.0525
IMP	C10H13N4O8P	348.0471
GMP	C10H14N5O8P	363.058
CMP	C9H14N3O8P	323.0519
Homocystine	C8H16N2O4S2	268.0551
Glycylglycine	C4H8N2O3	132.0535
UDP	C9H14N2O12P2	404.0022
NADPH	C21H30N7O17P3	745.0911
D-Glucono-1,4-lactone	C12H20O2	196.1463

Table A-4. List of authentic standards mixture (group 4)

Metabolite	Formula	Molecular weight
Lipoamide	C8H15NOS2	205.0595
L-Kynurenine	C10H12N2O3	208.0848
Selenomethionine	C5H11NO2Se	196.9955
L-Tryptophan	C11H12N2O2	204.0899
L-Isoleucine	C6H13NO2	131.0946
L-Normetanephrine	C9H13NO3	183.0895
L-Phenylalanine	C9H11NO2	165.079
Glutathione disulfide	C20H32N6O12S2	307.0838
Choline phosphate	C5H15NO4P	184.0739
2-Aminobutan-4-olide	C4H7NO2	102.0555
N(pi)-Methyl-L-histidine	C7H11N3O2	169.0851
Urea	CH4N2O	60.03236
Agmatine	C5H14N4	130.1218
Phenylpyruvate	C9H8O3	164.0473
Leucinicacid	C6H12O3	132.0786
Salicyluric acid I have found it as 2-Hydroxyhippuric acid	C9H9NO4	195.0532
Hippurate	C9H9NO3	179.0582
Alpha-Hydroxyisobutyricacid	C4H8O3	104.0473
Methylmalonate	C4H6O4	118.0266
Pantothenate	C9H17NO5	219.1107
3-Methoxy-4-hydroxymandelate	C9H10O5	198.0528
Thymidine	C10H14N2O5	242.0903
4-Hydroxyphenylacetate	C8H8O3	152.0473
trans-Aconitate	C6H6O6	174.0164
Xanthine	C5H4N4O2	152.0334
UMP	C9H13N2O9P	324.0359
D-Glucose	C6H12O6	180.0634
D-Galacturonate	C6H10O7	194.0427
D-Fructose 6-phosphate	C6H13O9P	260.0297
AMP	C10H14N5O7P	347.0631
Acetaldehyde	C2H4O	44.02621
CDP	C9H15N3O11P2	403.0182
Deoxyribose	C5H10O4	134.0579
GDP	C10H15N5O11P2	443.0243
isobutanal	C4H8O	72.05751
Mercaptoethanol	C2H6OS	78.01394
NADH	C21H29N7O14P2	665.1248
NADP+	C21H28N7O17P3	745.0911
Sarcosine	C3H7NO2	89.04768

Table A-5. List of authentic standards mixture (group 5)

Metabolite	Formula	Molecular weight
Nicotinamide	C6H6N2O	122.048
Glutathione	C10H17N3O6S	612.152
Xanthosine	C10H12N4O6	284.0757
homovanillate	C9H10O4	182.0579
3',5'-Cyclic GMP	C10H12N5O7P	345.0474
Urate	C5H4N4O3	168.0283
D-Arabinose	C5H10O5	150.0528
L-Norleucine	C6H13NO2	131.0946
D-Galactose	C6H12O6	180.0634
D-glucose 6-phosphate	C6H13O9P	260.0297
DL-Glyceraldehyde 3-phosphate	C3H7O6P	169.998
L-Adrenaline	C9H13NO3	169.0739
(R)-Acetoin	C4H8O2	88.05243
1-Butanol	C4H10O	74.07316
Octadecanoic acid	C18H36O2	284.2715
Pyrophosphate	O7P2	173.9119
UTP	C9H15N2O15P3	483.9685
Ne,Ne dimethyllysine	C8H18N2O2	173.1295

Table A-6. Positive mode detected standard metabolites with their formula, and Coefficient of Variation error of peak area and retention time.

Metabolite	Formula	Peak Area CV%	Retention Time CV%
2-Ethylhexyl phthalate	C16H22O4	4.26	0.32
Melatonin	C13H16N2O2	2.87	0.35
N-Acetyl-L-phenylalanine	C11H13NO3	6.60	0.31
4-Aminobenzoate	C7H7NO2	13.96	0.25
Glutarate	C5H8O4	33.47	0.13
4-Aminohippuricacid	C9H10N2O3	34.96	0.18
O-Butanoylcarnitine	C11H21NO4	14.45	0.48
Inosine	C10H12N4O5	14.62	0
5'-Methylthioadenosine	C11H15N5O3S	1.44	0.19
Adenosine	C10H13N5O4	11.52	0
Imidazole	C3H4N2	6.68	0.17
Guanine	C5H5N5O	10.6	0.22
L-Proline	C5H9NO2	11.5	0
L-Lysine	C6H15N2O2	10.44	0.07
sn-Glycero-3-Phosphocholine	C8H20NO6P	3.87	0.14
Imidazole-4-acetate	C5H6N2O2	15.21	0
Glycine	C2H5NO2	15.40	0.14
Creatinine	C4H7N3O	9.60	0
Guanidinoacetate	C3H7N3O2	16.32	0
Cytidine	C9H13N3O5	15.11	0
L-Cystathionine	C7H14N2O4S	4.79	0.26
D-Glucosamine	C6H13NO5	5.19	0.29
L-Arginine	C6H14N4O2	6.68	0.18
Phenolsulfonphthalein	C19H14O5S	13.39	0.08
[ST hydrox] 3alpha,7alpha-Dihydroxy-5beta-cholan-24-oic Acid	C24H40O4	10.6	0.32
3-Hydroxyphenylacetate	C8H8O3	12.8	0.22
3-(3-Hydroxy-phenyl)-propanoic acid	C9H10O3	13.83	16.77
(R)-Lactate	C3H6O3	6.1	0
(R)-2-Hydroxyglutarate	C5H8O5	7.41	0.43
pyrazinoate	C5H4N2O2	20.32	0.21
Uridine	C9H12N2O6	20.62	0.27
D-Glycerate	C3H6O4	17.99	0.39
3,4-Dihydroxymandelate	C8H8O5	10.67	0.29
2-Methylcitrate	C7H10O7	20.04	0.06
N-Acetyl-D-glucosamine	C8H15NO6	26.36	0.24
D-Erythrose	C4H8O4	10.72	0.18
MOPS	C7H15NO4S	5.67	0
Taurine	C2H7NO3S	6.58	0.17
N6-Acetyl-L-lysine	C8H16N2O3	8.21	0
Adenine	C5H5N5	3.98	0.22

Table A-6. (Cont.) Positive mode detected standard metabolites with their formula, and Coefficient of Variation error of peak area and retention time.

Metabolite	Formula	Peak Area CV%	Retention Time CV%
L-Glutamate	C5H9NO4	12.78	0.14
Pyridoxine	C8H11NO3	1.63	0.28
L-Citrulline	C6H13N3O3	22.51	0.14
L-2-Aminoadipate	C6H11NO4	9.65	0.31
L-Histidine	C6H9N3O2	9.93	0.04
L-2,4-Diaminobutanoate	C4H10N2O2	24.78	0.15
L-2,3-Diaminopropanoate	C3H8N2O2	26.43	0.22
L-Threonine	C4H9NO3	9.96	0.15
4-Hydroxybutanoic acid	C4H7O3	41.53	48.84
ATP	C10H16N5O13P3	58.55	0
Glycerol	C3H8O3	11.76	0.2
GTP	C10H16N5O14P3	28.58	0.25
Picolinic acid	C6H5NO2	5.64	0.22
Hypoxanthine	C5H4N4O	3.78	0.21
Deoxyguanosine	C10H13N5O4	29.47	0
Deoxyadenosine	C10H13N5O3	0.88	0
Guanosine	C10H13N5O5	9.11	0
5-Methoxytryptamine	C11H14N2O	50.25	0.16
L-Homoserine	C4H9NO3	11.05	0.2
1-Aminocyclopropane-1-carboxylate	C4H7NO2	16.13	0.25
L-Asparagine	C4H8N2O3	4.25	0.18
L-Serine	C3H7NO3	5.86	0.22
4-Trimethylammoniobutanoate	C7H15NO2	2.88	0.23
N-Acetylornithine	C7H14N2O3	9.87	0.27
Methylguanidine	C2H7N3	7.86	0.25
1-Aminopropan-2-ol	C3H9NO	13.87	0.25
Cytosine	C4H5N3O	6.18	0.21
HEPES	C8H18N2O4S	1.26	0
meso-2,6-Diaminoheptanedioate	C7H14N2O4	49.94	0.16
L-Ornithine	C5H12N2O2	5.66	0.18
Deoxycarnitine	C7H16NO2	2.88	0.23
FAD	C27H33N9O15P2	9.56	0
Taurocholate	C26H45NO7S	7.45	0
Lipoate	C8H14O2S2	5.07	0
Mesaconate	C5H6O4	4.32	0
Thymine	C5H6N2O2	5.01	0.21
5-Oxoproline	C5H7NO3	3.15	0
N-Acetylglutamine	C7H12N2O4	7.51	0
Folate	C19H19N7O6	15.07	0.12
Uracil	C4H4N2O2	5.31	0.31

Table A-6. (Cont.) Positive mode detected standard metabolites with their formula, and Coefficient of Variation error of peak area and retention time.

Metabolite	Formula	Peak Area CV%	Retention Time CV%
D-Ribose	C5H10O5	7.21	0.38
dUMP	C9H13N2O8P	9.9	0.27
N-Acetylneuraminate	C11H19NO9	14.43	0.14
dIMP	C10H13N4O7P	19.75	0.18
sn-Glycerol 3-phosphate	C3H9O6P	15.82	0
L-Cysteate	C3H7NO5S	3.78	0.13
L-Aspartate	C4H7NO4	48.09	0
Creatine	C4H9N3O2	2.06	0.13
Thiamin diphosphate	C12H18N4O7P2S	21.56	0.24
Acetyl-CoA	C23H38N7O17P3S	3.55	0
ADP	C10H15N5O10P2	21.79	0.16
CTP	C9H16N3O14P3	24.92	0.11
Glyceraldehyde	C3H6O3	13.35	0
IDP	C10H14N4O11P2	22.86	0.12
UDP-Glucose	C15H24N2O17P2	12.90	0.12
O-Acetyl-L-serine	C5H9NO4	18.16	0.33
dGMP	C10H14N5O7P	9.12	0.21
dAMP	C10H14N5O6P	58.38	0.11
Betaine	C5H11NO2	2.28	0.22
L-Homocysteine	C4H9NO2S	4.72	0.17
O-Acetylcarnitine	C9H17NO4	0.98	0.08
L-Glutamine	C5H10N2O3	13.35	0.17
L-Carnitine	C7H15NO3	0.86	0
5-Aminolevulinate	C5H9NO3	31.44	0
S-Adenosyl-L-homocysteine	C14H20N6O5S	8.99	0.2
Benzoate	C7H6O2	9.06	0.23
4-Coumarate	C9H8O3	17.22	0.26
2-Oxobutanoate	C4H6O3	6.78	0
N-Acetyl-L-glutamate	C7H11NO5	26.25	0.14
Isonicotinic acid	C6H5NO2	3.21	0.43
FMN	C17H21N4O9P	4.03	0.32
Ascorbate	C6H8O6	16.55	0.14
3',5'-Cyclic AMP	C10H12N5O6P	4.17	0
IMP	C10H13N4O8P	4.24	0.18
GMP	C10H14N5O8P	3.77	0.22
CMP	C9H14N3O8P	5.42	0.1
Homocystine	C8H16N2O4S2	4.72	0.17
Glycylglycine	C4H8N2O3	13.96	3.51
UDP	C9H14N2O12P2	6.60	0.04
NADPH	C21H30N7O17P3	3.50	0

Table A-6. (Cont.) Positive mode detected standard metabolites with their formula, and Coefficient of Variation error of peak area and retention time.

Metabolite	Formula	Peak Area CV%	Retention Time CV%
Lipoamide	C8H15NOS2	33.69	0.42
L-Kynurenine	C10H12N2O3	18.08	2.70
Selenomethionine	C5H11NO2Se	19.27	0.23
L-Tryptophan	C11H12N2O2	22.49	0.21
L-Isoleucine	C6H13NO2	19.2	0.16
L-Normetanephrine	C9H13NO3	13.3	0.22
L-Phenylalanine	C9H11NO2	4.04	0.25
Glutathione disulfide	C20H32N6O12S2	9.77	0.12
Choline phosphate	C5H15NO4P	12.99	0.24
N(pi)-Methyl-L-histidine	C7H11N3O2	9.62	0.18
Salicyluric acid I have found it as 2-Hydroxyhippuric acid	C9H9NO4	23.10	0.06
Hippurate	C9H9NO3	14.22	0.07
Methylmalonate	C4H6O4	18.04	0.22
Pantothenate	C9H17NO5	11.73	0.21
Thymidine	C10H14N2O5	19.26	0.27
4-Hydroxyphenylacetate	C8H8O3	9.02	0.22
UMP	C9H13N2O9P	4.43	0.15
AMP	C10H14N5O7P	5.62	0.22
CDP	C9H15N3O11P2	6.05	0.08
GDP	C10H15N5O11P2	10.77	0.1
Nicotinamide	C6H6N2O	1.69	0.28
Glutathione	C10H17N3O6S	5.86	0.13
3',5'-Cyclic GMP	C10H12N5O7P	2.73	0.19
Urate	C5H4N4O3	91.75	0.63
L-Norleucine	C6H13NO2	10.34	0
(R)-Acetoin	C4H8O2	13.13	0.06
Octadecanoic acid	C18H36O2	6.09	0.85
UTP	C9H15N2O15P3	6.2	0.21

Table A-7. Negative mode detected standard metabolites with their formula, and Coefficient of Variation error of peak area and retention time.

Metabolite	Formula	Peak Area CV%	Retention Time CV%
Melatonin	C13H16N2O2	13.33	0.3
N-Acetyl-L-phenylalanine	C11H13NO3	6.68	0.31
4-Aminobenzoate	C7H7NO2	11.46	0.23
Glutarate	C5H8O4	7.06	0.1
4-Aminohippuricacid	C9H10N2O3	7.7	0.21
Deoxyuridine	C9H12N2O5	24.49	0.45
5-Hydroxyindoleacetate	C10H9NO3	12.64	0.32
Inosine	C10H12N4O5	13.9	0.1
5'-Methylthioadenosine	C11H15N5O3S	8.54	0.41
Biopterin	C9H11N5O3	28.28	0.43
L-Rhamnose	C6H12O5	4.96	0.27
Adenosine	C10H13N5O4	22.62	4.42
Guanine	C5H5N5O	10.87	0.28
5-Methoxytryptamine	C11H14N2O	16.58	0.28
L-Proline	C5H9NO2	10.24	0.08
L-Lysine	C6H15N2O2	10.14	0.25
sn-Glycero-3-Phosphocholine	C8H20NO6P	27.87	0.28
Imidazole-4-acetate	C5H6N2O2	17.3	0.24
Creatinine	C4H7N3O	10.53	0.11
Guanidinoacetate	C3H7N3O2	8.9	0.37
Cytidine	C9H13N3O5	15.29	0.22
L-Cystathionine	C7H14N2O4S	21.06	0.34
Putrescine	C4H12N2	21.08	0.3
L-Arginine	C6H14N4O2	8.88	0.2
L-Methionine sulfone	C4H9NO5S	15.71	0.79
Phenylhydrazine	C6H8N2	14.08	0.34
Phenolsulfonphthalein	C19H14O5S	7.77	0
[ST hydrox] 3alpha,7alpha-Dihydroxy-5beta-cholan-24-oic Acid	C24H40O4	10.36	0.1
1-Naphthylacetic acid	C12H10O2	8.6	0.36
3-Hydroxyphenylacetate	C8H8O3	35.35	0.49
3-(4-Hydroxyphenyl)pyruvate	C9H8O4	7.41	0.46
Acetylcysteine	C5H9NO3S	10.54	0.39
3-(3-Hydroxy-phenyl)-propanoic acid	C9H10O3	9.29	0.48
(R)-Lactate	C3H6O3	23.58	0.22
3,4-Dihydroxyphenylacetate	C8H8O4	11.01	0.23
3-Methoxy-4-Hydroxyphenylglycolsulfate	C9H12O7S	10.47	0.33
Malonate	C3H4O4	12.43	0.16
(R)-2-Hydroxyglutarate	C5H8O5	12.15	0.19
2-Oxoglutarate	C5H6O5	3.22	0.17

Table A-7. (Cont.) Negative mode detected standard metabolites with their formula, and Coefficient of Variation error of peak area and retention time.

Metabolite	Formula	Peak Area CV%	Retention Time CV%
Glycolate	C2H4O3	25.96	0.57
Orotate	C5H4N2O4	21.16	0.22
pyrazinoate	C5H4N2O2	9.31	0.18
Uridine	C9H12N2O6	30.54	0.2
Gallate	C7H6O5	27.55	0.31
3,4-Dihydroxymandelate	C8H8O5	10.44	0.04
2-Methylcitrate	C7H10O7	9.79	0.19
N-Acetyl-D-glucosamine	C8H15NO6	13.24	0.42
D-Erythrose	C4H8O4	21.73	0.31
Mannitol	C6H14O6	9.39	0.2
MOPS	C7H15NO4S	11.42	0.31
Pyridoxal phosphate	C8H10NO6P	12.81	0.43
D-Gluconic acid	C6H12O7	12.48	0.18
D-Ribose 5-phosphate	C5H11O8P	11.73	0.13
Taurine	C2H7NO3S	11.06	0.28
N6-Acetyl-L-lysine	C8H16N2O3	8.34	0.04
Adenine	C5H5N5	9.89	0.23
L-Glutamate	C5H9NO4	23.1	0.15
Pyridoxine	C8H11NO3	8.48	0.24
Ethanolamine phosphate	C2H8NO4P	19.12	0.2
L-Histidine	C6H9N3O2	4.99	0.48
L-2,4-Diaminobutanoate	C4H10N2O2	87.48	0.65
L-Threonine	C4H9NO3	9.95	0.17
ATP	C10H16N5O13P3	76.88	0.23
CoA	C21H36N7O16P3S	31	2.82
GTP	C10H16N5O14P3	64.58	0.31
(S)-Malate	C4H6O5	35.95	0.26
Phosphoenolpyruvate	C3H5O6P	46.91	0.22
Picolinic acid	C6H5NO2	10.22	0.25
Deoxyguanosine	C10H13N5O4	7.58	0.2
Deoxyadenosine	C10H13N5O3	10.42	0.27
Guanosine	C10H13N5O5	9.81	0.19
5-Methoxytryptamine	C11H14N2O	6.15	0
L-Valine	C5H11NO2	9.95	0.11
L-Metanephrine	C10H15NO3	11.98	0.3
1-Aminocyclopropane-1-carboxylate	C4H7NO2	8.85	0.25
L-Serine	C3H7NO3	19.02	0.19
N-Acetylornithine	C7H14N2O3	9.12	0.13
HEPES	C8H18N2O4S	8.12	0.29

Table A-7. (Cont.) Negative mode detected standard metabolites with their formula, and Coefficient of Variation error of peak area and retention time

Metabolite	Formula	Peak Area CV%	Retention Time CV%
meso-2,6-Diaminoheptanedioate	C7H14N2O4	5.37	0
FAD	C27H33N9O15P2	9.19	0
Taurocholate	C26H45NO7S	2.88	0.42
[ST hydrox] 3alpha,12alpha-Dihydroxy-5beta-cholan-24-oic Acid	C24H40O4	1.97	0
Lipoate	C8H14O2S2	8.25	0.63
Mesaconate	C5H6O4	15.81	0.36
Succinate	C4H6O4	10.45	0.18
Thymine	C5H6N2O2	2.93	0.24
5-Oxoproline	C5H7NO3	5.36	0.17
N-Acetylglutamine	C7H12N2O4	6.99	0.22
Folate	C19H19N7O6	4.9	0.17
Orotidine	C10H12N2O8	8.91	0
Uracil	C4H4N2O2	4.98	0.15
dUMP	C9H13N2O8P	7.35	0.18
N-Acetylneuraminate	C11H19NO9	6.64	0.22
dIMP	C10H13N4O7P	6.91	0
sn-Glycerol 3-phosphate	C3H9O6P	14.91	0.23
Sucrose	C12H22O11	7.65	0.12
L-Cysteate	C3H7NO5S	8.39	0
Pyridoxal	C8H9NO3	18.63	0.52
Acetyl-CoA	C23H38N7O17P3S	8.3	0
ADP	C10H15N5O10P2	20.37	0.28
Biotin	C10H16N2O3S	10.95	0.31
Glyceraldehyde	C3H6O3	18.06	0.44
Oxalate	C2H2O4	19.63	0.2
UDP-Glucose	C15H24N2O17P2	4.72	0.53
O-Acetyl-L-serine	C5H9NO4	7.72	0.39
dGMP	C10H14N5O7P	27.08	0.17
dAMP	C10H14N5O6P	26.58	0.19
Betaine	C5H11NO2	21.06	0.41
L-Homocysteine	C4H9NO2S	17.63	0.45
O-Acetylcarnitine	C9H17NO4	38.72	0.33
L-Glutamine	C5H10N2O3	36.63	0.24
L-Carnitine	C7H15NO3	29.88	0.36
S-Adenosyl-L-homocysteine	C14H20N6O5S	17.84	0.18
Benzoate	C7H6O2	5.39	0
Maleic acid	C4H4O4	12.56	0.32
4-Coumarate	C9H8O3	5.55	0.26
2-Oxobutanoate	C4H6O3	5.9	0

Table A-7. (Cont.) Negative mode detected standard metabolites with their formula, and Coefficient of Variation error of peak area and retention time.

Metabolite	Formula	Peak Area CV%	Retention Time CV%
Itaconate	C5H6O4	23.79	0.14
Pyruvate	C3H4O3	10.5	0.93
N-Acetyl-L-glutamate	C7H11NO5	16.01	0.13
Isonicotinic acid	C6H5NO2	13.21	0
FMN	C17H21N4O9P	11.74	0.22
Ascorbate	C6H8O6	25.95	0.17
3',5'-Cyclic AMP	C10H12N5O6P	6.38	0.14
IMP	C10H13N4O8P	23.93	0
GMP	C10H14N5O8P	19.24	0
CMP	C9H14N3O8P	26.46	0.24
Homocystine	C8H16N2O4S2	17.63	0.45
Glycylglycine	C4H8N2O3	22.36	0.27
NADPH	C21H30N7O17P3	23.74	0.2
Lipoamide	C8H15NOS2	14.63	0.41
L-Kynurenine	C10H12N2O3	9.78	0.4
Selenomethionine	C5H11NO2Se	30.49	0.2
L-Tryptophan	C11H12N2O2	14.21	0
L-Isoleucine	C6H13NO2	18.63	0.17
Glutathione disulfide	C20H32N6O12S2	17.49	0.23
N(pi)-Methyl-L-histidine	C7H11N3O2	31.86	0
Phenylpyruvate	C9H8O3	18.17	0.33
Leucinicacid	C6H12O3	5.83	0.31
Salicyluric acid I have found it as 2-Hydroxyhippuric acid	C9H9NO4	23.39	0.31
Hippurate	C9H9NO3	7.4	0
Alpha-Hydroxyisobutyricacid	C4H8O3	17.77	0.61
Methylmalonate	C4H6O4	6.33	0.15
3-Methoxy-4-hydroxymandelate	C9H10O5	27.04	0.25
Thymidine	C10H14N2O5	7.98	0.38
4-Hydroxyphenylacetate	C8H8O3	10.73	0.32
trans-Aconitate	C6H6O6	14.14	0
Xanthine	C5H4N4O2	10.73	0.3
UMP	C9H13N2O9P	24.79	0
D-Glucose	C6H12O6	9.86	0.25
D-Galacturonate	C6H10O7	26.35	0.56
D-Fructose 6-phosphate	C6H13O9P	14.81	0.24
AMP	C10H14N5O7P	12.84	0
CDP	C9H15N3O11P2	58.07	0.25
GDP	C10H15N5O11P2	58.9	0.23
Nicotinamide	C6H6N2O	26.64	0.52

Table A-7. (Cont.) Negative mode detected standard metabolites with their formula, and Coefficient of Variation error of peak area and retention time.

Metabolite	Formula	Peak Area CV%	Retention Time CV%
Glutathione	C10H17N3O6S	17.49	0.082
homovanillate	C9H10O4	22.8	0.18
3',5'-Cyclic GMP	C10H12N5O7P	20.51	0.27
Urate	C5H4N4O3	26.15	0.04
L-Norleucine	C6H13NO2	10.1	0.08
D-glucose 6-phosphate	C6H13O9P	20.22	0.25
(R)-Acetoin	C4H8O2	28.16	0.7
Octadecanoic acid	C18H36O2	15.31	0.47
UTP	C9H15N2O15P3	25.41	0.09

Table A-8. Composition of pig tracheal mucus before and after the cleaning (0 class indicates unclassified, unmapped, metabolite)

Mass	RT	Formula	Putative metabolite	Class	Maximum intensity	Fold Change Cleaned mucus	Fold Change Raw mucus
70.0418	4.217	C4H6O	Crotonaldehyde	0	11263	1.00	1.00
176.0797	6.719	C6H12N2O4	N5-formyl-N5-hydroxy-L-ornithine	0	122172	48.75	1.00
220.1058	8.105	C8H16N2O5	N-Acetyl-beta-D-glucosaminylamine	0	31291	23.77	1.00
190.0953	8.11	C7H14N2O4	N5-acetyl-N5-hydroxy-L-ornithine	0	62462	5.83	1.00
295.1281	6.667	C12H17N5O4	N6,N6-Dimethyladenosine	0	34308	2.04	1.00
124.0636	11.02	C6H8N2O	N-Propanoylimidazole	0	30062	0.51	1.00
133.0738	5.728	C5H11NO3	3-nitro-2-pentanol	0	548046	0.46	1.00
191.0615	4.592	C7H13NO3S	N-Acetylmethionine	0	582794	0.44	1.00
147.0355	9.276	C5H9NO2S	Thiomorpholine 3-carboxylate	0	130609	0.44	1.00
79.9663	10.4	[PO3]3-	Phosphite	0	4037704	0.64	1.00
127.0633	18.22	C6H9NO2	alpha-(Methylenecyclopropyl)glycine	0	106674	0.44	1.00
89.0477	6.661	C3H7NO2	Urethane	0	553019	0.43	1.00
247.1419	8.807	C11H21NO5	Hydroxybutyrylcarnitine	0	854354	0.42	1.00
95.0371	6.788	C5H5NO	2-Hydroxypyridine	0	50632	0.41	1.00
84.0211	4.576	C4H4O2	4-Hydroxy-2-butynal	0	51001	0.17	1.00
96.9690	10.62	[H2PO4]-	Dihydrogenphosphate	0	41599	0.41	1.00
84.0575	3.978	C5H8O	3-Methylbut-2-enal	Biosynthesis of Secondary Metabolites	19905	1.02	1.00
145.0527	6.782	C9H7NO	3-Methyleneoxindole	0	75160	0.41	1.00
85.0527	6.635	C4H7NO	Acetone cyanohydrin	0	9828846	0.27	1.00
118.0532	6.729	C7H6N2	Benzimidazole	0	79232	0.39	1.00
99.0684	6.642	C5H9NO	2-Piperidinone	0	157890	0.37	1.00

Mass	RT	Formula	Putative metabolite	Class	Maximum intensity	Fold Change Cleaned mucus	Raw mucus
301.0582	10.5	C10H12ClN5O4	5'-chloroformycin	0	41331	0.37	1.00
246.0503	9.581	C6H15O8P	Glycerophosphoglycerol	0	564869	0.36	1.00
297.1072	8.444	C11H15N5O5	Psicofuranin	0	228757	0.36	1.00
129.0578	7.946	C9H7N	3-Methylene-indolenine	0	19364	0.36	1.00
174.1368	16.12	C8H18N2O2	Ne,Ne dimethyllysine	0	356728	0.34	1.00
75.0320	11.99	C2H5NO2	Nitroethane	0	2988161	0.33	1.00
191.0979	4.204	C8H17NO2S	trihomomethionine	0	45050	0.32	1.00
297.0894	6.676	C11H15N5O3S	5'-methylthioformycin	0	3496267	0.31	1.00
71.0734	10.09	C4H9N	3-Buten-1-amine	0	20108442	0.31	1.00
96.0939	5.292	C14H24	5-Ethyl-7-methyl-3E,5E,7E-undecatriene	Lipids: Fatty Acyls	22848	0.35	1.00
145.0197	5.618	C5H7NO2S	3,4-Dehydrothiomorpholine-3-carboxylate	0	31317	0.30	1.00
87.0320	6.7	C3H5NO2	2-Oxazolidinone	0	45319	0.30	1.00
152.0507	7.578	C5H12O3S	pentanesulfonate	0	213094	0.30	1.00
97.9768	11.87	H3O4P	Orthophosphate	Energy Metabolism	397022	0.20	1.00
98.0367	11.95	C5H6O2	[FA (5:2)] 2,4-pentadienoic acid	Lipids: Fatty Acyls	26059	0.34	1.00
99.0142	4.607	C4H5NS	Allylisothiocyanate	0	6482	0.69	1.00
99.0683	10.56	C5H9NO	N-Methyl-2-pyrrolidinone	0	114844	0.54	1.00
149.0702	12.17	C6H7N5	3-Methyladenine	0	51047	0.30	1.00
99.0684	11.68	C5H9NO	N-Methyl-2-pyrrolidinone	0	291178	0.42	1.00
191.0616	6.528	C7H13NO3S	N-Acetylmethionine	0	167398	0.30	1.00
226.0954	6.815	C10H14N2O4	carbidopa	0	37550	0.30	1.00
153.9935	11.97	C3H6O5S	3-sulfopropanoate	0	85814	0.29	1.00

Mass	RT	Formula	Putative metabolite	Class	Maximum intensity	Fold Change Cleaned mucus	Raw mucus
100.0524	3.785	C5H8O2	Pentane-2,4-dione	0	16294	0.88	1.00
100.0524	11.68	C5H8O2	Tiglic acid	Lipids: Fatty Acyls	449079	0.37	1.00
115.0997	7.677	C6H13NO	hexanamide	0	16981	0.28	1.00
75.9982	9.343	C2H4OS	Thioacetate	0	18720	0.28	1.00
451.2142	3.403	C22H33N3O5S	Formylmethionyl-leucyl-phenylalanine methyl ester	0	11744	0.28	1.00
146.0400	9.858	C6H10O2S	THTA	0	21058	0.27	1.00
285.0961	7.262	C11H15N3O6	N4-Acetylcytidine	0	44982	0.26	1.00
103.0633	11.63	C4H9NO2	N,N-Dimethylglycine	Amino Acid Metabolism	4106324	0.82	1.00
125.0588	7.9	C5H7N3O	2-O-Methylcytosine	0	170084	0.26	1.00
129.0578	4.419	C9H7N	Isoquinoline	0	18135	0.26	1.00
204.1109	20.59	C8H16N2O4	N5-(L-1-Carboxyethyl)-L-ornithine	0	17250	0.26	1.00
174.1004	10.31	C7H14N2O3	N5-Ethyl-L-glutamine	0	4975116	0.26	1.00
108.0687	9.601	C6H8N2	Phenylenediamine	0	36775	0.26	1.00
105.0789	15.86	C4H11NO2	Diethanolamine	Lipid Metabolism	183400	0.49	1.00
105.0790	8.809	C4H11NO2	Diethanolamine	Lipid Metabolism	169184	0.20	1.00
149.0687	11.8	C5H11NO4	4-amino-4-deoxy-L-arabinose	0	513488	0.26	1.00
227.1521	3.952	C12H21NO3	VAI-2	0	67130	0.25	1.00
147.0895	9.629	C6H13NO3	Fagomine	0	1613444	0.24	1.00
110.0480	9.781	C5H6N2O	Imidazole-4-acetaldehyde	Amino Acid Metabolism	14998	0.63	1.00
110.1095	3.56	C16H28	4,8,12-Trimethyl-1,3E,7E,11-tridecatetraene	Lipids: Fatty Acyls	86425	1.55	1.00
111.0320	4.621	C5H5NO2	2,6-Dihydroxypyridine	Metabolism of Cofactors and Vitamins	50175	0.13	1.00

Mass	RT	Formula	Putative metabolite	Class	Maximum intensity	Fold Change Cleaned mucus	Fold Change Raw mucus
111.0321	6.981	C5H5NO2	Pyrrole-2-carboxylate	Amino Acid Metabolism	24418	0.66	1.00
111.9925	10.42	CH5O4P	Hydroxymethylphosphonate	Amino Acid Metabolism	4168371	0.71	1.00
111.9926	8.383	CH5O4P	methylphosphate	0	71654	0.56	1.00
112.0160	12.68	C5H4O3	2-Furoate	0	420020	0.28	1.00
129.0578	6.672	C9H7N	Quinoline	0	20700	0.24	1.00
168.0534	6.686	C7H8N2O3	2,3-Diaminosalicylic acid	0	94538	0.23	1.00
147.0684	5.08	C9H9NO	3-Methyloxindole	0	27757	0.22	1.00
133.0197	12.15	C4H7NO2S	L-thiazolidine-4-carboxylate	0	63582	0.22	1.00
160.1099	3.654	C8H16O3	Ethyl (R)-3-hydroxyhexanoate	0	31760	0.22	1.00
160.1212	13.78	C7H16N2O2	Bethanechol	0	12342	0.21	1.00
114.0429	9.208	C4H6N2O2	5,6-Dihydrouracil	Nucleotide Metabolism	409676	1.04	1.00
169.0851	9.65	C7H11N3O2	Nalpha-Methylhistidine	0	6951731	0.21	1.00
292.1423	4.438	C15H20N2O4	Phenylbutyrylglutamine	0	23487	0.20	1.00
131.0735	9.564	C9H9N	Skatole	0	88791	0.20	1.00
193.0738	4.516	C10H11NO3	Gentioflavine	0	433061	0.20	1.00
256.1059	7.713	C11H16N2O5	1-(beta-D-Ribofuranosyl)-1,4-dihydronicotinamide	0	162224	0.20	1.00
84.0575	6.88	C5H8O	Cyclopentanone	0	16489	0.20	1.00
116.0473	4.536	C5H8O3	3-Methyl-2-oxobutanoic acid	Amino Acid Metabolism	1055889	0.07	1.00
146.0942	3.862	C7H14O3	ethyl-(2R)-methyl-(3S)-hydroxybutanoate	0	170002	0.20	1.00
243.1470	7.05	C12H21NO4	Tiglylcarnitine	0	147273	0.19	1.00
369.2878	4.169	C21H39NO4	cis-5-Tetradecenoylcarnitine	0	24330	0.19	1.00
281.1122	12.11	C11H15N5O4	1-Methyladenosine	0	1279928	0.19	1.00

Mass	RT	Formula	Putative metabolite	Class	Maximum intensity	Fold Change Cleaned mucus	Fold Change Raw mucus
223.1056	9.481	C8H17NO6	N-acetyl -D- glucosaminitol	0	17385	0.19	1.00
202.1429	16.66	C8H18N4O2	NG,NG-Dimethyl-L-arginine	0	27605024	0.19	1.00
159.1008	9.246	C6H13N3O2	delta-Guanidinovaleric acid	0	40224	0.18	1.00
114.0793	9.528	C5H10N2O	L-proline amide	0	124174	0.18	1.00
185.1052	4.344	C9H15NO3	8-keto-7-aminoperlagonate	0	37995	0.18	1.00
425.3505	3.929	C25H47NO4	Elaidiccarnitine	0	38709	0.18	1.00
282.0962	7.311	C11H14N4O5	8-Oxocoformycin	0	111006	0.18	1.00
150.0541	7.416	C6H6N4O	1-Methylhypoxanthine	0	541633	0.18	1.00
119.0583	6.651	C4H9NO3	(-)-erythro-(2R,3R)-dihydroxybutylamide	0	1857757	0.49	1.00
197.0800	7.818	C8H11N3O3	N-Acetyl-L-histidine	0	35070	0.17	1.00
101.0476	6.631	C4H7NO2	Diacetylmonoxime	0	24168	0.17	1.00
166.0663	6.826	C6H14O3S	hexanesulfonate	0	104395	0.16	1.00
324.1532	16.78	C12H24N2O8	Procollagen 5-(D-galactosyloxy)-L-lysine	0	41296	0.16	1.00
147.0353	11.65	C5H9NO2S	Thiomorpholine 3-carboxylate	0	16093	0.16	1.00
123.0319	10.28	C6H5NO2	Picolinic acid	0	114773	1.19	1.00
123.0320	6.75	C6H5NO2	Picolinic acid	0	453918	0.27	1.00
423.3350	3.958	C25H45NO4	Linoelaidylcarnitine	0	14426	0.16	1.00
179.0808	7.384	C7H9N5O	7-Aminomethyl-7-carbaguanine	0	162298	0.16	1.00
173.1052	4.429	C8H15NO3	Hexanoylglycine	0	21257	0.15	1.00
140.0585	5.071	C6H8N2O2	N3-methylthymine	0	926348	0.15	1.00
125.0476	9.732	C6H7NO2	N-Ethylmaleimide	0	266329	0.54	1.00
125.0588	11.7	C5H7N3O	5-Methylcytosine	Nucleotide Metabolism	309480	0.17	1.00

Mass	RT	Formula	Putative metabolite	Class	Maximum intensity	Fold Change Cleaned mucus	Raw mucus
154.1218	16.66	C7H14N4	α -ethynylagmatine	0	72159	0.15	1.00
311.1230	7.388	C12H17N5O5	N2-N2-Dimethylguanosine	0	382107	0.15	1.00
188.0797	8.026	C7H12N2O4	N-Acetylglutamine	0	46833	0.15	1.00
161.0688	6.635	C6H11NO4	L-Glutamate methylester	0	261689	0.15	1.00
181.0408	9.277	C5H11NO4S	DL-Methionine sulfone	0	118970	0.14	1.00
159.1259	10.05	C8H17NO2	DL-2-Aminooctanoicacid	0	1346268	0.14	1.00
397.3193	4.053	C23H43NO4	trans-Hexadec-2-enoylcarnitine	0	29000	0.14	1.00
127.0633	9.921	C6H9NO2	2,3,4,5-Tetrahydropyridine-2-carboxylate	Amino Acid Metabolism	24704	0.52	1.00
157.1102	7.482	C8H15NO2	Homostachydrine	0	69743	0.14	1.00
128.0585	8.309	C5H8N2O2	5,6-Dihydrothymine	Nucleotide Metabolism	101412	0.55	1.00
128.0837	6.725	C7H12O2	Cyclohexane-1-carboxylate	Xenobiotics Biodegradation and Metabolism	32956	0.19	1.00
128.0837	4.282	C7H12O2	3-Isopropylbut-3-enoic acid	Biosynthesis of Secondary Metabolites	121328	0.10	1.00
241.1062	6.764	C10H15N3O4	5-Methyl-2'-deoxycytidine	0	46341	0.13	1.00
128.1201	3.662	C8H16O	1-Octanal	0	7922	0.85	1.00
321.0695	13.51	C11H15NO10	beta-Citryl-L-glutamic acid	0	275582	0.13	1.00
129.0426	8.742	C5H7NO3	L-1-Pyrroline-3-hydroxy-5-carboxylate	Amino Acid Metabolism	705652	2.06	1.00
129.0577	9.571	C9H7N	Isoquinoline	0	30074	0.23	1.00
179.0582	4.602	C9H9NO3	N-Acetylanthranilate	0	1448633	0.13	1.00
193.0408	8.515	C6H11NO4S	γ-thiomethyl glutamate	0	5829937	0.13	1.00

Mass	RT	Formula	Putative metabolite	Class	Maximum intensity	Fold Change Cleaned mucus	Raw mucus
191.0793	7.848	C7H13NO5	2-amino-3,7-dideoxy-D-threo-hept-6-ulosonate	0	202134	0.12	1.00
245.1626	6.879	C12H23NO4	N-(octanoyl)-L-homoserine	0	2712275	0.11	1.00
265.1314	7.077	C14H19NO4	N(alpha)-Benzyloxycarbonyl-L-leucine	0	23511	0.11	1.00
129.0915	4.009	C14H26O4	[FA (14:0/2:0)] Tetradecanedioic acid	Lipids: Fatty Acyls	532996	0.06	1.00
246.1368	7.495	C14H18N2O2	Hypaphorine	0	36813	0.11	1.00
130.0629	4.156	C6H10O3	(S)-3-Methyl-2-oxopentanoic acid	Amino Acid Metabolism	5707200	0.03	1.00
196.1211	7.644	C10H16N2O2	Fasoracetam	0	90383	0.10	1.00
131.0404	6.677	C5H9NOS	4-methylthiobutanonitrile oxide	0	69236	0.45	1.00
159.1259	7.236	C8H17NO2	DL-2-Aminooctanoicacid	0	70254	0.10	1.00
245.1626	4.777	C12H23NO4	2-Methylbutyroylcarnitine	0	1013072	0.10	1.00
196.0768	6.707	C10H13N2Cl	m-Chlorophenylpiperazine	0	90122	0.09	1.00
247.0513	3.942	C12H10ClN3O	CPPU	0	220357	0.08	1.00
223.1056	6.708	C8H17NO6	N-acetyl -D- glucosaminitol	0	48500	0.07	1.00
235.1208	3.894	C13H17NO3	Lophophorine	0	12292	0.07	1.00
195.0531	4.012	C9H9NO4	1,2-Epoxy-3-(p-Nitrophenoxy)propane	0	11012	0.06	1.00
129.0578	11.5	C4H8N2O3	N-Carbamoylsarcosine	Amino Acid Metabolism	2561191	0.56	1.00
132.0534	9.343	C4H8N2O3	3-Ureidopropionate	Nucleotide Metabolism	242170	1.24	1.00
273.1939	4.611	C14H27NO4	Heptanoylcarnitine	0	65428	0.04	1.00
249.0306	12.9	C8H11NO6S	Norepinephrinesulfate	0	164757	0.04	1.00
118.0266	11	C4H6O4	2-keto-4-hydroxybutyrate	0	2096570	0.04	1.00
125.0952	20.43	C6H11N3	4-methylhistamine	0	2327296	0.03	1.00
206.1055	7.76	C11H14N2O2	Phenylethylmalonamide	0	23055	0.03	1.00
133.0527	10.44	C8H7NO	Indoxyl	Amino Acid Metabolism	12749	1.03	1.00

Mass	RT	Formula	Putative metabolite	Class	Maximum intensity	Fold Change Cleaned mucus	Fold Change Raw mucus
133.0561	4.482	C5H11NOS	4-methylthiobutanaldoxime	0	13562	0.26	1.00
120.0058	12.3	C3H4O5	2-Hydroxymalonate	0	142658	0.03	1.00
321.0994	9.462	C11H19N3O6S	gamma-L-Glutamyl-L-cysteinyl-beta-alanine	0	22096	0.02	1.00
189.1001	6.525	C8H15NO4	(2S)-2-{[1-(R)-Carboxyethyl]amino}pentanoate	0	372977	0.01	1.00
131.0405	9.536	C5H9NOS	4-methylthiobutanonitrile oxide	0	27370	0.01	1.00
189.0637	6.648	C7H11NO5	Glutarylglycine	0	17544	0.00	1.00
135.0915	3.915	C15H26O4	(10S)-Juvenile hormone III acid diol	Biosynthesis of Secondary Metabolites	15206	0.15	1.00
243.1041	7.85	C10H17N3O2S	Biotin amide	0	15118	0.00	1.00
253.0949	6.705	C12H15NO5	N-Acetylvanilalanine	0	18291	0.00	1.00
136.0384	11	C5H4N4O	allopurinol	0	1761145	0.07	1.00
193.0739	6.542	C10H11NO3	5,6-Dihydroxy-3-methyl-2-oxo-1,2,5,6-tetrahydroquinoline	0	149530	0.17	1.00
136.0524	4.414	C8H8O2	Phenylacetic acid	Amino Acid Metabolism	34948	0.93	1.00
100.0160	6.682	C4H4O3	2-oxobut-3-enanoate	0	76335	0.15	1.00
138.0317	4.324	C7H6O3	Gentisate aldehyde	Amino Acid Metabolism	27967	0.89	1.00
249.0860	6.803	C10H19NO2S2	S-Acetyldihydrolipoamide	0	8302977	0.06	1.00
161.0510	6.681	C6H11NO2S	allylcysteine	0	62016	0.12	1.00
183.0565	9.361	C5H13NO4S	Choline sulfate	0	51880	0.26	1.00
161.1051	10.16	C7H15NO3	(S)-Carnitine	0	78566040	0.31	1.00
115.0997	17.16	C6H13NO	Trimethylaminoacetone	0	73038	0.16	1.00
122.0479	6.791	C6H6N2O	Picolinamide	0	57815820	0.39	1.00

Mass	RT	Formula	Putative metabolite	Class	Maximum intensity	Fold Change Cleaned mucus	Raw mucus
141.0789	7.069	C7H11NO2	L-Hypoglycin	0	142350	0.16	1.00
147.0895	6.804	C6H13NO3	N-hydroxyisoleucine	0	66214	0.34	1.00
142.0742	10.17	C6H10N2O2	Ectoine	Amino Acid Metabolism	1741330	0.57	1.00
142.0993	3.677	C16H28O4	(10S)-Juvenile hormone III diol	Biosynthesis of Secondary Metabolites	228907	0.16	1.00
142.0993	4.748	C8H14O2	[FA (8:1)] 2Z-octenoic acid	Lipids: Fatty Acyls	37025	0.56	1.00
143.0404	4.483	C6H9NOS	5-(2-Hydroxyethyl)-4-methylthiazole	Metabolism of Cofactors and Vitamins	13444	0.05	1.00
143.0582	5.474	C6H9NO3	Vinylacetylglycine	0	207887	0.95	1.00
261.1211	9.33	C11H19NO6	Lotaustralin	0	1206104	0.09	1.00
143.1072	3.533	C16H30O4	[FA hydroxy,oxo(16:0)] 9-hydroxy-16-oxo-hexadecanoic acid	Lipids: Fatty Acyls	117524	0.17	1.00
144.0422	8.743	C6H8O4	2,3-Dimethylmaleate	Metabolism of Cofactors and Vitamins	147437	1.04	1.00
144.0423	11.37	C6H8O4	Methylitaconate	Metabolism of Cofactors and Vitamins	125214	0.29	1.00
99.06841	4.676	C5H9NO	2-hydroxy-2-methylbutyronitrile	0	194108	0.33	1.00
145.0197	8.575	C5H7NO2S	3,4-Dehydrothiomorpholine-3-carboxylate	0	819071	0.12	1.00
191.0430	12.11	C6H9NO6	Nitrilotriacetic acid	0	67702	0.10	1.00
143.0946	8.629	C7H13NO2	Stachydrine	0	4304691	0.23	1.00
145.0527	8.94	C9H7NO	3-Methyleneoxindole	0	8240	0.37	1.00
80.96466	11.61	HO3S	HSO3-	0	131936	0.19	1.00
89.0840	15.43	C4H11NO	N-dimethylethanolamine	0	876450	0.16	1.00

Mass	RT	Formula	Putative metabolite	Class	Maximum intensity	Fold Change Cleaned mucus	Raw mucus
133.0738	6.77	C5H11NO3	N-hydroxyvaline	0	1033686	0.55	1.00
247.1054	9.548	C10H17NO6	Linamarin	0	86549	0.20	1.00
149.0510	9.265	C5H11NO2S	D-Methionine	Amino Acid Metabolism	36120628	0.32	1.00
128.0949	6.775	C6H12N2O	L-Lysine 1,6-lactam	Amino Acid Metabolism	69795	0.21	1.00
204.0898	9.573	C11H12N2O2	D-Tryptophan	Amino Acid Metabolism	7743199	0.19	1.00
145.1578	20.67	C7H19N3	Spermidine	Amino Acid Metabolism	220626	1.35	1.00
160.1211	17.65	C7H16N2O2	N6-Methyl-L-lysine	Amino Acid Metabolism	525628	0.15	1.00
188.1272	18.16	C7H16N4O2	Homoarginine	Amino Acid Metabolism	5508530	0.12	1.00
133.0375	11	C4H7NO4	L-Aspartate	Amino Acid Metabolism	6909254	0.43	1.00
146.0691	6.881	C5H10N2O3	3-Ureidoisobutyrate	Nucleotide Metabolism	410904	0.83	1.00
89.0476	11.35	C3H7NO2	L-Alanine	Amino Acid Metabolism	12194454	0.61	1.00
123.9924	10.64	C2H5O4P	Phosphonoacetaldehyde	Amino Acid Metabolism	218555	0.73	1.00
146.1306	4.922	C8H18O2	Octane-1,8-diol	0	7266	0.92	1.00
217.1425	12.03	C9H19N3O3	gamma-L-Glutamylputrescine	Amino Acid Metabolism	438771	234.11	1.00
129.0789	6.78	C6H11NO2	N4-Acetylaminobutanal	Amino Acid Metabolism	77375	0.45	1.00
131.0582	6.685	C5H9NO3	L-Glutamate 5-semialdehyde	Amino Acid Metabolism	795507	0.44	1.00
240.1221	10.36	C10H16N4O3	Homocarnosine	Amino Acid Metabolism	506267	0.41	1.00
147.0644	12.52	C4H9N3O3	L-Albizziine	0	4989	0.08	1.00
145.0851	19.85	C5H11N3O2	4-Guanidinobutanoate	Amino Acid Metabolism	17535	0.40	1.00
115.0632	10.12	C5H9NO2	D-Proline	Amino Acid Metabolism	158378384	0.39	1.00
147.0895	4.648	C6H13NO3	N-hydroxyisoleucine	0	7644	0.39	1.00
144.1011	19.74	C5H12N4O	4-Guanidinobutanamide	Amino Acid Metabolism	34127	0.33	1.00
148.0735	7.974	C6H12O4	[FA methyl,hydroxy(5:0)] 3R-methyl-3,5-dihydroxy-pentanoic acid	Lipids: Fatty Acyls	38837	0.33	1.00

Mass	RT	Formula	Putative metabolite	Class	Maximum intensity	Fold Change Cleaned mucus	Raw mucus
149.0510	6.59	C5H11NO2S	ethylcysteine	Xenobiotics Biodegradation and Metabolism	6036026	0.26	1.00
145.0851	11.62	C5H11N3O2	4-Guanidinobutanoate	Amino Acid Metabolism	57988	0.28	1.00
147.0531	8.171	C5H9NO4	L-4-Hydroxyglutamate semialdehyde	Amino Acid Metabolism	1246140	0.20	1.00
129.0426	7.7	C5H7NO3	L-1-Pyrroline-3-hydroxy-5-carboxylate	Amino Acid Metabolism	14268859	0.13	1.00
259.1167	9.46	C10H17N3O5	Linatine	Amino Acid Metabolism	22849	0.10	1.00
246.1328	10.84	C9H18N4O4	N2-(D-1-Carboxyethyl)-L-arginine	Amino Acid Metabolism	795074	0.07	1.00
150.0165	12.18	C4H6O6	(R,R)-Tartaric acid	Carbohydrate Metabolism	7917	0.28	1.00
290.1225	11.8	C10H18N4O6	N-(L-Arginino)succinate	Amino Acid Metabolism	194316	0.07	1.00
104.0221	9.417	C2H4N2O3	Urea-1-carboxylate	Amino Acid Metabolism	38557	0.12	1.00
174.1116	19.77	C6H14N4O2	L-Arginine	Amino Acid Metabolism	15327172	0.30	1.00
150.1044	3.849	C10H14O	[PR] Perillyl aldehyde	Lipids: Prenols	8764	1.09	1.00
151.0303	7.321	C4H9NO3S	methiin	0	146512	0.23	1.00
151.0493	10.32	C5H5N5O	2-Hydroxyadenine	0	22618256	0.83	1.00
113.0477	5.351	C5H7NO2	1-Pyrroline-2-carboxylate	Amino Acid Metabolism	402920	5.45	1.00
132.0898	17.15	C5H12N2O2	L-Ornithine	Amino Acid Metabolism	1091027	0.28	1.00
147.0530	10.77	C5H9NO4	L-Glutamate	Amino Acid Metabolism	37419536	0.34	1.00
152.1200	4.193	C10H16O	Perillyl alcohol	Lipids: Prenols	25440	0.31	1.00
153.0425	9.23	C7H7NO3	3-Hydroxyanthranilate	Amino Acid Metabolism	9134	0.05	1.00
217.1061	11.79	C8H15N3O4	N-Acetyl-L-citrulline	Amino Acid Metabolism	132970	0.38	1.00
245.1486	12.14	C9H19N5O3	beta-Alanyl-L-arginine	Amino Acid Metabolism	225560	109.66	1.00
119.0218	12.04	C3H5NO4	beta-Nitropropanoate	Amino Acid Metabolism	16470	0.09	1.00

Mass	RT	Formula	Putative metabolite	Class	Maximum intensity	Fold Change Cleaned mucus	Raw mucus
219.1106	6.816	C9H17NO5	Pantothenate	Amino Acid Metabolism	3860178	0.52	1.00
154.9888	6.12	C8H13Cl3O6	trichloroethanol glucoside	0	2355	0.91	1.00
240.0237	11.5	C6H12N2O4S2	L-Cystine	Amino Acid Metabolism	126564	5.46	1.00
160.0847	6.781	C6H12N2O3	D-Alanyl-D-alanine	Amino Acid Metabolism	1263262	0.44	1.00
173.0800	19.75	C6H11N3O3	5-Guanidino-2-oxopentanoate	Amino Acid Metabolism	16618	0.26	1.00
146.0691	11.4	C5H10N2O3	D-Glutamine	Amino Acid Metabolism	26547894	0.46	1.00
145.0375	8.173	C5H7NO4	2-Oxoglutaramate	Amino Acid Metabolism	35865	0.11	1.00
156.1150	4.369	C9H16O2	[FA hydroxy(9:1)] 4-hydroxy-2-nonenal	Lipids: Fatty Acyls	5352	0.54	1.00
156.1150	3.48	C18H32O4	[FA (18:2)] 9S-hydroperoxy-10E,12Z-octadecadienoic acid	Lipids: Fatty Acyls	288574	0.10	1.00
259.0456	11.09	C6H14NO8P	D-Glucosamine 6-phosphate	Amino Acid Metabolism	78084	0.25	1.00
158.0578	7.825	C7H10O4	2-Isopropylmaleate	Amino Acid Metabolism	9940	0.12	1.00
158.0942	4.218	C8H14O3	[FA oxo(8:0)] 3-oxo-octanoic acid	Lipids: Fatty Acyls	30329	0.78	1.00
301.0561	10.82	C8H16NO9P	N-Acetyl-D-glucosamine 6-phosphate	Amino Acid Metabolism	97716	0.23	1.00
113.0477	7.343	C5H7NO2	(S)-1-Pyrroline-5-carboxylate	Amino Acid Metabolism	792406	4.46	1.00
113.0476	11.17	C5H7NO2	(S)-1-Pyrroline-5-carboxylate	Amino Acid Metabolism	1400710	0.21	1.00
159.1259	5.079	C8H17NO2	[FA amino(8:0)] 3-amino-octanoic acid	Lipids: Fatty Acyls	280817	0.29	1.00
105.0425	11.97	C3H7NO3	D-Serine	Amino Acid Metabolism	6948041	0.39	1.00
119.0582	11.02	C4H9NO3	L-Allothreonine	Amino Acid Metabolism	16515633	0.34	1.00
160.0372	12.92	C6H8O5	2-Oxoadipate	Amino Acid Metabolism	9152	0.38	1.00
73.0527	8.19	C3H7NO	Aminoacetone	Amino Acid Metabolism	19383	0.18	1.00
160.0848	10.39	C6H12N2O3	N-gamma-Acetyldiaminobutyrate	Amino Acid Metabolism	110518	0.30	1.00
160.0848	8.167	C6H12N2O3	D-Alanyl-D-alanine	Amino Acid Metabolism	8575	5.71	0.00
131.0694	11.32	C4H9N3O2	Creatine	Amino Acid Metabolism	230106032	0.80	1.00

Mass	RT	Formula	Putative metabolite	Class	Maximum intensity	Fold Change Cleaned mucus	Raw mucus
117.0538	12.23	C3H7N3O2	Guanidinoacetate	Amino Acid Metabolism	20649038	0.19	1.00
103.0996	18.6	C5H13NO	Choline	Amino Acid Metabolism	256192464	0.30	1.00
141.0190	11.42	C2H8NO4P	Ethanolamine phosphate	Amino Acid Metabolism	8687535	0.21	1.00
104.0109	12.73	C3H4O4	Hydroxypyruvate	Amino Acid Metabolism	43102	0.04	1.00
222.0673	12.16	C7H14N2O4S	L-Cystathionine	Amino Acid Metabolism	1131909	0.19	1.00
161.0688	8.85	C6H11NO4	O-Acetyl-L-homoserine	Amino Acid Metabolism	4267893	1.81	1.00
75.0684	20.72	C3H9NO	(R)-1-Aminopropan-2-ol	Amino Acid Metabolism	301340	0.20	1.00
162.0350	6.817	C6H10O3S	1,2-Dihydroxy-5-(methylthio)pent-1-en-3-one	Amino Acid Metabolism	13168	0.35	1.00
131.0582	11.21	C5H9NO3	5-Aminolevulinate	Amino Acid Metabolism	352338	0.13	1.00
72.02110	8.805	C3H4O2	Methylglyoxal	Amino Acid Metabolism	1914888	0.14	1.00
138.0429	6.986	C6H6N2O2	Urocanate	Amino Acid Metabolism	11411724	0.62	1.00
162.0680	4.079	C10H10O2	Methyl cinnamate	0	3682	0.80	1.00
162.1004	16.88	C6H14N2O3	N6-Hydroxy-L-lysine	Amino Acid Metabolism	15915	0.27	1.00
162.1006	7.955	C6H14N2O3	N6-Hydroxy-L-lysine	Amino Acid Metabolism	10498	0.04	1.00
163.0844	11.84	C6H13NO4	1-deoxynojirimycin	0	344194	0.16	1.00
164.0473	4.128	C9H8O3	Phenylpyruvate	Amino Acid Metabolism	23788	0.13	1.00
124.0635	6.778	C6H8N2O	Methylimidazole acetaldehyde	Amino Acid Metabolism	78165	0.38	1.00
165.0425	4.364	C8H7NO3	4-Pyridoxolactone	Metabolism of Cofactors and Vitamins	17086	0.16	1.00
174.0640	9.708	C6H10N2O4	formyl-isoglutamine	Amino Acid Metabolism	35845	0.36	1.00
190.0589	11.03	C6H10N2O5	N-Carbamyl-L-glutamate	Amino Acid Metabolism	65834	0.32	1.00
125.0952	9.856	C6H11N3	N-Methylhistamine	Amino Acid Metabolism	34878	0.30	1.00
229.0884	11.47	C9H15N3O2S	Ergothioneine	Amino Acid Metabolism	293603	0.30	1.00

Mass	RT	Formula	Putative metabolite	Class	Maximum intensity	Fold Change Cleaned mucus	Raw mucus
166.0481	3.94	C14H21N2O3ClS	Tos-Lys-CH2Cl	0	57555	0.72	1.00
156.0535	8.555	C6H8N2O3	4-Imidazolone-5-propanoate	Amino Acid Metabolism	34786	0.19	1.00
258.0851	9.69	C10H14N2O6	(1-Ribosylimidazole)-4-acetate	Amino Acid Metabolism	53971	0.14	1.00
166.1357	4.164	C11H18O	[FA (11:2)] 2,5-undecadienal	Lipids: Fatty Acyls	27209	0.31	1.00
139.0745	6.925	C6H9N3O	L-Histidinal	Amino Acid Metabolism	139313	0.13	1.00
167.0365	12.47	C3H9N3O3S	Taurocyamine	Amino Acid Metabolism	13016	0.19	1.00
167.1059	5.448	C8H13N3O	2-Dimethylamino-5,6-dimethylpyrimidin-4-ol	0	8946	0.14	1.00
167.9823	9.375	C3H5O6P	3-Phosphonopyruvate	Amino Acid Metabolism	100404	0.28	1.00
168.0283	9.892	C5H4N4O3	Urate	Nucleotide Metabolism	954625	1.04	1.00
140.0585	7.333	C6H8N2O2	Methylimidazoleacetic acid	Amino Acid Metabolism	3044825	0.09	1.00
155.0694	11.13	C6H9N3O2	L-Histidine	Amino Acid Metabolism	30344750	0.52	1.00
190.0952	18.37	C7H14N2O4	LL-2,6-Diaminoheptanedioate	Amino Acid Metabolism	65413	0.26	1.00
169.0851	6.68	C7H11N3O2	histidine methyl ester	0	387546	0.41	1.00
169.9885	12.52	C3H6O6S	3-Sulfolactate	0	13394	0.28	1.00
169.9980	10.99	C3H7O6P	D-Glyceraldehyde 3-phosphate	Carbohydrate Metabolism	121427	1.64	1.00
171.0354	4.849	C7H9NO2S	4-Toluenesulfonamide	0	8299	1.17	1.00
171.1623	3.807	C10H21NO	decanamide	Lipids: Fatty Acyls	30379	1.31	1.00
283.0454	10.81	C8H14NO8P	N2-Acetyl-L-aminoadipyl-delta-phosphate	Amino Acid Metabolism	207935	0.23	1.00
172.0484	11.02	C6H8N2O4	Hydantoin-5-propionate	Amino Acid Metabolism	12490	1.00	1.00
172.0847	9.346	C7H12N2O3	Glycylproline	Peptide(di-)	215461	0.29	1.00
172.1099	4.072	C9H16O3	9-Oxononanoic acid	Lipids: Fatty Acyls	78717	1.13	1.00

Mass	RT	Formula	Putative metabolite	Class	Maximum intensity	Fold Change Cleaned mucus	Raw mucus
172.1323	16.65	C7H16N4O	Acetylagmatine	0	12404	0.10	1.00
146.1054	18.37	C6H14N2O2	L-Lysine	Amino Acid Metabolism	12893231	0.27	1.00
173.0688	6.704	C7H11NO4	N-Acetyl-L-glutamate 5-semialdehyde	Amino Acid Metabolism	157687	1.47	1.00
204.1110	7.103	C8H16N2O4	N6-Acetyl-N6-hydroxy-L-lysine	Amino Acid Metabolism	77829	5.85	1.00
188.1160	6.674	C8H16N2O3	N6-Acetyl-L-lysine	Amino Acid Metabolism	1042135	4.56	1.00
173.1164	17.03	C7H15N3O2	L-Indospicine	0	3981	0.25	1.00
173.1416	12.55	C9H19NO2	[FA amino(9:0)] 9-amino-nonanoic acid	Lipids: Fatty Acyls	23197	0.10	1.00
173.1416	6.859	C9H19NO2	[FA amino(9:0)] 3R-aminononanoic acid	Lipids: Fatty Acyls	10251	0.20	1.00
204.1473	14.77	C9H20N2O3	3-Hydroxy-N6,N6,N6-trimethyl-L-lysine	Amino Acid Metabolism	32637	0.41	1.00
145.0738	7.221	C6H11NO3	6-Amino-2-oxohexanoate	Amino Acid Metabolism	38155	0.30	1.00
174.0164	12.46	C6H6O6	trans-Aconitate	0	117463	0.20	1.00
174.0639	10.81	C6H10N2O4	N-Formimino-L-glutamate	Amino Acid Metabolism	38910	0.57	1.00
116.0949	18.24	C5H12N2O	5-Aminopentanamide	Amino Acid Metabolism	31967	0.29	1.00
159.0895	6.789	C7H13NO3	5-Acetamidopentanoate	Amino Acid Metabolism	60706	0.29	1.00
145.0738	10.23	C6H11NO3	[FA oxo,amino(6:0)] 3-oxo-5S-amino-hexanoic acid	Amino Acid Metabolism	443246	0.26	1.00
188.1524	16.52	C9H20N2O2	N6,N6,N6-Trimethyl-L-lysine	Amino Acid Metabolism	2630072	0.23	1.00
174.1255	3.61	C9H18O3	[FA hydroxy(9:0)] 2-hydroxy-nonanoic acid	Lipids: Fatty Acyls	19458	0.33	1.00
187.0844	6.783	C8H13NO4	6-Acetamido-2-oxohexanoate	Amino Acid Metabolism	36535	0.17	1.00
218.1265	10.86	C9H18N2O4	N2-(D-1-Carboxyethyl)-L-lysine	Amino Acid Metabolism	240777	0.08	1.00
175.0481	9.65	C6H9NO5	N-Acetyl-L-aspartate	Amino Acid Metabolism	118980	0.76	1.00
175.0481	12.87	C6H9NO5	N-Acetyl-L-aspartate	Amino Acid Metabolism	3861	0.12	1.00

Mass	RT	Formula	Putative metabolite	Class	Maximum intensity	Fold Change Cleaned mucus	Raw mucus
175.0956	11.89	C6H13N3O3	L-Citrulline	Amino Acid Metabolism	38204692	0.48	1.00
83.0735	9.885	C5H9N	Piperideine	Amino Acid Metabolism	80110	0.22	1.00
129.0789	9.825	C6H11NO2	L-Pipecolate	Amino Acid Metabolism	2084631	0.21	1.00
176.0797	17.12	C6H12N2O4	Thr-Gly	Peptide(di-)	10193	0.25	1.00
117.0789	9.06	C5H11NO2	5-Aminopentanoate	Amino Acid Metabolism	154125792	0.45	1.00
145.1102	7.937	C7H15NO2	3-Dehydroxycarnitine	Amino Acid Metabolism	731071	0.08	1.00
177.0790	6.686	C10H11NO2	5-Hydroxytryptophol	0	20060	0.57	1.00
177.0823	4.638	C7H15NO2S	dihomomethionine	0	62016	0.20	1.00
178.0412	10.34	C5H10N2O3S	Cys-Gly	Amino Acid Metabolism	103253	0.36	1.00
178.0477	10.02	C6H10O6	D-Glucono-1,5-lactone	Carbohydrate Metabolism	7802	0.49	1.00
179.0438	5.517	C6H13NOS2	5-methylthiopentylhydroximate	0	10680	2.75	1.00
179.0438	4.292	C6H13NOS2	5-methylthiopentylhydroximate	0	26952	2.13	1.00
180.0455	8.162	C6H12O4S	5-Methylthio-D-ribose	Amino Acid Metabolism	82652	0.37	1.00
177.0459	4.839	C6H11NO3S	N-Formyl-L-methionine	Amino Acid Metabolism	21927	0.26	1.00
165.0458	10.09	C5H11NO3S	L-Methionine S-oxide	Amino Acid Metabolism	1548596	0.15	1.00
179.0794	9.048	C6H13NO5	D-Galactosamine	Carbohydrate Metabolism	23946	0.44	1.00
101.0476	9.592	C4H7NO2	1-Aminocyclopropane-1-carboxylate	Amino Acid Metabolism	27003	0.35	1.00
219.0744	10.06	C8H13NO6	O-Succinyl-L-homoserine	Amino Acid Metabolism	85838	0.21	1.00
135.0354	9.362	C4H9NO2S	L-Homocysteine	Amino Acid Metabolism	21784	0.18	1.00
165.0789	8.253	C9H11NO2	D-Phenylalanine	Amino Acid Metabolism	68143752	0.33	1.00
179.0582	6.657	C9H9NO3	Hippurate	Amino Acid Metabolism	769693	0.14	1.00
181.0964	8.643	C7H11N5O	6-methyltetrahydropterin	0	44762	1.42	1.00

Mass	RT	Formula	Putative metabolite	Class	Maximum intensity	Fold Change Cleaned mucus	Raw mucus
182.0708	3.799	C6H15O4P	triethyl phosphate	0	41826	1.28	1.00
182.0790	10.89	C6H14O6	D-Sorbitol	Carbohydrate Metabolism	46203	0.57	1.00
150.0680	4.219	C9H10O2	Phenylpropanoate	Amino Acid Metabolism	78880	0.07	1.00
166.0629	4.427	C9H10O3	3-(3-Hydroxy-phenyl)-propanoic acid	Amino Acid Metabolism	199925	0.07	1.00
183.1259	6.745	C10H17NO2	Acetylpseudotropine	Biosynthesis of Secondary Metabolites	36202	0.49	1.00
184.1252	3.34	C14H16	Chamazulene	Lipids: Prenols	1877	2.75	1.00
114.0317	11.01	C5H6O3	2-Hydroxy-2,4-pentadienoate	Amino Acid Metabolism	35366	0.39	1.00
186.0639	10.89	C7H10N2O4	(S)-AMPA	0	18704	2.40	1.00
186.1004	8.431	C8H14N2O3	Ala-Pro	Peptide(di-)	71144	1.09	1.00
122.0368	6.738	C7H6O2	Benzoate	Amino Acid Metabolism	264831	0.31	1.00
135.0683	10.55	C8H9NO	2-Phenylacetamide	Amino Acid Metabolism	5398098	0.27	1.00
109.0197	11.54	C2H7NO2S	Hypotaurine	Amino Acid Metabolism	2893451	0.27	1.00
187.1082	13.21	C16H30N4O6	Leu-Lys-Asp	Peptide(tri-)	68090	0.66	1.00
187.1208	4.577	C9H17NO3	8-Amino-7-oxononanoate	Metabolism of Cofactors and Vitamins	683964	0.29	1.00
187.1208	6.777	C9H17NO3	(E)-2-Butenyl-4-methyl-threonine	0	109226	0.49	1.00
187.1572	4.283	C10H21NO2	[FA amino(10:0)] 2-amino-decanoic acid	Lipids: Fatty Acyls	178869	0.27	1.00
139.9779	12.87	C2H4O5S	Sulfoacetate	Amino Acid Metabolism	79014	0.13	1.00
125.9987	8.571	C2H6O4S	2-Hydroxyethanesulfonate	Amino Acid Metabolism	133524	0.11	1.00
208.0848	8.896	C10H12N2O3	Formyl-5-hydroxykynurenamine	Amino Acid Metabolism	4828557	0.38	1.00
188.1201	3.353	C13H16O	[FA (13:1/2:0)] 2-tridecene-4,7-diynal	Lipids: Fatty Acyls	3760	1.36	1.00

Mass	RT	Formula	Putative metabolite	Class	Maximum intensity	Fold Change Cleaned mucus	Fold Change Raw mucus
191.0583	8.922	C10H9NO3	5-Hydroxyindoleacetate	Amino Acid Metabolism	67018	0.32	1.00
220.0848	7.791	C11H12N2O3	5-Hydroxy-L-tryptophan	Amino Acid Metabolism	103250	0.13	1.00
167.0218	11.15	C7H5NO4	Pyridine-2,3-dicarboxylate	Amino Acid Metabolism	909684	0.18	1.00
189.0095	5.538	C6H7NO4S	2-Pyridyl hydroxymethane sulfonic acid	0	8061	0.07	1.00
189.0425	6.663	C10H7NO3	Kynurenate	Amino Acid Metabolism	228759	0.07	1.00
189.0425	4.616	C10H7NO3	N-Acetylisatin	Amino Acid Metabolism	162309	0.09	1.00
153.0425	6.789	C7H7NO3	3-Hydroxyanthranilate	Amino Acid Metabolism	151198	0.13	1.00
189.0637	10.15	C7H11NO5	L-2-Amino-6-oxoheptanedioate	Amino Acid Metabolism	31663	0.54	1.00
117.0578	7.944	C8H7N	Indole	Amino Acid Metabolism	286973	0.33	1.00
181.0739	10.41	C9H11NO3	3-Amino-3-(4-hydroxyphenyl)propanoate	Amino Acid Metabolism	30219110	0.27	1.00
189.1113	12.54	C7H15N3O3	L-Homocitrulline	0	7084	0.12	1.00
190.0477	8.299	C7H10O6	[FA hydroxy,oxo(7:0/2:0)] 4-hydroxy-2-oxo-Heptanedioic acid	Amino Acid Metabolism	422238	0.12	1.00
103.0633	9.666	C4H9NO2	L-3-Amino-isobutanoate	Amino Acid Metabolism	2342894	0.32	1.00
190.0742	7.632	C10H10N2O2	L-5-benzyl-hydantoin	0	8449	0.51	1.00
190.0952	11	C7H14N2O4	Thr-Ala	Peptide(di-)	122446	0.41	1.00
131.0946	8.835	C6H13NO2	L-Leucine	Amino Acid Metabolism	56958000	0.36	1.00
116.0473	7.139	C5H8O3	3-Methyl-2-oxobutanoic acid	Amino Acid Metabolism	27587	0.29	1.00
190.0994	3.34	C12H14O2	[FA (12:5)] 3,5,7,9,11-dodecapentaenoic acid	Lipids: Fatty Acyls	2173	1.40	1.00
155.0946	7.796	C8H13NO2	Retronecine	Biosynthesis of Secondary Metabolites	21303	0.27	1.00

Mass	RT	Formula	Putative metabolite	Class	Maximum intensity	Fold Change Cleaned mucus	Raw mucus
240.1474	8.232	C12H20N2O3	Slaframine	Biosynthesis of Secondary Metabolites	725495	0.13	1.00
330.2558	3.273	C22H34O2	Taxa-4(20),11(12)-dien-5alpha-yl acetate	Biosynthesis of Secondary Metabolites	20242	2.41	1.00
335.1593	4.493	C15H21N5O4	Isopentenyl adenosine	Biosynthesis of Secondary Metabolites	141052	0.19	1.00
309.1058	9.889	C11H19NO9	N-Acetylneuraminate	Carbohydrate Metabolism	85718	0.22	1.00
179.0794	12.21	C6H13NO5	D-Glucosamine	Carbohydrate Metabolism	38871	0.20	1.00
175.0243	11.04	C6H7O6	Monodehydroascorbate	Carbohydrate Metabolism	44405	0.33	1.00
166.0477	9.81	C5H10O6	L-Arabinonate	Carbohydrate Metabolism	437157	0.30	1.00
192.0269	12.67	C6H8O7	Citrate	Carbohydrate Metabolism	2414323	0.29	1.00
192.0270	8.933	C6H8O7	5-Dehydro-4-deoxy-D-glucarate	Carbohydrate Metabolism	268602	0.42	1.00
210.0377	12.15	C6H10O8	D-Glucarate	Carbohydrate Metabolism	93440	0.10	1.00
136.0371	11.93	C4H8O5	[FA trihydroxy(4:0)] 2,3,4-trihydroxy-butanoic acid	Carbohydrate Metabolism	1133849	0.06	1.00
130.0266	6.67	C5H6O4	2,5-Dioxopentanoate	Carbohydrate Metabolism	412068	0.21	1.00

Mass	RT	Formula	Putative metabolite	Class	Maximum intensity	Fold Change Cleaned mucus	Fold Change Raw mucus
174.0164	10	C6H6O6	L-Dehydroascorbate	Carbohydrate Metabolism	262817	0.29	1.00
176.0320	11.09	C6H8O6	Ascorbate	Carbohydrate Metabolism	8602653	0.27	1.00
134.0215	11.53	C4H6O5	(R)-Malate	Carbohydrate Metabolism	13918534	0.32	1.00
194.0579	4.109	C10H10O4	Ferulate	Biosynthesis of Secondary Metabolites	6183	4.93	1.00
194.0790	8.799	C7H14O6	1-O-Methyl-myo-inositol	Carbohydrate Metabolism	11561	1.75	1.00
194.1306	3.748	C12H18O2	4-Hexyloxyphenol	0	46154	0.26	1.00
70.0418	7.165	C4H6O	3-Butyn-1-ol	Carbohydrate Metabolism	46572	0.28	1.00
195.0895	4.521	C10H13NO3	L-Tyrosine methyl ester	Amino Acid Metabolism	177906	0.70	1.00
88.0524	6.773	C4H8O2	Butanoic acid	Carbohydrate Metabolism	1865108	0.24	1.00
104.0473	6.779	C4H8O3	4-Hydroxybutanoic acid	Carbohydrate Metabolism	4315442	0.11	1.00
84.0211	8.661	C4H4O2	3-Butynoate	Carbohydrate Metabolism	269867	0.10	1.00
88.0524	4.581	C4H8O2	(R)-Acetoin	Carbohydrate Metabolism	1097746	0.24	1.00
197.0816	9.71	C20H26O8	Glaucarubolone	0	739688	0.39	1.00
197.1164	9.553	C9H15N3O2	Hercynine	Amino Acid Metabolism	11895	0.39	1.00
198.1619	3.562	C12H22O2	[PR] Citronellyl acetate	Lipids: Prenols	96903	1.39	1.00

Mass	RT	Formula	Putative metabolite	Class	Maximum intensity	Fold Change Cleaned mucus	Raw mucus
200.0086	9.387	C4H9O7P	D-Erythrose 4-phosphate	Carbohydrate Metabolism	223912	0.46	1.00
200.1412	3.947	C11H20O3	[FA hydroxy(11:1)] 2-hydroxy-10-undecenoic acid	Lipids: Fatty Acyls	11555	0.69	1.00
200.1776	3.365	C12H24O2	Dodecanoic acid	Lipid Metabolism	111010	0.82	1.00
200.9766	12.54	C3H7NO5S2	S-Sulfo-L-cysteine	Amino Acid Metabolism	9203	0.30	1.00
201.1365	4.465	C10H19NO3	Capryloylglycine	0	129716	0.26	1.00
202.1204	4.583	C10H18O4	[FA (10:0/2:0)] Decanedioic acid	Lipids: Fatty Acyls	18031	0.35	1.00
116.0109	8.919	C4H4O4	Maleic acid	Carbohydrate Metabolism	41117	0.10	1.00
202.1317	6.724	C9H18N2O3	Ile-Ala	Peptide(di-)	270682	3.89	1.00
146.0215	10.42	C5H6O5	Methyloxaloacetate	Carbohydrate Metabolism	886066	0.09	1.00
202.1721	3.34	C15H22	alpha-Curcumene	0	2785	1.29	1.00
203.0794	9.713	C8H13NO5	N2-Acetyl-L-aminoadipate	Amino Acid Metabolism	1162689	0.52	1.00
203.0905	9.475	C7H13N3O4	Ala-Asn	Peptide(di-)	15539	0.64	1.00
132.0058	8.279	C4H4O5	Oxaloacetate	Carbohydrate Metabolism	10504	0.07	1.00
204.0745	11.01	C7H12N2O5	Glu-Gly	Peptide(di-)	2229523	0.40	1.00
164.0685	9.772	C6H12O5	L-Rhamnose	Carbohydrate Metabolism	127936	0.14	1.00
162.0528	10.04	C6H10O5	2-Dehydro-3-deoxy-L-rhamnonate	Carbohydrate Metabolism	338909	0.10	1.00

Mass	RT	Formula	Putative metabolite	Class	Maximum intensity	Fold Change Cleaned mucus	Raw mucus
74.0367	10.88	C3H6O2	(S)-Lactaldehyde	Carbohydrate Metabolism	473115	0.06	1.00
92.0473	8.852	C3H8O3	Glycerol	Carbohydrate Metabolism	2333236	0.19	1.00
204.1150	3.395	C13H16O2	4'-Hydroxy-3'-prenylacetophenone	0	4531	1.80	1.00
106.0265	8.968	C3H6O4	D-Glycerate	Carbohydrate Metabolism	891643	0.30	1.00
205.0738	4.252	C11H11NO3	5-Methoxyindoleacetate	Amino Acid Metabolism	11949	0.16	1.00
205.0950	7.858	C8H15NO5	N-Acetyl-D-fucosamine	0	14909	0.70	1.00
206.0725	7.533	C7H14N2O3S	Met-Gly	Peptide(di-)	19840	0.45	1.00
206.0902	8.864	C7H14N2O5	Thr-Ser	Peptide(di-)	6759	2.05	1.00
180.0633	12.89	C6H12O6	D-Glucose	Carbohydrate Metabolism	5223119	0.33	1.00
206.1670	3.664	C14H22O	[PR] (+)-15-nor-4-thujopsen-3-one	Lipids: Prenols	14562	0.31	1.00
207.0201	4.483	C15H15N4O6ClS	Chlorimuron ethyl	0	43249	0.50	1.00
207.0895	4.259	C11H13NO3	N-Acetyl-L-phenylalanine	Amino Acid Metabolism	8169	0.10	1.00
162.0528	6.694	C6H10O5	3-Ethylmalate	Carbohydrate Metabolism	149312	0.21	1.00
89.9953	12.7	C2H2O4	Oxalate	Carbohydrate Metabolism	256621	0.11	1.00
208.1827	3.734	C14H24O	[FA (14:2)] 5,8-tetradecadienal	Lipids: Fatty Acyls	7265	0.71	1.00
209.0689	7.193	C10H11NO4	4-Hydroxyphenylacetylglycine	Amino Acid Metabolism	7142	0.15	1.00
88.0160	6.78	C3H4O3	3-Oxopropanoate	Carbohydrate Metabolism	11483196	0.20	1.00

Mass	RT	Formula	Putative metabolite	Class	Maximum intensity	Fold Change Cleaned mucus	Raw mucus
210.1256	4.526	C12H18O3	(+)-7-Isojasmonic acid	Lipids: Fatty Acyls	8740	0.42	1.00
212.0085	9.723	C5H9O7P	P-DPD	0	27036	0.29	1.00
212.0911	12.03	C8H12N4O3	Gly-His	Peptide(di-)	36019	1.12	1.00
166.0479	12.37	C5H10O6	D-Xylonate	Carbohydrate Metabolism	96934	0.14	1.00
214.1317	7.211	C10H18N2O3	Dethiobiotin	Metabolism of Cofactors and Vitamins	85931	1.00	1.00
214.1568	3.437	C12H22O3	3-Oxododecanoic acid	Lipids: Fatty Acyls	13060	0.24	1.00
215.0558	11.52	C5H14NO6P	sn-glycero-3-Phosphoethanolamine	Lipid Metabolism	1151417	1.02	1.00
215.1157	4.34	C10H17NO4	2-Amino-9,10-epoxy-8-oxodecanoic acid	Lipids: Fatty Acyls	15397	0.28	1.00
215.1521	4.146	C11H21NO3	N-Nonanoylglycine	0	392644	0.24	1.00
215.1885	4.061	C12H25NO2	[FA amino(12:0)] 12-amino-dodecanoic acid	Lipids: Fatty Acyls	120516	0.38	1.00
196.0582	10.26	C6H12O7	L-Gulonate	Carbohydrate Metabolism	741457	0.49	1.00
194.0427	11.89	C6H10O7	D-Glucuronate	Carbohydrate Metabolism	173269	0.12	1.00
216.1361	4.119	C11H20O4	[FA (11:0/2:0)] Undecanedioic acid	Lipids: Fatty Acyls	8380	0.17	1.00
150.0527	8.887	C5H10O5	D-Ribose	Carbohydrate Metabolism	28450	0.17	1.00
154.0030	8.784	C3H7O5P	Propanoyl phosphate	Carbohydrate Metabolism	20397	2.53	1.00
74.0367	6.788	C3H6O2	Propanoate	Carbohydrate Metabolism	676329	0.24	1.00

Mass	RT	Formula	Putative metabolite	Class	Maximum intensity	Fold Change Cleaned mucus	Raw mucus
161.0687	10.91	C6H11NO4	N-Methyl-L-glutamate	Energy Metabolism	2637556	0.19	1.00
75.0684	8.72	C3H9NO	Trimethylamine N-oxide	Energy Metabolism	6619091	0.15	1.00
218.0901	10.38	C8H14N2O5	gamma-L-Glutamyl-D-alanine	Peptide	432642	0.34	1.00
125.0146	11.59	C2H7NO3S	Taurine	Lipid Metabolism	25771846	0.24	1.00
218.1055	4.961	C12H14N2O2	N-Acetylserotonin	Amino Acid Metabolism	8792	1.02	1.00
172.1463	3.479	C10H20O2	Decanoic acid	Lipid Metabolism	161381	0.50	1.00
218.1306	3.378	C14H18O2	[FA (14:5)] 5,7,9,11,13-tetradecapentaenoic acid	Lipids: Fatty Acyls	4928	1.42	1.00
172.0136	10.74	C3H9O6P	sn-Glycerol 3-phosphate	Lipid Metabolism	1490949	0.12	1.00
90.0317	7.29	C3H6O3	Glyceraldehyde	Lipid Metabolism	96085136	0.14	1.00
169.0503	10.63	C4H12NO4P	Phosphodimethylethanolamine	Lipid Metabolism	548202	0.63	1.00
149.1051	8.42	C6H15NO3	Triethanolamine	Lipid Metabolism	52819	0.55	1.00
220.1463	3.62	C14H20O2	Oblongolide	0	8369	0.58	1.00
221.0899	9.612	C8H15NO6	N-Acetyl-D-mannosamine	Carbohydrate Metabolism	187069	0.57	1.00
145.1102	10.14	C7H15NO2	Acetylcholine	Lipid Metabolism	12819063	0.24	1.00
155.0347	10.72	C3H10NO4P	N-Methylethanolamine phosphate	Lipid Metabolism	91418	0.04	1.00
222.1004	6.701	C11H14N2O3	Phe-Gly	Peptide(di-)	476518	2.47	1.00
102.0316	10.13	C4H6O3	Acetoacetate	Lipid Metabolism	101655	0.31	1.00
275.1732	7.369	C13H25NO5	[FA hydroxy(10:0)] N-(3S-hydroxydecanoyl)-L-serine	Lipids: Fatty Acyls	378421	0.12	1.00
224.1776	3.338	C14H24O2	[FA (14:2)] 5,8-tetradecadienoic acid	Lipids: Fatty Acyls	37173	0.50	1.00
224.1888	4.165	C13H24N2O	Cuscohygrine	0	8758	2.29	1.00

Mass	RT	Formula	Putative metabolite	Class	Maximum intensity	Fold Change Cleaned mucus	Raw mucus
302.2245	3.301	C20H30O2	[FA (20:5)] 5Z,8Z,11Z,14Z,17Z-eicosapentaenoic acid	Lipids: Fatty Acyls	128674	3.76	1.00
226.1065	11.64	C9H14N4O3	Carnosine	Amino Acid Metabolism	791685	0.47	1.00
226.1205	4.565	C12H18O4	[FA oxo,hydroxy(5:1/5:0)] (1S,2R)-3-oxo-2-(5'-hydroxy-2'Z-pentenyl)-cyclopentaneacetic acid	Lipids: Fatty Acyls	19615	0.33	1.00
226.1681	5.079	C12H22N2O2	1,8-Diazacyclotetradecane-2,9-dione	0	26609	0.18	1.00
226.1932	3.344	C14H26O2	(9Z)-Tetradecenoic acid	Lipids: Fatty Acyls	137071	0.59	1.00
288.2300	3.572	C16H32O4	10,16-Dihydroxyhexadecanoic acid	Lipids: Fatty Acyls	22805	0.09	1.00
322.2508	3.294	C20H34O3	[FA hydroxy(20:3)] 15S-hydroxy-8Z,11Z,13E-eicosatrienoic acid	Lipids: Fatty Acyls	44464	2.76	1.00
352.2248	3.526	C20H32O5	[FA oxo,hydroxy(2:0)] 9-oxo-11R,15S-dihydroxy-5Z,13E-prostadienoic acid	Lipids: Fatty Acyls	35108	0.19	1.00
227.2249	3.846	C14H29NO	myristic amide	0	5560	1.11	1.00
228.1361	3.868	C12H20O4	Traumatic acid	Lipids: Fatty Acyls	10916	0.39	1.00
326.2093	3.661	C18H30O5	[FA trihydroxy(2:0)] 9S,11R,15S-trihydroxy-2,3-dinor-5Z,13E-prostadienoic acid-cyclo[8S,12R]	Lipids: Fatty Acyls	16371	0.11	1.00
328.2249	3.825	C18H32O5	[FA trihydrox] 9S,11R,15S-trihydroxy-2,3-dinor-13E-prostaenoic acid-cyclo[8S,12R]	Lipids: Fatty Acyls	20282	0.08	1.00
228.2089	3.322	C14H28O2	Tetradecanoic acid	Lipid Metabolism	1458000	1.16	1.00
356.2563	3.567	C20H36O5	Prostaglandin F1alpha	Lipids: Fatty Acyls	21245	0.05	1.00
229.1677	3.893	C12H23NO3	N-Decanoylglycine	0	710130	0.21	1.00
229.2042	3.812	C13H27NO2	2S-Amino-tridecanoic acid	0	14767	0.58	1.00

Mass	RT	Formula	Putative metabolite	Class	Maximum intensity	Fold Change Cleaned mucus	Raw mucus
276.2089	3.423	C18H28O2	[FA (18:4)] 6Z,9Z,12Z,15Z-octadecatetraenoic acid	Lipids: Fatty Acyls	126041	2.17	1.00
292.2039	3.451	C18H28O3	[FA oxo(18:3)] 4-oxo-9Z,11E,13E-octadecatrienoic acid	Lipids: Fatty Acyls	20241	2.12	1.00
130.0993	3.818	C7H14O2	[FA methyl(6:0)] 2-methyl-hexanoic acid	Lipids: Fatty Acyls	239630	0.58	1.00
158.1306	3.526	C9H18O2	Nonanoic acid	Lipids: Fatty Acyls	508010	0.56	1.00
231.1331	12.61	C8H17N5O3	Gly-Arg	Peptide(di-)	30683	1.06	1.00
102.0680	4.555	C5H10O2	Pentanoate	Lipids: Fatty Acyls	1102170	0.34	1.00
232.1059	9.662	C9H16N2O5	N2-Succinyl-L-ornithine	Amino Acid Metabolism	35683	1.99	1.00
186.1255	3.49	C10H18O3	10-Oxodecanoate	Lipids: Fatty Acyls	17039	0.25	1.00
188.1412	3.514	C10H20O3	10-Hydroxydecanoic acid	Lipids: Fatty Acyls	19611	0.23	1.00
232.1463	3.347	C15H20O2	Costunolide	Biosynthesis of Secondary Metabolites	2202	1.55	1.00
233.0357	6.598	C8H11NO5S	Dopamine 3-O-sulfate	0	14150	0.00	1.00
212.1412	3.749	C12H20O3	[FA oxo(12:1)] 12-oxo-10E-dodecenoic acid	Lipids: Fatty Acyls	26693	0.22	1.00
233.1263	6.791	C10H19NO5	Hydroxypropionylcarnitine	0	50799	0.17	1.00
136.0371	9.591	C4H8O5	[FA trihydroxy(4:0)] 2,2,4-trihydroxy-butanoic acid	Lipids: Fatty Acyls	864797	0.21	1.00
234.0851	11.16	C8H14N2O6	Glu-Ser	Peptide(di-)	202159	0.29	1.00
234.1216	12.62	C9H18N2O5	2,6-Diamino-7-hydroxy-azelaic acid	0	6239	0.03	1.00
235.0739	7.644	C19H26N4O8S	Ala-Asp-Cys-Tyr	Peptide(tetra-)	4489	2.12	1.00
235.1062	3.804	C10H21NOS2	9-methylthiononylhydroximate	0	39441	1.05	1.00

Mass	RT	Formula	Putative metabolite	Class	Maximum intensity	Fold Change	
						Cleaned mucus	Raw mucus
230.1514	8.009	C12H22O4	Dodecanedioic acid	Lipids: Fatty Acyls	13015	0.19	1.00
236.0796	8.086	C11H12N2O4	L-Formylkynurenine	Amino Acid Metabolism	89950	0.11	1.00
236.1161	4.325	C12H16N2O3	Carbetamide	0	215659	10.50	1.00
118.0629	6.758	C5H10O3	5-Hydroxypentanoate	Lipids: Fatty Acyls	559836	0.17	1.00
236.1776	3.363	C15H24O2	Farnesoic acid	Biosynthesis of Secondary Metabolites	44856	0.98	1.00
237.0862	7.316	C9H11N5O3	6-Pyruvoyltetrahydropterin	Metabolism of Cofactors and Vitamins	75084	0.10	1.00
238.1933	3.615	C15H26O2	[FA (15:0)] 3-pentadecynoic acid	Lipids: Fatty Acyls	4640	0.75	1.00
239.1019	8.658	C9H13N5O3	Dihydrobiopterin	Metabolism of Cofactors and Vitamins	21127	2.43	1.00
100.0524	10.24	C5H8O2	Tiglic acid	Lipids: Fatty Acyls	35656	0.16	1.00
332.2563	3.601	C18H36O5	[FA trihydroxy(18:0)] 9,10,18-trihydroxy-octadecanoic acid	Lipids: Fatty Acyls	16804	0.08	1.00
132.0786	4.297	C6H12O3	[FA hydroxy(6:0)] 4-hydroxy-hexanoic acid	Lipids: Fatty Acyls	632679	0.05	1.00
240.1725	3.621	C14H24O3	[FA oxo(5:2/5:0/4:0)] (1S,2S)-3-oxo-2-pentyl-cyclopentanebutanoic acid	Lipids: Fatty Acyls	36227	0.17	1.00
259.1782	6.703	C13H25NO4	[FA (6:0)] O-hexanoyl-R-carnitine	Lipids: Fatty Acyls	319498	0.12	1.00
241.2042	3.781	C14H27NO2	[SP (14:0/2:0)] tetradecasphinga-4E,6E-dienine	Lipids: Sphingolipids	59986	0.98	1.00
242.0190	11.56	C6H11O8P	6-deoxy-5-ketofructose-1-phosphate	0	414274	0.26	1.00
231.1470	7.237	C11H21NO4	O-Butanoylcarnitine	Lipids: Fatty Acyls	6072763	0.11	1.00

Mass	RT	Formula	Putative metabolite	Class	Maximum intensity	Fold Change Cleaned mucus	Raw mucus
242.1882	3.653	C14H26O3	[FA oxo(14:0)] 3-oxo-tetradecanoic acid	Lipids: Fatty Acyls	17974	0.76	1.00
242.2247	3.309	C15H30O2	[FA methyl(14:0)] 12-methyl-tetradecanoic acid	Lipids: Fatty Acyls	433413	0.99	1.00
243.0853	9.774	C9H13N3O5	gamma-Glutamyl-beta-cyanoalanine	Amino Acid Metabolism	4466993	0.65	1.00
118.0629	4.569	C5H10O3	formyl 3-hydroxy-butanoate	Lipids: Fatty Acyls	2283309	0.10	1.00
294.2195	3.313	C18H30O3	[FA oxo(5:1/5:0/8:0)] (1S,2S)-3-oxo-2-(2'Z-pentenyl)-cyclopentaneoctanoic acid	Lipids: Fatty Acyls	297595	2.69	1.00
243.1582	17.25	C11H21N3O3	Lys-Pro	Peptide(di-)	58960	0.00	1.00
243.1834	3.732	C13H25NO3	N-Undecanoylglycine	0	161104	0.54	1.00
243.2198	3.798	C14H29NO2	[FA amino(14:0)] 2-amino-tetradecanoic acid	Lipids: Fatty Acyls	20020	0.82	1.00
244.1786	3.798	C12H24N2O3	Leucyl-leucine	Peptide(di-)	190039	1.56	1.00
244.2040	3.429	C14H28O3	2S-Hydroxytetradecanoic acid	Lipids: Fatty Acyls	121611	0.14	1.00
217.1313	7.909	C10H19NO4	O-Propanoylcarnitine	Lipids: Fatty Acyls	2594574	0.16	1.00
116.0837	4.107	C6H12O2	Hexanoic acid	Lipids: Fatty Acyls	1035697	0.71	1.00
72.0211	11.78	C3H4O2	Propenoate	Lipids: Fatty Acyls	623377	0.27	1.00
229.2405	4.142	C14H31NO	[SP (14:0)] 1-deoxy-tetradecasphinganine	Lipids: Sphingolipids	192525	7.32	1.00
317.2929	6.702	C18H39NO3	[SP hydrox] 4-hydroxysphinganine	Lipids: Sphingolipids	54954	0.21	1.00
207.0929	7.735	C8H17NO3S	CHES	Medium Component	24558	0.04	1.00
191.0252	11.05	C6H9NO4S	a Cysteine adduct	Medium Contaminant	535917	0.12	1.00
191.0252	4.379	C6H9NO4S	a Cysteine adduct	Medium Contaminant	68323	0.09	1.00

Mass	RT	Formula	Putative metabolite	Class	Maximum intensity	Fold Change Cleaned mucus	Raw mucus
139.0269	7	C6H5NO3	6-Hydroxynicotinate	Metabolism of Cofactors and Vitamins	4278269	0.71	1.00
97.0527	6.904	C10H14N2O2	6-Hydroxypseudooxynicotine	Metabolism of Cofactors and Vitamins	29197	0.29	1.00
115.0269	6.62	C4H5NO3	Maleamate	Metabolism of Cofactors and Vitamins	10524	0.24	1.00
254.0901	20.72	C11H14N2O5	N-Ribosylnicotinamide	Metabolism of Cofactors and Vitamins	56224	0.12	1.00
247.1168	12.38	C9H17N3O5	Thr-Ala-Gly	Peptide(tri-)	16225	4.86	1.00
152.0585	6.725	C7H8N2O2	N1-Methyl-2-pyridone-5-carboxamide	Metabolism of Cofactors and Vitamins	75235	0.10	1.00
247.1530	11.98	C10H21N3O4	Lys-Thr	Peptide(di-)	12266	7.91	0.00
127.0269	8.176	C5H5NO3	2,3,6-Trihydroxypyridine	Metabolism of Cofactors and Vitamins	96222	0.06	1.00
248.1009	10.53	C9H16N2O6	Glu-Thr	Peptide(di-)	114971	0.24	1.00
248.1194	4.24	C10H20N2O3S	Met-Val	Peptide(di-)	93856	2.95	1.00
248.1775	3.559	C16H24O2	[FA (16:4)] 4,7,10,13-hexadecatetraenoic acid	Lipids: Fatty Acyls	6284	0.64	1.00
299.0768	10.51	C9H18NO8P	D-4'-Phosphopantothenate	Metabolism of Cofactors and Vitamins	137510	0.20	1.00
276.1068	10.34	C9H16N4O6	4-(1-D-Ribitylamino)-5-amino-2,6-dihydroxypyrimidine	Metabolism of Cofactors and Vitamins	19179	14.49	0.00
249.1728	7.809	C15H23NO2	Lophocerine	0	4944	3.48	0.00
73.01636	11.89	C2H3NO2	Iminoglycine	Metabolism of Cofactors and Vitamins	17773	0.29	1.00

Mass	RT	Formula	Putative metabolite	Class	Maximum intensity	Fold Change Cleaned mucus	Raw mucus
251.1017	7.091	C10H13N5O3	Deoxyadenosine	Nucleotide Metabolism	19939	3.74	1.00
251.1156	3.659	C13H17NO4	Ac-Tyr-OEt	0	9271	0.00	1.00
73.0163	9.649	C2H3NO2	Iminoglycine	Metabolism of Cofactors and Vitamins	463428	0.25	1.00
252.1109	4.615	C12H16N2O4	3-Hydroxyhexobarbital	0	93205	4.94	1.00
252.1361	3.4	C14H20O4	ubiquinol-1	0	5326	0.61	1.00
252.2092	3.307	C16H28O2	[FA (16:2)] 9,12-hexadecadienoic acid	Lipids: Fatty Acyls	154366	0.71	1.00
73.0163	8.277	C2H3NO2	Iminoglycine	Metabolism of Cofactors and Vitamins	39879	0.22	1.00
253.2405	3.744	C16H31NO	Palmitoleamide	Lipids: Fatty Acyls	36204	1.18	1.00
254.0578	5.489	C15H10O4	[PK] Chrysophanol	Lipids: Polyketides	70314	3.65	1.00
264.1043	19.9	C12H16N4OS	Thiamin	Metabolism of Cofactors and Vitamins	384948	0.14	1.00
254.2247	3.298	C16H30O2	(9Z)-Hexadecenoic acid	Lipid Metabolism	6913301	0.72	1.00
255.2198	3.76	C15H29NO2	9-Decenoylcholine	0	64381	0.80	1.00
255.2561	3.74	C16H33NO	Palmiticamide	0	109115	1.41	1.00
183.0531	7.632	C8H9NO4	4-Pyridoxate	Metabolism of Cofactors and Vitamins	71462	0.09	1.00
256.2402	3.295	C16H32O2	Hexadecanoic acid	Lipid Metabolism	8181059	0.82	1.00
257.1990	3.614	C14H27NO3	N-Lauroylglycine	0	28401	0.33	1.00
258.0140	12.24	C6H11O9P	D-Glucono-1,5-lactone 6-phosphate	Carbohydrate Metabolism	127011	0.32	1.00
80.0374	11.09	C4H4N2	Pyrimidine	Nucleotide Metabolism	65554	0.80	1.00
149.0701	9.743	C6H7N5	7-Methyladenine	Nucleotide Metabolism	55206	0.29	1.00

Mass	RT	Formula	Putative metabolite	Class	Maximum intensity	Fold Change Cleaned mucus	Raw mucus
120.0436	6.832	C5H4N4	Purine	Nucleotide Metabolism	26902	0.00	1.00
259.1419	4.584	C12H21NO5	N-(3-oxooctanoyl)-L-homoserine	0	10302	0.22	1.00
259.1782	4.615	C13H25NO4	Hexanoylcarnitine	0	296061	0.12	1.00
136.0385	8.699	C5H4N4O	Hypoxanthine	Nucleotide Metabolism	109787360	0.35	1.00
329.0525	7.649	C10H12N5O6P	3',5'-Cyclic AMP	Nucleotide Metabolism	11520	0.31	1.00
260.0295	11.7	C6H13O9P	D-Glucose 6-phosphate	Carbohydrate Metabolism	222583	0.25	1.00
252.0858	7.507	C10H12N4O4	Deoxyinosine	Nucleotide Metabolism	21148	0.19	1.00
152.0333	9.058	C5H4N4O2	Xanthine	Nucleotide Metabolism	7370014	0.34	1.00
284.0756	9.546	C10H12N4O6	Xanthosine	Nucleotide Metabolism	64968	0.18	1.00
260.2139	3.586	C18H28O	[FA (6:0)] 6-[5]-ladderane-1-hexanol	Lipids: Fatty Acyls	13569	0.94	1.00
74.0003	8.767	C2H2O3	Glyoxylate	Nucleotide Metabolism	30293	0.20	1.00
97.9673	12.82	H2O4S	Sulfate	Nucleotide Metabolism	4940593	0.30	1.00
128.0585	6.622	C5H8N2O2	5,6-Dihydrothymine	Nucleotide Metabolism	23304	0.15	1.00
262.0800	12.03	C9H14N2O7	Glu-Asp	Peptide(di-)	36279	0.56	1.00
262.1317	6.614	C14H18N2O3	Phe-Pro	Peptide(di-)	21120	0.61	1.00
262.1350	3.934	C11H22N2O3S	Leu-Met	Peptide(di-)	23082	0.44	1.00
263.0463	12.83	C9H13NO6S	Epinephrinesulfate	0	18806	0.04	1.00
126.0429	6.749	C5H6N2O2	Thymine	Nucleotide Metabolism	1153863	0.15	1.00
323.0517	11.17	C9H14N3O8P	CMP	Nucleotide Metabolism	329205	0.09	1.00
264.1109	3.982	C13H16N2O4	Formyl-N-acetyl-5-methoxykynurenamine	Amino Acid Metabolism	24393	0.00	1.00
264.1725	3.52	C16H24O3	Dehydrojuvabione	0	6856	0.33	1.00
227.0906	7.818	C9H13N3O4	Deoxycytidine	Nucleotide Metabolism	973602	0.08	1.00

Mass	RT	Formula	Putative metabolite	Class	Maximum intensity	Fold Change Cleaned mucus	Raw mucus
266.1125	10.25	C10H14N6O3	5'-amino-5'-deoxyadenosine	0	346242	0.59	1.00
266.1266	4.55	C13H18N2O4	Phe-Thr	Peptide(di-)	32895	2.64	1.00
266.1646	3.599	C12H27O4P	Tributyl phosphate	0	490906	0.92	1.00
266.1882	3.36	C16H26O3	[PR] Juvenile hormone III	Lipids: Prenols	11574	0.82	1.00
267.0966	7.747	C10H13N5O4	Adenosine	Nucleotide Metabolism	8129692	1.55	1.00
268.0806	9.051	C10H12N4O5	Inosine	Nucleotide Metabolism	2188104	0.57	1.00
268.2038	3.386	C16H28O3	[FA oxo(5:2/5:0/6:0)] (1R,2R)-3-oxo-2-pentyl-cyclopentanehexanoic acid	Lipids: Fatty Acyls	51710	0.78	1.00
270.2194	3.318	C16H30O3	[FA oxo(16:0)] 3-oxo-hexadecanoic acid	Lipids: Fatty Acyls	279470	1.34	1.00
271.1242	3.511	C23H43O12P	PI(14:1(9Z)/0:0)	Lipids: Glycerophospholipids	28668	1.48	1.00
271.2147	3.525	C15H29NO3	Tridecanoylglycine	0	38085	0.42	1.00
271.2511	4.112	C16H33NO2	[FA amino(16:0)] 2R-aminohexadecanoic acid	Lipids: Fatty Acyls	11895	1.66	1.00
272.1722	12.95	C22H44N10O6	Arg-Leu-Thr-Arg	Peptide(tetra-)	7209	0.38	1.00
272.6460	16.29	C21H39N9O8	Arg-Lys-Asp-Gln	Peptide(tetra-)	11899	0.75	1.00
305.0412	9.555	C9H12N3O7P	2',3'-Cyclic CMP	Nucleotide Metabolism	87180	0.05	1.00
112.0273	7.7	C4H4N2O2	Uracil	Nucleotide Metabolism	10851468	0.35	1.00
114.0429	6.913	C4H6N2O2	5,6-Dihydrouracil	Nucleotide Metabolism	440876	0.05	1.00
274.0454	11.07	C7H15O9P	1-Deoxy-D-altro-heptulose 7-phosphate	0	96742	2.39	1.00
274.1276	9.432	C10H18N4O5	N2-Succinyl-L-arginine	Amino Acid Metabolism	16759	0.85	1.00
274.2005	17.68	C12H26N4O3	Lys-Lys	Peptide(di-)	2259	0.19	1.00
275.1115	10.92	C10H17N3O6	Gamma-Glutamylglutamine	Peptide	1858213	0.29	1.00

Mass	RT	Formula	Putative metabolite	Class	Maximum intensity	Fold Change Cleaned mucus	Fold Change Raw mucus
275.1479	12.85	C11H21N3O5	L-a-glutamyl-L-Lysine	Peptide(di-)	94240	0.00	1.00
276.0956	11.7	C10H16N2O7	GammaGlutamylglutamicacid	Peptide	178671	0.28	1.00
250.0622	10.33	C8H14N2O5S	Glu-Cys	Peptide(di-)	68525	5.32	1.00
248.0643	12.1	C8H12N2O7	Asp-Asp	Peptide(di-)	139594	0.17	1.00
230.0902	10.93	C9H14N2O5	Aspartyl-L-proline	Peptide(di-)	121937	0.14	1.00
278.0725	7.56	C13H14N2O3S	5-hydroxyindole thiazolidine carboxylate	0	6990	0.10	1.00
278.0936	8.965	C10H18N2O5S	Glu-Met	Peptide(di-)	132708	0.34	1.00
278.1631	3.72	C15H22N2O3	Leu-Phe	Peptide(di-)	57719	0.25	1.00
278.2245	3.421	C18H30O2	[FA (18:3)] 9Z,12Z,15Z-octadecatrienoic acid	Lipids: Fatty Acyls	770583	2.06	1.00
279.2561	3.692	C18H33NO	Linoleamide	Lipids: Fatty Acyls	838385	1.04	1.00
280.1422	4.514	C14H20N2O4	Val-Tyr	Peptide(di-)	35612	3.36	1.00
280.2038	3.337	C17H28O3	Methyl (2E,6E)-(10R,11S)-10,11-epoxy-3,7,11-trimethyltrideca-2,6-dienoate	0	9202	1.36	1.00
280.2406	3.282	C18H32O2	Linoleate	Lipids: Fatty Acyls	16395685	0.88	1.00
218.0902	7.864	C8H14N2O5	L-Ala-L-Glu	Peptide(di-)	1016200	0.07	1.00
281.1123	6.721	C11H15N5O4	O6-Methyl-2'-deoxyguanosine	0	631528	0.49	1.00
281.2717	3.681	C18H35NO	[FA (18:1)] 9Z-octadecenamide	Lipids: Fatty Acyls	1824874	1.37	1.00
233.1375	12.09	C9H19N3O4	Lys-Ser	Peptide(di-)	256046	187.71	0.00
282.1830	3.577	C16H26O4	12-trans-Hydroxy juvenile hormone III	Biosynthesis of Secondary Metabolites	6317	0.27	1.00
282.2195	3.327	C17H30O3	[FA hydroxy(17:0)] 12S-hydroxy-16-heptadecynoic acid	Lipids: Fatty Acyls	5497	0.91	1.00

Mass	RT	Formula	Putative metabolite	Class	Maximum intensity	Fold Change	
						Cleaned mucus	Raw mucus
282.2562	3.274	C18H34O2	[FA (18:1)] 9Z-octadecenoic acid	Lipids: Fatty Acyls	14225621	0.88	1.00
273.1799	10.38	C11H23N5O3	Val-Arg	Peptide(di-)	32228	22.84	0.00
283.0914	10.34	C10H13N5O5	Guanosine	Nucleotide Metabolism	2135843	0.76	1.00
283.2873	3.738	C18H37NO	Octadecanamide	Lipids: Fatty Acyls	16456	1.25	1.00
284.0684	5.309	C16H12O5	Glycitein	Biosynthesis of Secondary Metabolites	11907	2.27	1.00
242.1014	9.331	C9H14N4O4	Ser-His	Peptide(di-)	26947	19.06	0.00
284.1119	10.65	C11H16N4O5	Coformycin	0	56418	0.33	1.00
284.1623	3.655	C30H48O10	Deoxycholicacid3-glucuronide	0	2745	1.01	1.00
284.2351	3.427	C17H32O3	[FA methoxy(16:1)] 2-methoxy-5Z-hexadecenoic acid	Lipids: Fatty Acyls	13123	1.13	1.00
260.1483	11.99	C10H20N4O4	Lys-Asn	Peptide(di-)	25691	18.10	0.00
287.1480	4.2	C12H21N3O5	N-Acetyl-ala-ala-ala-methylester	0	8444	0.92	1.00
287.2096	4.588	C15H29NO4	L-Octanoylcarnitine	Lipids: Fatty Acyls	88993	0.02	1.00
287.2460	3.766	C16H33NO3	[SP hydroxy,hydroxy,methyl(10:2/2:0)] 6R-(8-hydroxydecyl)-2R-(hydroxymethyl)-piperidin-3R-ol	Lipids: Sphingolipids	181162	6.08	1.00
203.1269	12.43	C8H17N3O3	Lys-Gly	Peptide(di-)	449644	13.71	1.00
288.1544	12.04	C10H20N6O4	Asn-Arg	Peptide(di-)	8245	5.49	0.00
261.1436	12.15	C9H19N5O4	Ser-Arg	Peptide(di-)	32842	7.51	1.00
303.1543	12.92	C11H21N5O5	Glu-Arg	Peptide(di-)	241000	0.20	1.00
289.1386	12.94	C10H19N5O5	Asp-Arg	Peptide(di-)	7523	0.04	1.00
261.1324	12.89	C10H19N3O5	Lys-Asp	Peptide(di-)	19333	0.19	1.00
245.1738	17.18	C11H23N3O3	Lys-Val	Peptide(di-)	365906	0.13	1.00

Mass	RT	Formula	Putative metabolite	Class	Maximum intensity	Fold Change Cleaned mucus	Raw mucus
259.1894	15.02	C12H25N3O3	Leu-Lys	Peptide(di-)	62104	0.13	1.00
293.1991	3.652	C17H27NO3	(+/-)-5-[(tert-Butylamino)-2'-hydroxypropoxy]-1,2,3,4-tetrahydro-1-naphthol	0	4997	1.41	1.00
294.1579	4.434	C15H22N2O4	Leu-Tyr	Peptide(di-)	26872	1.02	1.00
245.1375	6.734	C10H19N3O4	Leu-Asn	Peptide(di-)	85848	5.06	1.00
294.2558	3.634	C19H34O2	[FA methyl(18:0)] 9,10-methylene-9-octadecenoic acid	Lipids: Fatty Acyls	7174	0.20	1.00
174.1004	7.069	C7H14N2O3	Val-Gly	Peptide(di-)	142400	3.42	1.00
295.1282	5.447	C12H17N5O4	N6,N6-Dimethyladenosine	0	37397	0.81	1.00
295.2510	3.693	C18H33NO2	[SP (3:0)] sphinga-4E,8E,10E-trienine	Lipids: Sphingolipids	262529	1.73	1.00
296.1194	3.814	C14H20N2O3S	Met-Phe	Peptide(di-)	9764	0.05	1.00
296.2351	3.316	C18H32O3	[FA hydroxy(18:2)] 9S-hydroxy-10E,12Z-octadecadienoic acid	Lipids: Fatty Acyls	963299	2.36	1.00
188.1160	9.836	C8H16N2O3	Glycyl-leucine	Peptide(di-)	446517	0.52	1.00
246.1215	9.253	C10H18N2O5	Glu-Val	Peptide(di-)	74181	0.47	1.00
297.2667	3.673	C18H35NO2	[SP (2:0)] sphinga-4E,14Z-dienine	Lipids: Sphingolipids	116116	1.15	1.00
298.0114	9.536	C7H12N2O7P2	herbicide 14A	0	26707	1.52	1.00
298.2507	3.283	C18H34O3	2-Oxooctadecanoic acid	Lipids: Fatty Acyls	407784	1.87	1.00
218.1266	9.571	C9H18N2O4	Leu-Ser	Peptide(di-)	136001	0.25	1.00
299.2824	5.071	C18H37NO2	[FA (16:2)] N-hexadecyl-ethanolamine	Lipids: Fatty Acyls	140957	0.32	1.00
232.1423	8.652	C10H20N2O4	Leu-Thr	Peptide(di-)	147911	0.24	1.00
310.1163	10.19	C14H18N2O6	Glu-Tyr	Peptide(di-)	107391	0.20	1.00
301.1637	4.485	C13H23N3O5	(Ac)2-L-Lys-D-Ala	0	11141	0.66	1.00

Mass	RT	Formula	Putative metabolite	Class	Maximum intensity	Fold Change Cleaned mucus	Raw mucus
301.2001	4.011	C14H27N3O4	Leu-Leu-Gly	Peptide(tri-)	10271	5.54	0.00
301.2252	4.562	C16H31NO4	2-6dimethylheptanoylcarnitine	0	46737	0.00	1.00
301.2980	6.681	C18H39NO2	Sphinganine	Lipids: Sphingolipids	2410819	0.04	1.00
204.1110	12.74	C8H16N2O4	Val-Ser	Peptide(di-)	31728	0.20	1.00
202.1317	9.665	C9H18N2O3	Leu-Ala	Peptide(di-)	301610	0.16	1.00
333.1324	9.498	C16H19N3O5	Glu-Trp	Peptide(di-)	39646	0.16	1.00
304.1381	10.92	C11H20N4O6	D-Nopaline	Amino Acid Metabolism	285669	0.51	1.00
304.1382	8.485	C11H20N4O6	Ala-Gln-Ser	Peptide(tri-)	36828	0.56	1.00
264.0779	9.571	C9H16N2O5S	Met-Asp	Peptide(di-)	20461	0.15	1.00
307.0836	10.2	C10H17N3O6S	Glutathione	Amino Acid Metabolism	3627420	0.33	1.00
307.2147	3.748	C18H29NO3	dihydrocapsaicin	0	5413	1.65	1.00
308.1988	3.355	C18H28O4	5-O-Methylembelin	0	19262	0.58	1.00
308.2352	3.355	C19H32O3	[FA methyl(18:2)] methyl 9,10-epoxy-12,15-octadecadienoate	Lipids: Fatty Acyls	5459	1.24	1.00
228.1473	7.739	C11H20N2O3	Leu-Pro	Peptide(di-)	3304286	0.15	1.00
260.1371	8.174	C11H20N2O5	Glu-Leu	Peptide(di-)	448479	0.14	1.00
228.1473	9.489	C11H20N2O3	Ile-Pro	Peptide(di-)	817305	0.14	1.00
313.2252	4.549	C17H31NO4	9-Decenoylcarnitine	0	15448	0.00	1.00
313.2617	3.455	C18H35NO3	[FA (16:0)] N-hexadecanoyl-glycine	Lipids: Fatty Acyls	65711	1.67	1.00
314.1882	3.377	C20H26O3	momilactone A	0	4324	0.69	1.00
314.1952	18.33	C14H26N4O4	Lys-Ala-Pro	Peptide(tri-)	3339	0.50	1.00
314.2457	3.39	C18H34O4	[FA hydroxy(18:1)] 9,10-dihydroxy-12Z-octadecenoic acid	Lipids: Fatty Acyls	161679	0.25	1.00
315.2409	4.478	C17H33NO4	[FA (10:0)] O-decanoyl-R-carnitine	Lipids: Fatty Acyls	44640	0.10	1.00

Mass	RT	Formula	Putative metabolite	Class	Maximum intensity	Fold Change Cleaned mucus	Raw mucus
315.2773	3.769	C18H37NO3	[SP hydrox] 6-hydroxysphing-4E-enine	Lipids: Sphingolipids	33771	1.06	1.00
232.1423	12.13	C10H20N2O4	Ile-Thr	Peptide(di-)	11564	0.13	1.00
316.1857	10.75	C12H24N6O4	Ala-Ala-Arg	Peptide(tri-)	245081	0.27	1.00
316.2037	3.377	C20H28O3	[FA oxo(4:0)] 11-oxo-5Z,9,12E,14E-prostatetraenoic acid	Lipids: Fatty Acyls	67870	1.13	1.00
316.2613	3.404	C18H36O4	[FA hydroxy(18:0)] 9,10-dihydroxy-octadecanoic acid	Lipids: Fatty Acyls	27652	0.31	1.00
186.1004	6.774	C8H14N2O3	Ala-Pro	Peptide(di-)	162972	2.68	1.00
317.1586	7.58	C13H23N3O6	Leu-Ala-Asp	Peptide(tri-)	7140	0.23	1.00
218.0725	6.687	C8H14N2O3S	Cys-Pro	Peptide(di-)	90266	0.15	1.00
318.1539	12.52	C12H22N4O6	Lys-Asp-Gly	Peptide(tri-)	9046	0.13	1.00
318.2195	3.337	C20H30O3	Leukotriene A4	Lipids: Fatty Acyls	78899	1.70	1.00
189.0750	10.11	C6H11N3O4	Asn-Gly	Peptide(di-)	26711	17.55	1.00
162.0640	9.61	C5H10N2O4	Gly-Ser	Peptide(di-)	88060	9.30	1.00
321.2667	3.576	C20H35NO2	[FA (18:3)] N-(6Z,9Z,12Z-octadecatrienoyl)-ethanolamine	Lipids: Fatty Acyls	3971	1.09	1.00
192.0746	9.836	C6H12N2O5	Ser-Ser	Peptide(di-)	34008	6.57	1.00
176.0797	9.474	C6H12N2O4	Ala-Ser	Peptide(di-)	21231	2.41	1.00
323.1481	4.619	C15H21N3O5	Ala-Ala-Tyr	Peptide(tri-)	9340	0.53	1.00
323.2824	3.667	C20H37NO2	[FA (18:2)] N-(9Z,12Z-octadecadienoyl)-ethanolamine	Lipids: Fatty Acyls	38632	1.12	1.00
324.0357	10.8	C9H13N2O9P	UMP	Nucleotide Metabolism	499119	0.06	1.00
193.0772	11.99	C14H22N6O7	His-Gly-Ser-Ser	Peptide(tetra-)	64416	1.28	1.00

Mass	RT	Formula	Putative metabolite	Class	Maximum intensity	Fold Change Cleaned mucus	Raw mucus
324.1937	3.492	C18H28O5	[FA oxo,hydroxy(18:3)] 12-oxo-14,18-dihydroxy-9Z,13E,15Z-octadecatrienoic acid	Lipids: Fatty Acyls	4188	0.43	1.00
324.2664	3.325	C20H36O3	[FA hydroxy(20:2)] 11R-hydroxy-12E,14Z-eicosadienoic acid	Lipids: Fatty Acyls	33857	2.16	1.00
325.2000	6.697	C16H27N3O4	Ile-Pro-Pro	Peptide(tri-)	154080	0.32	1.00
325.2001	4.579	C16H27N3O4	Leu-Pro-Pro	Peptide(tri-)	237946	0.28	1.00
325.2075	3.885	C18H31NO2S	Farnesylcysteine	0	9282	0.46	1.00
325.2981	3.639	C20H39NO2	[FA (18:0)] N-(9Z-octadecenoyl)-ethanolamine	Lipids: Fatty Acyls	22417	0.93	1.00
325.3709	7.084	C22H47N	di-n-Undecylamine	0	72739	0.63	1.00
226.6475	15.21	C22H39N5O5	Ile-Lys-Pro-Pro	Peptide(tetra-)	17509	0.21	1.00
326.2457	3.627	C19H34O4	[FA methoxy,hydroxy(18:2)] 8-methoxy-13-hydroxy-9,11-octadecadienoic acid	Lipids: Fatty Acyls	6554	0.50	1.00
326.2821	3.27	C20H38O3	2-Oxophytanate	0	9343	1.68	1.00
327.2158	4.043	C16H29N3O4	Leu-Val-Pro	Peptide(tri-)	21239	0.26	1.00
327.2409	3.716	C18H33NO4	10-nitro-9E-octadecenoic acid	Lipids: Fatty Acyls	6127	0.89	1.00
328.1522	3.485	C16H24O7	[FA dioxo,hydroxy(4:0/2:0)] 9,15-dioxo-11R-hydroxy-2,3,4,5-tetranor-prostan-1,20-dioic acid	Lipids: Fatty Acyls	2273	1.17	1.00
356.2422	15.81	C17H32N4O4	Leu-Lys-Pro	Peptide(tri-)	415308	0.15	1.00
350.1589	4.598	C16H22N4O5	Phe-Ala-Asn	Peptide(tri-)	29622	13.83	1.00
344.2059	4.57	C15H28N4O5	Leu-Val-Asn	Peptide(tri-)	14147	9.17	0.00

Mass	RT	Formula	Putative metabolite	Class	Maximum intensity	Fold Change Cleaned mucus	Raw mucus
331.1380	7.611	C13H21N3O7	Glu-Pro-Ser	Peptide(tri-)	29274	0.56	1.00
332.1696	7.466	C13H24N4O6	Leu-Asn-Ser	Peptide(tri-)	11869	2.67	1.00
316.1746	6.656	C13H24N4O5	Leu-Ala-Asn	Peptide(tri-)	35536	6.35	1.00
245.1375	7.866	C10H19N3O4	Leu-Gly-Gly	Peptide(tri-)	24546	2.74	1.00
334.2144	3.377	C20H30O4	Prostaglandin A2	Lipids: Fatty Acyls	55795	0.43	1.00
302.1589	6.787	C12H22N4O5	Leu-Asn-Gly	Peptide(tri-)	121585	2.60	1.00
335.2096	3.306	C19H29NO4	Ankorine	Biosynthesis of Secondary Metabolites	30879	5.61	1.00
337.0674	9.165	C10H16N3O8P	5-Hydroxymethyldeoxycytidylate	Nucleotide Metabolism	292739	0.36	1.00
338.2456	3.341	C20H34O4	[FA hydroxy(20:3)] 8,9-dihydroxy-5Z,11Z,14Z-eicosatrienoic acid	Lipids: Fatty Acyls	26749	0.81	1.00
340.1746	7.707	C15H24N4O5	Gln-Pro-Pro	Peptide(tri-)	24006	0.30	1.00
340.2614	3.346	C20H36O4	[FA (20:2)] 15S-hydroperoxy-11Z,13E-eicosadienoic acid	Lipids: Fatty Acyls	14124	0.57	1.00
341.2565	4.36	C19H35NO4	trans-2-Dodecenoylcarnitine	0	10069	0.27	1.00
341.2930	3.551	C20H39NO3	[FA (18:0)] N-octadecanoyl-glycine	Lipids: Fatty Acyls	9811	1.46	1.00
342.2770	3.337	C20H38O4	[FA (20:0/2:0)] Eicosanedioic acid	Lipids: Fatty Acyls	6866	0.64	1.00
343.2721	4.293	C19H37NO4	1,2-dioctanoyl-1-amino-2,3-propanediol	0	54792	0.14	1.00
373.2212	4.595	C17H31N3O6	Glu-Ile-Ile	Peptide(tri-)	36517	0.32	1.00
346.2507	3.298	C22H34O3	Taxa-4(20),11(12)-dien-5alpha-acetoxy-10beta-ol	Biosynthesis of Secondary Metabolites	27222	2.03	1.00
347.0627	9.572	C10H14N5O7P	AMP	Nucleotide Metabolism	2301227	0.08	1.00
348.2664	3.286	C22H36O3	Anacardic acid	0	8764	2.29	1.00

Mass	RT	Formula	Putative metabolite	Class	Maximum intensity	Fold Change Cleaned mucus	Raw mucus
349.1485	7.561	C13H23N3O8	Glu-Thr-Thr	Peptide(tri-)	29027	0.54	1.00
289.1273	9.669	C11H19N3O6	Val-Asp-Gly	Peptide(tri-)	119560	0.12	1.00
351.2233	3.24	C37H67O10P	PG(13:0/18:3(6Z,9Z,12Z))	Lipids: Glycerophospholipids	4644	1.05	1.00
231.1218	6.712	C9H17N3O4	Ala-Ala-Ala	Peptide(tri-)	30223	23.97	0.00
260.1121	9.439	C9H16N4O5	Ala-Asn-Gly	Peptide(tri-)	29719	21.71	0.00
317.1335	9.492	C11H19N5O6	Ala-Asn-Asn	Peptide(tri-)	31876	6.44	1.00
359.1805	7.306	C14H25N5O6	Leu-Asn-Asn	Peptide(tri-)	23801	1.76	1.00
359.1844	4.363	C19H25N3O4	Phe-Pro-Pro	Peptide(tri-)	54604	0.33	1.00
362.2457	3.358	C22H34O4	[FA hydroxy(22:5)] (+/-)-19,20-dihydroxy-4Z,7Z,10Z,13Z,16Z-docosapentaenoic acid	Lipids: Fatty Acyls	10291	0.73	1.00
362.2821	3.236	C23H38O3	[ST (3:0)] 24-Nor-5beta-chol-22-ene-3alpha,7alpha,12alpha-triol	Lipids: Sterol lipids	4806	1.65	1.00
363.0577	11.81	C10H14N5O8P	GMP	Nucleotide Metabolism	593186	0.09	1.00
364.2613	3.348	C22H36O4	[FA oxo,hydroxy,dimethyl(2:0)] 9-oxo-15R-hydroxy-16,16-dimethyl-5Z,13E-prostadienoic acid	Lipids: Fatty Acyls	17680	0.61	1.00
367.2722	4.23	C21H37NO4	3, 5-Tetradecadiencarnitine	0	6428	0.49	1.00
368.3443	4.642	C27H44	[ST] (5Z,7E)-9,10-seco-5,7,10(19)-cholestatriene	Lipids: Sterol lipids	11252	0.50	1.00
288.1433	7.782	C11H20N4O5	Ala-Ala-Gln	Peptide(tri-)	18058	5.67	1.00
371.3035	4.126	C21H41NO4	Tetradecanoylcarnitine	0	121603	0.20	1.00
233.1011	9.532	C8H15N3O5	Ala-Gly-Ser	Peptide(tri-)	29631	3.78	1.00

Mass	RT	Formula	Putative metabolite	Class	Maximum intensity	Fold Change Cleaned mucus	Raw mucus
379.1047	9.624	C13H21N3O8S	(R)-S-Lactoylglutathione	Carbohydrate Metabolism	124026	0.02	1.00
383.1802	6.692	C16H25N5O6	Dihydrozeatin-7-N-dihydrozeatin	0	179529	0.64	1.00
383.1804	4.616	C16H25N5O6	Dihydrozeatin-O-glucoside	Biosynthesis of Secondary Metabolites	292589	0.61	1.00
384.1211	10.18	C21H20O7	Anthocyanin 3'-O-beta-D-glucoside	0	275394	0.54	1.00
384.2988	3.283	C21H40N2O4	N-palmitoyl glutamine	Lipids: Fatty Acyls	5885	0.76	1.00
385.2828	4.407	C21H39NO5	3-Hydroxy-cis-5-tetradecenoylcarnitine	0	5298	0.49	1.00
387.2985	4.435	C21H41NO5	2-Hydroxymyristoylcarnitine	0	10311	0.48	1.00
389.1910	7.513	C15H27N5O7	Ala-Thr-Ala-Gln	Peptide(tetra-)	8010	1.96	1.00
393.1648	7.418	C17H23N5O6	Phe-Asn-Asn	Peptide(tri-)	18080	1.63	1.00
393.2702	3.55	C43H79O10P	PG(15:1(9Z)/22:2(13Z,16Z))	Lipids: Glycerophospholipids	3678	1.34	1.00
395.3035	4.082	C23H41NO4	9,12-Hexadecadienoylcarnitine	0	9208	0.03	1.00
397.2829	3.453	C22H39NO5	[FA trihydroxy(2:0)] N-(9S,11R,15S-trihydroxy-5Z,13E-prostadienoyl)-ethanolamine	Lipids: Fatty Acyls	5784	1.31	1.00
217.1062	8.955	C8H15N3O4	Ala-Ala-Gly	Peptide(tri-)	49726	2.98	1.00
399.3348	4.003	C23H45NO4	[FA] O-Palmitoyl-R-carnitine	Lipids: Fatty Acyls	37733	0.38	1.00
402.2254	3.48	C20H34O8	5S-HETE di-endoperoxide	Lipids: Fatty Acyls	6889	1.19	1.00
410.3145	3.262	C23H42N2O4	N-oleoyl glutamine	Lipids: Fatty Acyls	37365	0.35	1.00
411.1642	7.204	C18H25N3O8	Glu-Thr-Tyr	Peptide(tri-)	31633	0.50	1.00
413.3141	4.289	C23H43NO5	3-Hydroxy-9-hexadecenoylcarnitine	0	6082	0.30	1.00

Appendix II

Mass	RT	Formula	Putative metabolite	Class	Maximum intensity	Fold Change Cleaned mucus	Raw mucus
416.3291	3.799	C27H44O3	[ST (3:0)] (5Z,7E)-(1S,3R)-9,10-seco-5,7,10(19)-cholestatriene-1,3,25-triol	Lipids: Sterol lipids	6465	1.21	1.00
247.1167	7.987	C9H17N3O5	Ala-Ala-Ser	Peptide(tri-)	122842	0.08	1.00
273.1324	8.589	C11H19N3O5	Ala-Pro-Ser	Peptide(tri-)	23910	0.00	1.00
426.0875	11.7	C13H22N4O8S2	Asp-Cys-Cys-Ser	Peptide(tetra-)	193555	0.45	1.00
427.3662	3.918	C25H49NO4	Stearoylcarnitine	0	14308	0.08	1.00
430.3082	3.432	C27H42O4	[ST (2:0)] 22S,25S-furospirost-5-en-3beta,26-diol	Lipids: Sterol lipids	5811	0.53	1.00
443.0243	12.51	C10H15N5O11P2	GDP	Nucleotide Metabolism	73840	0.02	1.00
449.3142	3.741	C26H43NO5	Glycodeoxycholate	Lipid Metabolism	13165	0.78	1.00
122.0367	4.571	C7H6O2	4-Hydroxybenzaldehyde	Xenobiotics Biodegradation and Metabolism	119132	0.34	1.00
456.1045	8.412	C17H21N4O9P	FMN	Energy Metabolism	28840	1.33	1.00
456.1045	4.792	C17H21N4O9P	FMN	Energy Metabolism	19874	2.56	1.00
477.2855	3.945	C23H44NO7P	LysoPE(0:0/18:2(9Z,12Z))	Lipids: Glycerophospholipids	16875	0.50	1.00
479.3011	3.891	C23H46NO7P	[PE (18:1)] 1-(9Z-octadecenoyl)-sn-glycero-3-phosphoethanolamine	Lipids: Glycerophospholipids	23467	0.44	1.00
481.3168	3.899	C23H48NO7P	[PC (15:0)] 1-pentadecanoyl-sn-glycero-3-phosphocholine	Lipids: Glycerophospholipids	14927	0.51	1.00
493.3167	4.097	C24H48NO7P	[PC (16:1)] 1-(9Z-hexadecenoyl)-sn-glycero-3-phosphocholine	Lipids: Glycerophospholipids	32190	0.53	1.00
495.3323	4.057	C24H50NO7P	[PC (16:0)] 1-hexadecanoyl-sn-glycero-3-phosphocholine	Lipids: Glycerophospholipids	93254	0.59	1.00

Mass	RT	Formula	Putative metabolite	Class	Maximum intensity	Fold Change Cleaned mucus	Fold Change Raw mucus
510.2958	3.263	C24H47O9P	[PG (18:1)] 1-(9E-octadecenoyl)-sn-glycero-3-phospho-(1'-sn-glycerol)	Lipids: Glycerophospholipids	5146	1.17	1.00
521.3480	3.994	C26H52NO7P	1-Oleoylglycerophosphocholine	0	87836	0.48	1.00
523.2910	3.456	C24H46NO9P	[PS (18:1)] 1-(9Z-octadecenoyl)-sn-glycero-3-phosphoserine	Lipids: Glycerophospholipids	12334	1.17	1.00
523.3640	3.973	C26H54NO7P	[PC (18:0)] 1-octadecanoyl-sn-glycero-3-phosphocholine	Lipids: Glycerophospholipids	11138	0.39	1.00
523.4963	3.39	C33H65NO3	Cer(d16:1/17:0)	Lipids: Sphingolipids	7246	0.25	1.00
537.5119	3.4	C34H67NO3	[SP (16:0)] N-(hexadecanoyl)-sphing-4-enine	Lipids: Sphingolipids	374097	0.25	1.00
551.5278	3.387	C35H69NO3	Cer(d18:1/17:0)	Lipids: Sphingolipids	14468	0.30	1.00
565.5432	3.386	C36H71NO3	[SP (18:0)] N-(octadecanoyl)-sphing-4-enine	Lipids: Sphingolipids	15663	0.35	1.00
593.5746	3.377	C38H75NO3	[SP (20:0)] N-(eicosanoyl)-sphing-4-enine	Lipids: Sphingolipids	7953	0.54	1.00
647.6217	3.387	C42H81NO3	[SP (24:0)] N-(15Z-tetracosenoyl)-sphing-4-enine	Lipids: Sphingolipids	8317	0.42	1.00